THE UNIVERSITY OF READING

Department of Meteorology

The Semi-Direct Aerosol Effect

Benjamin Thomas Johnson

A thesis submitted for the degree of Doctor of Philosophy

September 2003

Declaration

I confirm that this is my own work and the use of all material from other sources has been properly and fully acknowledged.

Benjamin Thomas Johnson

Abstract

This thesis investigates the 'semi-direct effect' whereby absorption of solar radiation by aerosols leads to changes in cloud cover and liquid water path. For example, solar heating in the atmosphere may reduce ambient relative humidity, suppress convective overturning, and lead to evaporation of clouds. The semi-direct effect is distinct from the indirect aerosol effect, whereby increases in aerosol concentration lead to increases in cloud albedo and lifetime via microphysical interactions. The semi-direct aerosol effect may have a significant warming impact on climate by 'burning off' low clouds that scatter solar radiation back to space but have little impact on outgoing longwave radiation. However, there are few model estimates of the semi-direct forcing, and its mechanisms are little understood.

In this thesis the semi-direct aerosol effect is investigated using the UK Met Office Large-Eddy-Model that explicitly resolves clouds and convection. The sensitivity of the semi-direct forcing to the amount and type of cloud is investigated using a number of stratocumulus and cumulus cases.

The presence of a moderate amount of absorbing aerosol in stratocumulus-capped boundary layers led to large positive semi-direct forcings that were several times greater in magnitude, and opposite in sign to the conventional direct forcing. For cumulus conditions, the semi-direct forcing was much smaller, about equal in magnitude to the direct forcing. When absorbing aerosols were located above clouds they actually promoted further cloud leading to a small a negative forcing. In summary, the semi-direct effect of absorbing aerosols, produced by human activity, may have a significant impact on climate change. However, local forcings depend on cloud conditions and the distribution of absorbing aerosols.

Some experiments were repeated using a single column climate model. The comparison shows that simple general circulation models do not adequately capture the semi-direct effect, and may underestimate the semi-direct forcing.

Acknowledgements

Who has the wisdom to count the clouds?

– Job 38:37a

Contents

CHAPTER 1

Introduction to aerosol radiative forcing and the semi-direct effect

1.1 Introduction

Over the past few decades international concern has grwon about human-caused (anthropogenic) climate change. The surface temperature of the globe has warmed by about 0.7 K since 1850 and much of this warming has been attributed to the release of greenhouse gases through the combustion of fossil fuels (IPCC, 2001, p698-699). With growth in worldwide use of fossil fuels, and other changes in the climate system, the global mean surface temperature is projected to rise a further 2 - 5 K by the year 2100. This would be accompanied by a 0.2 - 1.0 m rise in sea levels due to thermal expansion of the oceans and melting of ice sheets. Even if the temperature change is toward the lower end of the projected range it will have far reaching ecological and socio-economic consequences. Changes in precipitation patterns are also likely compounding the problem of flooding in some areas, and drought in others (IPCC, 2001, p549-551).

The main sources of uncertainty in projected temperature rises are uncertainties in future emissions of greenhouse gases and uncertainty in the sensitivity of the climate system, due to climate feedbacks. Changes in cloud cover and cloud properties are potentially a great source of feedback in the climate system but as yet cloud-climate feedbacks are poorly understood; it is not even clear whether the overall cloud feedback would be positive, negative, or neutral. Another source of considerable uncertainty in global warming scenarios is the impact of tropospheric aerosols on the climate. Aerosols (micron, or submicron sized particles) are produced both naturally (e.g. wind-blown sea salt) and by human activities, such as the combustion of fossil fuels and biomass burning. There is considerable evidence that the concentration of aerosols in the troposphere has increased over the last 150 years due to human activity (Fischer *et al.* (1998), Lavanchy *et al.* (1999), IPCC (2001) p306), and may increase further as developing countries grow in population and industrialise. However, the influence of tropospheric aerosols on climate is poorly understood at present, largely due to the complexity of their physical, chemical and optical properties, their variability in space and time, and their interactions with clouds.

Tropospheric aerosols have several effects on climate. Firstly, they interact directly with radiation (the

direct effect) either through scattering or absorption. Secondly, they have indirect effects on climate by altering microphysical and radiative properties of clouds. Furthermore, aerosols that are highly absorbing of solar radiation, such as soot (black carbon), may reduce cloud cover and liquid water content by heating the cloud and the environment within which the cloud forms. This is known as the semi-direct effect (Hansen *et al.*, 1997) because it is the result of direct interaction of aerosols with radiation but also influences climate indirectly by altering clouds. A more imaginative term for the process is the 'cloud-burning effect', which illustrates the link between increased solar heating and diminishing cloud amounts. The semi-direct effect is a relatively new concept within the aerosol-cloud-climate research field and has received much less attention in the literature than either the direct effect or the indirect effect. At present, the semi-direct effect is poorly understood, and it unclear how important it is in comparison to the direct and indirect effects. It is important to develop a better understanding of the the role of aerosols in climate to reduce uncertainty in understanding of past climate change and projections of future climate change. To this end, this thesis aims to build a fundamental understanding of how the semi-direct effect works and show what is required to accurately capture it in climate models.

1.2 Climate change and radiative forcing

1.2.1 Climate change in the past

Dramatic climate changes have occurred in the past. The earth has swung between ice ages and warm interglacial periods several times over the past few hundred thousand years. These changes have been slow, occurring over thousands or tens of thousands of years, driven predominantly by changes in the earths orbit. For the past ten thousand years the global climate has been relatively stable with only small variations related mainly to variability in the sun's output and volcanic emissions. However, an outstanding rise in temperatures has occurred in the last 150 years (since the industrial revolution), with much of the change occurring in the past 50 years (see Fig. 1.1). Although the level of increase (0.7 K) is modest in comparison to past climate changes through the iceages, the rate of increase is unprecedented, and it is very unlikely to have been caused by natural changes (IPCC, 2001, p130-136).

The recent global warming has been accompanied by rapid human-caused (anthropogenic) changes in the composition of the atmosphere. Carbon dioxide concentrations have risen from around 280 ppmv in 1850, at the start of the industrial revolution, to about 360 ppmv in the present day (see Fig. 3.3(b)
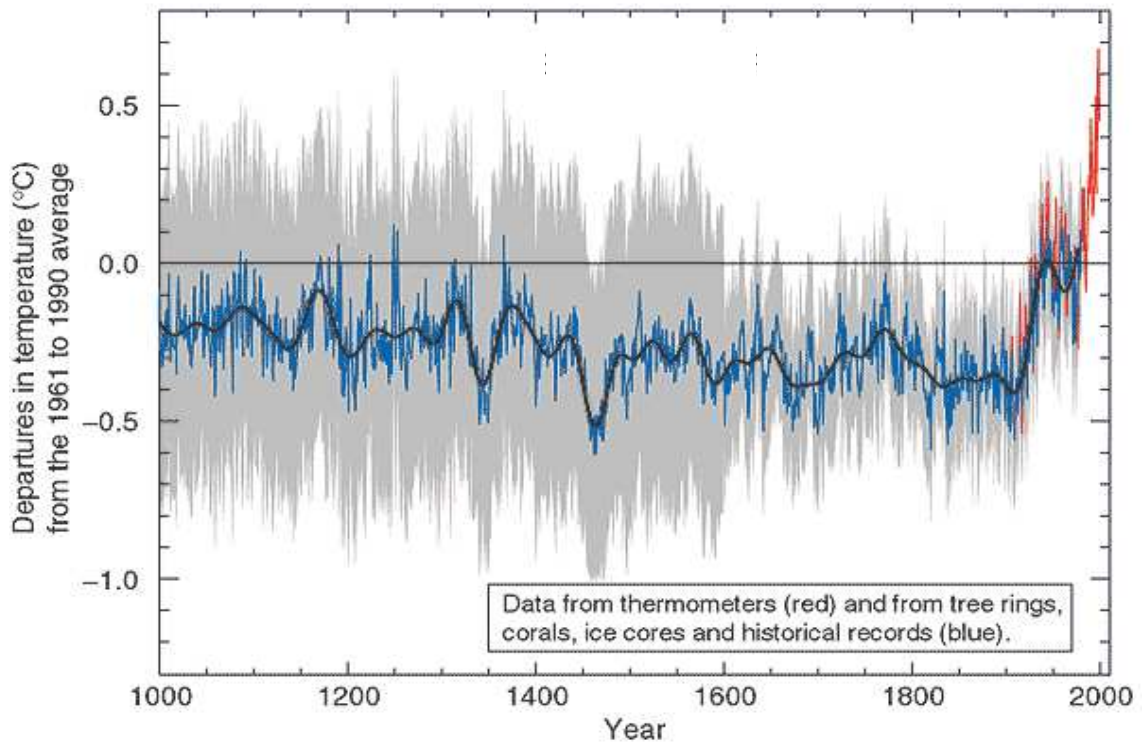
Figure 1.1: *The variation of annual mean surface temperature in the northern hemisphere, over the last 1000 years (taken from the summary for policy makers, IPCC (2001)).*

in IPCC (2001)). Carbon dioxide is a greenhouse gas; it absorbs outgoing infra-red radiation, thereby reducing the radiative loss of heat to space. There are many other greenhouse gases, such as water vapour and methane which occur naturally in the atmosphere and keep global temperatures some 33K higher than they would otherwise be. Anthropogenic emission of greenhouse gases, including carbon dioxide, methane, nitrous oxide and CFCs enhance the greenhouse effect, and are believed to be the main cause of global warming (e.g. Tett *et al.* (1999)).

Several other factors have either contributed to the global warming, or restrained it. These include natural processes, namely volcanic emissions and small changes in the sun's output over time, plus other human-caused (anthropogenic) changes in the composition of the atmosphere. For example, depletion of ozone in the stratosphere, due to emissions of chloro-flurocarbons (CFCs), has to some extent counteracted the warming. Increases in the concentration of atmospheric aerosols (small, micron to sub-micron sized particles) are also thought to have counteracted the warming. The contribution of these factors to changes in global surface temperature is estimated by calculating their radiative forcing.

1.2.2 The radiative forcing concept

Radiative forcing is a measure of the influence that an externally-caused change has on the radiative budget of the troposphere-surface system. For example, emissions of greenhouse gases leads to positive radiative forcing as they reduce the outgoing longwave radiation, forcing the earth out of radiative balance and towards a warmer state. More precisely, radiative forcing is defined as the change in net irradiance (in W m^{-2}) at the tropopause and after allowing stratospheric temperatures to re-adjust to radiative equilibrium, but with surface and tropospheric temperatures held fixed at their unperturbed values (IPCC, 2001, p353). Radiative forcing is a useful measure as it allows a straightforward estimate of the impact of some perturbation on global annual mean surface temperature. A radiative forcing (Δ F) is linked to a change in global annual mean surface temperature (Δ T) through the climate sensitivity parameter (λ):

$$\Delta T = \Delta F \lambda \tag{1.1}$$

The climate sensitivity parameter depends on various feedbacks within the climate system and can be determined by General Circulation Model (GCM) simulations. Although estimates vary widely between models, within individual models the climate sensitivity parameter is found to be reasonably independent of the radiative forcing mechanism or the global distribution of the radiative forcing for many, although not all radiative forcing mechanisms (Hansen *et al.* (1997), Joshi *et al.* (2003)). Thus, in general radiative forcing provides a quick and straightforward way of comparing the relative importance of various forcing agents to global warming despite uncertainties in climate sensitivity between GCMs. The radiative forcing concept assumes that the surface-troposphere is one coupled system so that the increase in surface temperature is independent of the height at which radiative energy is absorbed, so long as it is below the tropopause. This assumption, holds reasonably well for most forcing agents except ozone in the upper troposphere (discussed in next section), and absorbing aerosols (due to the semi-direct effect).

1.2.3 Radiative forcing since pre-industrial times

Figure 1.2, taken from IPCC (2001), shows estimates of the radiative forcing, of all major known sources since pre-industrial times (1750). The error bars indicate the uncertainty range judged from the range in current model estimates. The current level of scientific understanding of each source is
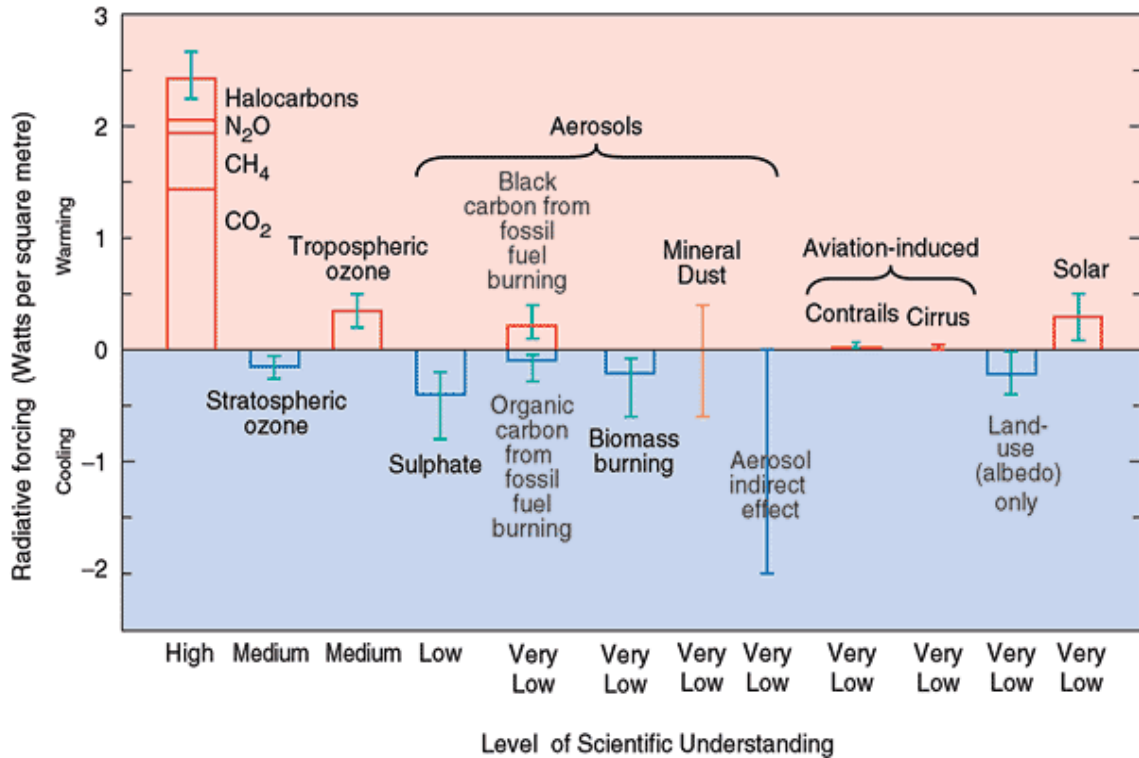
Figure 1.2: *The global annual mean radiative forcing of the climate system for the year 2000, relative to 1750 for all major known forcings (taken from the summary for policy makers, IPCC (2001)).*

also indicated below the axis. The radiative forcing from well-mixed greenhouse gases is well understood because their spectral absorption cross-sections and atmospheric concentrations are accurately known. Carbon dioxide (CO_2), produced by combustion of hydrocarbon fuels is the principal contributor. Other greenhouse gases include methane (CH_4), from increased agricultural activity, Nitrogen dioxide (N_2O) from fuel combustion, and halocarbons, including CFCs from propellants and refrigerants.

Ozone absorbs both longwave and shortwave radiation and acts as a greenhouse gas when in the stratosphere, and as a source of shortwave heating when in the troposphere. Depletion of stratospheric ozone, due to CFCs, has led to a negative radiative forcing, whereas increases of ozone in the troposphere, due to reactions with other pollutants (NO_x, CO, and CH_4) has led to a positive radiative forcing. There is a medium level of understanding for the radiative forcing of changes in ozone concentration because the spectral absorption cross section of ozone is well known but changes in the global distribution are less well known because the of the lack of quality of global observations. The distribution of ozone is very variable in space and time depending on detailed chemical processes, concentrations of many other gases and photo-chemical reactions. This means that there is a reliance on models. A further issue is

that the climate sensitivity to ozone depends strongly on the height at which it is located. Ozone in the upper troposphere tends to increase the temperature in the upper troposphere, reducing the coupling between the upper troposphere and the surface (Joshi *et al.*, 2003). This means that a smaller temperature increase occurs at the surface than expected from the direct radiative forcing. Thus, the radiative forcing concept does not hold well for ozone in the upper troposphere.

It is believed that aerosols have an overall negative radiative forcing; (IPCC, 2001, p322) estimates a total radiative forcing of -0.6Wm^{-2} $\pm$ 0.4Wm^{-2} for sulphates, dust, biomass burning aerosol, and fossil fuel organic carbon and black carbon aerosols. The individual contribution from each of these sources is shown in Fig. 1.2. Sulphate and organic carbon aerosol produce a negative radiative forcing by scattering solar radiation back to space, whereas black carbon strongly absorbs solar radiation, producing a positive radiative forcing. Biomass burning produces a mixture of aerosols including organic matter and black carbon (soot). The radiative forcing of biomass burning aerosol is negative because of the dominance of scattering materials over black carbon. The sign of the radiative forcing associated with mineral dust is unclear because it scatters in the shortwave and absorbs in both the shortwave and the longwave. For further details on the direct radiative forcing of aerosols see section 1.3. The influence of aerosols on cloud properties (the indirect aerosol effect) is also highly uncertain (see section 1.4), such that no best guess for the radiative forcing of the indirect aerosol effect was given in IPCC (2001).

The radiative forcing due to aerosols is poorly understood, mainly because of uncertainties in their physical, optical and chemical properties. These quantities are difficult to measure, and vary considerably in both space and time. The relative importance of absorption by aerosols is particularly uncertain, owing to incomplete knowledge of black carbon emissions, the difficulty of inferring absorption from observations, and uncertainties in the amount of solar radiation that is absorbed when black carbon becomes internally mixed with scattering materials. In addition, aerosols that absorb solar radiation (black carbon and dust) may give a greater warming than would be inferred from their direct radiative forcing, due to the semi-direct effect. The semi-direct effect was not included in IPCC (2001) as it is a relatively new concept and, it is not certain whether it has a major influence on global climate.

Other radiative forcing agents include, the impact of aviation on contrails and cirrus, land use changes, which impact surface albedo, and variability of solar output. These forcings are poorly understood. These uncertainties, including the semi-direct effect, are a major source of uncertainty in quantifying recent climate change, and on predicting climate change in the future. Investigation of the semi-direct effect is important to show whether it has a significant influence on anthropogenic climate change.

1.3   Direct interaction of aerosols with radiation

Aerosols absorb and scatter radiation in both the solar (shortwave) and the thermal infra-red (long-wave) spectrums. Most aerosol constituents are non-absorbing and lead to a negative radiative forcing by scattering shortwave radiation back to space. Shortwave absorption leads to a positive radiative forcing and a positive heating rate in the atmosphere, which is important for the semi-direct effect. The principal absorber of shortwave radiation is black carbon, although mineral dust and some organic aerosols also absorb in the shortwave. Interaction with longwave radiation is negligible for most aerosols except large (> 1 μ m) dust particles (e.g. Highwood *et al.* (2003)). These can exhert a positive radiative forcing by reducing outgoing longwave radiation.

The interaction of aerosols with radiation can be determined from the specific extiction coefficient (K_{ext}), the single scattering albedo (ω), and the scattering phase function P, all of which vary with wavelength (λ). The extinction coefficient is the extinction cross-sectional area per unit mass, given in m^2 g^{-1}. This depends on the particle size distribution and complex refractive index. Smaller particles have a larger cross-sectional area per unit mass, but the extinction efficiency rapidly increases with particle size until comparable to the size of the wavelength. For dry ammonium sulphate, at a wavelength of 0.55 μm, K_{ext} maximises at 8 m^2 g^{-1} for a particle size of 0.3 μm. For dry externally mixed soot, at the same wavelength, K_{ext} maximises at 14 m^2 g^{-1} for a particle size of 0.1 μm. These optimal sizes are just a little bigger than the mass-weighted average sizes given by WCP (1986) size distributions; both soot and ammonium sulphate aerosols are not far from being the optimal size to maximise their radiative effect (at visible wavelengths). WCP (1986) gives K_{ext} values of 5.0 and 9.3 m^2 g^{-1} for ammonium sulphate and soot, respectively, at a wavelength of 0.55 μm. Soot has a higher complex refractive index than ammonium sulphate (both real and imaginary parts are larger), which gives it a higher extinction efficiency at lower particle sizes, explaining the larger value of K_{ext}.

The single scattering albedo is the ratio of scattering to extinction:

$$\omega = \frac{K_{sca}}{K_{ext}} \tag{1.2}$$

$$K_{ext} = K_{sca} + K_{abs} \tag{1.3}$$

K_{sca} and K_{abs} are the specific scattering and absorptions coefficients, respectively. The value of ω is

1 for a pure scatterer and 0 for a pure absorber. The departure of ω from 1, i.e. the co-albedo (1 - ω) gives the relative importance of absorption, which is particularly important in determining the sign of direct radiative forcing, and the atmospheric heating rate. In the atmosphere aerosol ω for typical aerosol mixtures varies between 0.80 and 1.0, at visible wavelengths (e.g. Heintzenberg *et al.* (1997)). The value of ω largely depends on the black carbon content of an aerosol mixture.

The Phase function describes the directionality of scattering (the relative intensity of scattered radiation as a function of angle relative to the angle of the incident radiation). Most radiation schemes used in GCMS use the two-stream approximation, which assumes that radiation travels wither up or down. In this case the directionality of scattering by particles can be summarised by the asymmetry parameter g_asy, which is calculated by integrating the phase function over the forward and backward directions:

$$g_{asym} = \frac{fwd - bck}{fwd + bck} \tag{1.4}$$

where fwd and bck denote the proportion of radiation scattered forwards and backwards relative to the direction of the incident radiation. These can be calculated by integrating the phase function over the forward and backward hemispheres:

$$fwd = \int_0^{\pi/2} P(\theta)cos(\theta)d\theta \tag{1.5}$$

$$bck = \int_{\pi/2}^{\pi} P(\theta)cos(\theta)d\theta \tag{1.6}$$

where θ is the angle from the incident radiation. The asymmetry parameter would be 1 if all radiation was scattered forward, 0 if radiation was scattered backwards and forwards in equal proportions. The directionality of scattering is important in determining the fraction of scattered radiation that is scattered back to space, and therefore is important in determining the radiative forcing of scattering aerosols. Typically, sulphate aerosols have an asymmetry factor of between 0.6 and 0.8, and scatter 15 - 20% of intercepted radiation back to space Haywood and Shine (1995).

The column extinction optical depth (τ) is given by integrating the extinction coefficient and aerosol mass mixing ratio, r_a over the column:

$$\tau(Z) = \int_0^Z \rho sec(\theta) K_{ext} r_a dz \tag{1.7}$$

where z is height, ρ is the density of the air, and θ is zenith angle. The extinction efficiency and mass mixing ratio are therefore important in determining τ, which determines the magnitude of the radiative forcing, the atmospheric heating rate, and the reduction of net radiation at the surface.

The radiative heating rate (H) in the atmosphere is given by:

$$H = -\frac{1}{\rho c_p} \nabla F \tag{1.8}$$

where F is the net radiative flux and c_p is the specific heat capacity of the air at constant pressure (1004 J kg^{-1} K^{-1}). For the two-stream approximation this becomes:

$$H = -\frac{1}{\rho c_p} \frac{dF}{dz} \tag{1.9}$$

1.3.1 Modelling and measurement of aerosol optical properties

Aerosol optical properties, are determined through a combination of modelling and measurement techniques, these include: direct measurements of collected aerosols, remote sensing, and numerical solutions of the scattering and absorption. The most common method for determining the specific scattering coefficient is the integrating nephelometer, developed by Charlson *et al.* (1967). Many instruments have been devised to measure the specific absorption coefficient of aerosols. These include instruments that infer absorption from transmission, e.g. the integrating plate method (Lin *et al.*, 1973), or from the heating rate when irradiated at high intensity, e.g. the photo-acoustic method (Adams, 1988), and the calorimeter method (Foot, 1979). Such methods are summarised in Horvath (1993).

Most remote sensing methods employ a flux best-fit approach, whereby model aerosol parameters are fitted to give agreement between modelled and measured fluxes. This method only works in perfectly cloudless conditions and requires careful instrument calibration. For example, sun-photometers measure direct solar radiance at high spectral resolution. Discrepancies between the measured and modelled radiance are counted as the signal from aerosols and used to infer aerosol optical depth and single scattering albedo (e.g. Livingstone *et al.* (2000)). Satellite measurements of aerosol optical depth and single scattering albedo (e.g. Satheesh and Ramanathan (2000)) work on the same principal but measure reflected radiation from the surface-atmosphere system. At present most satellite techniques only work over the ocean; the variability of surface albedo of land is more difficult to account for.

The optical properties of aerosols can be calculated numerically using the scattering theory of Mie (1908). This provides a method for solving the interaction of plane monochromatic electro-magnetic waves with spheres (see Liou (1980) or Bohren and Huffman (1983) for a mathematical description). To derive the optical parameters, aerosols are assumed to be spheres and information is required on the size distribution, density, and wavelength-dependent complex refractive index of the aerosols. Size distributions can be determined from in-situ field measurements using a variety of instruments, these include: differential mobility analysers (e.g. Brand *et al.* (1992)), cascade impactors (e.g. Adams (1994)), and the Passive Cavity Aerosol Spectrometer Probe (Strapp *et al.* (1992)). Densities for aerosols composed of basic compounds such as sea salt, and sulphates are well known. However, the presence of air holes within aggregates, such as soot makes it difficult to constrain their density (Horvath, 1993). The density of soot is estimated to be between 1000 and 2000 kg m^{-3} (Chylek *et al.*, 1996). The complex refractive index depends on the particle chemical composition and is determined inversely from direct measurements of aerosol optical parameters (see examples above). The complex refractive index of soot is also uncertain by nearly a factor of 2. However, refractive index and density are correlated with one another and can be determined together for one particular aerosol sample. Therefore, the actual uncertainty in calculated optical parameters is not as large as the individual uncertainty in either density or refractive index.

One complication in determining aerosol optical properties is that certain aerosol materials are soluble in water and therefore attract water when ambient relative humidity is high. For example, sulphates are highly soluble and their volume grows by a factor of about 5 as relative humidity increases from 30 to 90% (see Fig. 2.9 of Haywood (1995), or Whitby (1984), and d'Almeida *et al.* (1991)). Consequently, the extinction coefficient per unit mass of sulphate increases by nearly the same factor. Water mostly

scatters shortwave radiation so that, within a partly absorbing mixture, the uptake of water increases the relative importance of scattering, and hence increases the single scattering albedo. Given the relative humidity, wet growth can be accounted for through empirical relationships (Tang *et al.* (1981), Whitby (1984), d'Almeida *et al.* (1991)).

Another complication is that the absorption efficiency of black carbon is amplified when it is mixed internally within other non-absorbing aerosols, or water droplets. The sphere of water or scattering material can refract photons towards the centre the sphere (depending on the size of the host sphere), thereby increasing the effective absorption cross-section of any black carbon inside. The degree of internal mixing (versus external mixing), and the manner of internal mixing are difficult to determine from measurements, and are thus highly uncertain. Horvath (1993) suggests that, close to their sources, aerosol constituents are likely be mixed externally, but with time they will coagulate creating internal mixtures.

Several methods exist to calculate the absorption of black carbon in internal mixtures. The simplest method is to assume that the aerosol constituents are well-mixed internally (as if the black carbon was dissolved in the mixture). This allows straightforward calculation of optical properties with Mie scattering theory, using the volume-weighted average refractive index. Using this approach, Haywood and Shine (1995) suggest an amplification factor of 2.3 (at 0.7 μm) from external to well-mixed internal mixtures, for soot and ammonium sulphate with a mass ratio of 10:1, respectively, and accounting for wet growth at a relative humidity of 70%. The theoretical justification for the well-mixed assumption is weak since black carbon is insoluble and would exist as discrete particles in any internal mixture. Nevertheless, a similar amplification factor was found for model calculations of soot cores surrounded by ammonium sulphate (Haywood, 1995). Similar amplification factors (2 - 2.5) were also found for black carbon particles randomly located within ammonium sulphate aerosols (Chylek, 1995) and cloud droplets (Chylek *et al.*, 1996).

Other studies suggest more modest amplification factors. For example, Lesins *et al.* (2002) gives a 20% increase in absorption, and Liu *et al.* (2002) gives a 0 - 30% increase in absorption between external and internal mixtures of black carbon and sulphate aerosol or cloud droplets. One reason for the large disagreement between these studies and those previously mentioned is that the amplification factor depends on the assumed size distributions of the soot when externally mixed, and the size distribution of the host aerosols. Different studies also use different radiative transfer methods; for example Lesins *et al.* (2002) uses the ray-tracing/Monte Carlo approach (Macke, 2000), whereas others have used either Mie calculations or an exact solution (e.g. Fuller (1994)). In complete contrast to all these studies

Markel and Shalaev (1999) found an amplification factor of 14-22 for soot clusters when located in water droplets. The large amplification was due to presence of very strong resonances at particular wavelengths or droplet sizes (when the droplet diameter was an integer number of half wavelengths in diameter). The effect of resonances was missed in previous studies as they used particular wavelengths and particular host particle sizes. Rather, Markel and Shalaev (1999) integrate over a large range of droplet sizes at very high resolution to include each resonance peak. The disagreement between Markel's result and previous results has not yet been resolved and the amplification of black carbon absorption through internal mixing is still a matter of debate.

1.3.2   Direct radiative forcing of aerosols

The direct radiative forcing of aerosols can be calculated using output from Chemical Transport Models (CTM). CTMs predict the mass mixing ratio distribution of various aerosol species and gaseous pre-cursors through emissions data, transport, and treatment of various chemical and physical processes, including nucleation, condensational growth, coagulation, and wet and dry deposition. The predicted aerosol mass mixing ratio fields can then be used in conjunction with a radiation scheme to calculate the direct aerosol radiative forcing. Initially CTMs only included sulphate aerosols and their pre-cursors, sulphur dioxide and dimethyl sulphide (e.g. Langner and Rodhe (1991)). Later, black carbon aerosols were introduced by assuming a constant mass fraction between black carbon and sulphate (Haywood and Shine, 1995). More recently, a black carbon emissions database (Cooke *et al.*, 1999) has allowed separate treatment of black carbon within CTMs. Some GCMs now have fully integrated treatment of aerosol chemistry and include separate treatment of sulphates, black carbon, organic carbon, dust, sea salt and many pre-cursor gases (e.g. Jacobson (2001)). The major sources of uncertainty in predicting the global distribution of aerosols are emissions rates (e.g. black carbon emissions are uncertain by a factor of 2 Cooke *et al.* (1999)), and uncertainty in deposition rates. In particular, the efficiency with which falling precipitation collects aerosols (wet deposition) is poorly constrained.

Figure 1.3 shows a GCM-CTM estimate of the global distribution of radiative forcing of black carbon from fossil fuel use and biomass burning (taken from Cooke *et al.* (1999)). Because aerosols only remain in the atmosphere for about a week their concentration is much higher in the northern hemisphere and near major source regions, explaining the high radiative forcing in regions such as eastern Europe, southeast Asia and northeast America. Globally the positive radiative forcing of black carbon is believed to be overwhelmed by the negative radiative forcing of other anthropogenic aerosols that scatter solar radiation (sulphates, organic carbon etc., see Fig. 1.2). However, positive radiative forcing
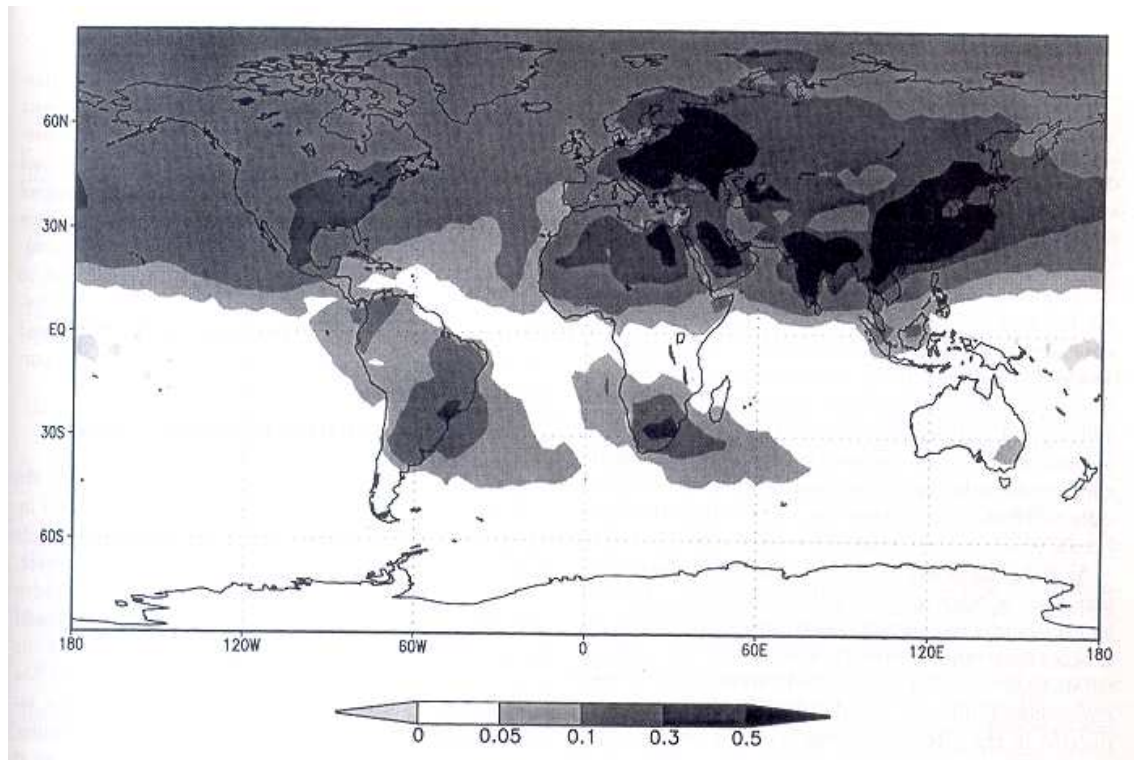
Figure 1.3: *Global distribution of direct aerosol radiative forcing (W m^{-2}) from fossil fuel black carbon and organic carbon, estimated from the ECHAM4 model incorporating carbonaceous aerosol emission data (Cooke* et al.*, 1999).*

from black carbon can dominate in some highly polluted regions, e.g. China (Chung *et al.*, 2002).

The sign of direct aerosol radiative forcing also depends on the albedo of the underlying surface. Reflection from other high albedo surface, e.g. snow or low clouds also increases the radiative forcing of absorbing aerosols and can change the sign of the forcing from negative to positive (Haywood, 1995). For example, Keil and Haywood (2003) find strong positive aerosol radiative forcing (11.5 W m^{-2}) from biomass burning aerosols over marine stratocumulus clouds along the coast of Namibia. In contrast the clear-sky radiative forcing was -13 W m^{-2}. Absorbing aerosols will absorb much more solar radiation when above, or near the top of cloud, than when below cloud. Therefore, the presence of low cloud, and the vertical distribution of aerosols relative to any cloud are important factors in determining the radiative forcing and shortwave heating rate of the aerosols.

1.3.3   Problems, progress and prospects

Large uncertainties in the radiative heating and direct radiative forcing of aerosols arise through incomplete knowledge of their optical properties, and global mass mixing ratio distributions. Optical properties are difficult to constrain because they vary with the size distribution, chemical composition, and the uptake of water (wet-growth). Uncertainty about the mixing state of black carbon, and disagreement on how internal mixing amplifies absorption of black carbon are particular issue concerning shortwave absorption rates. Aerosol mass mixing ratio distributions are also uncertain because of uncertainties in emissions rates and model parameters for processes such as deposition.

However, recent field campaigns have greatly improved the understanding of aerosols and aerosol radiative forcing, and have helped constrain physical, chemical, and optical properties of aerosols. Recent, major field experiments include: the Tropospheric Aerosol Radiative Forcing Observational Experiment (TARFOX), off the northeastern coast of USA in 1996 (Russell *et al.*, 1999), the Indian Ocean Experiment (INDOEX), 1998-99 (Ramanathan *et al.*, 2001b), and the Aerosol Characterisation Experiment (ACE), which included an experiment in the Southern Ocean in 1992 (Bates *et al.*, 1998), an experiment in the north east Pacific in 1997 (ACE-2) Raes *et al.* (2000), and an experiment off the coast of East Asia in 2001 (ACE-ASIA) (Huebert *et al.* (2003)). Continuous measurements are also available from Satellites and AERONET, a global network of aerosol sun-photometers (Holben *et al.*, 1998)). Together these provide data to help constrain aerosols optical parameters and radiative forcing estimates (e.g. Ichoku *et al.* (2003)).

New instrumental techniques promise advances in satellite remote sensing. For instance, it is now becoming possible to observe aerosols over both land and ocean using the Moderate Resolution Imaging Spectroradiometer (MODIS) (Chu *et al.*, 2003), mounted on a low earth-orbiting satellite. Recent advances in assimilation techniques have now been employed to assimilate satellite aerosol observations from the Advanced Very High Resolution Radiometer (AVHRR) into the National Center for Atmospheric Research (NCAR) Climate System Model (Collins *et al.* (2001)). Thus, there is potential to reduce uncertainties in the direct interaction of aerosols with radiation. The influence of aerosol on clouds via their radiative heating (the semi-direct effects) therefore emerges as an important issue. Similarly, the indirect effect of aerosols on clouds is another important issue to resolve in establishing the overall influence of aerosols on radiative forcing and climate change.

1.4 The indirect aerosol effect

Some species of anthropogenic aerosols, such as sulphates are effective cloud condensation nuclei (Hegg *et al.*, 1993), and are found to increase cloud droplet number concentrations (e.g. Martin *et al.* (1994); Boucher and Lohmann (1995)). This leads to an increase in cloud optical depth and albedo because a greater number of smaller droplets have a higher total surface area for a given mass of liquid water. This is known as the first indirect aerosol effect, or Twomey effect, as it was proposed by Twomey (1977). The Twomey effect leads to an increase in the planetary albedo and therefore a negative radiative forcing. In addition it has been suggested that the indirect aerosol effect leads to a lower precipitation efficiency. Increasing the cloud droplet number concentration decreases the average cloud droplet size. Smaller droplets have a lower terminal velocity and are therefore less likely to coalece and form precipitation (Albrecht, 1989). As a result clouds will retain higher liquid water contents and have a longer lifetime. This is termed the second indirect effect, or cloud lifetime effect, and it also has a negative radiative forcing, contributing to the negative forcing from the first indirect effect, or Twomey effect.

The influence of anthropogenic aerosols on cloud microphysics is well supported in theory and by observations (see Schwartz and Slingo (1995) for a review). For example, distinctive bright streaks or so-called 'ship tracks' are observed in satellite images of marine stratocumulus clouds associated with plumes of ship exhaust (e.g. Coakley *et al.* (1987)). Also, aircraft-based studies (e.g. Martin *et al.* (1994); Taylor *et al.* (2000)) and satellite retrievals (Han *et al.*, 1998) have found higher droplet number concentrations in clouds forming in polluted airmasses than those forming in pristine marine air. However, quantifying the indirect effect has proved difficult because aerosol physical and chemical properties are highly complex the way that the aerosols interact with cloud microphysics depends on cloud type (Haywood and Boucher, 2000) and other factors such as updraught velocities. It has been even more difficult to quantify the second indirect effect, or cloud-lifetime effect because it also relies on accurate knowledge of parameters such as autoconversion rate and droplet collection efficiency. It is also difficult to capture the second indirect effect in observations because cloud water content and cloud cover are naturally very variable quantities (Haywood and Boucher, 2000).

No best estimate was given for the indirect aerosol effect in IPCC (2001) because the uncertainty was considered to be too great. A range of 0 to -2 W m^{-2} is given in Fig. 1.2, which approximately covers the range of current global circulation model estimates of the first indirect aerosol effect (see chapter 5.4 of IPCC (2001) for a review of recent indirect radiative forcing estimates).

1.5   The semi-direct aerosol effect

The term 'semi-direct effect' was coined by Hansen *et al.* (1997) to describe the impact of absorbing aerosols on clouds. A series of experiments with a simple GCM showed that shortwave absorption reduced low cloud cover by reducing relative humidity. The semi-direct effect had a warming influence on climate because low clouds have a high albedo but do not significantly reduce outgoing longwave radiation. In their study, Hansen *et al.* (1997) investigated the climate impact of globally uniform aerosol layers with an optical depth of 0.1, and for a range of single scattering albedos. In a run with an aerosol located in the lower troposphere, a mid-visible single scattering albedo (ω) of 0.90, and fixed cloud properties, the direct radiative forcing was -0.82 W m^{-2} and there was a global annual mean surface temperature change of -0.41 K. However, when cloud feedbacks were included there was a warming of 0.17 K due to the reduction of low clouds. In Hansen *et al.* (1997) aerosols with $\omega < 0.91$ would give a warming, even though the direct radiative forcing was negative for $\omega > 0.85$. Thus, in the case of absorbing aerosols, the direct radiative forcing was a poor indicator of surface temperature response.

Similar results were later obtained by Cook and Highwood (2003), with a less simplistic GCM. The experimental approach was similar to Hansen *et al.* (1997), except that a higher optical depth of 0.2 was used. For $\omega = 0.8$ there was a direct radiative forcing of 1.15 W m^{-2} and, for fixed clouds, there was a warming of 0.2 K. When cloud feedbacks were included the warming increased to 2.9 K. The additional warming was related to decreases in the fractional coverage of large-scale clouds, particularly at mid and high latitudes, and at every level in the vertical. There was also a decrease in convective clouds in the tropics. These cloud responses were unique compared to cloud responses to increased carbon dioxide concentration or an increased solar constant. The absorbing aerosols led to warming throughout the troposphere, but the warming was greater in the lower troposphere so that static stability was increased. This helped to explain the decreased cloud cover and reduced convective activity. Cook and Highwood (2003) found that a surface temperature increase would occur for aerosols with $\omega < 0.93$, similar to the value of 0.91 found in Hansen *et al.* (1997). These critical values lie within the estimated range of ω values for anthropogenic aerosols (see section 1.3 for details). Thus, Hansen *et al.* (1997) and Cook and Highwood (2003) suggest that, given the current uncertainty in ω and the strength of the semi-direct effect, anthropogenic aerosols could have a warming influence on climate (excluding indirect aerosol effects).

The semi-direct aerosol effect was also investigated by Ackerman *et al.* (2000) using Large-Eddy-

Simulations (LES) based on observation from the Indian Ocean Experiment (INDOEX), 1998-99. During the winter and spring months (December - May) low level northeasterly winds advect highly polluted air from southern Asia over the northern Indian Ocean (Ramanathan *et al.*, 2001b). These have a relatively high black carbon content ($\sim$11% by mass), a low mid-visible single scattering albedo ($\sim$ 0.88), and high mid-visible optical depths (0.2 - 0.7) (Satheesh and Ramanathan, 2000). One of the most striking results of INDOEX was the high shortwave heating rate (0.3 - 1 K day^{-1}) in the lower troposphere (0 - 3 km) associated with these aerosols ((Satheesh and Ramanathan, 2000), Podgorny *et al.* (2000)). Ackerman *et al.* (2000) found that these absorbing aerosols reduced the relative humidity in the boundary layer (BL) and reduced cumulus clouds fraction by 5 - 10 % . The solar heating was maximum at the top of the BL where cloud cover was greatest. This had the effect of stabilising the BL, tending to reducing turbulence and moisture fluxes through the BL, suppressing convection. The lower relative humidity also meant that cumulus clouds would evaporate more quickly when mixing with ambient air. In a previous hypothetical experiment (Ackerman and Toon, 1994) it had been shown that high amounts of black carbon would completely dissipate a layer of marine stratocumulus. The daytime reduction of cloud cover led to a positive difference in cloud radiative forcing (semi-direct forcing) of 7.5 W m^{-2} . This was comparable in magnitude to the indirect and direct aerosol radiative forcings. It was also noted that the semi-direct forcing depended on local meteorological conditions; in experiments with a higher humidity and a higher cloud cover the semi-direct forcing was greater.

Lohmann and Feichter (2001) provided the first assessment of the global annual mean semi-direct forcing, using the ECHAM4 GCM. This incorporates emissions data and a coupled aerosol-chemistry module to predict the global distribution of aerosol constituents and their optical properties. Transport, nucleation, growth and deposition of aerosols, and the interaction of aerosols with cloud microphysics are represented. Both first and second indirect aerosol effects are accounted for, in addition to the direct and semi-direct effects. The model showed significant reductions of liquid water path in regions where the black carbon burden was high ($>$ 2 mg m^{-2}). However, black carbon burdens were low over the majority of the globe and the global mean semi-direct effect was negligible (0.1 W m^{-2}) compared to the indirect and direct aerosol effects. It was noted, however, that there was an uncertainty factor of 2 in the emission data for black carbon. Also, the radiative properties of aerosols were based on external mixtures, whereas internal mixtures may absorb 2 - 2.5 times more shortwave radiation (e.g. Chylek *et al.* (1996), see section 1.3 for a discussion). Furthermore, the climate simulations were run for only 5 years and it is questionable as to whether this was long enough to detect the semi-direct effect above natural variability in the simulated climate. Given these uncertainties the semi-direct effect is still an important process to quantify.

The strong warming influence of absorbing aerosols was also emphasised by Jacobson (2002), in a study using the Gas Aerosol Transport Radiation General Circulation and Mesoscale Meteorological Model (GATOR-GCMM). This model uses emission data and detailed treatment of gas-aerosol processes to predict the present-day global distributions of various aerosols, including sulphates and fossil fuel black carbon and organic mater. In equilibrium climate simulations the climate sensitivity (λ) for the mixture of black and organic carbon aerosol was over twice the λ for the greenhouse gases CO_2 and CH_4. Present day emissions of fossil fuel organic and black carbon aerosols led to a positive radiative forcing (ΔF) of 0.25 Wm^{-2} and raised global average surface temperature (T_s) by 0.35K, giving a λ ($T_s/\Delta F$) of 1.4, compared to 0.6 for greenhouse gases. This implies that there were strong positive climate feedbacks associated with the absorbing aerosol mixture. The study found a global average decrease in column liquid water and ice associated with the semi-direct effect. There was an increase in near-surface temperature relative to the surface, due to the absorbing aerosols, resulting in lower surface sensible and latent heat fluxes. There was also a reduction in cumulus convection in the lower and mid-troposphere, and a reduction in global mean near-surface wind speed, related to the stabilising effect of the aerosols. However, the fossil fuel black carbon and organic matter mixture also affected clouds through the indirect aerosol effects. In the global mean the indirect effects dominated the semi-direct effect such that the global mean cloud optical depth was increased. Therefore, the semi-direct effect alone did not explain the strong climate warming associated with the fossil fuel black carbon and organic matter.

Jacobson (2002) suggests several other positive feedbacks associated with the black carbon aerosols that might explain the warming. Most of the reduction of cloud and water and ice took place in the mid-troposphere (800 - 400 mb), whereas liquid water slightly increased at low level (950 - 800 mb) because of the indirect effect. Both these changes tended to increase the shortwave absorption by black carbon, water vapour and carbon dioxide in the mid and upper troposphere. Here, the evaporation of clouds into water vapour was believed to enhanced absorption of thermal infra-red radiation, although this effect was not quantified. Furthermore, there was also a strong snow-albedo feedback (melting fresh snow reveals darker underlying surfaces) over northeast Asia associated with a large warming pattern over East Asia. This warming pattern was unique to the absorbing aerosol forcing and may have been related in some way to the strong sources of fossil fuel black carbon in China and southeast Asia. Whilst Jacobson (2002) confirmed the semi-direct effect of absorbing aerosols it was shown to be less important than the indirect effect, and possibly equal in importance to other positive feedbacks, although these were difficult to quantify individually. Furthermore, the climate simulations were only 5 years in length, and it is questionable as to whether this was long enough to fully measure the warming

signal from the aerosols as there was thermal inertia in the simulated climate system deriving from the 60 m deep mixed-layer ocean.

A recent study (Penner and Zhang (2003)) using a coupled chemical transport model and GCM reports a negative semi-direct forcing from fossil-fuel-related carbonaceous aerosol and biomass burning aerosols, suggesting that soot and smoke may not warm the climate. However, their definition of the semi-direct forcing was quite different from the definition in other studies. In addition to changes in cloud distributions the "forcing" included responses in the longwave radiation budget due to changes in land surface temperature, and consequent changes in tropospheric temperature. Considering only changes in cloud cover, the semi-direct forcing would have been positive due to reductions of stratiform and convective clouds. This highlights difficulties in defining the semi-direct effect and seperating it from other climate responses or feedbacks. Perhaps a better way of measuring the semi-direct forcing in a GCM would be to allow the temperature profile in the atmosphere and the distribution of clouds to vary, but maintain fixed sea and land surface temperatures.

A study by Hongbin *et al.* (2002), using a 1D atmospheric boundary layer model, implies that absorbing aerosols could either increase or decrease BL cloud cover, depending on whether they are located above or below the inversion. When located in the BL, absorbing aerosols were found to heat and dry the BL by reducing surface moisture fluxes, implying a lower probability of cloud formation. However, absorbing aerosols above the BL increased the strength of the capping inversion leading to a lower entrainment rate and a moistening of the BL, implying a higher probability of cloud formation. Although the simulations did not involve clouds, the findings may be relevant to stratocumulus-capped BL where entrainment and surface fluxes are key processes in determining the thickness and persistence of the cloud. The study opens the possibility that the semi-direct aerosol effect could locally be negative if significant amounts of absorbing aerosols were located above a cloudy BL.

1.6   Influence of aerosols on the surface energy budget and hydrological cycle

Over the past 5-10 years interest has grown in the extent to which aerosols can modify the hydrological cycle. Aerosols, whether scattering or absorbing, reduce the net shortwave radiation at the surface. About two-thirds of the absorbed solar radiation at the Earth's surface is balanced by evaporation (global annual mean) (Ramanathan *et al.*, 2001a). A reduction in net solar radiation at the surface may

be partly balanced by a reduction of evaporation, leading to reduced precipitation (Satheesh and Ramanathan (2000), Ramanathan *et al.* (2001a)). A number of studies have shown that sulphate aerosol leads to a notable decrease in global annual mean precipitation, and changes in the global distribution of precipitation (Mitchell and Johns (1997), Roeckner *et al.* (1999)). For example, Roeckner *et al.* (1999) present a GCM climate simulation, which includes the direct and indirect aerosol effects of sulphate, and increases in greenhouse gases. These forcings led to a 1.5 K warming of surface temperature between 1900 and 2050, but a 0.5% decrease in global precipitation. Most, if not all, GCMs simulations, including those by Roeckner *et al.* (1999) show a 1 - 2% K^{-1} increase of precipitation with the warming associated with increased greenhouse gases.

Absorbing aerosols potentially have a much greater influence on the hydrological cycle because they strongly reduce the shortwave radiation at the surface and also heat the atmosphere. This was particularly brought to light during INDOEX. For example, Satheesh and Ramanathan (2000) showed that the absorbing haze over the Indian Ocean during January-April reduces the net shortwave at the surface by 10-30 W m^{-2} , and heats the lower troposphere (< 3 km) at 0.3 - 1 K day^{-1} (diurnal mean). Heating the atmosphere, whilst cooling the surface increases near-surface stability tending to reduce vertical transport of moisture through the BL (Ramanathan *et al.*, 2001b). Globally, radiative cooling in the atmosphere is balanced by latent heat release through precipitation (Kaufman *et al.*, 2002). By redistributing heat between the surface and the atmosphere, absorption by aerosols is likely to slow down the hydrological cycle.

The regionality of aerosol forcing also has interesting consequences on large-scale circulations and rainfall patterns (Mitchell and Johns (1997), Chung *et al.* (2002), Menon *et al.* (2002), Rotstayn and Lohmann (2002)). Southeast Asia and China are major sources of anthropogenic sulphate and black carbon aerosol. Mitchell and Johns (1997) showed that the cooling over the continent due to sulphate aerosols led to a weakening of the summer Asian monsoon. However, the strong heating perturbation in the atmosphere, due to the black carbon also has a profound effect on regional circulations (Chung *et al.*, 2002). The absorbing aerosol haze over southern Asia and the northern Indian Ocean, during the dry season heats the lower troposphere (< 3km) by up to 1 K. In a GCM study by Chung *et al.* (2002) the regional atmospheric heating anomaly led to low-level convergence and increased convection and precipitation over the northern Indian Ocean, and a northward shift of the ITCZ. To compensate other regions, such as the Pacific warm pool (Indonesia and surrounding areas) had decreased precipitation.

In a similar study, Menon *et al.* (2002) suggest that black carbon aerosols are responsible for shifts in rainfall patterns over China that have led to flooding in the South and droughts in the North. In the GCM

experiment, the absorbing aerosols over China and southern Asia, during the summer months led to increased low level convergence and enhanced precipitation (1 - 4 mm day^{-1}) over southern China. To compensate, there was greater subsidence and reduced precipitation in northern China, and southeast Asia (Thailand, Philipines etc). Much weaker dynamic feedbacks occurred in an experiment with purely scattering aerosols, showing that the dynamic responses were mainly driven by the atmospheric heating perturbation from black carbon aerosols. The absorbing aerosols also led to interesting changes in surface temperature patterns. The absorbing aerosols led to strong surface cooling (1 K) over china, but moderate heating (0.2 - 0.5 K) in adjacent regions, such as central Asia and the northern Indian Ocean, and other parts of the globe, such as Africa. The overall impact was a small increase in global annual mean surface temperature, as expected from the positive radiative forcing. These results show that the influence of aerosols on climate is a complex issue. The debate revolves, not only on how much they heat or cool the globe, but also on how they alter surface temperature and precipitation patterns across the globe.

1.7   Summary

In summary, recent studies have uncovered a new mechanism called the semi-direct aerosol effect. Aerosols are generally believed to exert a cooling influence on climate by scattering solar radiation, and their indirect effects on clouds. However, the semi-direct effect has the potential to offset this cooling by reducing low cloud cover. This calls into question the overall role of aerosols in climate. Conclusions about the relative importance of the semi-direct effect are mixed amongst the few modelling studies that have addressed this problem. Comparison between different studies is difficult because the experimental approach, and the method of evaluating the semi-direct effect has varied.

Hansen *et al.* (1997) and Cook and Highwood (2003) used simple GCMs with idealised aerosol properties, whereas Lohmann and Feichter (2001) and Jacobson (2002) use more sophisticated treatments of clouds and aerosols, and predict aerosol properties and distributions within the model from emissions data. Ackerman *et al.* (2000) measure only the local effect of aerosols on BL structure and clouds for a particular scenario. Penner and Zhang (2003) uses a GCM with simple treatment of clouds but uses a CTM to predict the distribution of aerosols from fossil fuel combustion and biomass burning. Ackerman *et al.* (2000) and Lohmann and Feichter (2001) evaluate the semi-direct forcing in terms of a change in cloud radiative forcing (semi-direct forcing). Hansen *et al.* (1997), Cook and Highwood (2003) and Jacobson (2002) measure the semi-direct effect by relating the surface temperature

response to the direct radiative forcing through λ, the climate sensitivity parameter (see equation 1.1. Comparisons based on λ are problematic as λ varies enormously with aerosol ω, even changing sign, and is also model dependent. Alternatively, Penner and Zhang (2003) evaluates a 'relaxed forcing', which is actually the radiative imbalance at the top of the atmosphere after land surface and tropospheric temperatures have adjusted to the aerosols. Understanding of the semi-direct effect has also hindered by the large number of possible feedbacks between the aerosols and clouds (e.g. Jacobson (2002)), and difficulties in distinguishing between these in large-scale models. Therefore, to increase understanding a focused study of the semi-direct effect is needed. This should address what conditions lead to a significant semi-direct effect, and what is required for GCMs to accurately capture the semi-direct effect.

1.8   Thesis approach

The main aims of the thesis are to gain a better understanding of the mechanisms of the semi-direct effect, to assess its dependence on meteorological conditions, and the dependence on the distribution of aerosols and their optical properties. This has been achieved using the UK Met Office Large-Eddy-Model (LEM). This is a high resolution model (10 - 100 m), designed to study the structure of the atmospheric boundary layer, and boundary layer clouds (stratocumulus and cumulus). The major advantage of LES is that cloud dynamics and turbulence are explicitly resolved (down to the scale of tens of meters) so that interactions with radiative heating will be simulated explicitly. This is of prime importance in accurately representing the response of clouds to heating by aerosols, i.e. the semi-direct aerosol effect. For further details on the LEM see Appendix A.

LES are computational very expensive, mainly because the time step has to be very small (less than a second) due to the high resolution. Consequently, LES are usually run for a few hours. However, in this thesis LES were generally run for two days to include the diurnal cycle of shortwave radiation and residual effects from a previous day. Due to the computational expense, experiments have been selective of a number of cloud and aerosol simulations.

The thesis focuses on marine boundary layer clouds; stratocumulus and cumulus, as these exhibit a strong diurnal cycle in response to shortwave heating. Furthermore, marine stratocumulus and cumulus cover around 25 % of the globe and lead to a big increase in the planetary albedo (Hartmann *et al.*, 1992). Chapters 2 and 3, present LES of marine stratocumulus and shallow cumulus cloud systems. The influence of absorbing aerosols is investigated using idealised aerosol distributions. The sensitivity

of the semi-direct effect to the aerosol vertical distribution is investigated using further LES of marine stratocumulus and shallow cumulus (see chapter 5). In Chapter 6 the semi-direct effect is evaluated using the LEM for a specific observed case of marine stratocumulus forming within a polluted airmass.

LEM results have also been compared with simulations using the National Center for Atmospheric Research (NCAR) Single Column Community Climate Model (SCCM) to assess the ability of large-scale models to capture the semi-direct effect (see chapter 4). The community climate model is a typical climate-oriented GCM with simple, but widely used physical parameterizations. By using the single column version of this model, the response to aerosol heating can be investigated without variability from large-scale motions. An outline of the SCCM and its physical parameterizations is given Appendix B.

In this thesis the semi-direct aerosol effect will be taken to mean the influence that aerosols have on clouds through solar heating. The semi-direct forcing will be defined as the instantaneous change in net irradiance at the Top Of the Atmosphere (TOA) caused by the cloud changes. The relative importance of the semi-direct effect is gauged by comparison of the semi-direct forcing with direct and indirect radiative forcings, and other radiative forcings (e.g. greenhouse gases).

CHAPTER 2

Marine Stratocumulus Experiments

In this chapter the semi-direct aerosol effect is investigated for a marine stratocumulus case using the Large-Eddy-Model (LEM). The key question here is: How important is the semi-direct effect compared to the direct and indirect aerosol effects, and other radiative forcings? Also an understanding is built of some underlying processes that govern the semi-direct effect.

2.1   Introduction to marine stratocumulus

Stratocumulus is a type of layer cloud that forms at low levels in the atmosphere due to vertical mixing, driven by turbulence, in a relatively moist layer. Stratocumulus commonly forms the top of the atmospheric boundary layer (BL) producing a layer of cloud 100-500 m thick. These clouds are relatively uniform in the horizontal, though may be partially broken and somewhat 'lumpy' in appearance due to weak convective activity. Stratocumulus can form large horizontally homogeneous sheets of up 10^6 km^2 over the oceans (Bennetts *et al.*, 1986). The global annual mean coverage of stratus and stratocumulus over the ocean was estimated to be 34% (Hartmann *et al.*, 1992) by the International Satellite Cloud Climatology Project (ISCCP). Stratocumulus is particularly prevalent on the eastern side of the ocean basins in the subtropics, associated regions of large-scale subsidence and relatively low Sea Surface Temperatures (SSTs) (Hanson, 1991). Figure 2.1 identifies the three most significant region of high stratocumulus coverage in the south-east and north-east Pacific, and the south-east Atlantic. Minor regions also found in the north-east Atlantic and in the southern Indian ocean.

Because of their high albedo ($30 - 60\%$) compared to the ocean surface (10%), and their high fractional coverage marine stratocumulus greatly increases the amount of solar radiation that it scattered (reflected) back to space (e.g. Ramanathan *et al.* (1989)). Also, because of their low altitude they have a similar temperature to the surface and have little impact on outgoing longwave radiation. Thus, they have an overall cooling influence on climate. As an illustration of their importance to climate, Randall *et al.* (1984) estimate that a 4% change in the area of the globe covered by low level stratus cloud would be equal in magnitude to the radiative forcing from a doubling of carbon dioxide concentrations
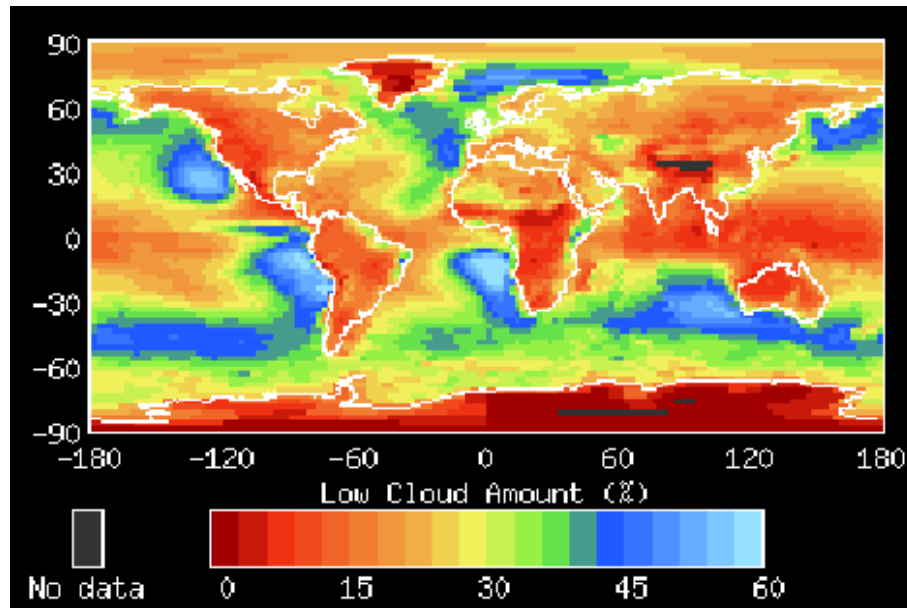
Figure 2.1: *Annual mean daytime stratocumulus fractional coverage from the International Satellite Cloud Climatology Project (ISCCP) D-data: Stratocumulus is defined as having a cloud top at pressure greater than 680 mb and a visible optical depth of between 3.6 and 23. Figure produced from [http://isccp.giss.nasa.gov].*

in the atmosphere. The shortwave radiation flux at the surface is also greatly reduced by marine stratocumulus, which acts to cool the ocean surface. For example, a coupled ocean-atmosphere modelling study found that SSTs along, and downstream of the Peruvian coast are as much as 5K lower on account of the persistent marine stratocumulus cloud cover in that region (Ma *et al.*, 1996). By limiting fluxes of heat and moisture into the atmosphere, this reduction of SST dampens the intensity of tropical convection and tropical circulations as a whole, also influencing the mean position of the inter-tropical convergence zone (Philander *et al.*, 1996).

Thus, marine stratocumulus play a major role in the global radiation budget and the general circulation in the atmosphere. A future change in stratocumulus coverage or their radiative properties would significantly influence climate change. For example, in an idealised study of the tropical circulation, subtropical marine stratocumulus cover was found to increase as the climate warmed, in response to increased concentrations of greenhouse gases (Larson *et al.*, 1999). The increased marine stratocumulus cover exerted a negative feedback on climate change, limiting the rate of temperature increase. A reduction of marine stratocumulus, for example, through the semi-direct effect would have the opposite effect, hastening global warming.

Therefore, it is important to investigate how sensitive marine stratocumulus is to the semi-direct effect.

Understanding the semi-direct effect for marine stratocumulus is a key step in understanding the semi-direct effect in the climate system as a whole.

2.1.1   Formation process and basic structure

The marine stratocumulus regime has long been identified as interesting and important component of the climate system (e.g. Lilly (1968)). Over the past 2-3 decades there have been many observational and numerical modelling studies of the Stratocumulus-Capped Boundary Layer (SCBL). For example, a two day observational study of the stratocumulus-topped mixed layer took place off the coast of California, June 1976 (Brost *et al.* (1982) and Albrecht *et al.* (1985)). A detailed field study of nocturnal stratocumulus took place over the UK in November 1976 (Roach *et al.* (1982), Caughey *et al.* (1982) and Slingo *et al.* (1982)). Also, stratocumulus was studied during six flights over the North sea, 1982-83 (Nicholls (1984) and Nicholls and Leighton (1986)). Modelling studies include mixed-layer models (e.g. Lilly (1968), Pelly and Belcher (2001)), one-dimensional models with high-order turbulence closure schemes (e.g. Bougeault (1985), Duynkerke (1989), Smith and Kao (1996)), and Large-Eddy Simulations (e.g. Duynkerke *et al.* (1999), Duynkerke *et al.* (2000), Moeng (2000), Chlond and Wolkau (2000), Bretherton (2002)). Together, modelling and observational studies have led to a good qualitative understanding of the SCBL and the role of turbulence, entrainment, radiation and microphysical processes in determining the mean thermodynamic structure. This section summarises the general understanding of marine stratocumulus obtained through these studies.

Figure 2.2, taken from Nieuwstadt and Duynkerke (1996) summarises the structure, and the key processes governing the SCBL. Stratocumulus forms at the top of well-mixed BLs that are capped by a strong low-level inversion. The inversion, across which potential temperature increases by 5-20 K (e.g. Duynkerke *et al.* (2000), Lock (1996)), is maintained by subsidence associated with synoptic scale anticyclones. This inversion strongly constrains vertical mixing between the boundary layer (BL) and the free troposphere above, which is usually much drier. To sustain a stratocumulus layer the turbulent flux of moisture through the BL must be sufficient to balance the drying related to mixing with air from the free troposphere.

Longwave cooling at the cloud top is the main driver of turbulence in the SCBL. Cold downdraughts descend from the cloud top and fill the depth of the BL leading to turbulent mixing (e.g. Lock *et al.* (2000)). Surface heat fluxes and wind shear can also contribute to the generation of turbulence depending on SST and geostrophic flow, respectively. Longwave warming at the cloud base and latent heat

release also tend to generate instability in the cloud layer.

During the day, solar radiation is absorbed throughout the cloud, warming and stabilising the layer. This leads to a marked reduction of liquid water path (LWP) and tends to separate (decouple) the cloud layer from the sub cloud layer so that turbulent motions arising from cloud top cooling are mostly confined to the cloud layer. Decoupling greatly reduces the moisture flux to the cloud (Nicholls, 1984), contributing significantly to the daytime thinning of the cloud. The cloud thickens at night as it cools through longwave emission and recouples with the surface layer, resuming the moisture fluxes.
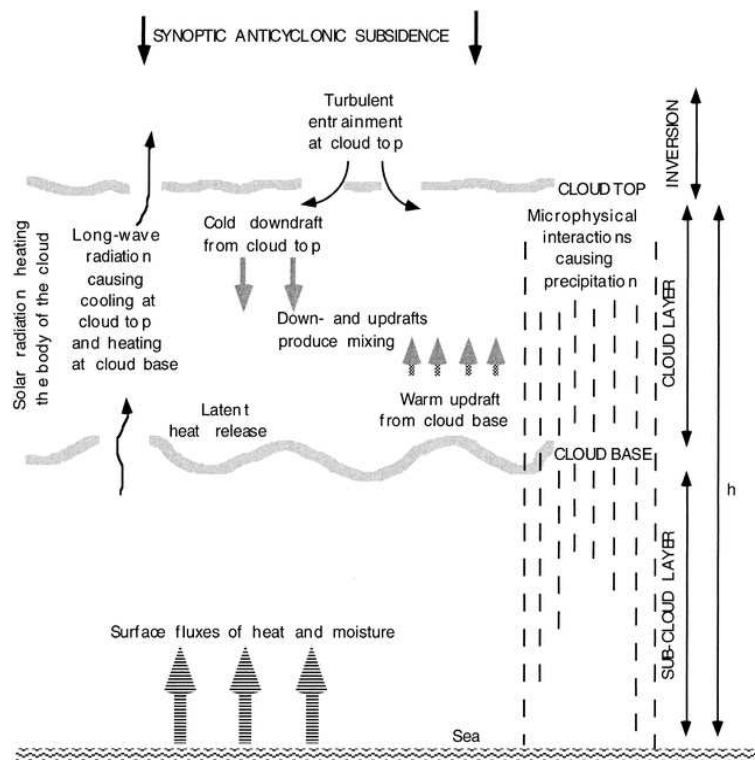
Figure 2.2: *Summary of physical processes important for the development of the marine stratocumulus-capped BL [from Nieuwstadt and Duynkerke (1996)].*

The persistence of the cloud layer also depends on the rate at which warmer, drier air from the free troposphere is entrained into the BL across the inversion. Entrainment is caused by turbulence at the BL top which deforms the inversion interface so that tongues of stable air are engulfed and mixed into the BL. Although the details of the entrainment process are not fully understood there is a well-established link between the entrainment rate and the generation of turbulence by cloud-top cooling and evaporative cooling near the cloud top (e.g. Moeng (2000), Lock and Macvean (1999)). Entraining eddies can become negatively buoyant as they mix with cloudy air, if evaporative cooling is sufficient to overcome the initial contrast in potential temperature between the cloudy and free tropospheric air (Randall

(1980), Deardorff (1980)). Furthermore, if the potential energy released by the descent of the nega-
tively buoyant mixed air exceeds that required to deform the inversion interface into an entrainment
tongue then the entrainment process becomes unstable and increases rapidly, leading to the evaporation
of the cloud layer (Cloud-Top Entrainment Instability) (Siems *et al.* (1990), Vean and Mason (1990).
Entrainment is inhibited by the stability of the inversion (increase in potential temperature across the
inversion) and as such strong temperature inversions are favorable for the persistence of stratocumulus,
as shown by Macvean (1993), although other factors such as decoupling are also crucial (Wang and
Wang, 1994).

Drizzle can occur in thick stratocumulus layers depending on the cloud droplet concentration and
whether there is sufficient liquid water. The main action of drizzle is to reduce the liquid water content
of the cloud layer and to cool the sub-cloud layer by evaporation (Wang and Albrecht, 1994). This helps
to stabilise the BL and can promote the decoupling of the BL (see later). Evaporation of drizzle can
also moisten the subcloud layer and it has been suggested that this enhances the transition to cumulus
Paluch and Lenschow (1991).

2.1.2 Stratocumulus to cumulus transition

Over the subtropical and tropical oceans there is a gradual transition in cloudiness from stratocumulus
to cumulus. This is associated with the equatorward advection of the marine BL over warmer water and
towards regions of lower mean subsidence. This is accompanied by a deepening of the BL, a reduction
in the strength of the temperature inversion and changes in turbulent processes. The Atlantic Stratocu-
mulus Transition Experiment (ASTEX) (Albrecht *et al.*, 1995a) 1992 off the coast of North Africa
involved Lagrangian flights, intensive field observations and subsequent modelling studies, which led
to a conceptual model for the stratocumulus to trade cumulus transition (Bretherton (1992), Klein and
Hartmann (1993), Wyant *et al.* (1997)).

On the eastern side of ocean basins in the subtropics, SSTs increase rapidly with distance from the
coasts, and equatorwards. However, the potential temperature at levels above the BL is comparatively
uniform with longitude in the subtropics and varies more slowly in the equatorward direction since it
is controlled mainly by large scale advection and subsidence associated with the Hadley circulation
(Miller, 1997). As a consequence, the strength of the inversion, and the structure of the marine BL
varies mainly with SST.

Relatively cool SSTs and strong subsidence near to the western coastline in the subtropics lead to the

development of shallow (400-700m) well-mixed BLs capped by a strong inversion. Although surface fluxes are low, moisture levels may be sufficient for the development of a cloud layer at the BL top. Subsidence restricts the growth of the BL, and entrainment is inhibited by the strength of the inversion. Surface fluxes increase as the BL is advected equatorward and into the ocean interior over warmer waters. Cloud LWP may either increase or decrease depending on the relative impacts of increased entrainment and the increased surface moisture flux.

As the BL depth increases, the cloud-top driven turbulence is no longer sufficient to maintain turbulent fluxes throughout the depth of the BL. Once the link between surface fluxes and the cloud breaks down, the BL separates (decouples) into a surface well-mixed layer and an upper layer, with a transition layer between them. The cloud base of the stratocumulus rises above the top of the surface layer and shallow cumulus may form at the top of the surface layer. These cumulus may penetrate into the stratocumulus layer above and can reinforce it, transporting moisture from the surface to the cloud.

The deepening-decoupling process is accompanied by an increase in horizontal variability of cloud top height and LWP and a gradual decrease in cloud fraction and area averaged cloud albedo. With increasing SST downstream, cumulus convection becomes more vigorous and penetrates the inversion leading to greater mixing across the inversion and break up of the stratocumulus layer. Stratocumulus eventually gives way to open trade cumulus with a much lower cloud fraction. See section 3.1 for an introduction to trade cumulus.

Thus, the characteristics of marine stratocumulus BLs vary considerably both in space and time due to their transitional nature. The simulations in this chapter, and chapter 5 are based on the shallow well-mixed phase of the SCBL using observations of Californian coastal stratocumulus from the FIRE campaign (described in the next section). The shallow well-mixed SCBL is ideal for the LES investigation because cloud top height and LWP are relatively homogeneous in the horizontal, and there is a clear strong diurnal cycle, showing potential for a large semi-direct effect.

2.1.3   Marine stratocumulus case study - FIRE

The First International Satellite Cloud Climatology Project Regional Experiment (FIRE) took place off the coast of California, July 1987 and was the first major field experiment to provide a comprehensive observational dataset on marine stratocumulus, incorporating airborne, ground-based and satellite instruments (Albrecht *et al.*, 1988). One of the main objectives of the FIRE campaign was to provide reliable data for modelling studies of the SCBL. The Californian coastal region had previously been

studied in the summer of 1976 (Brost *et al.* (1982), Albrecht *et al.* (1985)) and had proven an ideal location because of the prevalent meteorological conditions, and the proximity of the region to the US west coast. The FIRE campaign was also able to make good use of a pre-established meteorological station on San Nicholas Island (33°N, 119°W), which provided an ideal platform for ground-based observations.

Several instruments were installed on San Nicholas Island to monitor cloud properties with high temporal frequency during the period 1-19 July. These included a celiometer (operated by Colorado State University; Schubert *et al.* (1987a)) to measure cloud base every 30 s, a Doppler acoustic sounder, or sodar (operated by Pennsylvania State University; White (1989)) that estimated the inversion height every hour (derived from the peak acoustic echo strength), and a 3-channel passive microwave radiometer (operated by NOAA/ Environmental Research Laboratories (Snider, 1988)) to estimate column water vapour and LWP every minute (Hogg *et al.*, 1983). Frequent temperature and relative humidity soundings were taken from the cross-chain Loran atmospheric sounding system (CLASS) installed on San Nicholas Island (Schubert *et al.*, 1987b). A total of 69 soundings were taken between 30 June and 19 July, but the frequency of launches was variable, sometimes just once a day, and up to nine times a day. Also, a UHF wind profiler provided a continuous record of wind profiles (Syrett, 1988).

Persistent stratocumulus was observed over San Nicholas Island for much of the FIRE period (1-19 July, 1987); Albrecht *et al.* (1995b) estimate an average cloud fraction of 0.83. The large-scale synoptic flow changed very little during this period. The consistency of the large-scale flow meant that synoptic timescale variations could easily be removed from the data (by calculating departures from the daily averages) and diurnal variation could be examined (Blaskovic *et al.* (1991), Duynkerke and Hignett (1993)).

Observing and modelling diurnal variability was a particular aspect of the FIRE stratocumulus experiment (Duynkerke (1989), Betts (1990b), Hignett (1991), Blaskovic *et al.* (1991), Duynkerke and Hignett (1993), Smith and Kao (1996), Duynkerke and Teixeira (2001)). Figure 2.3 shows the diurnal variation of cloud top and cloud base for 1-19 July (taken from Blaskovic *et al.* (1991)), estimated from hourly averaged celiometer and sodar data. The mean cloud top height was around 650 m, with a diurnal range of 150 ± 30 m, and cloud base height was around 450 m, with a similar diurnal range: 130 ± 30 m (errors were estimated from the sample variance in hourly values). The cloud top height was maximum in the morning and declined throughout the afternoon due to a reduction in the entrainment rate, related to solar heating and the daytime reduction of LWP (Fig. 2.4), which both lead to a lower cloud-top cooling rate. Cloud base is lowest around dawn but rises in the day as the cloud
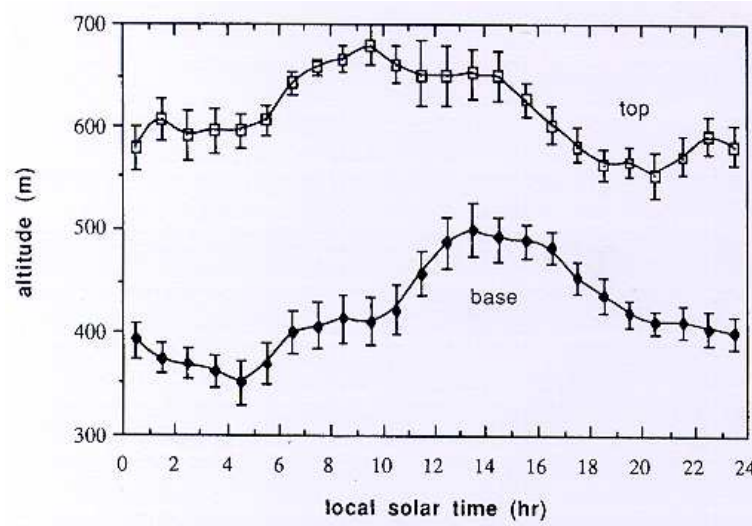
Figure 2.3: *Diurnal variation of cloud top and cloud base heights (m) observed at San Nicholas Island during FIRE: 1-19 July, 1987 (taken from Blaskovic* et al. *(1991)).*
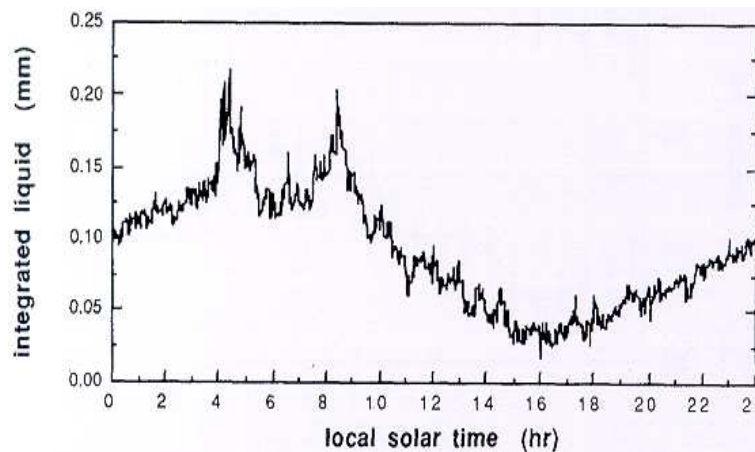
Figure 2.4: *Diurnal variation of liquid water path (kg m^{-2}) observed at San Nicholas Island during FIRE: 1-19 July, 1987 (taken from Blaskovic* et al. *(1991)).*

layer is heated and the lifting condensation level rises. Cloud base height was maximum at 1400 h, but the cloud layer is thinnest at 1600 h because the cloud top is declining at this time. Figure 2.4 shows the diurnal variation of LWP, from the same study (Blaskovic *et al.*, 1991), estimated using 10-minute averaged radiometer data. The two peaks in LWP at 0400 h and 0800 h can be traced back to two individual times when there was anomalously high LWP; they are not part of the typical diurnal trend. LWP varies from about 150 g m^{-2} around dawn (0500 h) to around 30 g m^{-2} at 1600 h (Fig. 2.4, note that the units mm and Kg m^{-2} are equivalent). The LWP was found to vary approximately with square of cloud thickness because the cloud liquid water content increased roughly linearly with height from cloud base, close to the adiabatic rate (Duynkerke and Hignett, 1993).
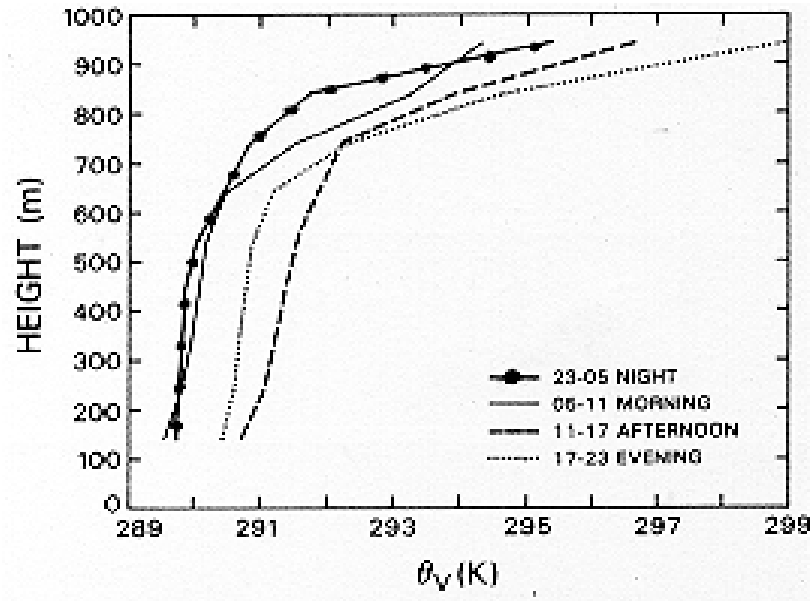
Figure 2.5: *Averaged radiosonde-derived profiles of virtual potential temperature (K) observed at San Nicholas Island from 10-12 July, during FIRE (taken from Betts (1990b)).*

More frequent sounding were taken during the periods of 10-12 July and 14-15 July when the synoptic situation was particularly steady, with light winds, and virtually unbroken stratocumulus over San Nicholas Island. Betts (1990b) summarises a subset of 20 soundings taken 10-12 July, which were averaged into four six-hour blocks. Figure 2.5 shows the averaged virtual potential temperature during each six-hour block. It reveals a diurnal temperature range of about 1.5 K in the BL, and a 100m variation of inversion height. The cloud top height, base and LWP on 14-15 July were fairly representative of the conditions throughout the FIRE period (compare Fig. 2.6, taken from Hignett (1991), with Figs. 2.3 and 2.4, taken from Blaskovic *et al.* (1991)). Figure 2.7 shows six temperature and humidity soundings taken between 0014 UTC 14 July, and 1935 UTC 15 July, along with straight-line approximations that were used to initialise model simulations the model intercomparison of the European Project on Cloud Systems in Climate Models (EUROCS) (Duynkerke *et al.*, 2000).

Figure 2.8 shows Large-Eddy-Simulation results from EUROCS. LWP varies between 50 and 150 g m^{-2}, which agrees reasonably well with the measurements of LWP on that day (Fig. 2.6). Other numerical studies that have used the observations from FIRE include one-dimensional models (e.g. Duynkerke and Hignett (1993), Smith and Kao (1996)) and Large-Eddy-Simulations (LES) (e.g. Wang *et al.* (2003)).

In summary, the FIRE stratocumulus experiment is one of the main sources of field data for marine stratocumulus studies. Other field experiments to date include the observations taken over the North
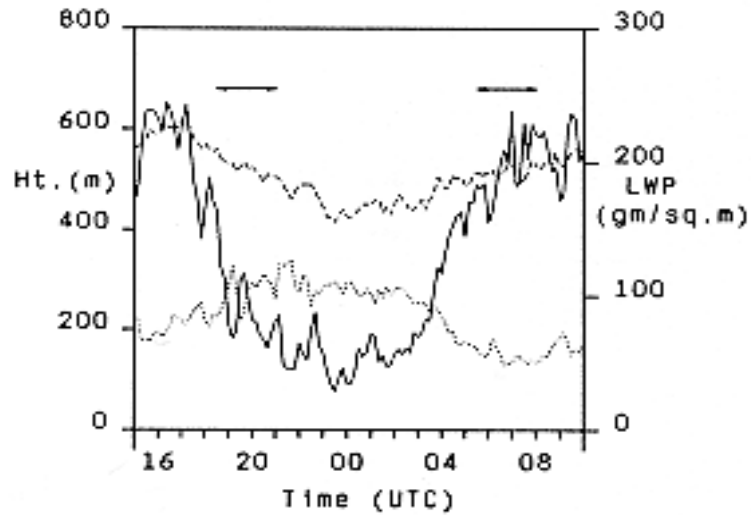
Figure 2.6: *Measurements of liquid water path (solid line), cloud top height (dashed line), and cloud base (dotted line) taken from San Nicholas Island between 1500 UTC 14 July to 1000 15 July. The measurements were made with the same instrument as used in Blaskovic* et al. *(1991), see text. Note that local noon is at 2100 UTC. This figure taken from Hignett (1991).*

(a) θ_l (K) vs Height (m)   (b) q$_t$ (g/kg) vs Height (m)
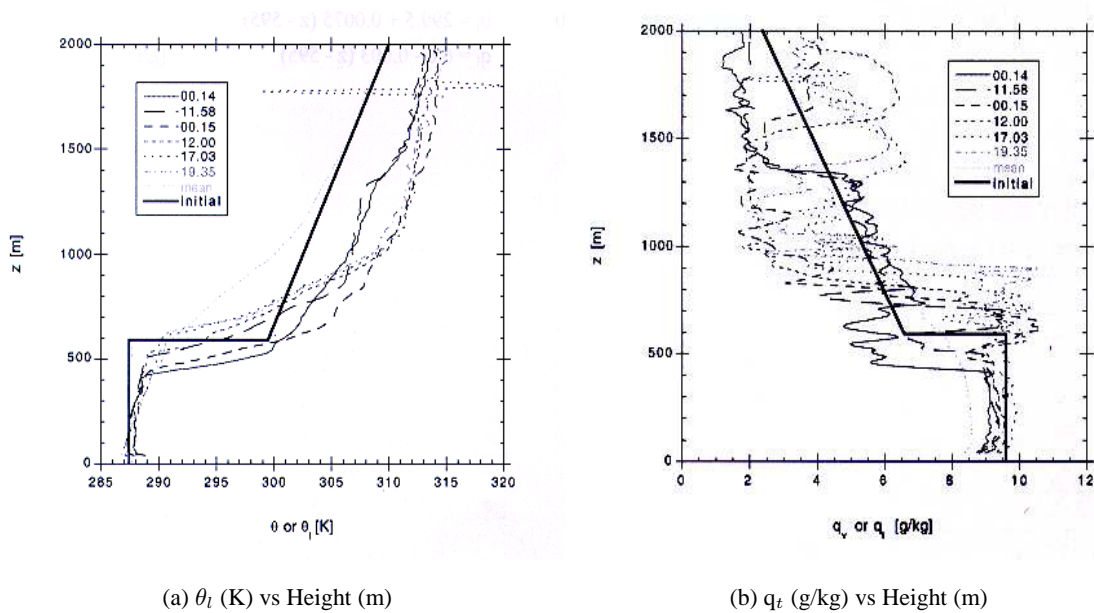
Figure 2.7: *Radiosonde profiles of a) liquid water potential temperature, and b) specific humidity profile at 0014 and 1158 UTC 14 July and 0015, 1200 1703 and 1935 UTC 15 July (Duynkerke and Teixeira, 2001). The thick lines are approximate fits used for the initial conditions in the LEM simulations.*

Sea during the summer of 1982 (Nicholls (1984), Nicholls and Leighton (1986)), the Atlantic Stratocumulus Transition Experiment (ASTEX) over the North-east Atlantic, June 1992 (Albrecht *et al.*,
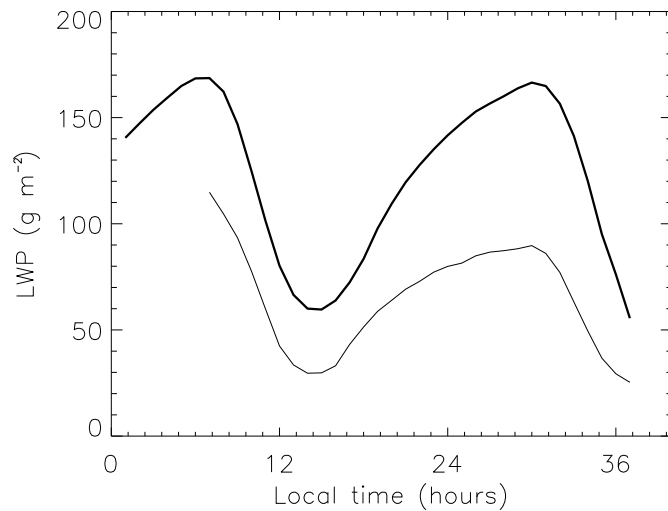
Figure 2.8: *Hourly averaged liquid water path (g m^{-2}) in the control simulation (thin line) and the average from six Large-Eddy-Simulation models for the EUROCS intercomparison study (data obtained from Duynkerke* et al. *(2000)).*

1995a), the second Aerosol Characterisation Experiment (ACE-2), July 1997 (Johnson *et al.*, 2000), in the same region. There are broad similarities between the meteorological conditions observed during FIRE and these other studies. Therefore, we consider the FIRE observations to be typical of marine stratocumulus conditions in general and ideal as a basis for the stratocumulus simulations in this thesis.

2.2   LEM simulations of marine stratocumulus

2.2.1   Experimental set-up

The Met Office Large-Eddy Model (LEM) has been used to simulate a marine stratocumulus-capped BL, using observations from the FIRE stratocumulus experiment (see previous section). The simulations are started with an idealised well-mixed BL structure. Liquid water potential temperature (θ_l) and total water (q_t) are constant in the BL, and there is a step change at 600m to represent the inversion (Table 2.1, see Appendix 1 for a definition of θ_l and q_t, and a description of the LEM). The initial θ_l and q_t profiles (Fig. 2.7) are based on 6 radiosonde ascents, taken from San Nicholas Island on 14-15 July (Duynkerke and Hignett, 1993), and are the same as those used in EUROCS model inter-comparison for stratocumulus over the ocean (Duynkerke *et al.*, 2000). Initially the cloud top was at 600 m and the cloud base was at 250 m giving a 350 m thick cloud layer with a liquid water path of 110 g m^{-2}.

SST was fixed at 288 K and the surface roughness length was 2 x 10^{-4} m, based on Duynkerke *et al.* (2000). The surface pressure of 1012.5 mb, and the components of the geostrophic winds, U and V (see Table 2.1) were taken from the ECMWF reanalysis for July 1987, and are consistent with surface observations from Hignett (1991). At the initial time the winds were set to the geostrophic values (given in Table 2.1). The subsidence rate was given by W_{subs} = Div x Z, where Div is the large-scale divergence rate and Z is height. The large-scale divergence rate was set to 5.5. x 10^{-6} s^{-1} so that W_{subs} roughly balanced the entrainment rate given by the model. This balance helped to prevent drift in the inversion height. The domain was cooled at a rate of 1 K day^{-1} to account for the large-scale advective temperature tendency. The cooling rate was derived from monthly mean NCEP reanalysis data for July 1987.

The horizontal grid spacing was 50 m, which allowed good resolution of large eddies in the BL. There were 80 levels in the vertical, and the resolution varied from 20 m in the sub cloud layer to 7 m near the inversion, and up to 40 m near the model top of 1200 m. The enhancement of vertical resolution at the inversion helped to better resolve the structure of the inversion, the cloud-top generation of turbulence, and the entrainment process. The vertical resolution was reduced elsewhere, especially above the inversion to minimise computational expense. A large domain size of (2.5 km x 2.5 km) was used to reduce the impact of small-scale horizontal variability on domain averaged results. However, the domain size was reduced to (1.0 km x 1.0 km) for the sensitivity experiments (see table 2.2) to reduce computational expense.

The simulations were started at 0600 h (just after dawn) and run for 42 hours, essentially two diurnal cycles, except for simulations control-10 and A-088-10, which were run for ten days (Table 2.2). Turbulence was initiated by applying small random perturbation to the temperature and moisture fields at the initial time. The temperature in the layer between 1000 m and the model top (1200 m) was relaxed towards the initial profile with a 3 hour time scale to prevent the temperature in the free troposphere from drifting with time. Microphysical parameterizations were switched off, as earlier tests showed that the liquid water concentration in the cloud was insufficient to generate significant precipitation. The cloud droplet effective radius (r_e) was specified as 10 μm, which meant that the cloud visible optical depth (τ_{cloud}) was directly proportional to the LWP:

$$\tau_{cloud} \approx (\frac{3}{2})\frac{LWP}{\rho_l r_e} \qquad (2.1)$$

Height (m)	θ_l (K)	q_t (g kg^{-1})	U (m s^{-1})	V (m s^{-1})	aerosol mass mixing ratio(kg kg^{-1})
0	287.5	9.6	1.0	-6.0	3x10^{-8}
595	287.5	9.6	1.0	-6.0	3x10^{-8}
605	299.5	6.6	1.0	-6.0	3x10^{-8}
900	301.75	6.6	1.0	-6.0	0.0
1200	304.0	6.6	1.0	-6.0	0.0

Table 2.1: *Initial conditions and aerosol mass mixing ratio. U and V are the zonal and meridional wind components, respectively.*

(where ρ_l is the density of liquid water = 1000 kg m^{-3}).

The radiation scheme was set-up for latitude 33°N and 15 July, corresponding to the FIRE observation period and location. Sunrise and sunset are at 0500 h and 1900 h, respectively and the solar zenith angle is about 12° at noon (1200 h). The diurnal mean downwelling shortwave at the top of the atmosphere is 473 W m^{-2}, compared to the annual mean of 357 W m^{-2} for that latitude. It is therefore important to note that the shortwave heating rates and radiative forcings in these experiments are representative of the summer season, not the annual mean. Due to the computational expense of using the LEM it was not possible to repeat experiments at different latitudes or different times of the year. The radiative fluxes and heating rates are calculated every 200 seconds, and for each column so that spatio-temporal variability in radiative heating rate is fairly well resolved. The use of a two-stream radiation scheme does however lead to errors in accounting for scattering by particles at high solar zenith angles, particularly in representing the path lengths of diffuse radiation and the amount of radiation that is backscattered. The radiation scheme also neglects horizontal transfer of radiation between column (the independent column approximation). Representing the full three dimensionality of the radiation field can lead to interesting interactions between inhomogeneities in cloud-top height and longwave radiative cooling, which potentially influence the generation of turbulence at the top of stratocumulus layers (Ovtchinnikov *et al.*, 2002). However, representing such interactions is not an important consideration in these experiments given the general difficulty in resolving cloud-top processes, even with a vertical grid spacing of 5 m (Chlond and Wolkau, 2000).

Aerosols were represented by a dry external mixture of soot and ammonium sulphate; optical properties are from WCP (1986) (see Appendix A for further details). The ratio of soot to ammonium sulphate is varied to give a range of mid-visible [1] single scattering albedos (ω) from 0.88 to 1.00 (Table 2.2). A

---

[1] All values of τ and ω given are for a wavelength 0.55μm.

mass mixing ratio of 3 x 10^{-8} was used, which gave a diurnal mean aerosol heating rate of about 1 K day^{-1} for the simulations with $\omega = 0.88$. The aerosol mixing ratio was constant in the BL and reduced linearly to zero 300 m above the inversion. This profile was based on the assumption that aerosols are confined mainly to the BL, and is intended to give a first estimate for semi-direct aerosol effect. Sensitivity of the semi-direct effect to the aerosol vertical distribution is investigated in chapter 5. The aerosol optical depth was 0.15 in all simulations that included aerosol, regardless of the ω used. The aerosols do not interact with the microphysics and therefore do not lead to indirect effects. This allows us to isolate the semi-direct aerosol effect separately from any indirect impacts on the cloud. However, an estimate of the indirect aerosol forcing is calculated separately in section 2.2.5.

Table 2.2 provides a summary of the simulations in this chapter, including details of the aerosol ω, domain size, and the duration. The no-sun simulation excludes solar radiation and is used to study to the nocturnal BL structure. The impact of solar absorption is investigated by comparing this with the control simulation, and the absorbing aerosol simulation (simulation A-088). Simulations A-088, A-092, A-096 and A-100 are used to explore the dependence of the semi-direct radiative forcing on the single scattering albedo, and to show how it compares with the direct radiative forcing. Finally, these results are tested for robustness to domain size, initial condition uncertainty, and the duration of the simulation.

2.2.2   BL structure in the absence of solar radiation

The first 12 hours of the no-sun simulation, are used to examine the structure and turbulent characteristics of the BL under nocturnal conditions. The simulation was continued for a further 30 hours without solar radiation because it is interesting to see how the absence of solar radiation impacts the evolution of the BL on longer time scales. The lack of a diurnal cycle also brings to view variability on time scales of several hours, related to internal variability, or turbulence.

In the first hour large eddies grow in the BL leading to an initial peak in the resolved eddy kinetic energy. The resolved eddy kinetic energy oscillates with a period of about 40 minutes (Fig. 2.9). These oscillations are probably the signature of the largest eddies in the BL, which have the greatest energy. The time series of maximum updraught velocity (Fig. 2.10) indicates that there is also a lot of smaller scale turbulence.

The main source of turbulent kinetic energy (TKE) is the cloud-top longwave cooling, as indicated by the TKE peak just below cloud top (Fig. 2.11). Here negatively buoyant parcels are created and

Simulation name	Aerosol ω at 0.55μm	Domain size (km)	Duration (hours)	Comment
No-sun	N/A	2.5 x 2.5	42	No solar radiation
Control	N/A	2.5 x 2.5	42	No aerosols (control)
A-088	0.88	2.5 x 2.5	42	Absorbing aerosols
A-092	0.92	2.5 x 2.5	42	Absorbing aerosols
A-096	0.96	2.5 x 2.5	42	Absorbing aerosols
A-100	1.00	2.5 x 2.5	42	Scattering aerosols
Control-10	N/A	1.0 x 1.0	234	Ten-day control
A-088-10	0.88	1.0 x 1.0	234	Ten-day with absorbing aerosols
A-088-E1	0.88	1.0 x 1.0	42	Initial condition ensemble
A-088-E2	0.88	1.0 x 1.0	42	''
A-088-E3	0.88	1.0 x 1.0	42	''
A-092-E1	0.92	1.0 x 1.0	42	''
A-092-E2	0.92	1.0 x 1.0	42	''
A-092-E3	0.92	1.0 x 1.0	42	''
A-096-E1	0.96	1.0 x 1.0	42	''
A-096-E2	0.96	1.0 x 1.0	42	''
A-096-E3	0.96	1.0 x 1.0	42	''

Table 2.2: *Outline of the simulations in this chapter*

sink through the cloud layer leading to mixing. Wind shear near the ground and convective instability driven by surface sensible heat fluxes (Fig. 2.13) also contribute to the turbulence. TKE is fairly evenly distributed in the BL indicating that eddies span the depth of the BL transporting and mixing the TKE throughout the layer. In contrast, TKE is virtually zero in the free troposphere where the high static stability greatly inhibits the development or vertical transport of eddies. There is a sharp transition between the turbulent BL and the quiescent free troposphere associated with the inversion. BL eddies distort the inversion surface leading to the envelopment of free tropospheric air into the cloud, followed by rapid mixing and evaporation. These incursions of entrained air create thin patches in the cloud layer. Figure 2.14 shows dark areas where the LWP is about half the mean value. One such area is shown in a distance-height cross-section of liquid water (Fig. 2.15). The drying extends about 200m into the cloud.
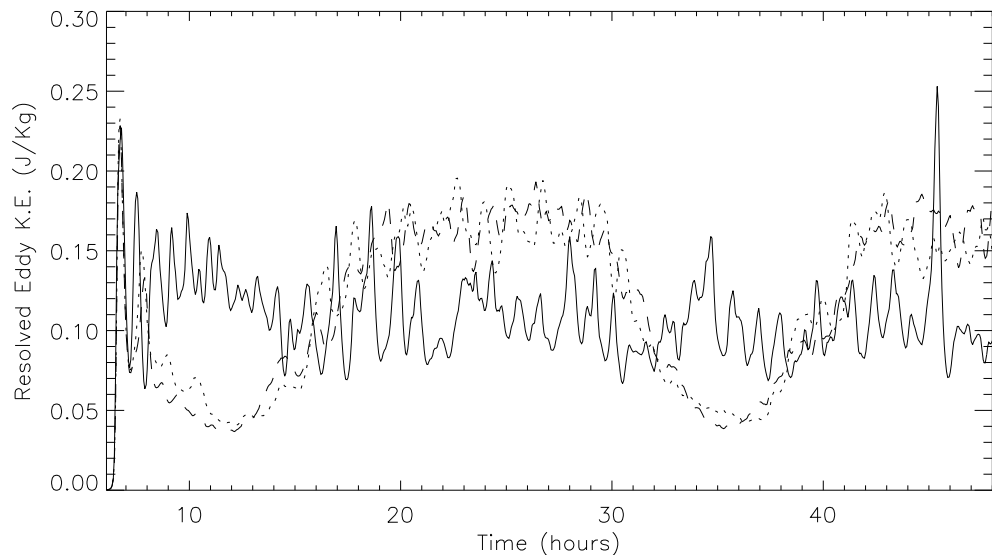
Figure 2.9: *Resolved eddy kinetic energy (J kg^{-1}) for the no-sun simulation (solid line), control simulation (dotted line), and simulation A-088 (dashed line).*

The turbulent vertical moisture flux is almost constant with height through the BL, and reduces rapidly towards zero across the inversion (Fig. 2.16), indicative of a well-mixed layer with entrainment occurring across the inversion. The turbulent moisture flux increases slightly with height and is about 10 percent higher at the inversion base than at the surface. This means that there is an imbalance between the surface moisture flux and the entrainment flux and the BL is gradually drying (compare the initial total water profile with the total water profile at 1200 h in the no-sun simulation, Fig. 2.17 (b)).

During the first 12 hours of the no-sun simulation the profiles of total water and liquid water potential
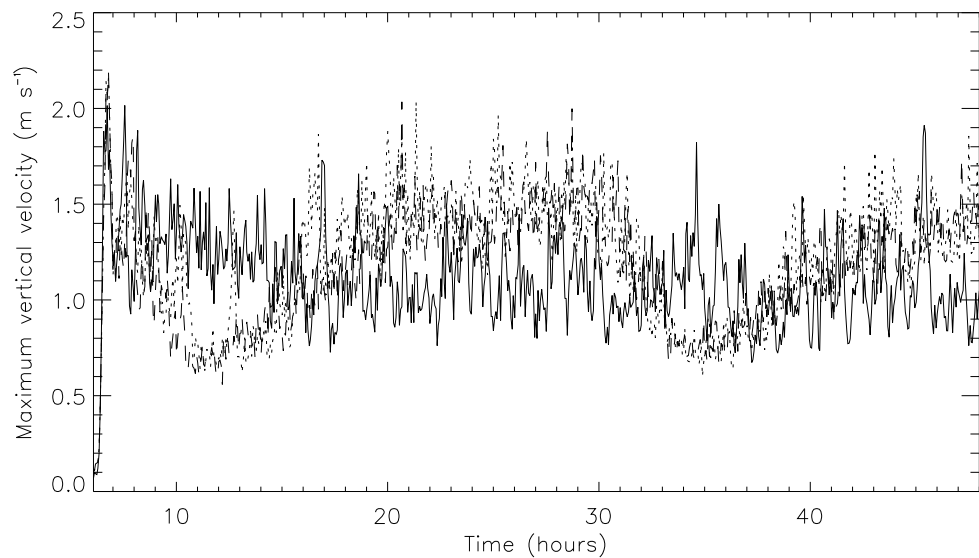
Figure 2.10: *Maximum values of vertical velocity, w (m s^{-1}) for the no-sun simulation (solid line), control simulation (dotted line), and simulation A-088 (dashed line).*
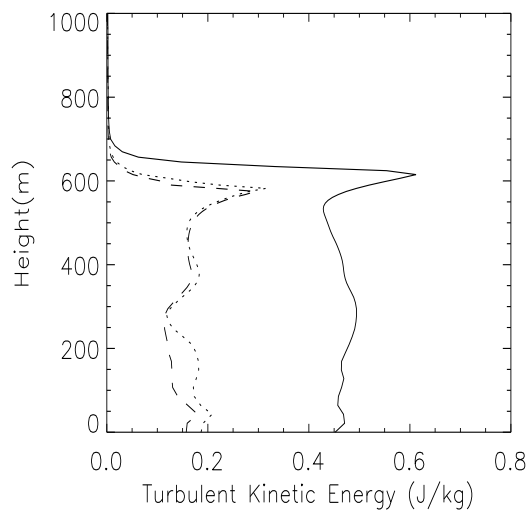
Figure 2.11: *Turbulent kinetic energy (J kg^{-1}) for the no-sun simulation (solid line), control simulation (dotted line), and simulation A-088 (dashed line).*

temperature profiles are very similar to the initial profiles, apart from smoothing of the discontinuities of the initial temperature and total water profiles at the inversion and the surface (Fig. 2.7). There is also a gradual warming, drying, and deepening of the BL with time, leading to a gradual rise of the cloud-top and cloud base, and a decline of LWP (Fig. 2.18 (a)).

Although the structure (Fig. 2.17) and turbulent characteristics (Fig. 2.9 & 2.10) remain qualitatively
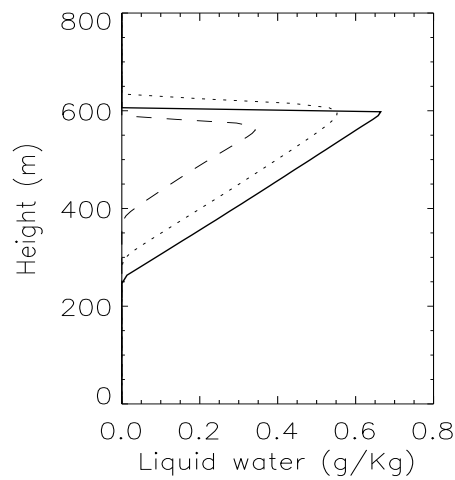
Figure 2.12: *Liquid water (g kg^{-1}) at the initial time (thick solid line), and 6 hours later (1200 h) for the no-sun simulation (dotted line), and control simulation (dashed line).*
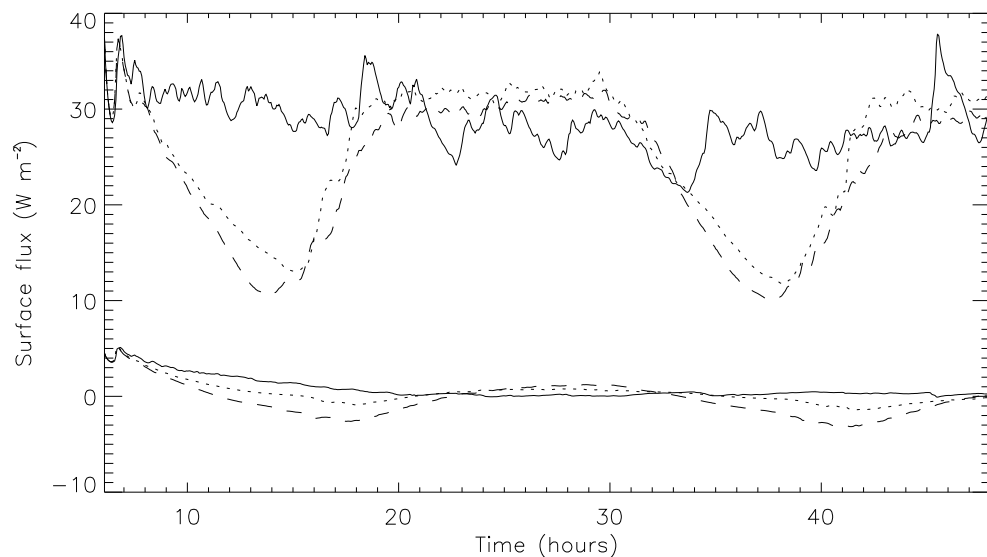
Figure 2.13: *Surface fluxes of latent heat (W m^{-2}) (upper lines), and sensible heat (W m^{-2}) (lower lines) for the no-sun simulation (solid line), control simulation (dotted line) and simulation A-088 (dashed line) with local time (hours).*

the same during the simulation, the BL is not in a steady state. The resolved eddy kinetic energy and maximum updraught velocity seem to be on a downward trend indicating a decrease in turbulence intensity with time (Fig. 2.10 & 2.9). This is related to a reduction of cloud top longwave cooling, related to the steady decline in LWP (Fig. 2.18 (a)). Also, there is a steady rise in cloud base and cloud top (Fig. 2.18 (b)), plus a slight warming and drying of the BL between 1200 h and the initial time
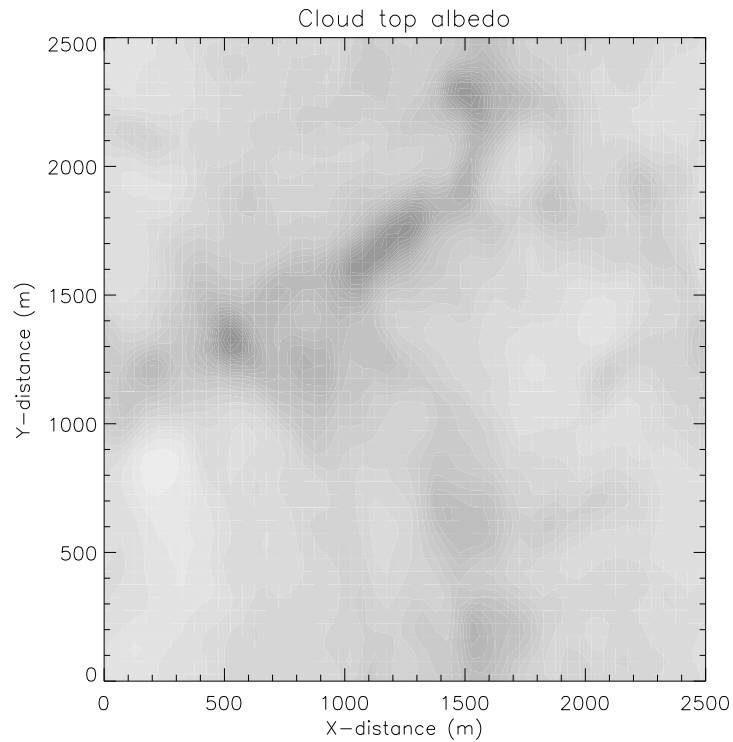
Figure 2.14: *Cloud top albedo vs X and Y horizontal distance (m) at 0300 h in the no-sun simulation. Values range from 0.38 in the darkest regions to 0.62 in lightest regions.*
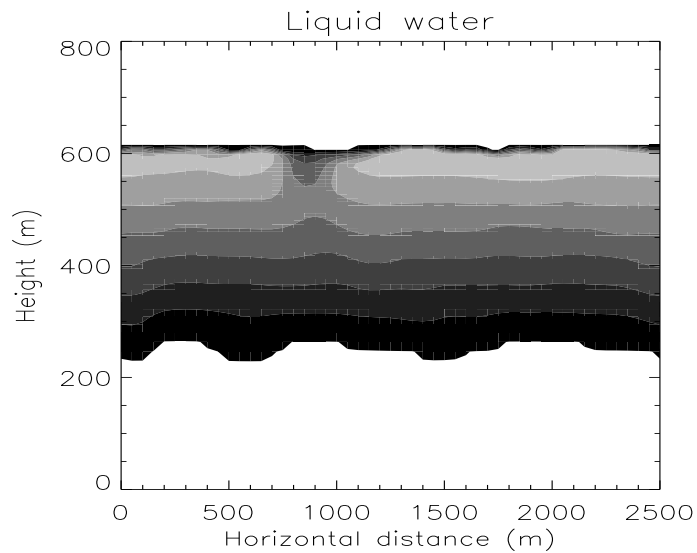
Figure 2.15: *Cross-section of liquid water (g kg^{-1}) with height (m) and horizontal distance (m) at 0300 h in the no-sun simulation. Contour interval is 0.1 g kg^{-1}, maximum values are around 0.65 g kg^{-1}.*

(Fig. 2.17). Thus the heat, moisture and mass budgets are out of balance due to the imbalance between the effects of entrainment and subsidence, surface fluxes and longwave radiative cooling.
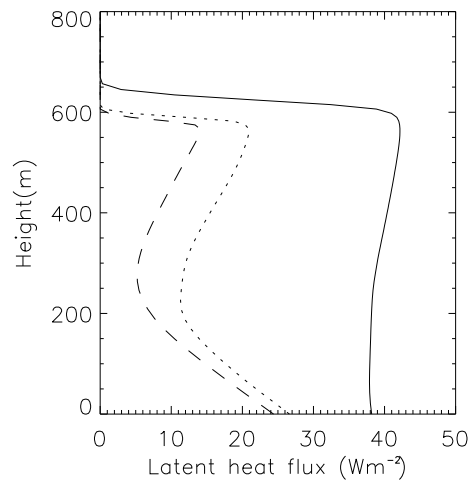
Figure 2.16: *Turbulent latent heat flux (W m^{-2}) at 1200 h for the no-sun simulation (solid line), control simulation (dotted line) and simulation A-088 (dashed line).*
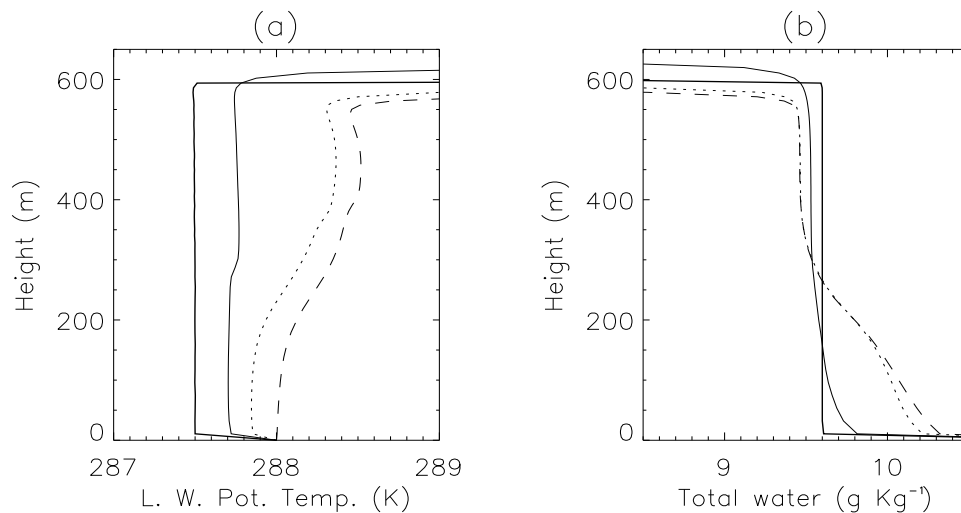
Figure 2.17: *(a) Liquid water potential temperature (K) and, (b) total water (g kg^{-1}) at 1200 h for the no-sun simulation (solid line), control simulation (dotted line) and simulation A-088 (dashed line). Also shown are the initial profiles (thick solid line).*

Cloud-top, cloud base and LWP appear to converge to equilibrium values towards the end of the simulation (Fig. 2.18), suggesting that a steady state has been reached. It is interesting to note that LWP converges to a similar value as the LWP in the control run at the end of the second night. The LWP may be controlled by feedback between the LWP, the cloud top longwave cooling rate, and the entrainment rate. For instance, a higher LWP leads to a higher cloud top longwave cooling rate, greater turbulence, and a higher entrainment rate, which would reduce LWP. Cloud top longwave cooling is also important
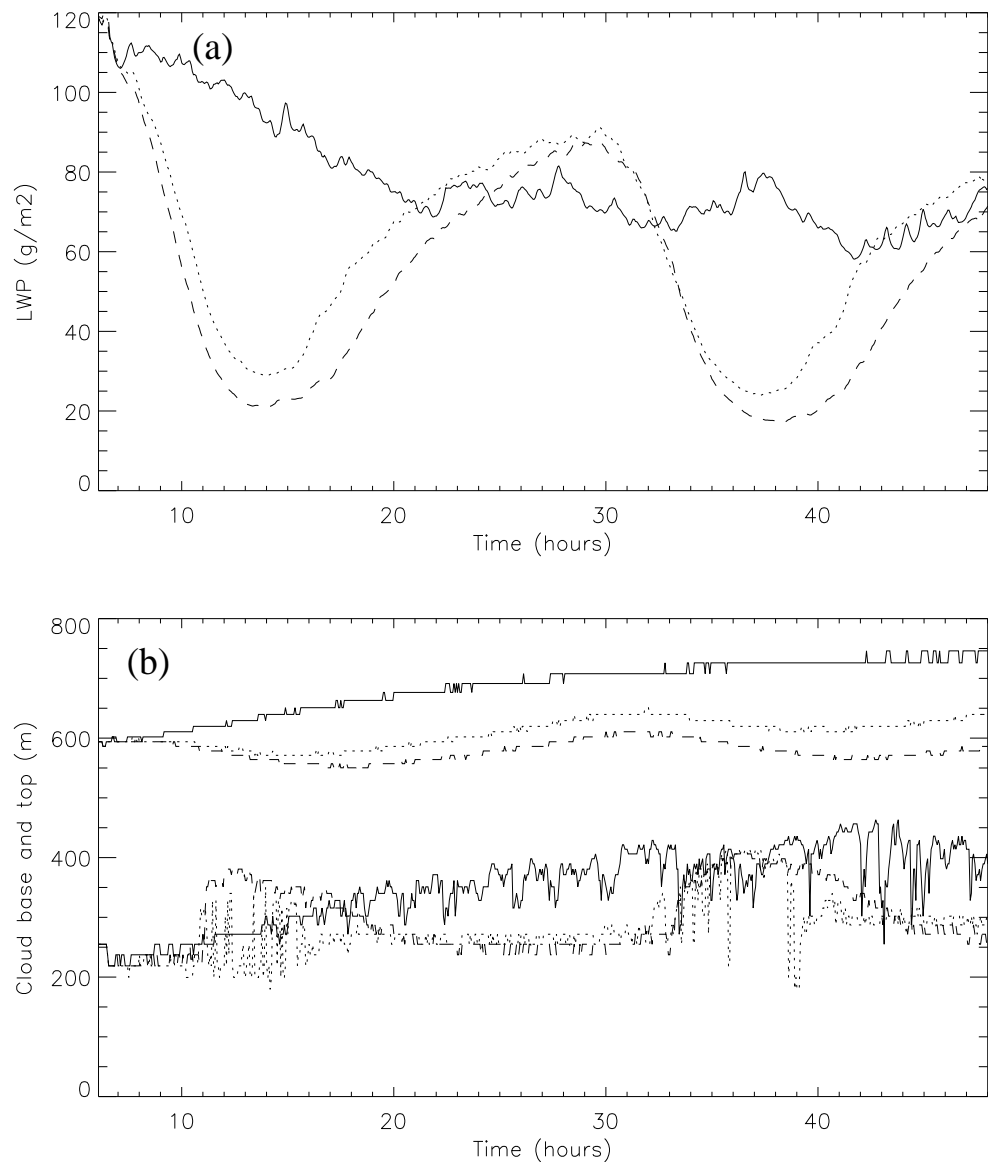
Figure 2.18: *(a) LWP (g m^{-2}), and (b) Cloud base and cloud top height for the no-sun simulation (solid line), control simulation (dotted line) and simulation A-088 (dashed line).*

in maintaining moisture fluxes through the BL. The turbulence and the overall cooling from longwave emission are important in maintaining the well-mixed state of the BL. However, the total emission from the cloud does not change very much with LWP, because the cloud layer is almost optically thick in the longwave, so the average longwave cooling rate in the cloud layer will be about the same. If the average longwave cooling in the cloud layer, and the turbulence in the BL, are sufficient to maintain a well-mixed BL state then perhaps an intensification of the longwave cooling at the cloud top would not greatly increase the supply of moisture to the cloud, whereas it would intensify entrainment. Through these feedbacks the LWP may adjust to maintain a balance between entrainment drying and moisture

fluxes through the BL.

2.2.3   Impact of solar radiation on BL structure

In this section, the diurnal variation of the SCBL is investigated by comparing the control simulation, which included solar radiation, with the no-sun simulation that did not include solar radiation. The control simulation is also compared with the absorbing aerosol simulation (simulation A-088, see table 2.2) to investigate the impact of solar absorption by aerosols, and to evaluate the semi-direct aerosol radiative forcing.
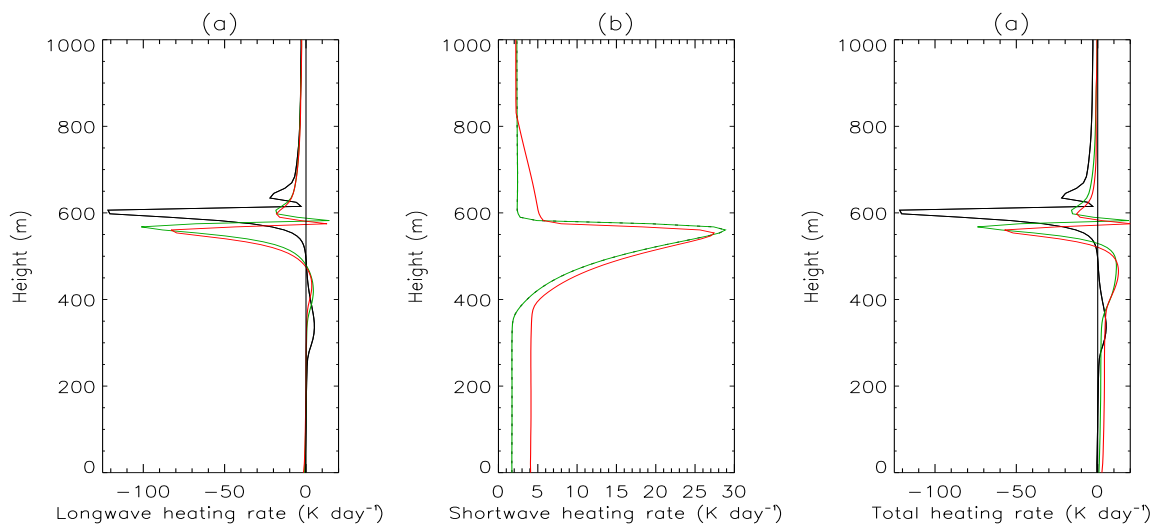
Figure 2.19: *(a) Longwave, (b) shortwave, and (c) total radiative heating rates (K day^{-1}) at 1200 h in the no-sun simulation (black line), the control simulation (green line), and simulation A-088 (red line).*

The main impact of solar radiation on the SCBL is a reduction of LWP (Fig. 2.18) due to an increase in temperature (Fig. 2.17) and evaporation of the cloud (Fig. 2.12). There is also a stabilisation of the BL (Fig. 2.17) and a reduction of cloud-top generated turbulence because the solar heating rate is greater in the cloud layer, and peaks at cloud-top (Fig. 2.19 (b)) offsetting the cloud top longwave cooling rate (Fig. 2.19 (a)). This leads to decoupling, and a reduction of the turbulent moisture flux at cloud base, contributing to the daytime reduction of LWP (Fig. 2.18 (a)).

LWP declines rapidly during the morning and reaches a minimum at 1400 h of about 28 g m^{-2} in the control simulation (Fig. 2.18 (a)). LWP is lower in the aerosol simulation, reaching 20 g m^{-2} at 1400 h, because of the additional shortwave heating in the BL (Fig. 2.19 (b)). The lower LWP results in a positive semi-direct aerosol radiative forcing (see section 2.2.4 for more details). It is interesting to
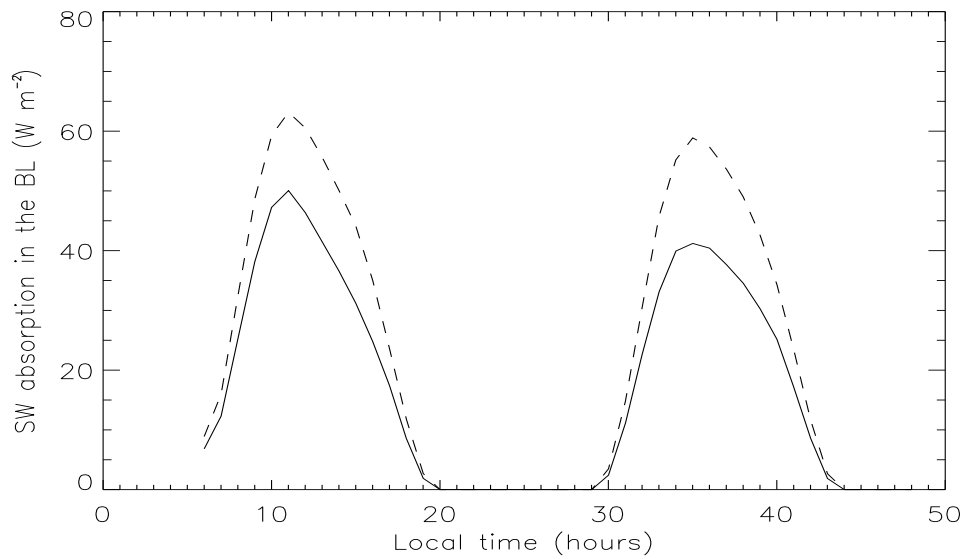
Figure 2.20: *Shortwave absorption in the BL ($W\,m^{-2}$) as a function of local time (hours) for the aerosol-free case (solid line), and the simulation A-088 (dashed line).*

note that the shortwave heating at the cloud top is actually lower in the absorbing aerosol simulation because of the reduction of liquid water content (Fig. 2.12). However, the total absorption in the BL is still higher in the absorbing aerosol simulation, as shown in Fig. 2.20. The shortwave absorption peaks one hour before noon because of the steady decline in LWP during the middle of the day. This highlights a negative feedback between LWP and shortwave heating. Shortwave heating reduces LWP, and the decline in LWP reduces the shortwave heating rate. This feedback will limit the rate at which LWP falls during the daytime.

Feedback between LWP and the longwave cooling may also help to sustain the LWP, as suggested in the previous section, and act to modulate the semi-direct effect. With a lower LWP in the absorbing aerosol simulation the cloud top longwave cooling is less intense (Fig. 2.19 (a)). This led to a lower entrainment rate, as inferred from the decline in the cloud top height between 0900 and 1600 h (Fig. 2.18 (b)), limiting the LWP reduction.

Domain average resolved eddy kinetic energy reduce by a factor of 2-3 in the daytime (Fig. 2.9), and the magnitude of temporal fluctuations decreases dramatically. This is indicates a reduction in the strength and size of the largest eddies in the BL, following the shortwave heating in the cloud (Fig. 2.19 (b)), the stabilisation of the BL (Fig. 2.17 (a)) and the decline in the intensity of cloud top longwave cooling (Fig. 2.19 (a)).

LWP increases rapidly in the evening as the shortwave heating declines, and the BL cools and recouples with the surface layer (Fig. 2.18). Through the night LWP rises slowly, stabilising at 85 - 90 g m^{-2} in both simulations. The LWP is lower on the second day. For example, the LWP at dawn is 30 g m^{-2} lower on day 2 (90 g m^{-2}, compared to 120 g m^{-2}). This trend reflects the divergence of the BL structure from the initial conditions, towards an equilibrium state with a lower LWP, and a deeper BL (discussed in the previous section).

The cloud base rises from 250 m at dawn to around 400 m in the afternoon, leading to a thinning of the cloud layer (Fig. 2.18). The cloud base roughly corresponds to the lifting condensation level in the no-sun case (Fig. 2.18), but during the daytime the lack of mixing means that the cloud layer is decoupled from the surface layer and cloud base is well above the lifting condensation level. In the control simulation the cloud base tends to switch between the lifting condensation level at 200 m, and a higher level at 350 - 400 m. This shows that clouds are occasionally forming at the top of the surface mixed layer, but the liquid at this level is negligible (Fig. 2.12) suggesting that the lower level cloud is either very diffuse or sparse and transient. The presence of low-level cumulus is typical of decoupled SCBLs (e.g Wyant *et al.* (1997)). There is no such low level cloud in the absorbing aerosol case because of the higher temperature (Fig. 2.17) and lower relative humidity.

The surface sensible heat flux is very small (Fig. 2.13) and becomes negative in the afternoon when the temperature near the surface rises above the SST. In simulation A-088, the temperature near the surface is even higher during the day (Fig. 2.17), leading to a larger negative surface sensible heat flux (Fig. 2.13). The surface latent heat flux (Fig. 2.13) reduces during the day because of the decoupling and the reduction in turbulence (Fig. 2.9 & 2.11). As the BL stabilises the moisture flux between surface layer and cloud layer is inhibited. This process is revealed by the minimum in the moisture flux at around 300 m in the control and simulation A-088 at 1200 h (Fig. 2.16). This means that water vapour accumulates in the surface layer but is diminished in the cloud layer (Fig. 2.17).

The stabilisation of the BL, (Fig. 2.17) and reduction of cloud base moisture flux (Fig. 2.16) are more pronounced in simulation A-088 compared to the control simulation. However, there is very little difference in the cloud layer total water. This is because of a compensating reduction in the entrainment flux so that the moisture fluxes divergence across the cloud is about the same (Fig. 2.16). However, from the increase in θ_l we can infer that more evaporation has occurred resulting in a lower liquid water content (Fig. 2.12), and lower LWP (Fig. 2.18).

In summary, the diurnal cycle of LWP is caused by solar heating in two ways. Firstly by heating

leading to evaporation. Secondly by stabilising the layer leading to decoupling and a reduction of the cloud base moisture flux. However, because of the feedback between temperature changes, turbulent mixing and entrainment rate it is difficult to separate out these effects. These results are consistent with observations of diurnal variability in the SCBL (e.g. Nicholls (1984), Nicholls and Leighton (1986), Betts (1990b), Hignett (1991), Blaskovic *et al.* (1991)).

The LWP in these simulation is somewhat lower than in the observations of Blaskovic *et al.* (1991) from FIRE (e.g. compare Fig. 2.18 (b) with Fig. 2.4, taken from Blaskovic *et al.* (1991)). The observations show LWP varies from 150 g m^{-2} in the morning to 30 g m^{-2} in the afternoon, whereas the LEM simulations have a variation of 20 - 70 g m^{-2}. The underestimation of nighttime LWP is probably due to an overestimation of subgrid-scale diffusion, leading to a higher entrainment rate than would occur in the real world. It is well recognised that LES tend to overestimate entrainment rates (e.g Bretherton *et al.* (1999)). Also, we have probably specified a higher than realistic subsidence rate because a balance between entrainment and subsidence was desired. In the real world however, SCBLs tend to deepen with time, implying that subsidence is somewhat less than the entrainment rate. In the EUROCS intercomparison the problem of excessive entrainment was compensated for by applying a high 'large-scale' cooling rate of up to 3 K day^{-1}, and a moistening rate of up to 1.5 g kg^{-1} day^{-1}. Instead, we used a cooling rate of 1 K day^{-1}, based on reanalysis data (see section 2.2.1 for more details) and had no moistening. Figure 2.8 compares the hourly average LWP from six LESs in the EUROCS intercomparison, with the control run. The simulations in the intercomparison study have a higher LWP and are closer to observed values. Had we raised the cooling rate and applied a moistening rate, the LWP values in our simulations would have been closer to observed values. However, this 'fix' may have interfered with the response of the BL to the heating perturbation from the absorbing aerosols.

2.2.4   Semi-direct aerosol forcing

The semi-direct radiative forcing (Fig. 2.21) is the difference in net radiation at the top of the atmosphere between the aerosol and control simulation (total forcing), minus the direct aerosol radiative forcing:

$$\text{Semi-direct forcing = total forcing - direct forcing} \qquad (2.2)$$

The direct aerosol radiative forcing (Fig. 2.21) is the direct impact of the aerosols on the net radiation at the top of the atmosphere. This is calculated as the difference between radiation calculations including and not including the aerosol, but using the same cloud field, the cloud field corresponding to the aerosol simulation. The semi-direct forcing depends only on the differences in the clouds fields between the aerosol and control simulation, and the incident solar radiation. A maximum of 70 W m^{-2} occurs in simulation A-088 at around 1200 h on day 1, and 3900 h on day 2 (Fig. 2.21), when the solar insolation is near the diurnal maximum, and differences in LWP are greatest (Fig. 2.18). This is equivalent to a 30% reduction of cloud radiative forcing from the control simulation at those times.
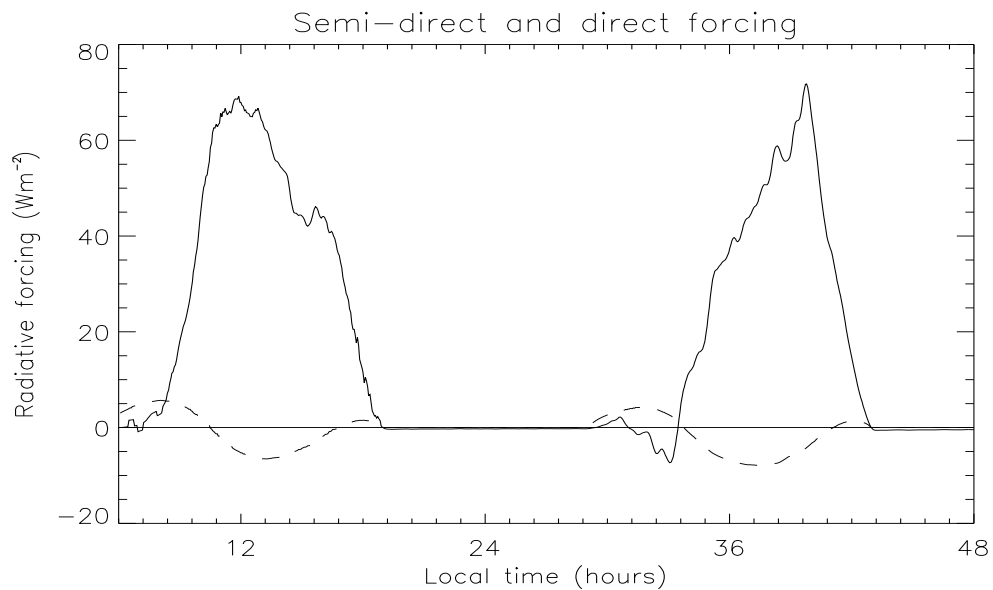
Figure 2.21: *Semi-direct (solid line) and direct (dashed line) aerosol radiative forcing (W m^{-2}), at the top of the atmosphere, for simulation A-088 (ω = 0.88).*

One contributor to the strength of the semi-direct effect is that the cloud layers are close to the optically thin limit during the middle of the day. For example, at 1400 h $\tau = 4.5$ and cloud albedo (α) = 0.25 in the control simulation, and $\tau = 3$, $\alpha = 0.18$ in exp. A-088. In the optically thin limit, the cloud albedo is most sensitive to differences in τ. This maximises the semi-direct radiative forcing for a given difference in LWP. Had both cloud layers been much thicker the same difference in LWP would have resulted in a smaller semi-direct radiative forcing.

Fluctuations in the semi-direct forcing reflect turbulent variations in the domain average cloud albedo. These fluctuations have time scales ranging from several minutes to several hours. For example, there is a secondary peak at 1600 h on day 1, and a period of negative forcing at 3300 h. The impact of such fluctuations on the diurnal mean semi-direct forcing is investigated in section 2.2.6.

Simulation	Aerosol ω	Semi-direct Day 1	Semi-direct Day 2	Direct Day 2	Total Day 2
A-088	0.88	18.5	14.0	-0.6	13.4
A-092	0.92	13.0	11.7	-1.2	10.5
A-096	0.96	7.0	6.1	-2.0	4.1
A-100	1.00	-0.1	0.9	-2.9	-2.0

Table 2.3: *The semi-direct, direct, and total aerosol radiative forcings (W m^{-2}) for different mid-visible aerosol single scattering albedos (ω). The total forcing is the sum of the semi-direct and direct forcings. The diurnal mean forcings are calculated by averaging between 0600 h and 3000 h for day 1 and from 2400h to 4800 h for day 2.*

The direct forcing in simulation A-088 is clearly an order of magnitude lower than the semi-direct forcing. It varies between 7 and -7 W m^{-2} (Fig. 2.21), depending on the solar zenith angle, and the evolution of the cloud layer during the day. The direct forcing is highest in the morning when the cloud layer is thicker, as more solar radiation is reflected upwards and absorbed by the aerosols above the cloud. In the middle of the day, when the cloud has a lower albedo, scattering by the aerosol becomes more important and the direct forcing becomes negative. Thus, the direct forcing is quite sensitive to cloud thickness; the direct forcing would have been slightly higher, maybe positive, had it been calculated using the the cloud fields from the control simulation. Alternatively, the direct forcing in clear skies would have been much lower (still negative, and greater in magnitude).

Table 2.3 shows the diurnal average semi-direct, direct and total forcings for all four simulations. The semi-direct forcing is clearly dominant over the direct forcing. Even for moderately absorbing aerosols (e.g. simulation A-096, $\omega = 0.96$) the semi-direct forcing is three times the magnitude of the direct forcing, and has the opposite sign. Both the semi-direct forcing, and the direct forcing increase linearly with increasing aerosol absorption, i.e. decreasing ω. However, the rate of change of radiative forcing with ω is about six times greater for the semi-direct forcing, than for the direct forcing (0.9 to 14.0 W m^{-2}, compared with -2.9 to -0.6 W m^{-2} (Table 2, day 2 values)). This shows that the changes in cloud LWP have a much greater impact on the radiation budget than the direct aerosol forcing. The semi-direct forcings for day 1 are also shown in Table 2.3 to highlight inter-day variability in the diurnal mean forcing. Day 1 was essentially a spin-up period and the cloud response is not representative compared to the response on subsequent days (as will be shown in the following section).
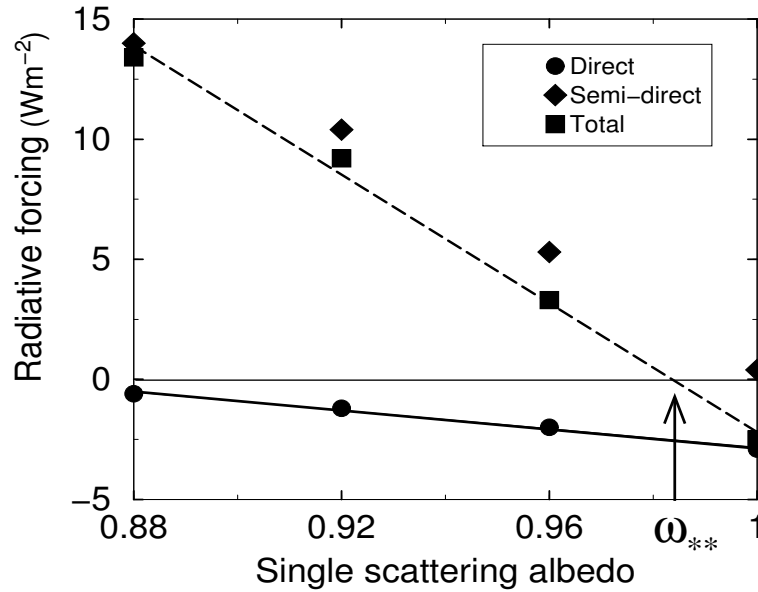
Figure 2.22: *The direct, semi-direct and total aerosol radiative forcings (W m^{-2}) for day 2 with linear fits to the direct forcing (solid line) and total forcing (dashed line).*

The relationship between the semi-direct forcing and ω appears to be linear over the range of ω values (0.88 - 1.00) used in the simulations (see Fig. 2.22). However, a lower single scattering albedo, or a higher aerosol optical depth could lead to the complete evaporation of the cloud layer, at which point the linearity of the relationship would break down. Using a linear interpolation (Fig. 2.22), the direct and semi-direct forcings would balance for $\omega = \omega_{**} = 0.985$ (where ω_{**} is the critical single scattering albedo for the sum of the semi-direct, and direct forcings). Hence, the total aerosol radiative forcing (excluding indirect effects) would be positive for $\omega < \omega_{**} = 0.985$. In contrast we find that the direct radiative forcing is positive only for $\omega < \omega_{*} = 0.85$ (where ω_{*} is the critical single scattering albedo for the direct effect only). Although observed values of $\omega < 0.85$ are rare, it is common to observed values of $\omega < 0.985$ (IPCC, 2001)). This suggests that the total aerosol radiative forcing (excluding indirect effects) is often likely to be positive, even though the direct forcing is usually negative. An estimate for the indirect forcing is made in the next section.

2.2.5   Comparison with indirect aerosol forcing

To evaluate the semi-direct in the above experiments it was necessary to exclude the indirect effects of aerosols. However, aerosol indirect effects potentially have a large influence on the radiative forcing of aerosols. It is therefore important to make at least a rough quantitative comparison between the

indirect and semi-direct effect in these experiments. The indirect aerosol effect can not be simulated explicitly in the LEM because the cloud droplet number concentration and size distribution are not predicted by the microphysics scheme. However, the influence of aerosols on droplet effective radius (the first indirect effect, or Twomey effect (Twomey, 1977)) can be represented simply by varying the value of effective radius used in the calculation of cloud optical depth.

In this section the indirect effect is crudely estimated by running a simulation with a reduced effective radius. An empirically-based parameterization is used to estimate the reduction in effective radius that would result from the aerosols that were used in the aerosol simulations above. The parameterization is taken from Boucher and Lohmann (1995) and relates the droplet number concentration, N_d (cm^{-3}), to the sulphate mass concentration, m (μ g of SO$_4$ m^{-3}), through the following formulae:

$$N_d = 114.8 \ m^{0.48} \quad \text{for marine airmasses / unpolluted conditions} \tag{2.3}$$

$$N_d = 173.8 \ m^{0.26} \quad \text{for continental airmasses / polluted conditions.} \tag{2.4}$$

This parameterization is based on several sets of aircraft data (Boucher and Lohmann (1995) and references therein). The cloud droplet effective radius, r$_e$ relates to the droplet number concentration in the following way:

$$r_e = (3LWC/4\pi\rho_l\kappa N_d)^{1/3} \tag{2.5}$$

where LWC is the liquid water content in kg m^{-3}, ρ_l is the density of liquid water (1000 kg m^{-3}), κ is an empirical constant, which is 0.80 for marine airmasses and 0.67 for continental airmasses (Martin *et al.*, 1994).

To estimate r_e for unpolluted conditions the sulphate mass concentration, m is taken to be 1.5 μg m^{-3} based on pre-industrial sulphate loading estimates in Rotstayn (1999a). In the aerosol simulations an aerosol mass mixing ratio of 3 x 10^{-8} kg kg^{-1} was used, of which 67% was sulphate, 25% was ammonium, and 8% was soot in the absorbing aerosol simulations with mid-visible ω = 0.88. This gives a sulphate mass concentration of 23 μg m^{-3} for the standard absorbing aerosol simulation A-088 (see Table 2.2). Using equation 2.3 above a droplet number concentration of 140 cm^{-3} is estimated for

unpolluted conditions, and using equation 2.4 a droplet number concentration of 395 cm^{-3} is estimated for the absorbing aerosol case. These values are consistent with observations from unpolluted marine clouds and marine clouds forming in polluted continental air, respectively (e.g. Jones and Slingo (1996), Taylor *et al.* (2000)). Using a liquid water content of 0.5 g m^{-3} (typical of the upper part of the cloud in the control simulation, see Fig. 2.12) the effective radius is estimated to be 10.2 μm for unpolluted conditions and 7.7 μm for the absorbing aerosol simulations.

To obtain an approximate estimate of the indirect effect a simulation was run with an effective radius of 8 μm and compared with the control simulation (see Table 2.2), which had an effective radius of 10 μm. This gave a diurnal mean indirect radiative forcing of -14.1 W m^{-2} at the top of the atmosphere due to the increased cloud-top albedo. This estimate can be upscaled to -17.7 W m^{-2} to account for the rounding of polluted and unpolluted r$_e$ values from 7.7 to 8 μm and 10.2 to 10 μm, respectively. This indirect forcing estimate is comparable in magnitude, but opposite in sign to the semi-direct forcing for the absorbing aerosol simulation A-088, which was 16.3 W m^{-2} (two-day mean). Thus, with highly absorbing aerosols (approximately, $\omega \leq 0.88$) the semi-direct effect may completely offset the indirect effect. With less absorbing aerosols the indirect effect is likely more important than the semi-direct effect. However, these conclusions are very tentative because the indirect forcing estimate is very uncertain. The influence of aerosols on number concentration and effective radius is poorly understood (e.g. Haywood and Boucher (2000)). Observational data shows considerable spread in number concentrations for similar sulphate mass concentrations (Boucher and Lohmann (1995) and references therein). Consequently empirical relationships are not well constrained and several parameterizations have been formulated for different datasets or subsets, according to cloud types and airmass characteristics (Boucher and Lohmann (1995)). Some alternative parameterizations (see Jones and Slingo (1996)) give a higher indirect forcing, whilst others give a lower indirect forcing. The estimate of pre-industrial (or natural) sulphate mass concentration is another significant source of uncertainty.

A further experiment showed that the indirect and semi-direct effects do not add together linearly. Including both the semi-direct effect (with aerosol $\omega = 0.88$) and the indirect effect (with r$_e$ reduced from 8 to 10μm) gave a radiative forcing of 5.7 W m^{-2}. The sum of the forcings when calculated independently was 2 W m^{-2} (16.3 - 14.3W m^{-2}), some 3.7 W m^{-2} lower. There are two explanations for this non-linearity. Firstly, the reduction of LWP from the semi-direct effect limits the strength of the indirect effect. Secondly, the enhancement of cloud albedo by the indirect effect means that the same reduction of LWP, leads to a greater change of cloud top albedo, and an enhanced semi-direct forcing. Therefore, calculating the semi-direct and indirect effects independently, as above, would lead

to an underestimate of the importance of the semi-direct effect, relative to the indirect effect.

2.2.6 Inter-day variability of semi-direct forcing

In this section the uncertainties due to inter-day variability, and the sensitivity to initial conditions are tested to examine the robustness of the LEM results.

The pattern of semi-direct forcing is notably different on the second day (Fig. 2.21). For example, the forcing is negative for the first few hours after dawn on day 2, whereas the forcing remains positive throughout the first day. Also, there is a secondary peak at 1600 h on day 1 but only one principal peak on day 2. The differences in these patterns lead to differences in the diurnal mean semi-direct forcing; the diurnal mean semi-direct forcing was 4.5 W m^{-2}, or 25% lower on the second day. The differences between day 1 and day 2 may be partly related to turbulent variations in the LWP, but may also be part of a downward trend. It is evident from table 2.3 that there is a consistent downward trend in the diurnal mean semi-direct forcings between day 1 and day 2 in simulations A-088, A-096 and A-092. It is important to establish the causes of these day-to-day variations, and to quantify their impact on estimates of the semi-direct forcing.

The problem has been tackled in two ways:

Firstly we examine the **long term trend in the semi-direct forcing** using the ten-day long simulations (section 2.2.6.1). This includes an aerosol-free control (control-10) and an absorbing aerosol simulation (A-088-10) using a mid-visible single scattering albedo of 0.88, as in simulation A-088 (see table 2.2).

Secondly, we quantify the **impact of turbulent variability on the semi-direct forcing** using initial condition ensembles (section 2.2.6.1). The ensembles consist of three simulations for each single scattering albedo value: 0.96, 0.92, and 0.88 (see table 2.2). In each simulation different randomly generated perturbations are applied to the initial temperature field, so that a different turbulence history is generated.

These simulations are performed over a 1 km x 1 km domain because the computation expense of the LEM prohibited continuing with the 2.5 km x 2.5 km domain that was used in the main set of simulations (A-100, A-096, A-0921, A-088, and the control), (see Table 2.2).

2.2.6.1   Long term trend in the semi-direct forcing
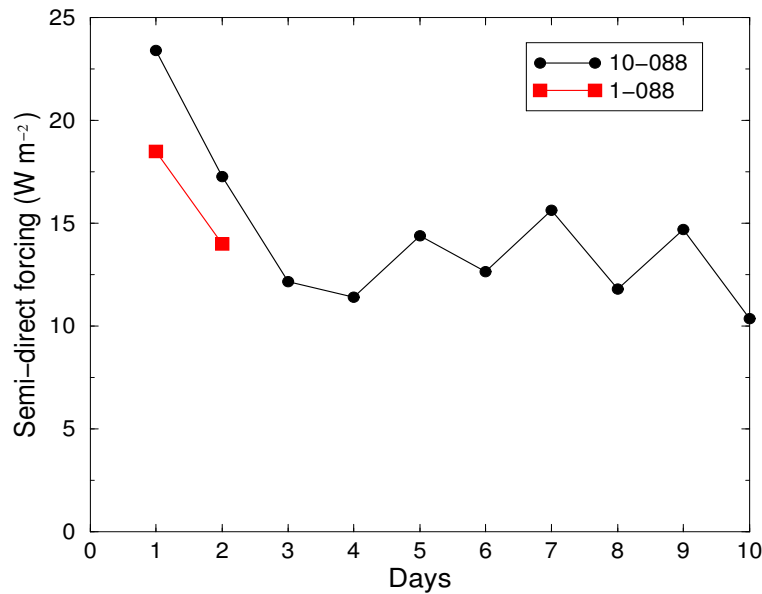
Figure 2.23: *Diurnal mean semi-direct forcing (W m^{-2}) on each day, for simulations A-088 and A-088-10*

The ten-day-long experiment involves one absorbing aerosol simulation (A-088-10), where aerosols have an aerosol mid-visible ω of 0.88, and a control simulation (control-10). The experiment shows an interesting trend in the diurnal mean semi-direct forcing (Fig. 2.23). There is rapid decline from 23 W m^{-2} on day 1, to 12 W m^{-2} on day 3. Between days 3 and 10 the diurnal mean semi-direct forcing seems to be roughly constant at around 13 W m^{-2}, which is roughly 60% of the day 1 value, but there are also day-to-day variations of $\pm$ 1-2 W m^{-2}. The convergence of the diurnal mean semi-direct forcing seems to be associated with the adjustment of the diurnal mean LWP, cloud top height, and cloud base height to long term equilibrium values by about day 5 (Figs. 2.24 & 2.25). This shows that a balance has been reached between the subsidence rate and the entrainment rate, and an equilibrium has also been reached between the various components of the BL heat and moisture budgets; entrainment warming and drying, radiative cooling, and surface latent and sensible heat fluxes. However, the control and absorbing aerosol simulations (control-10 and A-088-10) reach different equilibrium states. For example, the equilibrium cloud top height is about 70 m lower in simulation A-088-10 (Fig. 2.25). As shown in section 2.2.3, aerosol heating in cloud tends to reduce the entrainment rate during the daytime (Fig. 2.18). This leads to the aerosol simulation having a shallower moister BL in the long term (Fig. 2.26).

The convergence of the simulations to different equilibrium states correlates well with the convergence
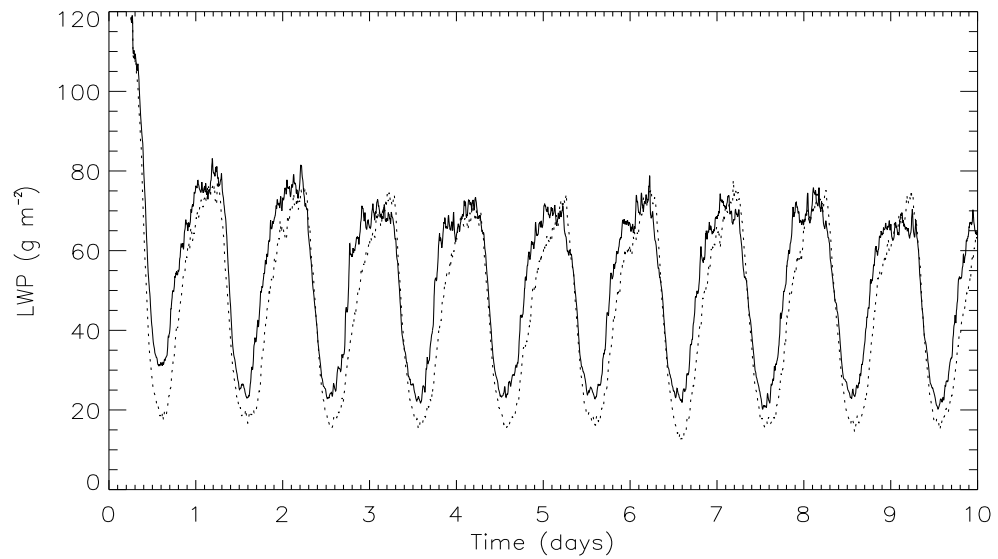
Figure 2.24: *Liquid water path (g m^{-2}) as a function of time for control-10 (solid line), and A-088-10 (dotted line).*
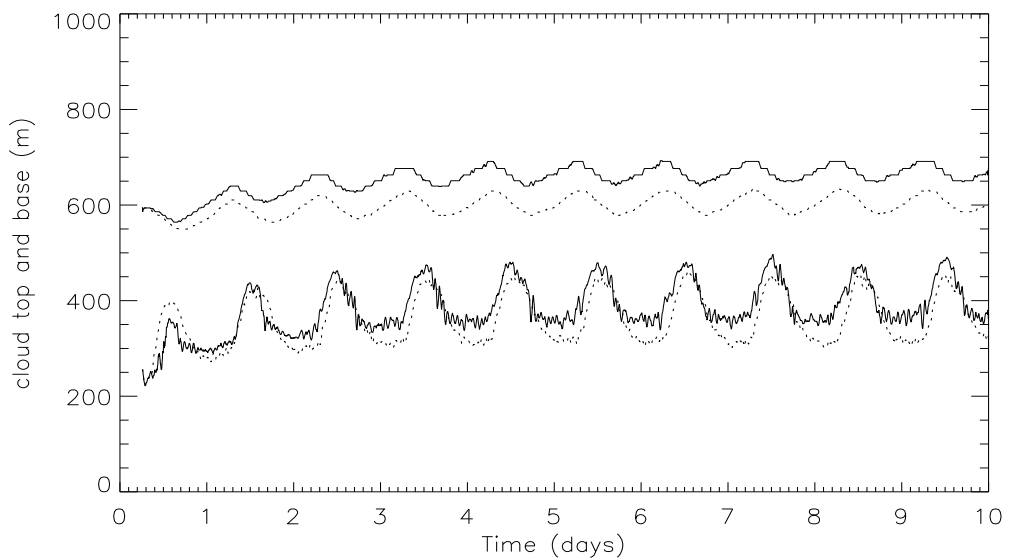
Figure 2.25: *Cloud top and cloud base (m) as a function of time for control-10 (solid line), and A-088-10 (dotted line).*

of the diurnal mean semi-direct forcing to a long-term average (Fig. 2.23). Thus, the semi-direct effect has two elements: an enhancement of the diurnal cycle of LWP, and a longer term moistening of the BL, leading to an opposing increase in LWP. The longer term moistening effect is evident from the increase of nighttime LWP, relative to the control run (Fig. 2.24). This nighttime increase of LWP
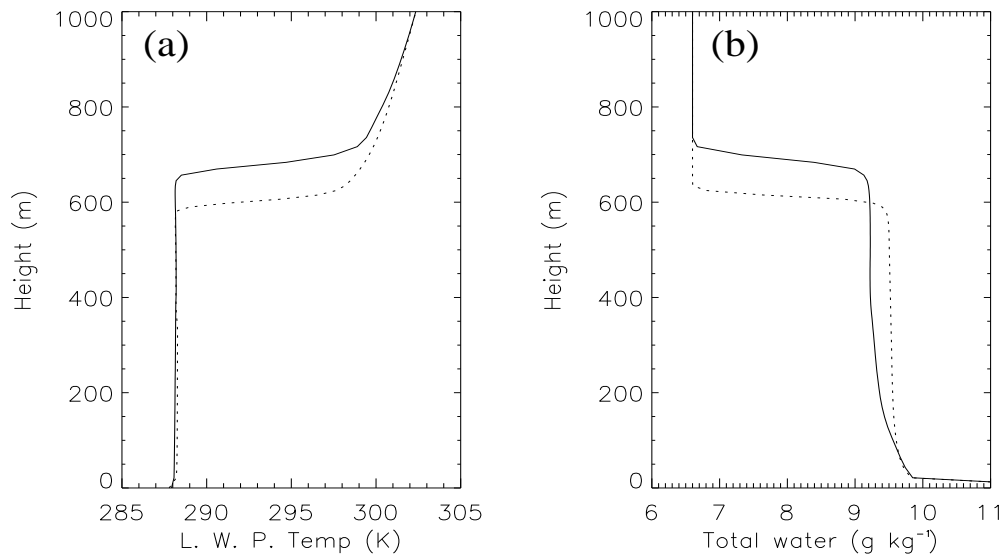
Figure 2.26: *(a) Liquid water potential temperature (K), and (b) total water (g kg^{-1}) at midnight of day 10 in control-10 (solid line), and A-088-10 (dotted line).*

helps to explains why the semi-direct forcing is negative for a few hours after dawn on most days, except the first (see Figs. 2.21 & 2.27).
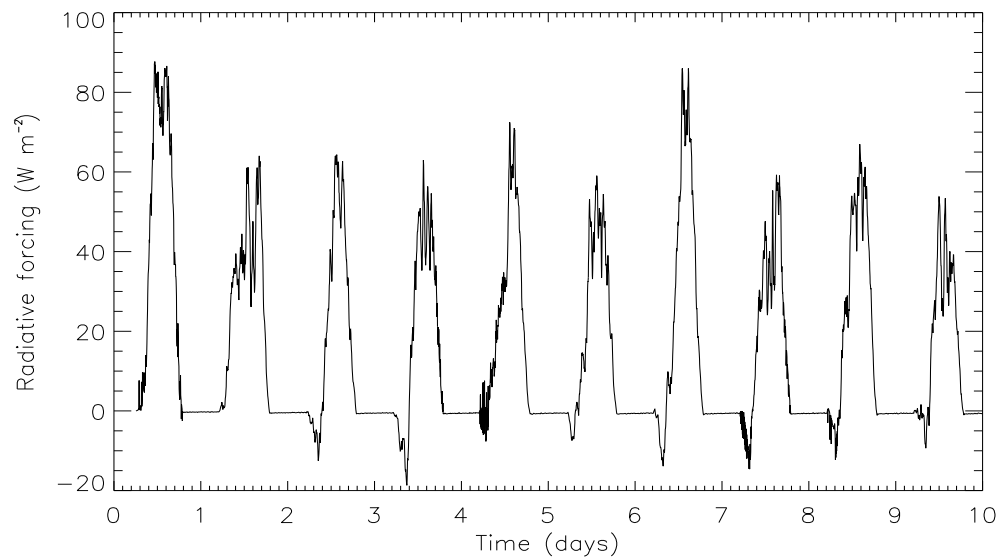
Figure 2.27: *Semi-direct forcing (W m^{-2}) as a function of time for the 10-day experiment.*

In simulations (A-088, A-092, and A-096) it was assumed that the diurnal mean semi-direct forcings for day 2 were representative of the response of the system. The ten-day long experiment seems to suggest that day 2 values are an overestimate; maybe 30% higher than the longer term mean (compare

day 2 with days 3 - 10 in Fig. 2.23). However, the long-term response is not necessary a relevant concept for the SCBL, which by nature is a transitory system. As described in section 2.1.2, observations show that, marine stratocumulus BLs are transient systems, and typical follow a transition to cumulus on time scales of a few days as they are advected over warmer sea surfaces (e.g. Krueger *et al.* 1995). Furthermore, wet and dry deposition processes, and entrainment of cleaner air from above the inversion would gradually reduce the aerosol mass concentration with time (e.g. Dore *et al.* (2000)). Although, rates of aerosol deposition are very difficult to estimate, observations suggest that the residence time for aerosols in the atmosphere is only a few days especially if most of the aerosols and are at low altitudes and there is the possibility for processing by clouds. The rate of dilution by entraining air depends on the aerosol mass concentration in the air above the inversion, and the entrainment rate relative to the BL depth. A simple calculation shows that the aerosol concentration in these simulations would decrease by a factor of 2 in approximately 2 days, given that the subsidence rate at the inversion (650 m) was about 300 m per day.

Therefore, the time scale of interaction between a polluted, aerosol-rich airmass, and a region of stratocumulus may be a matter of a few days, not ten. Therefore, the day 2 diurnal mean semi-direct forcing may be considered more representative of the response in real situations. It should be acknowledged however, that the long-term response trend is a significant source of uncertainty.

To assess the long term response of marine stratocumulus to absorbing aerosols more fully, it would be necessary to have an explicit representation of aerosol mass mixing ratio and aerosol processes in the model, and to force the simulation in a way that allowed the BL structure to evolve with time, reflecting the transition that occurs in observations (e.g. de Roode and Duynkerke (1997)). This would require long simulations (several days) and an increase in the size of the domain to at least 5 km to incorporate cumulus motions. This would be computational expensive, possible with current supercomputing power. Such expense could be avoided by using a 2-dimensional domain. This approach has already been employed successfully by Krueger *et al.* (1995) and Wyant *et al.* (1997) to simulate the stratocumulus to cumulus transition.

2.2.6.2 Impact of turbulent variability on the semi-direct forcing using initial condition ensembles

Variations in turbulence intensity are clearly evident in fields such as resolved eddy kinetic energy (Fig. 2.9) and maximum updraught velocity (Fig 2.10). Since turbulence plays an important role in
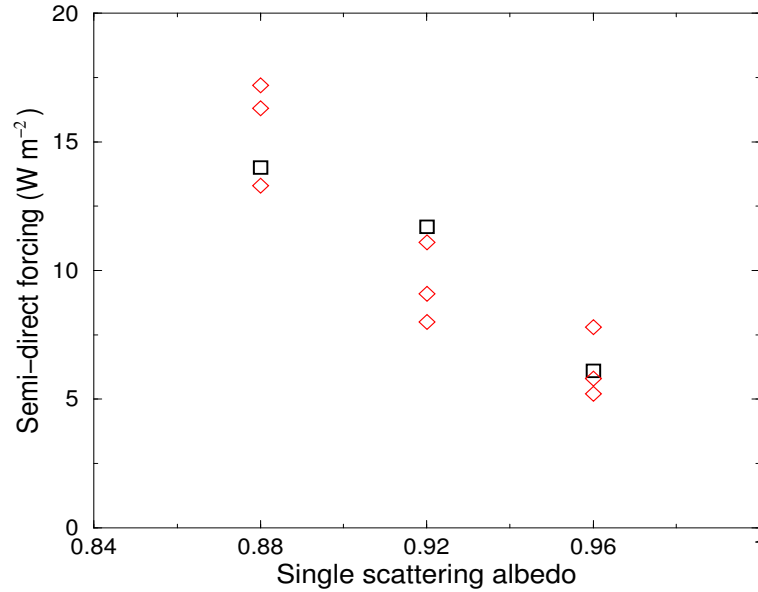
Figure 2.28: *Diurnal mean semi-direct forcing (W m^{-2}) on day 2 as a function of mid-visible single scattering albedo (ω), for all aerosol experiments. Experiments using the larger domain size of 2.5 km x 2.5 km are shown with squares. Experiments using the smaller domain size of 1.0 km x 1.0 km are shown by diamonds; each of these was started with slightly different initial conditions.*

transporting moisture through the BL, such variability manifests itself also in the LWP time series (Fig. 2.18), which has variability on timescales of a few minutes to a few hours. This in turn gives rise to variability in the semi-direct forcing, also on time scales of minutes to hours (as shown in Figs. 2.21 & 2.27, and discussed above). These fluctuation, especially those on longer time scales, do have an impact on the diurnal mean semi-direct forcing, and explain the variability between days 3 - 10 in the ten-day-long experiment (see Fig. 2.23). Figure 2.28 shows that the spread in diurnal mean semi-direct forcings between members of the initial condition ensembles is 3 - 4 W m^{-2} . From this it can be concluded that differences in turbulence histories lead to a fundamental uncertainty of about $\pm$ 2 W m^{-2} in the day 2 estimates of diurnal mean semi-direct forcing.

Due to computational limitations the initial condition ensembles were performed with a reduced do-main size of 1 km x 1 km, whereas the main simulations (A-088, A-092, A-06, A-100) had the full domain size of 2.5 km 2.5 km. Increasing the domain would have reduced the impact of small-scale turbulent variability and reduced the uncertainty in the semi-direct forcing. However, enlarging the domain size may have enabled larger spatial scales of variability. On comparison of the LWP and semi-direct forcing timeseries for simulations A-088 and A-088-10 (Figs. 2.18 & 2.24, and Figs. 2.21 & 2.27) it is not obvious whether turbulent variability is more or less important in the main simulations.

In conclusion, the uncertainty in the day 2 mean semi-direct forcings in the main experiments (A-088, A-092, A-096, A-100) due to the combined influence of turbulence is estimated as $\pm\,2\,\mathrm{W\,m^{-2}}$. This level of uncertainty does not undermine the main results of the chapter. For example, there is still reasonably high confidence in the magnitude of the semi-direct forcing for experiment A-088, as the uncertainty is $\pm\,20\%$. The uncertainty in semi-direct forcing translates into an uncertainty of 0.02 in the critical single-scattering albedo (ω_{**}). This leads to a possible range of 0.965-1.00. Thus, the results (summarised in figure 2.22) continue to show the potential for moderately absorbing aerosols to warm the climate.

2.3 Conclusions

The semi-direct effect has been investigated for a marine stratocumulus case, using the LEM with idealised aerosol distributions. The aerosols were assumed to be confined mainly to the BL, with only a little aerosol above the inversion. The aerosol optical depth (τ) was set to 0.15, and a range of single scattering albedos (ω) were used (0.88, 0.92, 0.96, and 1.00), which reflected the typical range from observations.

It was found that the semi-direct forcing is large and positive in comparison to the direct forcing, even for moderately absorbing aerosols ($\omega = 0.96$). Including the semi-direct forcing increased the critical single scattering albedo (ω_{**}) from 0.85 to 0.985. This is in the upper range of typically observed mid-visible ω values (IPCC, 2001), suggesting that the total aerosol radiative forcing for stratocumulus (excluding indirect effects) is likely to be positive. The strong positive semi-direct forcing was due to significant reductions (around $10\,\mathrm{g\,m^{-2}}$) in the daytime LWP. Since marine stratocumulus cover about 34% of the global oceans, even a small mean change in LWP could make an important contribution to the radiative forcing of climate change.

The absorbing aerosols affected the LWP in two ways. Firstly, the heating in the cloud layer led directly to evaporation, and secondly it led to a greater stabilisation of the BL because the aerosol heating rate was higher in the cloud layer, peaking at cloud top. The enhanced stabilisation (or decoupling) reduced the moisture fluxes between the surface and the cloud layer in the daytime, allowing the cloud to dry-out more than it otherwise would. Thus, the semi-direct effect is intimately linked to small scale processes, such as turbulent fluxes, entrainment, and the decoupling of the BL.

The semi-direct effect is therefore likely to depend greatly on the meteorological conditions. For ex-

ample, Ackerman *et al.* (2000) found a much smaller semi-direct forcing (7.5 W m^{-2}, compared to about 15 W m^{-2}) for the trade cumulus BL using LES with the same mid-visible ω (0.88), but more than twice the aerosol optical depth (0.4, compared to 0.15). This suggests that marine stratocumulus gives a higher semi-direct forcing than trade cumulus. The diurnal cycle exhibited by marine stratocumulus shows it is strongly sensitive to solar radiation; other cloud regimes, such as shallow convection or cloud formed through large-scale ascent may be less sensitive to solar radiation. Therefore, the semi-direct forcing for marine stratocumulus is probably much higher than the global average. This would also mean that the critical single scattering albedo ought to be higher for marine stratocumulus than for the globe. General circulation model studies by Hansen *et al.* (1997) and Cook and Highwood (2003) found $\omega_{**} = 0.91$ and 0.93, respectively, whereas the LEM experiments in this chapter gave $\omega_{**} = 0.985$. This suggests either that the semi-direct effect is model dependent, or that marine stratocumulus gives a particularly strong semi-direct forcing in comparison to the global mean cloud.

The sensitivity of the semi-direct forcing to the cloud regime, and meteorological conditions is examined in chapter 3 by performing LEM experiments for shallow cumulus cloud conditions. In addition, an attempt was made to evaluate the semi-direct effect for a deeper SCBL based on observations from the Atlantic Stratocumulus Transition Experiment (ASTEX). This case gave a 30-50% higher semi-direct forcing for the same aerosol distribution. This suggests that the semi-direct effect may depend on aspects such as the BL depth, the decoupling, and the inversion characteristics. Unfortunately these simulations were not very realistic. The inversion was not as strong as in the FIRE case and there was a much higher entrainment rate. To prevent the stratocumulus layer from dissipating, unrealistically high subsidence, cooling and moistening rates were necessary. Other authors have found that LES tend to overestimate the entrainment rate (e.g. Moeng *et al.* (1996), Bretherton *et al.* (1999)), particularly in case where there is a weaker inversion. Because of this problem the ASTEX stratocumulus case has not been shown in this thesis. [2]

To elucidate some of the mechanisms of the semi-direct effect the aerosol properties and distribution were idealised. The aerosols mass mixing ratio was constant in the BL and reduced linearly to zero 300 m above the inversion (as shown in Table 2.1), based on the assumption that the inversion height is the main constraint to the vertical mixing of aerosols. The vertical distribution is likely to be important in determining the semi-direct forcing. The experiments in this chapter showed that the semi-direct forcing was largely a response to the heating in the cloud layer. The vertical distribution of absorbing aerosol also has a great influence on the direct aerosol forcing. For example, absorbing aerosols above

---

[2]The ASTEX simulation mentioned here is different from the one presented in chapter 6

a stratocumulus layer can give a strong positive radiative forcing because they absorb the upwelling shortwave radiation scattered by the cloud. The sensitivity of the semi-direct forcing and direct forcing to the aerosol vertical distribution will be examined in chapter 5.

In these experiments there was no possibility for interaction between the aerosols and the cloud microphysics. This was necessary so that the semi-direct effect could be isolated from indirect aerosol effects. However, an experiment was performed to estimate the indirect forcing of the aerosols due to decreased cloud droplet effective radius (the Twomey effect, (Twomey, 1977)). This showed that the indirect effect was comparable, but opposite in sign to the semi-direct effect from the absorbing aerosol simulation with a mid-visible single scattering albedo of 0.88. However, the indirect forcing estimate is very uncertain because the relationships between effective radius and characteristics of the aerosol population are poorly understood. Furthermore, the experiments do not allow the SSTs or large-scale environment to respond to the aerosols or changes in cloud fields. Future studies of the semi-direct effect need to begin to account for the impact of such factors.

CHAPTER 3

Cumulus Experiments

In this chapter the semi-direct effect is evaluated using the LEM for two cases of shallow cumulus over tropical ocean. In the cumulus regime cloud amount is much lower than in the stratocumulus regime, and is dominated by different factors. The key question addressed in this chapter is: how does the semi-direct effect depend on the meteorological conditions, specifically, the amount and type of cloud?

3.1   Introduction to cumulus

Cumulus is generally defined as non-precipitating (or weakly precipitating) convective cloud. It has a limited vertical extent (typically less than 3 km) and forms individual clouds, or clusters of clouds rather than a layer. Cumulus is generally associated with deep (more than 1 km) conditionally unstable boundary layers (BL) and is driven by surface heat and moisture fluxes. Cumulus forms as air from near the surface is lifted, through turbulent eddy circulations, until it reaches its lifting condensation level. At this initial stage the cloud may be negatively buoyant and is said to be forced (e.g Stull (1985)). As condensation takes place latent heat is released and the cloud may become positively buoyant and accelerate vertically. These 'active' clouds ascend until they lose their buoyancy either through mixing with clear ambient air and the associated evaporative cooling, or as they reach a capping inversion. Once the cloud has become neutrally buoyant it will disperse (detrain) by mixing with ambient air. The lifetime and coverage of this 'passive' cloud is very sensitive to the ambient relative humidity, and rate of turbulent mixing. Where there is high relative humidity and a strong capping inversion cumulus tops may spread out horizontally beneath it either generating, or sustaining a stratiform cloud layer. Examples of forced, active and passive clouds generated by the LEM are illustrated later in this chapter (Fig. 3.10).

Cumulus clouds are common over large parts of the oceans, particularly the subtropical-tropical 'trade-wind' regions, and also over mid-latitude continents during the summer. Figure 3.1 shows the global annual mean daytime cover by cumulus derived from the International Satellite Cloud Climatology Project (ISCCP). ISCCP defines cumulus as clouds that do not exceed the height corresponding to the
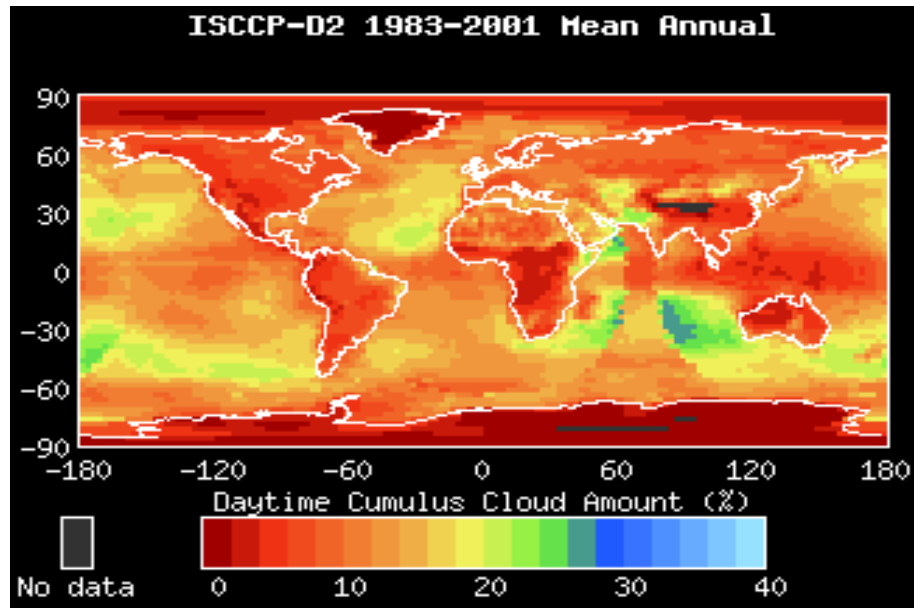
Figure 3.1: *Annual mean daytime cumulus fractional coverage from the International Satellite Cloud Climatology Project (ISCCP) D-data: Cumulus is defined as having a cloud top at a pressure greater than 680 mb, and a mid-visible optical depth of less than 3.6. Figure produced from [http://isccp.giss.nasa.gov].*

680 mb pressure level, and have a mid-visible area-average albedo equivalent to an optical depth of less than 3.6 (Rossow and Schiffer, 1999). By this classification cumulus is essentially low cloud that has a lower albedo than stratocumulus. However, because of their widespread coverage they still have an important influence on weather and climate by scattering solar radiation back to space, reducing the radiative flux at the surface and at the top of the atmosphere.

Shallow cumulus convection also plays an important role in determining the vertical structure of the the atmosphere by enhancing the vertical transports of heat and moisture into the lower troposphere. The enhancement of vertical mixing promotes further evaporation, particularly from the subtropical oceans (e.g. Siebesma *et al.* (2003)). Moisture collected in the trade-wind regions is then transported into the Inter-Tropical Convergence Zone (ITCZ) where it fuels deep convection. In this way cumulus convection helps to fuel deeper convection in ITCZ, which drives the Hadley circulation (e.g. Siebesma and Cuijpers (1995)). Thus cumulus plays a key role in the hydrological cycle and influences the large-scale atmospheric circulation, in addition to having an influence on planetary albedo. Therefore, cumulus is an important cloud regime; a change in mean cumulus cover, for example, due to the semi-direct effect could have a significant impact on global climate.

Cumulus is sometimes found in association with stratocumulus. For example cumulus may spread out

to form a stratocumulus layer (e.g. Betts (1990a)), or may develop beneath a pre-existing stratocumulus layer. Over the subtropical oceans there is often a gradual transition from stratocumulus to cumulus between eastern and central parts of the basin. The transition takes place as the marine BL is advected equatorward and westward by the quasi-permanent anticyclones that form in the subtropical oceans. The transition has been studied in the east Pacific (e.g. Riehl *et al.* (1951), Klein *et al.* (1995)), and in the North Atlantic during the Atlantic Stratocumulus Transition Experiment (ASTEX) (Albrecht *et al.*, 1995a). A conceptual model for the transition was proposed by Bretherton (1992) and has been supported by several modelling studies (Krueger *et al.* (1995), Wyant *et al.* (1997)). Figure 3.2 illustrates the general transition of cloud types and BL structure observed during the First Lagrangian of ASTEX. Cumulus developed below the stratocumulus layer during flight 3 as the BL deepened and became decoupled. The cumulus grew and eventually penetrated the stratocumulus layer during flight 4. This initially helped to sustain the stratocumulus layer by aiding the transport of moisture into the stratocumulus layer. Later in flight 5, over much warmer sea surfaces the cumulus had become much more vigorous and the stratocumulus cloud had diminished. At this stage surface fluxes rather than cloud-top longwave cooling were the dominant source of buoyancy in the BL.
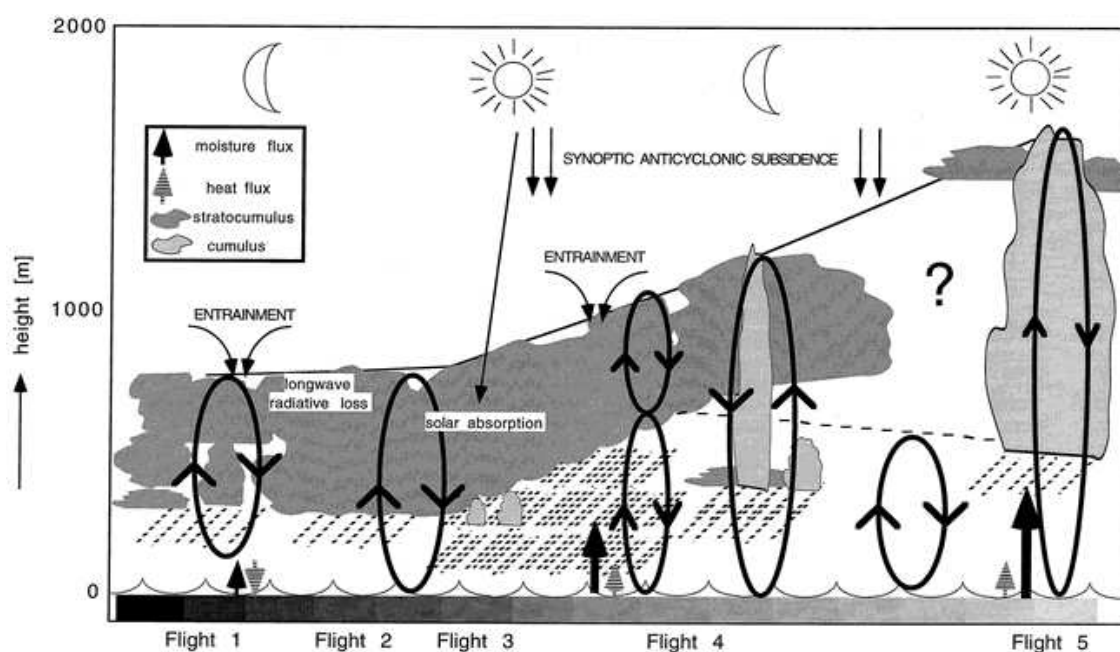
Figure 3.2: *A schematic of the cloud evolution observed during the First Lagrangian of ASTEX involving 5 flights between 1719 UTC 12 June and 1302 14 June 1992. The horizontal distance between flight 1 and 5 is about 1300 km. The greyscale bar below the surface indicates the rising sea surface temperatures from left to right. The sun and moon symbols indicate day-night changes. The figure is taken from de Roode and Duynkerke (1997).*
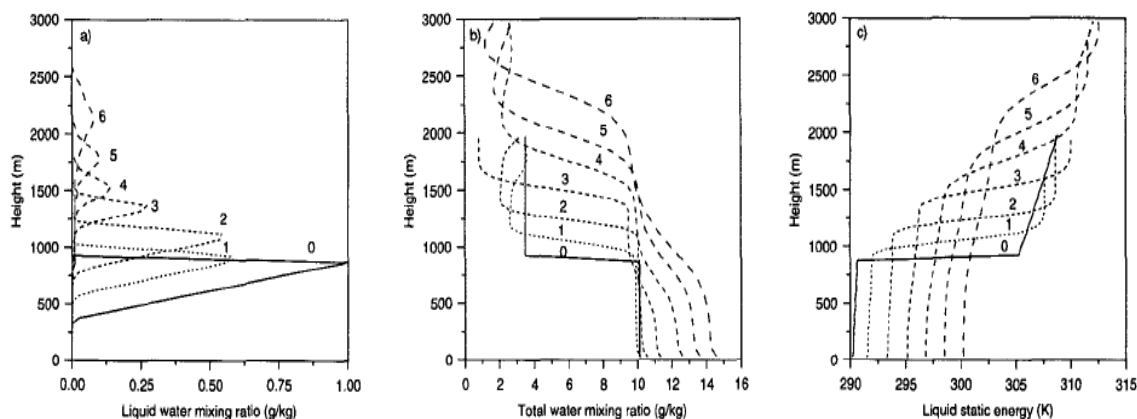
Figure 3.3: *Horizontally averaged (a) Liquid water mixing ratio, (b) total water mixing ratio, and (c) liquid static energy (equivalent to liquid water potential temperature) at 1-day intervals for numerical simulations of the stratocumulus to cumulus transition, taken from Krueger* et al. *(1995).*

As cumulus convection becomes more vigorous it promotes greater mixing between the BL and dry air from the free troposphere. This eventually leads to the erosion of the stratocumulus layer and the formation of a pure trade cumulus cloud field. This transition is accompanied by a warming, moistening and deepening of the BL, and a broadening and weakening of the inversion (the potential temperature contrast across the inversion reduces). These changes are illustrated by a series of thermodynamic profiles taken from a 2D eddy resolving simulation Krueger *et al.* (1995) (Fig. 3.3).

Several observational studies of the trade wind region have been conducted over the past 50 years. These include the pioneering study of Riehl *et al.* (1951) involving ship observations along a track from San Fransisco to Hawaii, and several major field experiments. Several experiments have taken place in the north Atlantic over the past 35 years: the locations and dates of four experiments are shown in Fig. 3.4. These are the Atlantic Trade-wind Experiment (ATEX), February 1969 (Augstein *et al.*, 1973), the Barbados Oceanographic and Meteorological Experiment (BOMEX), June 1969 (Holland and Rasmusson, 1973), and the GARP Atlantic Tropical Experiment (GATE) in summer 1974 (Houghton, 1974), and the Atlantic Stratocumulus Transition Experiment, June 1992 (Albrecht *et al.*, 1995a). These experiments provide comprehensive and diverse data on the meteorological conditions associated with trade cumulus.

In this chapter LEM simulations are performed firstly for an intermediate cumulus regime observed during ATEX. In this case both cumulus and stratocumulus are present. Figure 3.5 illustrates the main features of the intermediate trade cumulus regime. Secondly a case of pure trade cumulus based on observation from BOMEX is simulated. In this case there is no stratocumulus present. Both cases have
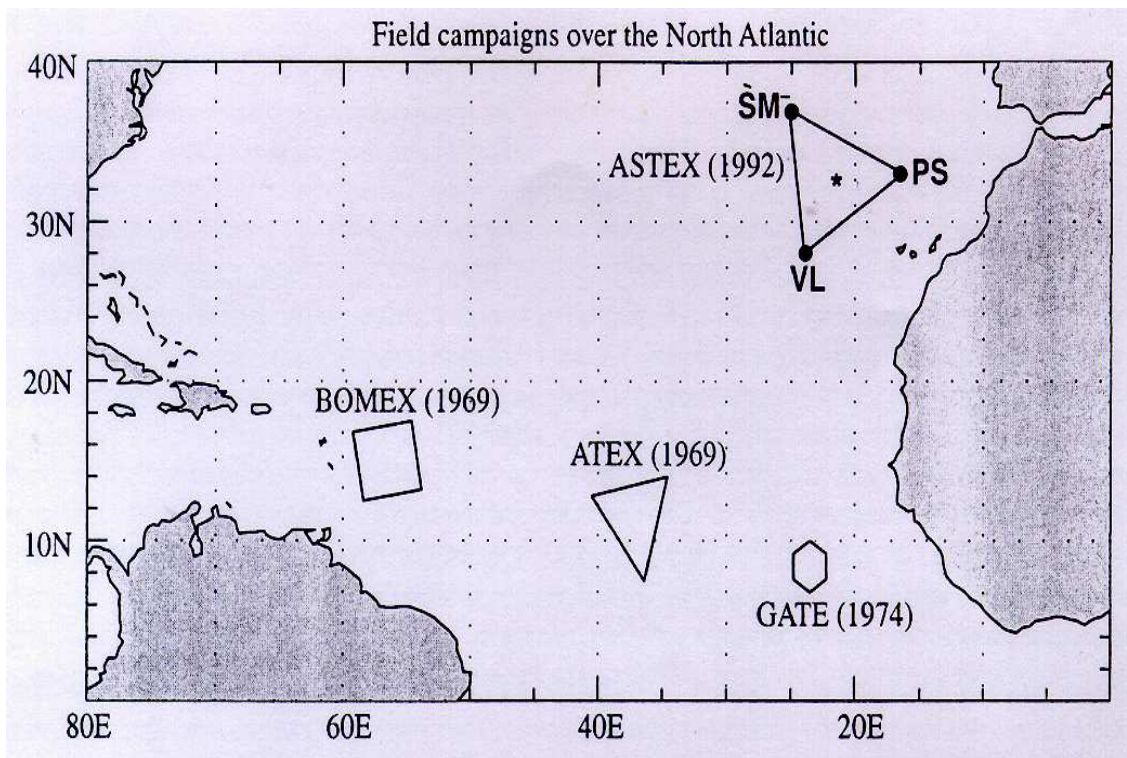
Figure 3.4: *The location of four major field experiments over the North Atlantic. The verticies of the polygons indicate the location of sounding sites during these experiments.*
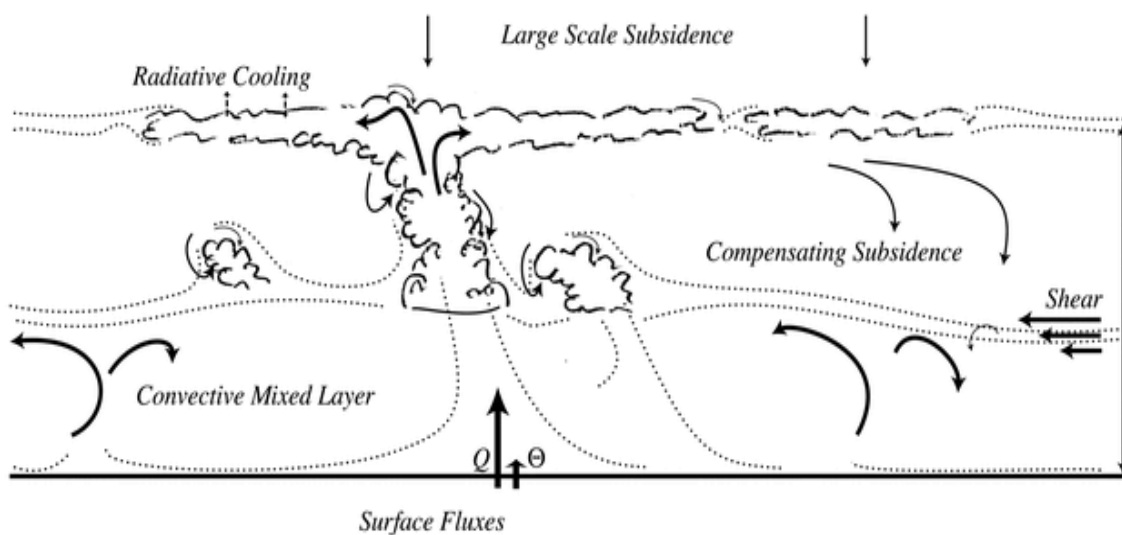
Figure 3.5: *Conceptual diagram of the intermediate trade cumulus regime, based on the undisturbed period of ATEX (taken from Stevens* et al. *(2001)).*

been studied extensively in modelling studies including LES intercomparison studies (see sections 3.1.1 & 3.1.2 for references and further details).

The ATEX case was chosen specifically so that our results can be compared with those of Ackerman *et al.* (2000), which is the only other paper to date to use the LES method to investigate the semi-direct effect (see section 1.5 for more details). In that paper mechanisms for the semi-direct effect were discussed but no analysis of those mechanism was presented. In this chapter a detailed analysis of the semi-direct effect will be presented, including changes in cloud fields, cloud energetics, turbulent fluxes, and aspects of the BL thermodynamic structure. Also, a comparison will be made between the ATEX and BOMEX cases, to show how subtle differences in the meteorology impact on the semi-direct effect.

3.1.1   ATEX intermediate trade cumulus case

The Atlantic Trade wind Experiment (ATEX) took place during February 1969, over the North Atlantic around 10ºN, 33ºW (Augstein *et al.* (1974), Brummer and Augstein (1974)). Surface observations and radiosondes were launched from a flotilla of three ships, arranged in the formation of an equilateral triangle of side 700 km (Fig. 3.4), for a three week period. ATEX generated an unprecedented dataset on the trade wind BL (for its time) that has been used in various observational studies of the trade cumulus regime. For example, Augstein *et al.* (1973) used the observations to examine mass and energy transports in the BL and their influence on the large scale circulation. Brummer and Augstein (1974) examines the low-level wind structure and Augstein *et al.* (1974) assess the mean vertical structure of the BL from radiosonde data.

Hourly observations of cloud cover (estimated visually, and given in oktas) from two of the ships that took part in ATEX (*Planet and Meteor*) are shown in Fig. 3.6, taken from Albrecht *et al.* (1995b). In these observations the cloud fraction varies from almost zero to 100% and has a mean of around 0.65 for the Meteor and 0.5 for the Planet. The high cloud fractions in the Meteor timeseries, particularly from February 13-16 are related to more disturbed weather conditions due to the influence of the inter-tropical convergence zone (Albrecht *et al.*, 1995b). The timeseries also show considerable diurnal variation in cloud fraction (0.1 - 0.4). Brill and Albrecht (1982) study the diurnal variation of the trade wind BL using data from the undisturbed period of ATEX, February 7-12, from the same two ships: *Planet and Meteor*. That study found a mean cloud fraction of 0.53 and a diurnal range of 0.18. Very similar values for the mean cloud fraction and diurnal range were found for GATE, a field experiment that took place nearby (see Fig. 3.4) in summer 1974 (Brill and Albrecht, 1982). In addition, mean values of cloud fraction observed during ASTEX, June 1992 were 0.4 and 0.67 from ships at 28ºN 24º, and 37ºN 24ºW, respectively.
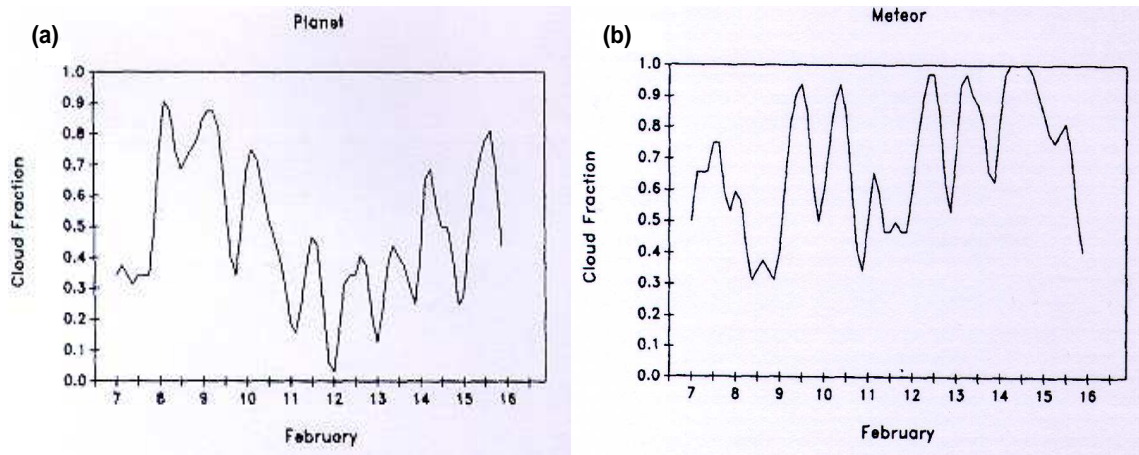
Figure 3.6: *Smoothed hourly observations of cloud fraction from the ATEX field campaign February 7-16 1969 from the ships (a) Planet, located at $14^o N$, $35^o W$ and (b) Meteor, located at $7^o N$, $36^o W$. Figure taken from Albrecht et al. (1995b).*

More recently ATEX data has been used as the basis for the Global Energy and Water cycle Experiment (GEWEX) Cloud Systems Study (GCSS) fifth intercomparison of the BL working group (Browning and the GEWEX Cloud System Science Team (1993), or www.gewex.org/gcss.html). The intercomparison comprised 10 simulations from 7 different groups (including the UK Met Office), each using a different 3-dimensional eddy-resolving model. The Met Office LEM and the University of California Los Angeles model were also used to assess sensitivity to numerical advection schemes and grid resolution down to 20 m in the horizontal and vertical. Mean cloud fractions varied from around 20% to almost 100% depending on the model, the choice of numerical advection scheme, and the grid resolution. Higher cloud fractions were simulated with higher resolution and numerical schemes that were less diffusive. Resolving the inversion, the peak in relative humidity at the inversion base, and small-scale mixing processes were key to simulating the production and persistence of stratiform cloud associated with spreading cumulus cloud tops ('cumulus anvils'). This stratocumulus cloud was extensive and thick enough in some simulations for cloud-top longwave cooling to become important as a mixing mechanism (see Fig. 3.5 for an illustration). Such mixing also reinforced the presence of the stratocumulus cloud by creating a quasi-well-mixed layer beneath the inversion.

A follow-on study (Stevens, 2002) used the University of California model to further explore the sensitivity of simulations to grid resolution, and also the dependence on domain size. This involved simulations on a domain size of $(20 \text{ km})^2$ with resolutions as low as 10 m in the horizontal and 5 m in the vertical! This massively expensive LES study was made possible by an unique opportunity to exploit the full power of a massive parallel-processing computer system. Even so, the highest resolu-

tion simulation could only be run for 15 minutes. Using such domain sizes and resolutions is currently unthinkable under normal circumstances. The study found that increasing the resolution gave a higher simulated cloud fraction. The increase came mainly from detraining clouds below the inversion with low liquid water contents. At lower resolution, mixing at the inversion and between the clouds and clear air was mainly through subgrid diffusion, whereas at the highest resolution those mixing processes were resolved. High resolution led to higher cloud-core velocities in the upper part of the cloud layer, but a lower entrainment rate across the inversion. This suggests that high resolution was beneficial in more accurately simulating the cloud fields in ATEX.

3.1.2 BOMEX pure trade cumulus case

The Barbados Oceanographic and Meteorological Experiment (BOMEX) took place during June 1969 over the North Atlantic a few hundred kilometres east of Barbados, as shown in Fig. 3.4. During phase 3 of the experiment (June 22-29) surface observations and radiosondes launches took place routinely 15 times a day from four ships that were arranged in a square formation centered around 15°N, 56°E (Nitta and Esbensen (1974), Holland and Rasmusson (1973)). Sea surface temperatures in BOMEX were 3 K higher than in ATEX, and the atmosphere was less stable at low levels. There were disturbed periods during BOMEX (e.g. 28-29 June) where there was mean ascent at low levels leading to much deeper convection (up to 500 mb) (Nitta and Esbensen, 1974). However, the period of June 22-26 was relatively undisturbed with a steady easterly flow, and mean descent at low-levels maintaining a moderate inversion around 1.5 - 2 km. These were typical trade cumulus conditions. Cloud fraction was generally lower than in ATEX because there was no stratocumulus present as cumulus tops did not spread out beneath the inversion (e.g. Siebesma *et al.* (2003)). However, observations of cloud fraction from BOMEX are limited and do not provide a useful sample (Siebesma *et al.*, 2003). As Cuijpers and Duynkerke (1993) point out, cloud fraction in the trades vary quite considerably on on mesoscales as well as on synoptic scales. Therefore, obtaining unbiased observations requires a large sample of data. Other sources of cloud fraction data for pure trade cumulus conditions are available, for example the Puerto Rico field experiment, which took place in December 1972 (Pennell and Monde, 1974). Again though cloud fraction observations are limited and data obtained from flight paths may be biased by the desire to study regions with particular characteristics.

The BOMEX dataset has played an equally large role as ATEX in the developing an understanding of the trade-wind regions. For example, Holland and Rasmusson (1973) used radiosonde data from BOMEX to evaluate mass, energy and momentum budgets over the BOMEX domain. Taking a similar

approach, Nitta and Esbensen (1974) and Esbensen (1975) focused on heat and moisture budgets. Nitta and Esbensen (1974) give a good overview of variation in vertical structure of convective fluxes during phase 3 of BOMEX, and Esbensen (1975) explores the heat and moisture budgets in the sub-cloud layer, and their relationship to the clouds, and the large scale. BOMEX data was also used extensively in the early development and validation 3D eddy-resolving models (e.g. Sommeria (1976), Soong and Ogura (1980)).

Phase 3 of BOMEX was also the basis of the fourth intercomparison study of the GCSS BL clouds working group. The main aim of this intercomparison was to use LES and single-column climate models to better understand how to parameterize shallow convection (Siebesma *et al.* (2003)). Several LES studies related to this intercomparison have appeared in the literature (Siebesma and Cuijpers (1995), Brown (1999), Jiang and Cotton (2000), Neggers *et al.* (2003)). The LES of Siebesma and Cuijpers (1995) agree well with the observations, and have been used to adjust lateral cloud entrainment and detrainment rates for mass-flux convection parameterization schemes and improve the performance of single column models (Siebema and Holtslag, 1996).

Using the LEM, Brown (1999) found that many of the cloud-ensemble averaged statistics such as cloud cover, core mass flux, heat and moisture fluxes and thermodynamic profiles were relatively insensitive to a five-fold increase in horizontal resolution (from 100 to 20 m). However, there were differences in the characteristics of the cloud fields. At the higher resolution individual clouds were generally smaller and more numerous in those studies. For example, in Brown (1999) the mean horizontal cloud radius was 250 m in the standard resolution (100 m) simulation, and 100 m in the highest resolution simulation (20 m). The cloud size statistics in both Brown (1999) and Neggers *et al.* (2003) agreed better with observations (e.g. Plank (1969), Nitta (1975)), for the higher resolution simulations, although, it was not clear whether the mixing processes between the clouds and the clear air were sufficiently resolved, even with 20m horizontal resolution (Brown (1999), Stevens (2002), Neggers *et al.* (2003)). Also, at higher resolution clouds had less buoyancy at the inversion base and did not penetrate as high into the inversion layer, tending to reduce mixing in that layer.

However, in the BOMEX case there was less sensitivity of cloud fraction to resolution and choice of numerical schemes, compared to the ATEX case. This lack sensitivity seems to be because the cloud fraction depends mainly on the cloud-core mass flux, which is controlled by energetic constraints on the system, and was invariant between simulations. This indicates that the cloud fraction may be less sensitive to aerosol heating than in ATEX, or sensitive in a different way.

In summary, ATEX and BOMEX provide very useful datasets on trade cumulus that have been well used in numerical modelling studies, particularly in LES. The BL structure and cloud fields in ATEX and BOMEX were subtly different, but, there is reason to believe a priori that these differences will be important in determining the semi-direct effect in each case. The generally lower cloud fraction in BOMEX, and lower sensitivity to modelling details points to the likelihood of a lower semi-direct effect.

3.2   Experimental setup

This chapter reports four simulations, including two absorbing aerosol simulations, one for the ATEX case (ATEX-aerosol), and one for the BOMEX case (BOMEX-aerosol), plus a control simulation for each case (ATEX-control and BOMEX-control). ATEX and BOMEX use different initial conditions, boundary conditions and large scale forcings, but other aspects of the experimental setup such as aerosols, radiation, domain size, and resolution are kept the same.
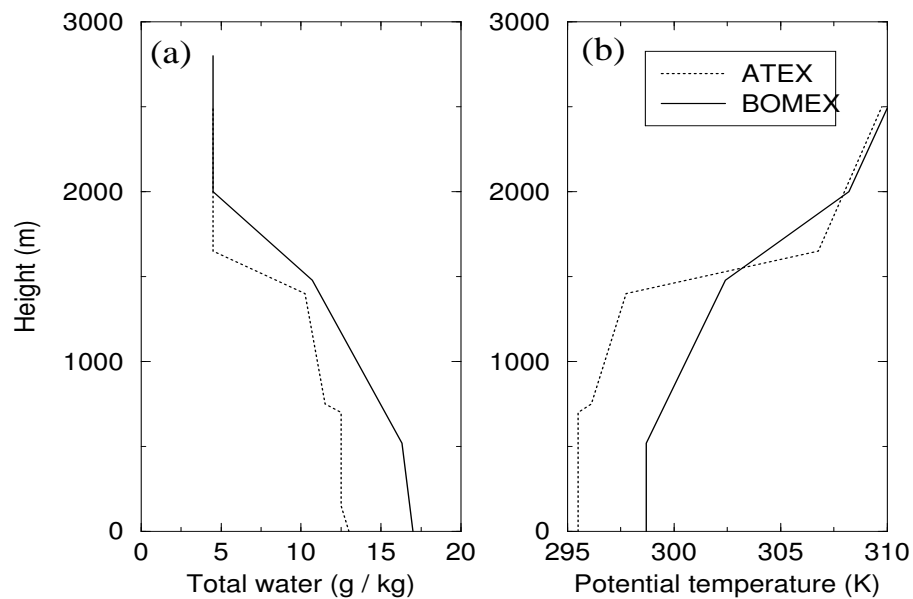
Figure 3.7: *Initial profiles of (a) q_t (g kg^{-1}) and (b) θ_l (K) for the ATEX (dotted line) and BOMEX (solid line) simulations, taken from Stevens* et al. *(2001), and Siebesma* et al. *(2003), respectively.*

The initial temperature are humidity profiles are shown in Fig. 3.7. The profiles used for the ATEX case are very similar to those used in the GCSS BL clouds fifth intercomparison (Stevens *et al.*, 2001) and are based on soundings taken from the R/V Planet ship (the northern-most ship of the formation, see Fig. 3.4) for the five days between 7 and 12 February 1969. The conditions during this time were

described by Augstein *et al.* (1973) as a 'nearly classical trade-wind situation', with an undisturbed synoptic flow. The soundings were scaled with the inversion height and transition layer height so that the sharpness of the features at those levels was preserved when averaging together many profiles. The initial temperature and humidity profiles for the BOMEX case follow the GCSS BL clouds fourth intercomparison (see Siebesma and Cuijpers (1995) or Siebesma *et al.* (2003)), and are based on a selection of soundings taken from the NOAA ship Oceanographer, the most northern ship of the square formation (see Fig. 3.4), over 22 and 23 June 1969 (Holland and Rasmusson (1973), Nitta and Esbensen (1974)). Comparison with soundings from other ships and at other times during BOMEX shows that the profiles are representative of the undisturbed period of BOMEX 22-26 June, during which there was a steady trade-wind flow with shallow (cloud tops up to 2km), non-precipitating cumuli. The BOMEX case has a warmer, moister, deeper BL with a broader weaker inversion and sea surface temperature is 3 K higher (300 K, compared to 297 K in ATEX). Also the profiles from BOMEX lack the sharp transition at the top of the surface layer.

The same initial and geostrophic winds profiles are used for ATEX and BOMEX cases because observed wind profiles were quite similar (e.g. compare Brummer and Augstein (1974), from ATEX with Holland and Rasmusson (1973), from BOMEX).

$$U_g = -11.0 + (0.003\ Z)\ \mathrm{m\ s}^{-1} \tag{3.1}$$

$$U_i = -8.0\ \mathrm{m\ s}^{-1} \quad \text{(for Z} < 1000\ \mathrm{m)}, \qquad\qquad U_i = U_g \quad \text{(for Z} > 1000\ \mathrm{m)} \tag{3.2}$$

$$V_g = 0.0, \qquad\qquad V_i = 0.0 \tag{3.3}$$

where U_g and V_g are the horizontal and meridional geostrophic winds, U_i and V_i are the zonal and meridional initial winds, and Z is height.

These are the same as used in the BOMEX-based GCSS intercomparison, and very similar to those used in the ATEX-based GCSS intercomparison.

The large-scale subsidence rate was given as:

$$W_{subs} = 3.33 \text{ x } 10^{-6} \; max(Z, 1500m) \text{ m s}^{-1} \qquad \text{for ATEX simulations, and} \qquad (3.4)$$

$$W_{subs} = 4.0 \text{ x } 10^{-6} \; max(Z, 1800m) \text{ m s}^{-1} \qquad \text{for BOMEX simulations.} \qquad (3.5)$$

A slightly higher subsidence rate was necessary in BOMEX to balance the higher cross-inversion entrainment rate and prevent the trade inversion from rising with time.

A cooling rate of 1 K day^{-1} was applied in both cases to account for the large-scale advective tendency, but no drying was applied because doing so led to a reduction in the cloud fraction, particularly in the ATEX case and those simulations were specifically designed to test a regime with intermediate cloud amounts. Surface pressure was fixed at 1020 mb in both simulations, and the surface roughness length was set to 2.0 x 10^{-4} m. As in chapter 2, the microphysics in the LEM is switched off because it was found that drizzle rates were very low, and it was cheaper to run without these processes active. Observations have shown that significant precipitation only occurs for clouds deeper than 2 km, and most LES simulations of the shallow cumulus regime have used the nonprecipitating assumption. Jiang and Cotton (2000) specifically test this assumption and find that very light drizzle can occur in some clouds but the impact on mean cloud fraction and water content was relatively low and thus any changes in the drizzle rate would have little bearing on the semi-direct effect.

In both cases the domain was 6 km x 6 km in the horizontal, with a resolution of 100 m. The vertical resolution was variable, ranging from 20 m in the cloud layer, to 50 m near the model top, which was at 2500 m in the ATEX case, and 2800 m in the BOMEX case. The increase in vertical resolution in the cloud layer led to a better simulation of mixing processes. This was particularly important in resolving the passive cloud that formed beneath the inversion in ATEX. The ATEX case used a total of 92 vertical levels, and the BOMEX case had 102. The higher model top in BOMEX was necessary because the convection was more vigorous and cloud tops reached 300 m higher.

Although, higher vertical and horizontal resolution would have been desirable (see discussion in section 3.1.1) it was not attainable given the limitations on computation expense. To help overcome problems associated with limited resolution a less diffusive advection scheme was selected, and the subgrid mixing length scale was reduced to half the standard value (from 23 to 11% of the horizontal grid spacing), following the suggestion from Andrew Brown from the Met Office. Reducing numerical

diffusion makes better use of the available resolution because the it allows the model to 'see' features that would have been smeared out by diffusion. Reducing numerical diffusion does increase the risk of numerical noise or instabilities arising, but fortunately these problems did not surface. The LEM ran successfully with the lower subgrid mixing length and produced a higher cloud fraction, particularly in the ATEX case.

The radiation scheme was set to 15 July at latitude 33°N so that the semi-direct forcing results would be directly comparable with the FIRE case (chapter 2). If the radiation scheme been set up to match the dates and latitudes of the real experiments then the mean solar heating rate would have been 20% lower in ATEX simulations (latitude 12°N in mid-February), and 5% lower in BOMEX simulations (latitude 15°N in late June). The simulations are run for 48 hours starting at midnight, which gives about 5 hours spin-up before sunrise. Previously, only one other study has run a LES of shallow cumulus with interactive radiation; this is Ackerman *et al.* (2000). Other shallow cumulus LES studies (e.g. Brown (1999), Siebesma *et al.* (2003)) have specified longwave cooling rates and have either specified, or not included shortwave heating rates. Also, most LES studies have run for 3-8 hours (e.g Cuijpers and Duynkerke (1993), Stevens *et al.* (2001)). Ackerman *et al.* (2000) ran their model for one day, whereas the simulations presented in this chapter have been run for two days; exactly 48 hours, starting at midnight. This allows 5 hours for the simulations to spin-up before sunrise.

The aerosol properties and mass mixing ratio were specified to give a diurnal mean solar heating rate of around 1 K day^{-1} in the BL. This is the same approach as was taken in chapter 2 (see section 2.2.1 for details relating to aerosol optical properties). The aerosol mass mixing ratio was 3 x 10^{-8} kg kg^{-1} from the surface up to the inversion (at 1500 m), and decreases linearly to zero at 2000 m, the aerosol optical depth was 0.4, and the single scattering albedo was 0.88 (at $\lambda = 0.55\mu m$). The aerosol optical depth was much higher than in the FIRE stratocumulus experiments of chapter 2 (0.4 compared to 0.15) because the aerosol mass mixing ratio was the same but the aerosol layer was much deeper because the BL was deeper. An alternative approach would have been to use the same optical depth as in the FIRE case (0.4) and reduced the aerosol mass mixing ratio accordingly. However, since the semi-direct effect appears to be linearly proportional to the aerosol heating rate (see Fig. 2.22, in section 2.2.4) it was considered better to keep the mass mixing ratio constant, rather than τ. Furthermore, the aerosol optical depth (0.15), and single scattering albedo (0.88) corresponds very well to the observations from INDOEX 1999 and are the same as the values used in Ackerman *et al.* (2000). This means that the experiments in this chapter can be compared directly with Ackerman *et al.* (2000), which was a similar large-eddy simulation study of the semi-direct effect (see section 1.5 for details).

3.3   Analysis method

Time series data, including cloud top and base heights, liquid water path (LWP), total cloud cover, surface heat and moisture fluxes, and radiative fluxes at the top of the atmosphere, were output from the LEM every 3 minutes. Some examples of the raw time series data for both ASTEX and BOMEX are presented in the next section.

Horizontally averaged profiles were calculated every 30 minutes. These included liquid water potential temperature, total and liquid water, relative humidity, turbulent kinetic energy, turbulent moisture fluxes, cloud fraction, cloud mass flux, and cloud updraught velocity. Time averages of these profiles were calculated for a pre-dawn period (0200 - 0500 h), and an afternoon period (1200 - 1700 h) on day 1. The pre-dawn profile is the average of 7 profiles, and the afternoon profile is the average of 11 profiles. This averaging helped to reduce the influence of temporal variability on results. Pre-dawn average profiles are shown along side afternoon profiles from the control and aerosol simulations so that differences between control and aerosol profiles can be compared with the diurnal variation.

The standard error (standard deviation divided by the root of the number of profiles) on afternoon profiles from the aerosol simulations is also shown to indicate how significant differences between aerosol and control simulations are, compared to the temporal variability. Using a student t-test, and assuming that the standard deviation in any given fields is the same in aerosol and control simulations, it turns out that the differences are significant at the 95% confidence level if they exceed the standard error; i.e. if the control profile lies outside the shaded region. This test also assumes that random variations in field quantities are independent between profiles half an hour apart. This is probably a reasonable assumption. Most of the variability is dominated by individual clouds, that have a life time of half an hour or less.

Convective Available Potential Energy (CAPE) was calculated every 30 minutes.CAPE is a useful measure of potential instability, and indicates the potential updraught velocity assuming no mixing between a lifted parcel and the ambient air. To calculate CAPE, parcels were lifted from the second layer above the surface (60 m) to their level of neutral buoyancy:

$$CAPE = \int_{LFC}^{LNB} g(T_p - T_e)/T_e \ dZ \qquad (3.6)$$

Simulation	Fractional cloud (%)		LWP (g m^{-2})		Cloud radiative
	mean	daytime	mean	daytime	forcing (W m^{-2})
ATEX-control	31.0	24.9	14.6	11.7	-17.5
ATEX-aerosol	24.0	15.3	10.4	6.0	-9.5
BOMEX-control	11.2	10.1	9.2	7.7	-7.7
BOMEX-aerosol	10.4	8.4	6.4	4.3	-5.7

Table 3.1: *Cloud fraction (%), liquid water path (g m^{-2}), and cloud radiative forcing (W m^{-2}) in the cumulus simulations. Daytime values are the mean of the periods 0600 - 1800 h, 3000 - 4200 h, which include 97% of the incident radiation.*

where g = acceleration due to gravity, T_p is the temperature of the cloud parcel, T_e is the temperature of the environment, and Z is height. LFC is the level of free convection, and LNB is the level of neutral buoyancy. In reality, the updraught kinetic energy will be much lower than the CAPE due to mixing between ascending air and the environment. Also, the cloud will not be sourced entirely from air near the surface, but possibly from air in the lowest few hundred metres of the atmosphere. Lifting air parcels lifted from a higher level, e.g. 400 m above the surface led to a lower CAPE (because the air wass less moist at that level), but did not alter the general findings.

The semi-direct forcing was calculated by subtracting the direct aerosol forcing from the total difference in net radiation at the top of the atmosphere, as in chapter 2 (see equation 2.2). From sensitivity tests it was found that the direct forcing depended to some degree on the clouds present. Therefore, it is worth noting that the direct forcings were calculated for the clouds conditions in the aerosol simulations, and not for cloud conditions of control simulations. Also, shown in Table 3.1 are the cloud radiative forcings. These are the differences in net radiation at the top of the atmosphere between a calculation including clouds but not aerosols, and a clear-sky calculation. The difference in cloud radiative forcing between the aerosol and control simulation is essentially the semi-direct effect, and is equivalent to the definition above.

3.4   Results: I. Simulated cloud fields

3.4.1   Cloud fraction

Cloud fraction in ATEX varies from around 40% at night to 20% in the middle of the day, with a mean of 31.0% in the control simulation (Fig. 3.8 (a) and Table 3.1). The mean cloud fraction in the ATEX control simulation (31.0%) is slightly lower than mean cloud fraction observed during the field campaign and presented in Albrecht *et al.* (1995b) (see Fig. 3.6). Brill and Albrecht (1982) estimate a mean cloud fraction of 53% for the undisturbed period of ATEX; on which our simulations are based (see section 3.1.1 for more details). However, the amplitude of the diurnal cycle in the ATEX simulations (see Fig. 3.8 (a)) agree well with those observations (Brill and Albrecht (1982) find a diurnal range in cloud fraction of 0.18. This shows that the simulations have a realistic level of response to solar heating, which is important in simulating the semi-direct aerosol effect.

Cloud cover is much lower in BOMEX, with a mean of 11.4% in the control simulation and only a small variation (about 3%) between day and night (Fig. 3.8 (b)). The nighttime cloud fraction (10-15 %, see Fig. 3.8 (b)) is in close agreement with all other recent LES simulations of the BOMEX case (Siebesma and Cuijpers (1995), Brown (1999), Jiang and Cotton (2000), Neggers *et al.* (2003), Siebesma *et al.* (2003)). This is reassuring as previous LES studies (see references above) found that mean cloud fraction for the BOMEX case was fairly robust to differences in models and variations in, grid resolution, initial conditions, and large scale forcing terms. Unfortunately, observations of cloud fraction from BOMEX are very limited and there is no published data to compare against. There is also no means of verifying the diurnal cycle in our simulations as all previous LES studies of the BOMEX case (see references above) exclude solar radiation.

The impact of aerosols on cloud cover is more notable in ATEX than in BOMEX. For example, mean cloud cover is reduced from 31.0 to 24.0% in ATEX, and from 11.2 to 10.4% in BOMEX (see Table 3.1). The aerosol-induced cloud cover reductions are greater in the daytime showing an enhancement of daytime clearing in addition to a general decrease.

3.4.2   Dependence of cloud fields on relative humidity profile

The high cloud fraction in ATEX is mainly due to the presence of passive clouds that spread out beneath the inversion (see the peak in cloud fraction at 1450 m in Fig. 3.9 (a)). This passive cloud is generated
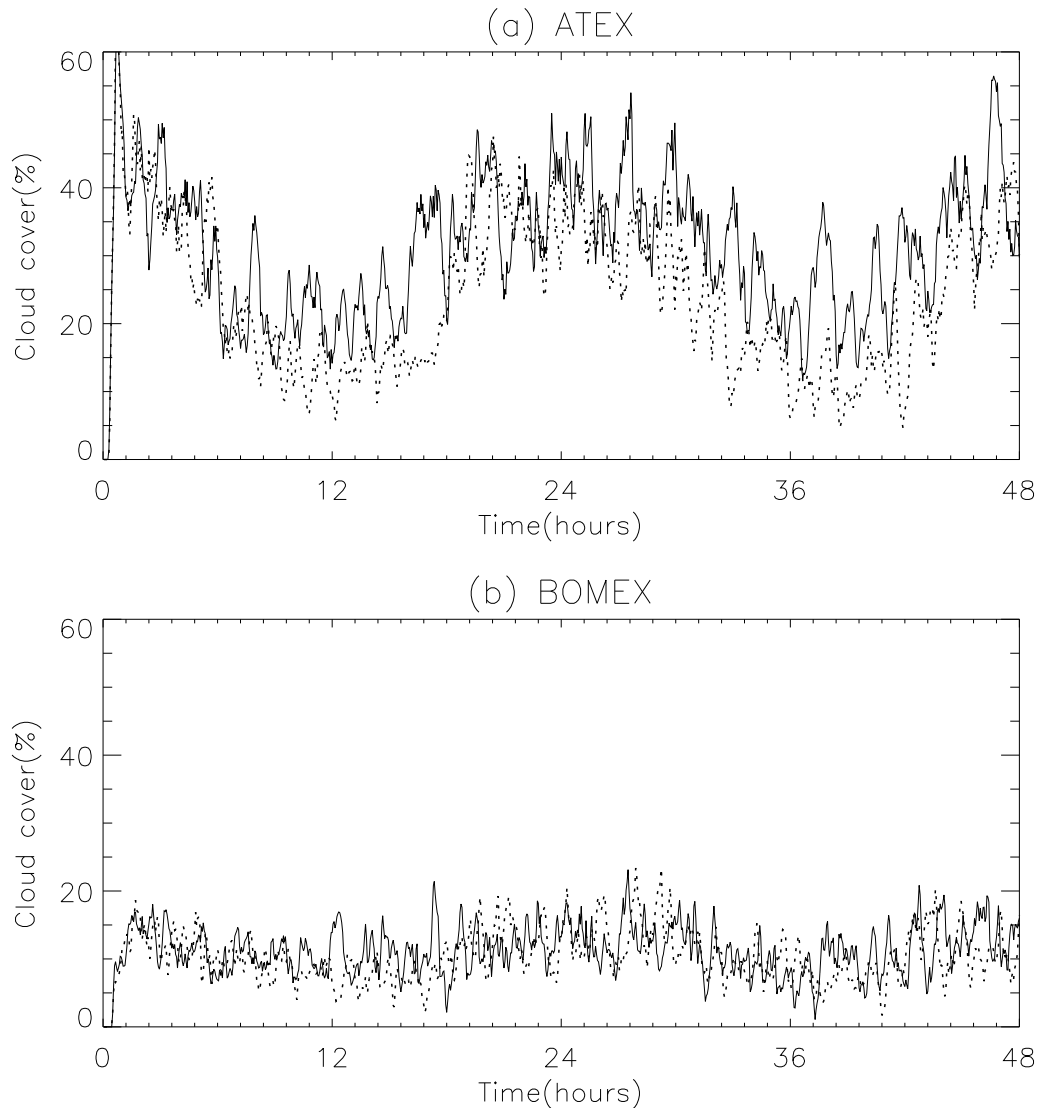
(a) ATEX

(b) BOMEX

Figure 3.8: *Total cloud fraction(%) in (a) ATEX, and (b) BOMEX, in the control simulations (solid lines) and absorbing aerosol simulations (dotted lines).*

by active cumulus that reach the inversion and diverge. Figure 3.10 is a visual representation of the cloud field at one instant of time during the ATEX control simulation. The image shows active clouds and patches of stratiform cloud, which are the remains of former cumulus towers, such as those seen in the centre of the image. There are also a few puffs of forced cloud. Relative humidity is one of the main factors controlling the fractional cover of passive cloud. In ATEX the relative humidity at the inversion base (1450 m) is almost 100% in the pre-dawn period, but drops to 98% by the afternoon in the control, and 95% in the aerosol run (Fig. 3.11 (a)). Cloud fraction at the inversion base declines from 25% in the pre-dawn period to 6% and 2% by the afternoon in control and aerosol simulations, respectively (Fig. 3.9 (a)). The relative humidity changes are a direct result of the rise in temperature in
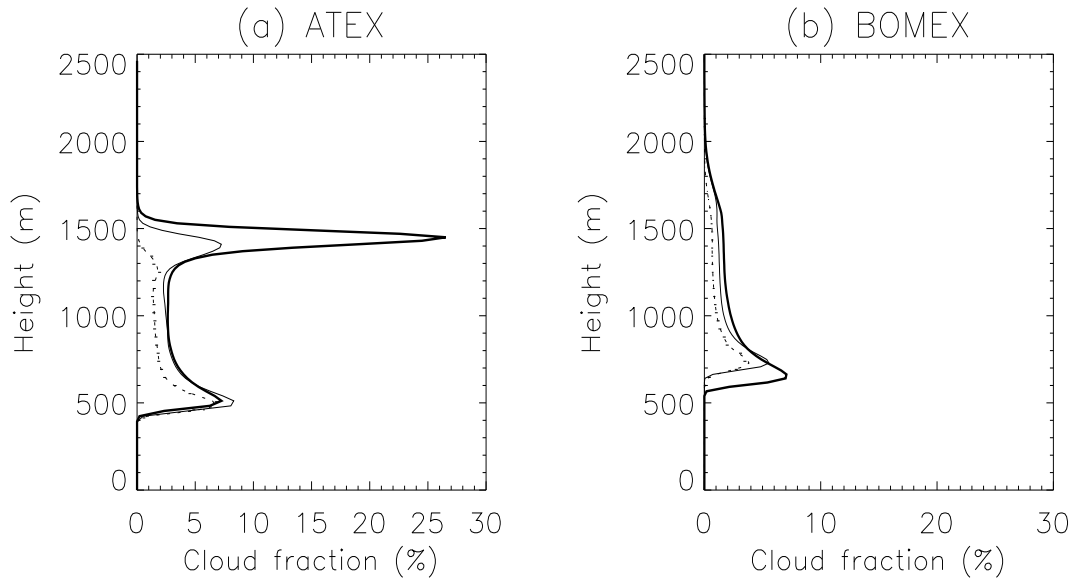
Figure 3.9: *Mean cloud fraction (%) as a function of height in (a) ATEX, and (b) BOMEX, for 0200-0500 h (thick solid line) and 1200-1700 h (thin solid line) in the control simulations, and 1200-1700 h in the absorbing aerosol simulations (dashed line).*
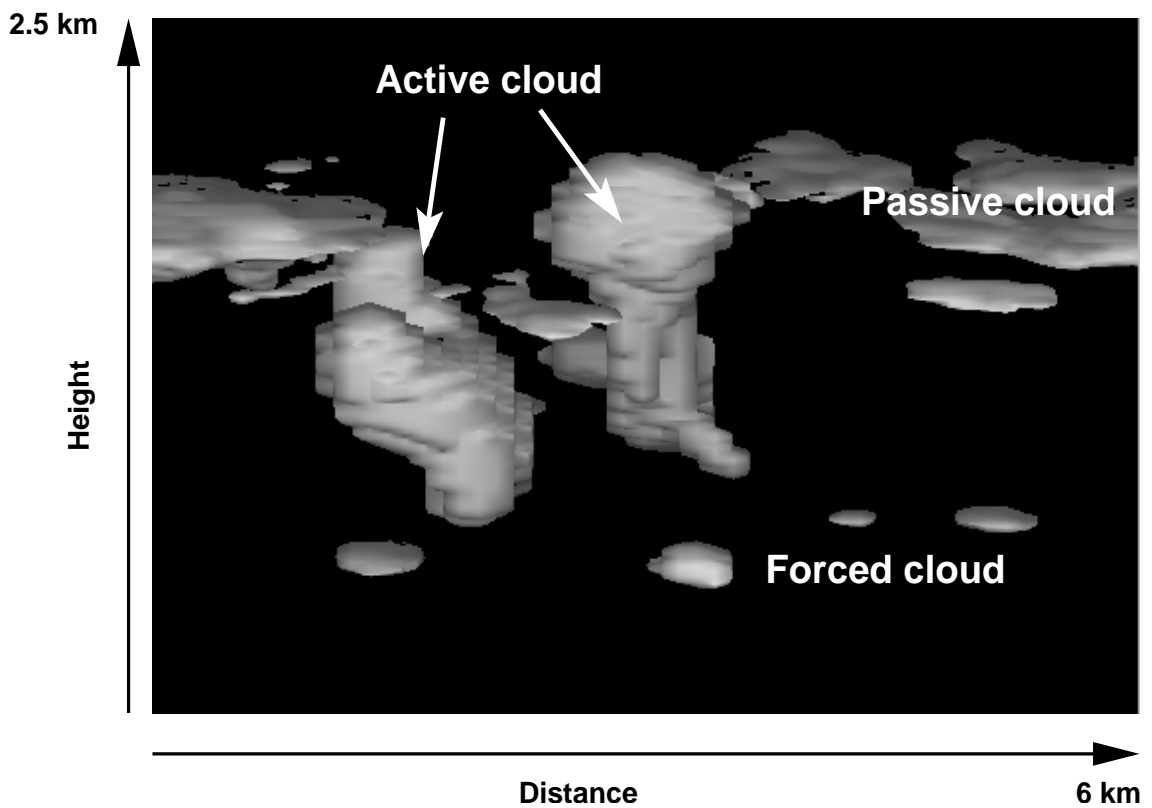
Figure 3.10: *Instantaneous visual representation of the 3D cloud field in ATEX control simulation at 0330 h.*
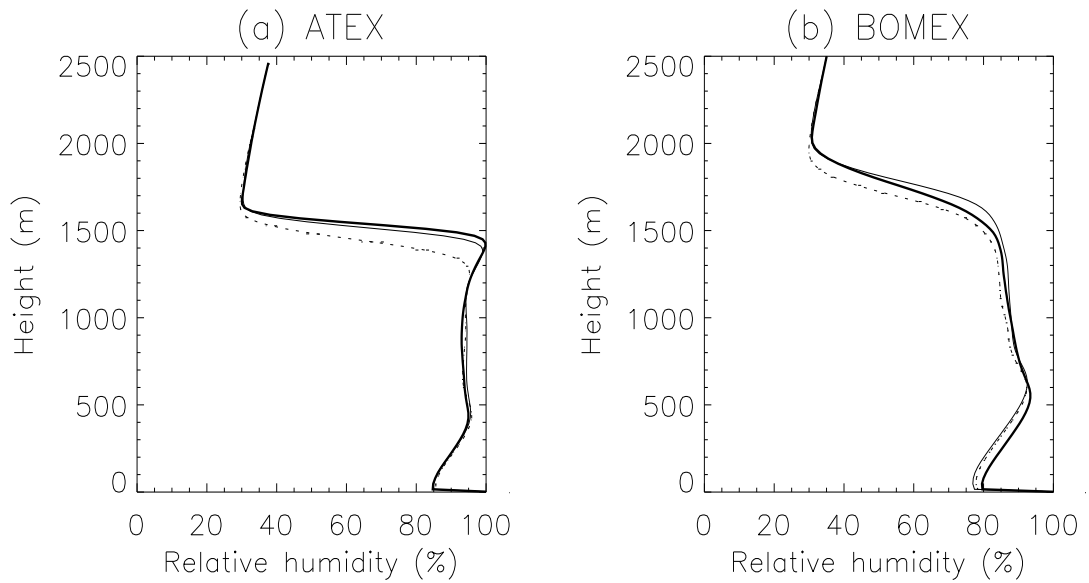
Figure 3.11: *Mean relative humidity (%) as a function of height in (a) ATEX, and (b) BOMEX, for 0200-0500 h (thick solid line) and 1200-1700 h (thin solid line) in the control simulations, and 1200-1700 h in the absorbing aerosol simulations (dashed line).*
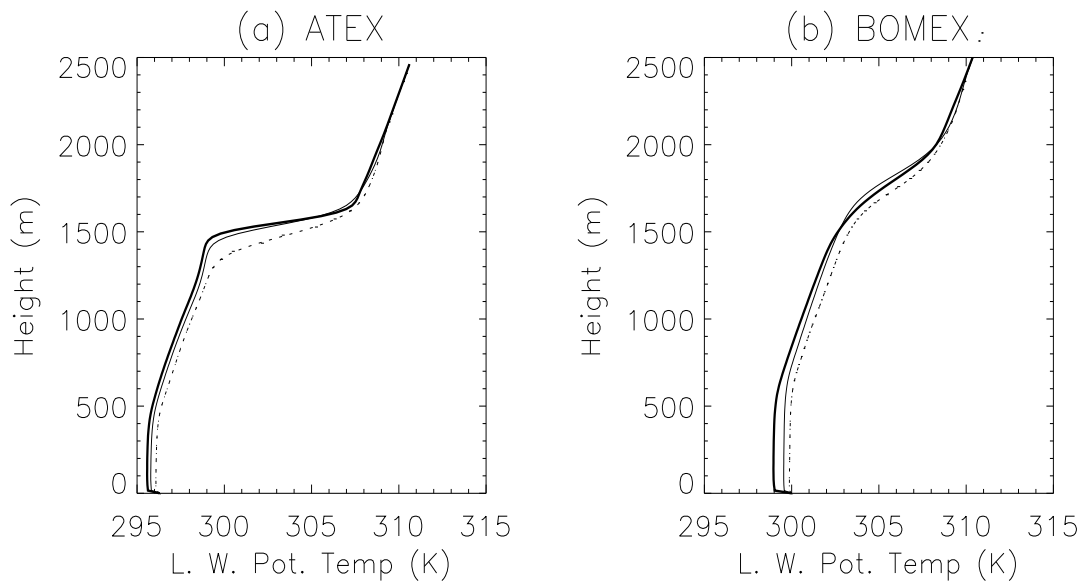
Figure 3.12: *Mean liquid water potential temperature (K) as a function of height in (a) ATEX, and (b) BOMEX, for 0200-0500 h (thick solid line) and 1200-1700 h (thin solid line) in the control simulations, and 1200-1700 h in the absorbing aerosol simulations (dashed line).*

the BL (Fig. 3.12 (a)), and changes in the total water mixing ratio (Fig. 3.13 (a)). At some heights, the total water mixing ratio increases and offsets the relative humidity drop expected from the temperature
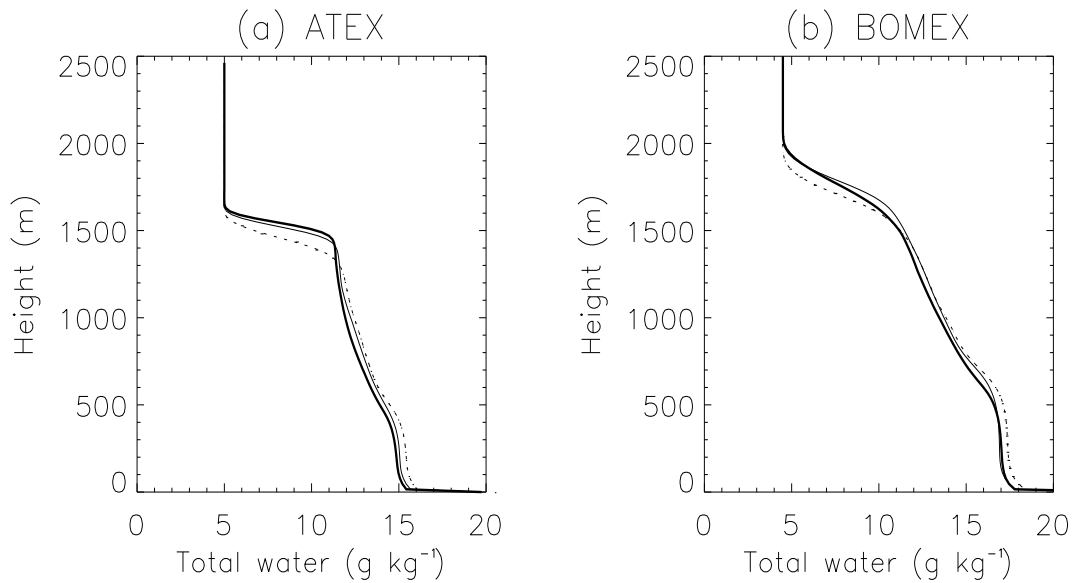
Figure 3.13: *Mean total water (g/kg) as a function of height in (a) ATEX, and (b) BOMEX, for 0200-0500 h (thick solid line) and 1200-1700 h (thin solid line) in the control simulations, and 1200-1700 h in the absorbing aerosol simulations (dashed line).*
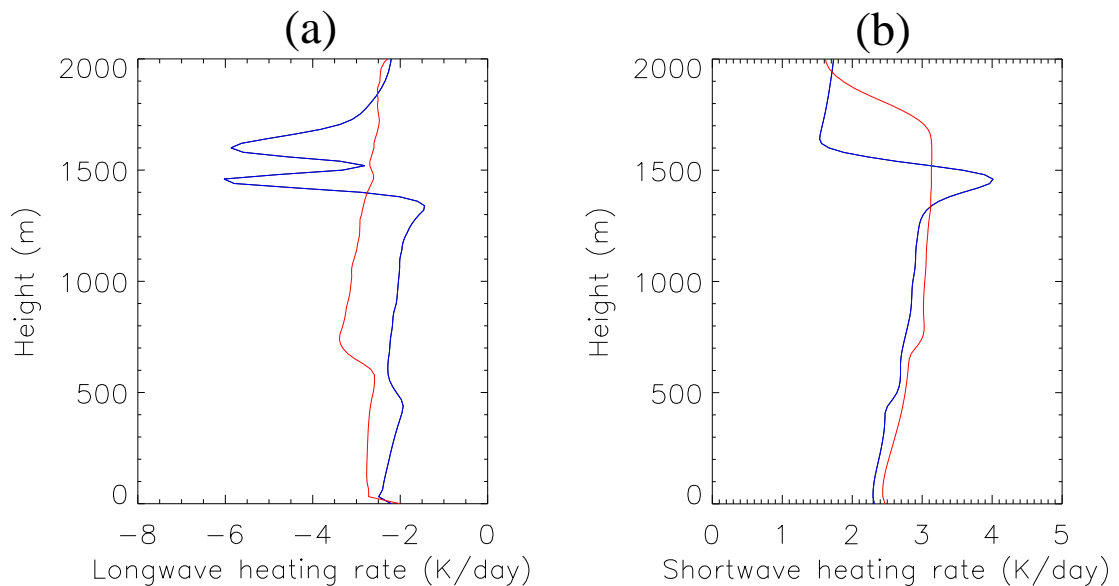
Figure 3.14: *(a) Mean longwave heating rates (K day^{-1}) as a function of height for 0200-0500 h, and (b) Mean shortwave heating rate (K day^{-1}) as a function of height for 1100-1300 h, in the control simulations for ATEX (blue lines), and BOMEX (red lines).*

change. The temperature in the BL rises by about 0.2 K between dawn and afternoon in the control simulation (Fig. 3.12 (a)), due to the solar heating (Fig. 3.14 (b)). The aerosol solar heating rate

in the BL is about the same magnitude as the shortwave heating (Fig. 3.14 (b)) in the control so it roughly doubles the heating (Fig. 3.12). Both have a diurnal mean of about 1 K day^{-1} in the BL. The cross-inversion entrainment rate declines during the daytime, as shown by the drop of inversion height in Figs. 3.12 and 3.13. The reduced entrainment warming and drying, explains why the BL moistens during the day, and why it does not heat as much as expected from the shortwave heating rates. The change in entrainment rate is linked to changes in the intensity of convection, which is discussed in the next section.

In BOMEX there is no peak in relative humidity at the inversion base (Fig. 3.11 (b)) and there is no anvil cloud beneath the inversion (Fig. 3.9 (b)). This mainly explains why cloud fraction is much lower in BOMEX than ATEX, and why cloud fraction varies less, both diurnally and with shortwave heating from aerosol (see Fig. 3.8). Instead cloud cover is dominated by forced and active clouds. A visual representation of a typical cloud field from the control simulation is shown in Fig. 3.15. This shows forced clouds forming at the cloud base. Many forced clouds form but do not become buoyant. Those that do become buoyant (active) rise rapidly through the cloud layer but detrain quickly as they mix with the relatively dry ambient air. This explains why cloud cover peaks at cloud base peak and general decreases with height (Fig. 3.9 (b)). The clouds have almost completely detrained by the time they reach the inversion so there is little opportunity for the generation of diverging cloud top (anvil cloud).

3.4.3 Liquid water path

Domain average LWP is very variable with time, in both ATEX and BOMEX (Fig. 3.16). At times when large active clouds are present LWP reaches 30, or even 50 g m^{-2}, but falls to almost zero during less active times when only small forced clouds, or diffuse, decaying clouds are present. There is a diurnal cycle in LWP: both peak and baseline values are higher in the night and lower in the day. The higher peaks may indicate greater convective fluxes (discussed in next section), and the higher baseline indicates greater persistence of clouds so that LWP remains higher in between times of peak activity. LWP is far more variable in time than cloud fraction (compare Figs. 3.16 & 3.8). This is because active clouds do not occupy a large area of the domain, even though they contribute most of the liquid water. Decaying clouds, however, may have a similar area, but little liquid water.

The LWP is generally higher in ATEX than in BOMEX. For example, table 3.1 shows a mean LWP of 14.6 g m^{-2} in ATEX, and 9.2 g m^{-2} in BOMEX. Corresponding daytime values are 11.7 and 7.7 g m^{-2}. Furthermore, there is a greater aerosol-induced LWP reduction in ATEX, again with the reduction
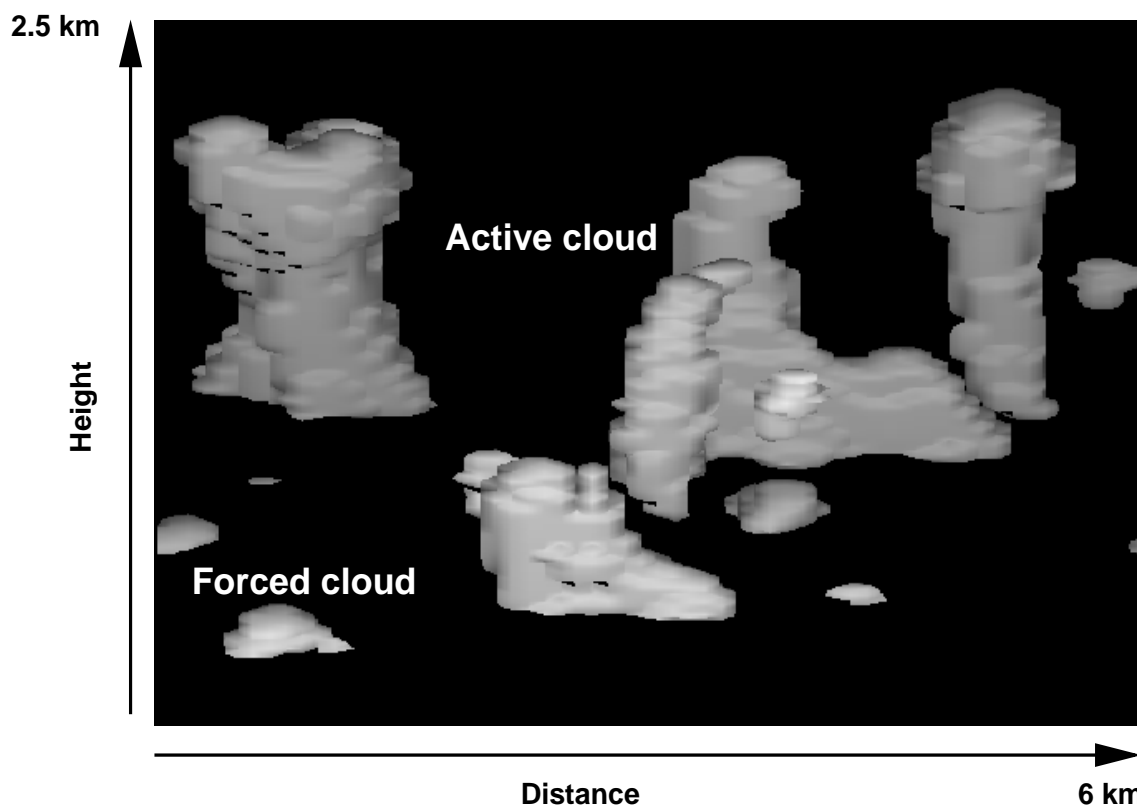
Figure 3.15: *Instantaneous visual representation of the 3D cloud field in BOMEX control simulation at 0300 h.*

being greater for the daytime mean than for the overall mean. These mean changes largely reflect the mean changes in cloud cover. One other difference is that the cloud fraction to LWP ratio in ATEX is nearly twice that in BOMEX. This is because much of the cloud cover in ATEX is associated with passive anvils, which have relatively low liquid water but develop large areas as they diverge beneath the inversion. In contrast most clouds in BOMEX are active and have a relatively high liquid water content but a small area.

3.4.4 Cloud top height

Figure 3.17 shows maximum cloud top heights and minimum cloud bases. Cloud top height reaches 2500 m in BOMEX, but no more than 1850 m in ATEX. Convection is more tightly constrained (vertically) in ATEX because the inversion is lower, and much stronger (Fig. 3.12). The broader inversion in BOMEX enables the strongest cumulus towers to overshoot some way into the free troposphere. Cloud top heights show considerable variability in BOMEX; less so in ATEX. There seems no prefered cloud top heights in BOMEX, whereas in ATEX the prefered height corresponds to the inversion base, with
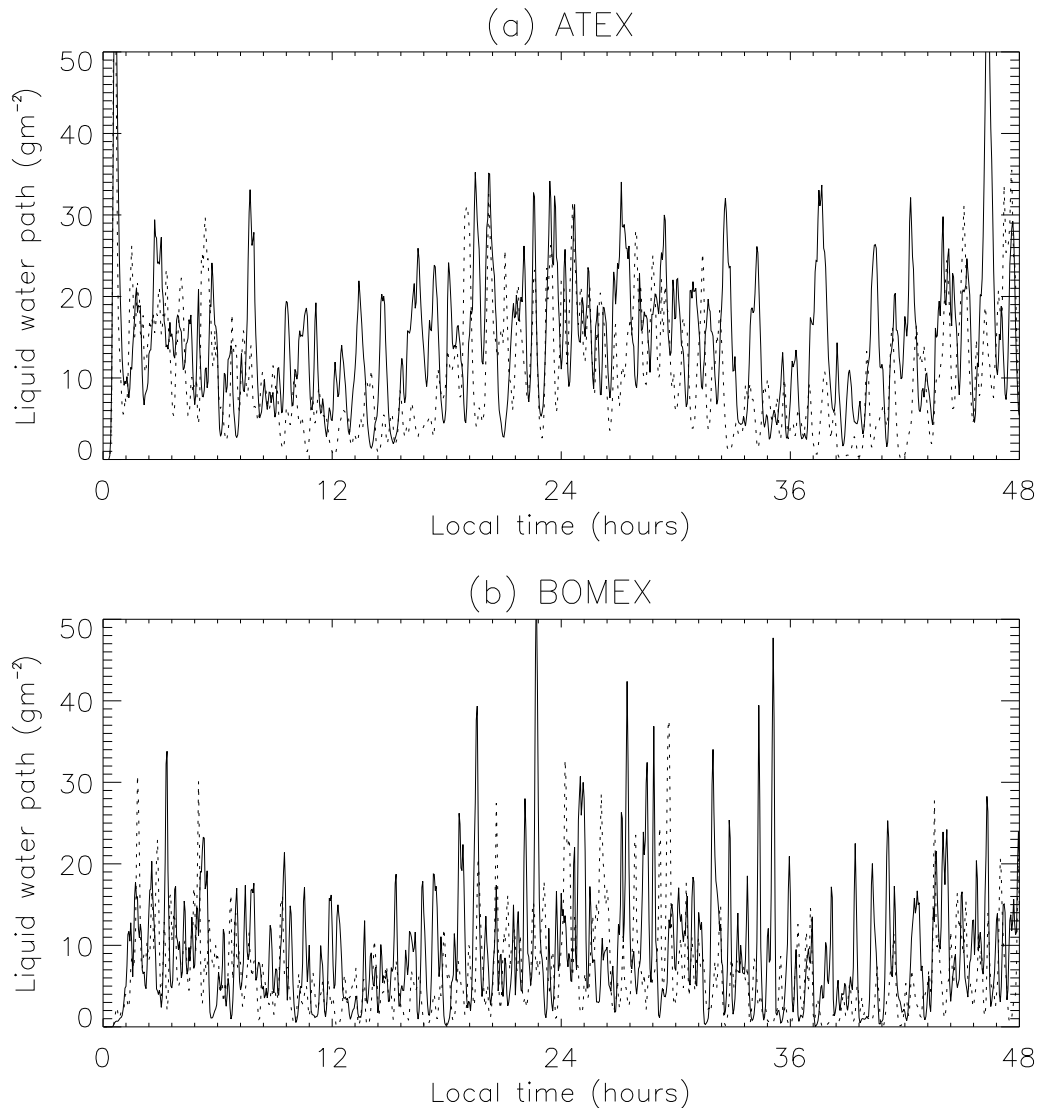
Figure 3.16: *Domain averaged liquid water path (g m^{-2}) in (a) ATEX, and (b) BOMEX, in the control simulations (solid lines) and absorbing aerosol simulations (dotted lines).*

small peaks 100-200 m above that level, associated with overshooting.

To summarise, most of the variability in cloud cover is related to the existence, and persistence of anvil cloud. In BOMEX there was no anvil cloud, but in ATEX there was 25-30% cover by anvil cloud in the nighttime, falling to practically zero in the aerosol run buy the afternoon. The amount of anvil cloud depended mainly on the relative humidity near cloud top. Cloud cover at cloud base, and in the middle of the cloud layer (1000 m) was also reduced and peak values of LWP were lower in the daytime. This suggests a reduced number, size or intensity of forced and active clouds; it hints of a reduction in convective activity. Indeed this is probably the main factor controlling cloud responses in BOMEX.
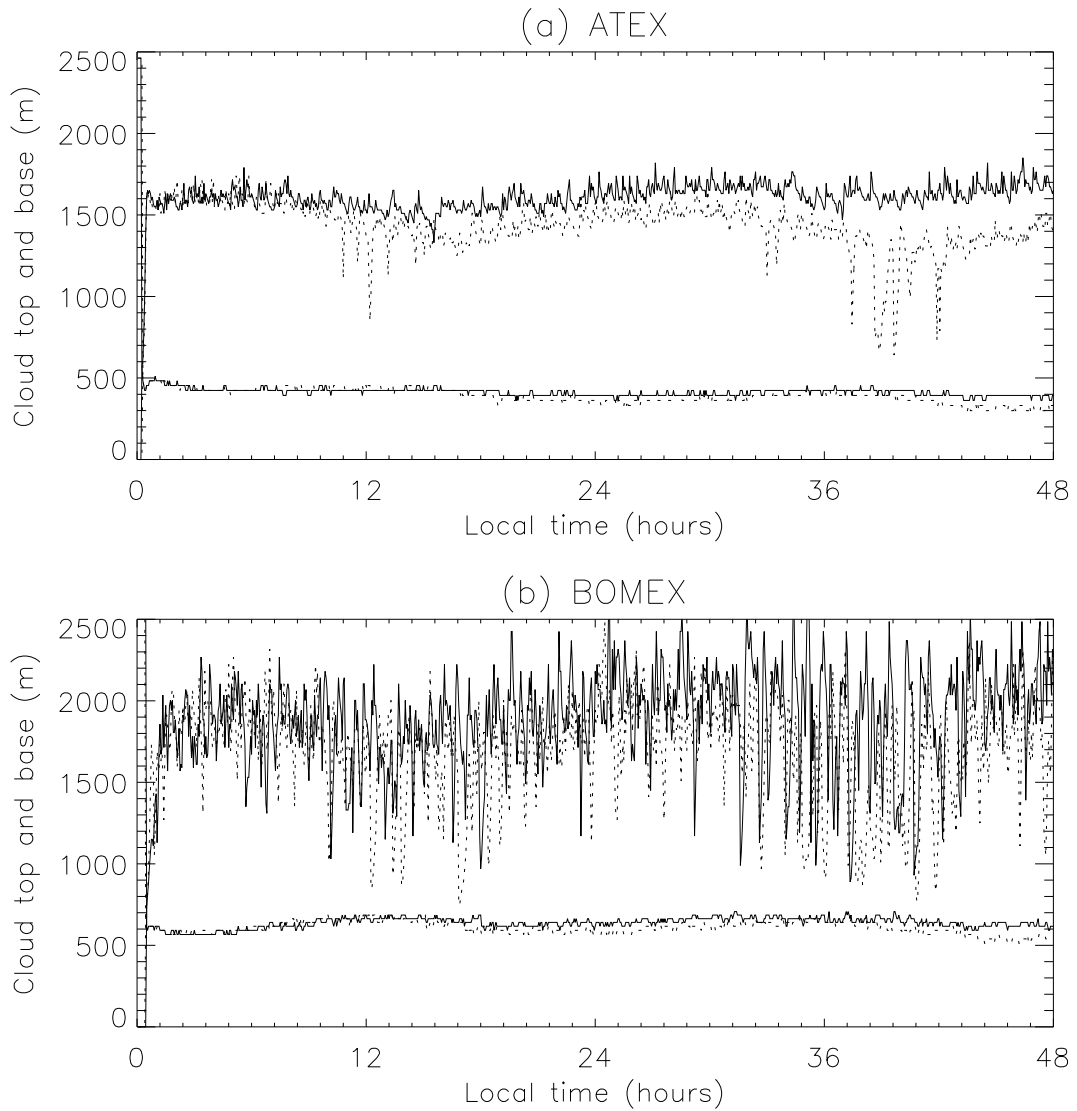
Figure 3.17: *Maximum cloud top height and minimum cloud base height (m) in (a) ATEX, and (b) BOMEX, in the control simulations (solid lines) and absorbing aerosol simulations (dotted lines).*

Variation in the intensity of convection probably also contributes to variability in cloud fraction and LWP in ATEX, in addition to the variation in anvil cloud. The two sources of variability are however related since the anvil cloud is generated by active clouds that reach the inversion. The extent to which convection intensity influences total cloud cover and LWP is therefore not straight forward, and is examined in the following section.

3.5   Results: II. Convection intensity

3.5.1   Cloud mass flux

Cumulus clouds are essentially the evidence of conditional instability in the BL. In this situation only saturated parcels (clouds) will develop enough buoyancy to convect. Vertical motion, turbulent mixing, and vertical transport of mass, moisture and energy are dominated by active (buoyant) clouds. The cloud mass flux (the integral of vertical velocity over all cloudy gridpoints at a particular level), is therefore a good measure of convective intensity. The cloud mass flux is maximum at the cloud base and decreases gradually with height at a rate controlled by the lateral entrainment and detrainment rates and the release or uptake of latent heat by condensation and evaporation, respectively. In ATEX the cloud mass flux suddenly drops to zero at the inversion where the clouds reach their level of neutral buoyancy and diverge (Fig. 3.18 (a)). In BOMEX the cloud mass flux goes gradually to zero as the clouds lose their buoyancy mainly through detrainment rather than by reaching a level of neutral buoyancy (Fig. 3.18 (b)).
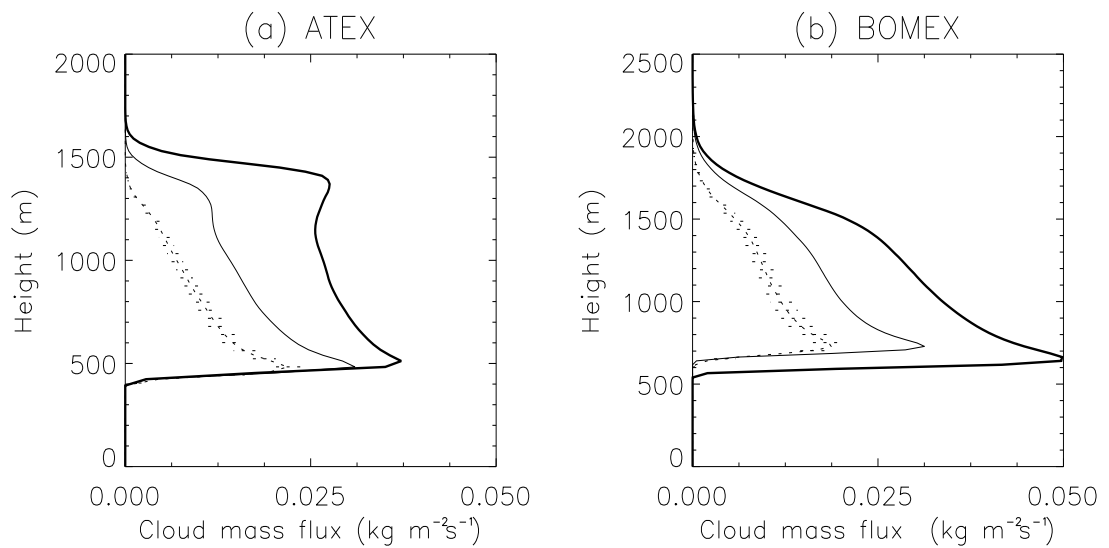
Figure 3.18: *Mean cloud mass flux (kg m^{-2} s^{-1}) as a function of height in (a) ATEX, and (b) BOMEX, for 0200-0500 h (thick solid line) and 1200-1700 h (thin solid line) in the control simulations, and 1200-1700 h in the absorbing aerosol simulations (dashed line). The shading represents the standard error on the afternoon profiles of the aerosol simulations (see section 3.3 for more details).*

The daytime, reductions of cloud mass flux (Fig. 3.18) are explained both by reductions of cloud amount (Fig. 3.9), and decline in mean updraught strengths (Fig. 3.19). The aerosols amplify the
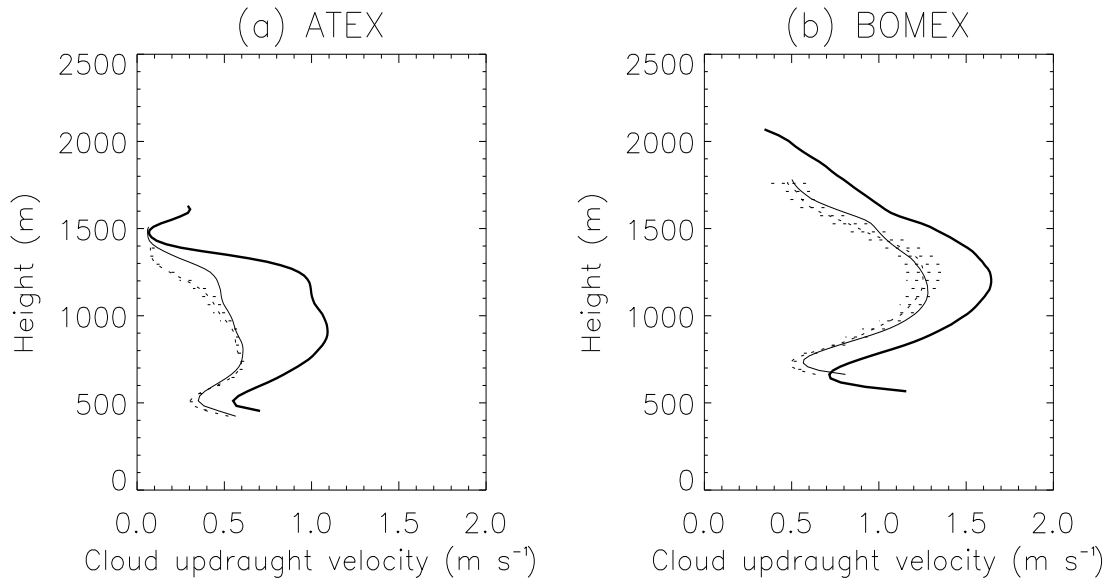
Figure 3.19: *Mean cloud updraught velocity (m s^{-1}) as a function of height in (a) ATEX, and (b) BOMEX, for 0200-0500 h (thick solid line) and 1200-1700 (thin solid line) in the control simulations, and 1200-1700 h in the absorbing aerosol simulations (dashed line). The shading represents the standard error on the afternoon profiles of the aerosol simulations (see section 3.3 for more details).*

reductions of mass flux and cloud amount, although they do not significantly reduce mean updraught strengths. In the aerosol simulations cloud mass flux goes to zero at a lower height, especially in ATEX. This is consistent with the relative decline in inversion height (e.g. Fig. 3.12) because the inversion constrains the vertical extent of convection. However, variation in the height of the inversion depends itself on the intensity of convection because convection largely determines the cross-inversion entrainment rate. Therefore, the relative decline in inversion height in the aerosol simulations indicates a reduction in convective activity, consistent with lower mass fluxes.

3.5.2 Convective Available Potential Energy (CAPE)

CAPE is a good measure of the potential intensity of convection intensity because it depends on the buoyancy of lifted parcels relative to their environment, and the depth of the layer over which they are buoyant (see section 3.3 for a full definition). CAPE (shown in Fig. 3.20) is higher in BOMEX because the cloud layer is deeper. The gradual rise of CAPE with time in BOMEX simulations (Fig. 3.20) is mostly explained by the rise in the inversion height. In the aerosol simulations CAPE declines relative to the control during the daytime. This decline is linked only to the relative decline in inversion height
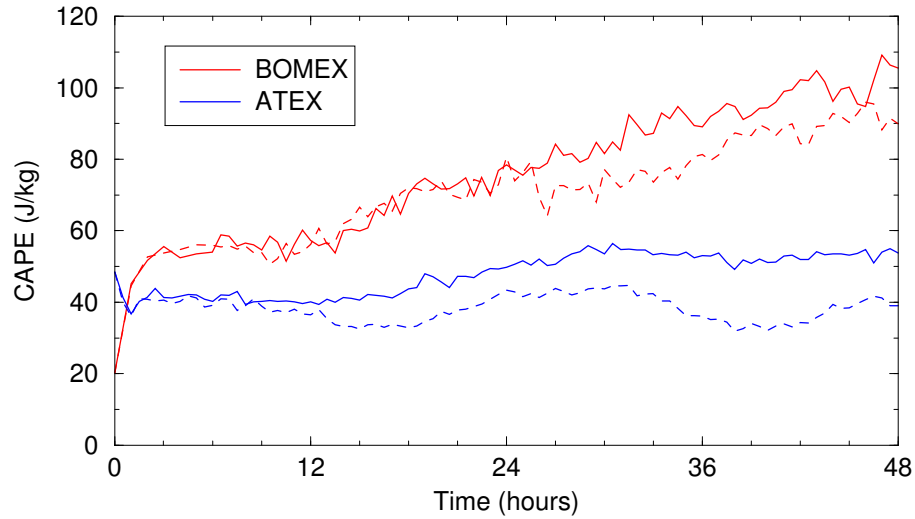
Figure 3.20: *Convective available potential temperature (J/kg) in ATEX (red lines), and BOMEX (blue), for control simulations (solid lines), and absorbing aerosol simulations (dotted lines).*

and the lifting of cloud base. Therefore, the solar heating may be acting to suppress the convection by limiting CAPE. However, the reduced CAPE is also a consequence of reduced convection, through the reduction of inversion height so it is difficult to imply causality.
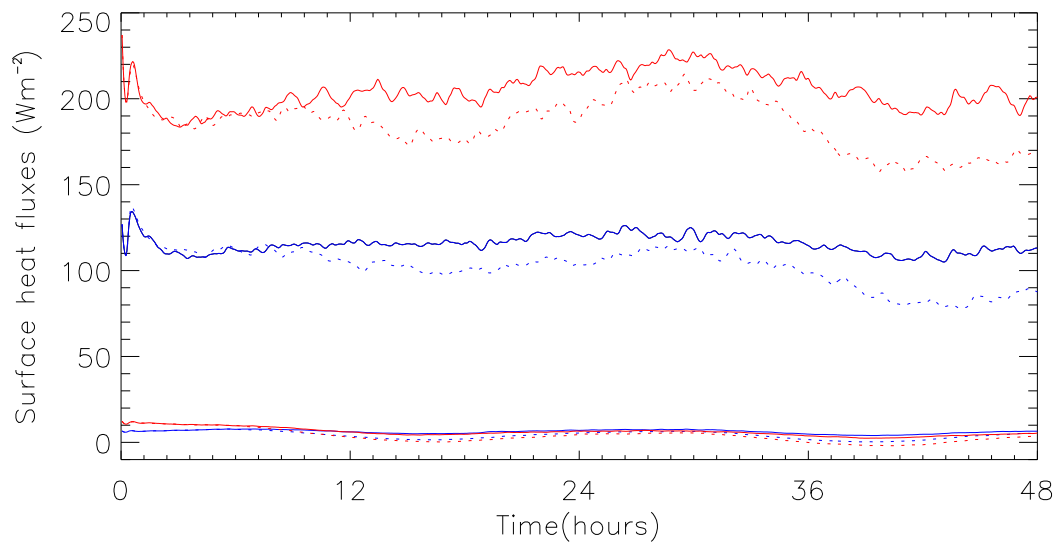
Figure 3.21: *Domain averaged surface latent (upper lines) and sensible (lower lines) heat fluxes (solid lines) ($W\,m^{-2}$), in ATEX (blue lines), and BOMEX (red lines), for control simulations (solid lines), and absorbing aerosol simulations (dotted lines).*

3.5.3 Surface heat and moisture fluxes

Surface moisture fluxes (shown in Fig. 3.21) are essentially what drive the convection; they supply latent heat at low levels, which is transported vertically (Fig. 3.23) through moist convection to balance the longwave cooling (see Fig. 3.14 (a)) and large-scale advective cooling (1 K day^{-1} in these cases). There is therefore a strong link between the solar heating (Fig. 3.14 (b)), the vertical latent heat flux, and the intensity of convection. The intensity of convection also feeds back on surface fluxes by generating turbulence. Latent heat fluxes are around 120 W m^{-2} in ATEX, and 200 W m^{-2} in BOMEX as the sea surface temperature is 3K higher in BOMEX (Fig. 3.21). Sensible heat fluxes are small (0-10 W m^{-2}) because the sea surface is only slightly warmer than the surface layer temperature. The surface heat fluxes show a slight decrease in the daytime, and are lower in the aerosol simulation: sensible heat fluxes are about 5 W m^{-2} lower, and latent heat fluxes are up to 30 W m^{-2} lower. Since the sea surface temperatures are held constant with time, the surface flux response must be due to reduced turbulence near the surface (Fig. 3.22) due to the heating of the surface layer (Fig. 3.12).
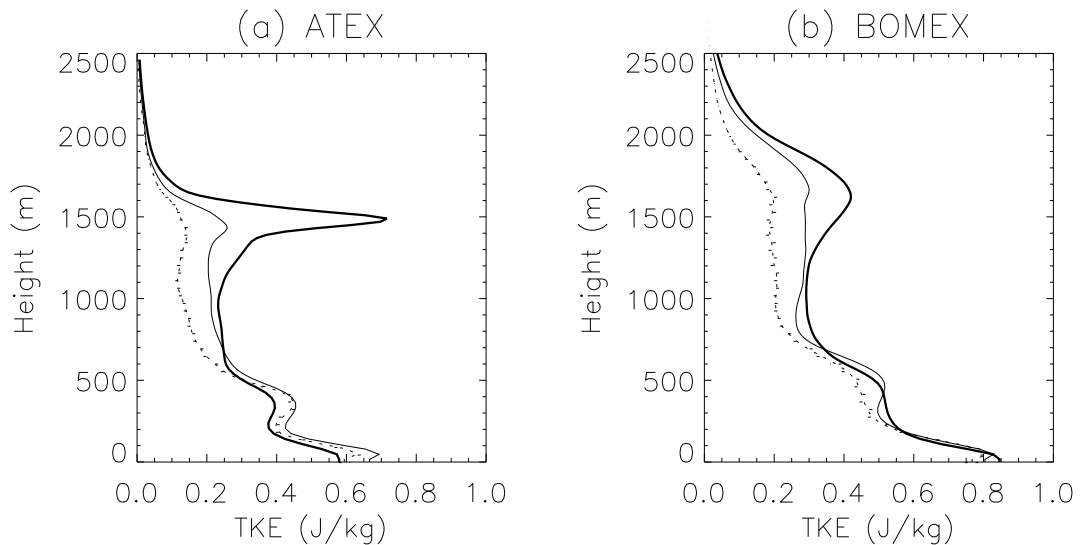
Figure 3.22: *Mean turbulent kinetic energy (J/kg) as a function of height in (a) ATEX, and (b) BOMEX, for 0200-0500 h (thick solid line) and 1200-1700 h (thin solid line) in the control simulations, and 1200-1700 h in the absorbing aerosol simulations (dashed line).*

3.5.4 Response of convection to changes in relative humidity

The intensity of convection may also be responding to reduced relative humidity (Fig. 3.11). A lower relative humidity in the cloud layer will lead to a higher evaporation rates at the edges of rising clouds
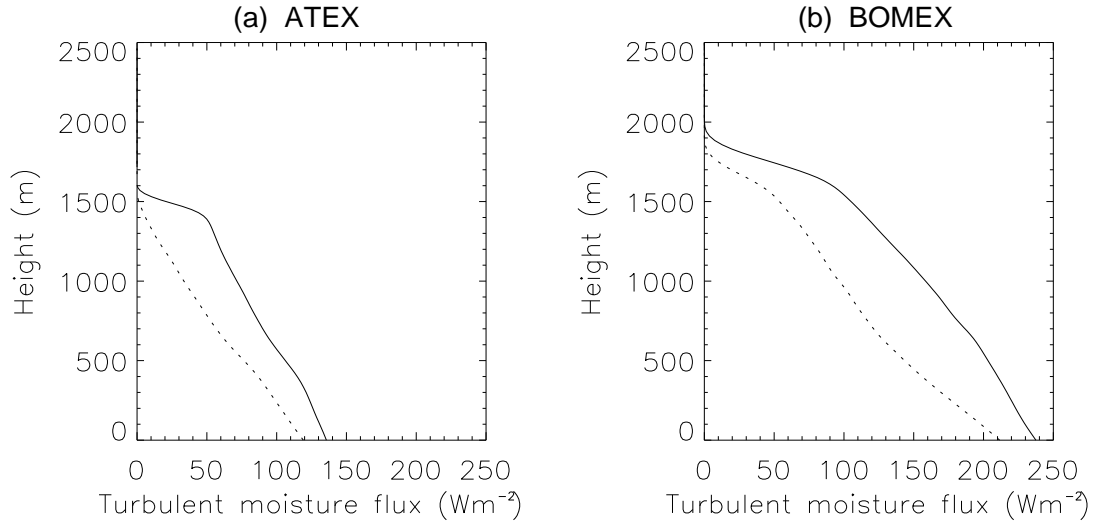
Figure 3.23: *Mean turbulent moisture flux (W m^{-2}) as a function of height in (a) ATEX, and (b) BOMEX, for 1200-1700 h (solid line) in the control simulations, and 1200-1700 h in the absorbing aerosol simulations (dashed line).*

as cloudy and clear air mixes. Thus, clouds will detrain and lose their buoyancy more quickly. This helps to explain why the convection does not extend as far in the vertical (Fig. 3.18), although it does not explain why there is lower cloud mass flux at cloud base. A lower relative humidity in the subcloud layer means that air parcels from near the surface must be lifted higher before they become saturated. This is shown by daytime rises of cloud base (Fig. 3.17) and possibly plays a role in reducing the number or clouds that form or become active. However, the diurnal cycle of cloud base is less obvious in ATEX and is offset by a general downward trend.

In summary, the aerosol heating clearly leads to reduced convection, and lower fractional coverage by cumulus clouds. This is consistent with energetic considerations, reduced surface fluxes of heat and moisture, and reduced vertical mixing. Cloud mass fluxes, turbulence and moisture fluxes all decrease in the daytime, and absorbing aerosols amplify that decrease. Cloud updraught strengths are not significantly different in the aerosol simulations, but the fractional cover by buoyant clouds is much lower.

3.5.5   Semi-direct forcing

Figure 3.24 shows the temporal variation of semi-direct forcing for the ATEX and BOMEX experiments. There are large fluctuations in the semi-direct forcing because of the variability in cloud amount
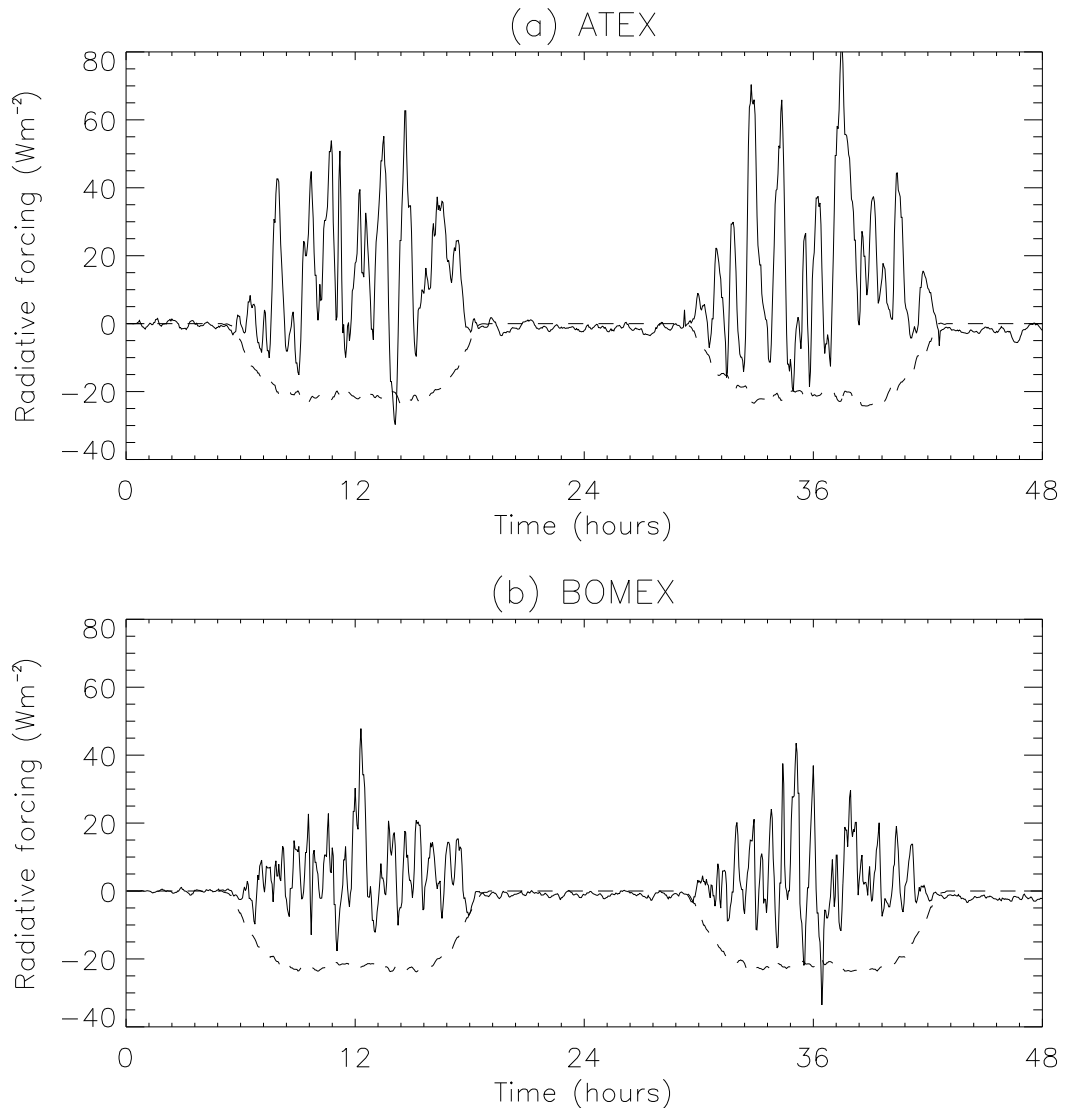
Figure 3.24: *Semi-direct forcing (solid lines), and direct aerosol forcing (dashed lines) in (a) ATEX, and (b) BOMEX.*

and LWP with time, but behind this noise there is clearly a positive signal. The mean semi-direct, direct and total forcings are shown in Table 3.2. The mean semi-direct forcing for ATEX is moderate and positive (8.0 W m^{-2}), and the mean semi-direct forcing for BOMEX is small and positive (1.9 W m^{-2}). These forcings are proportionate to the differences in daytime cloud fraction between the aerosol and control simulations. For example, in ATEX the daytime cloud fraction reduced from 24.9% to 15.3% , an absolute reduction of 8.6% , and in BOMEX the daytime cloud cover is reduced from 10.1 to 8.4% , a reduction of only 1.7%(see Table 3.1). The daytime LWP reductions are also greater in ATEX (Table 3.1).

Experiment	Semi-direct			Direct	Total
	Day 1	Day 2	Mean	Mean	Mean
ATEX	7.3	8.7	8.0	-9.6	-1.6
BOMEX	2.5	1.3	1.9	-10.3	-8.4

Table 3.2: *Semi-direct, direct, and total aerosol radiative forcings (W m^{-2}) for the ATEX and BOMEX experiments. Total forcing excludes any indirect effects.*

The semi-direct effect is essentially the difference in cloud radiative forcing between the control and aerosol simulation. The semi-direct effect in ATEX is also quite large in comparison to the cloud radiative forcing in the control case (8.0 W m^{-2} , compared to -17.5 W m^{-2} , see Table 3.1). It is equal to a 48% decrease in the magnitude of the cloud radiative forcing. In BOMEX the semi-direct forcing is only 25% the magnitude of the cloud radiative forcing in the control (1.9W m^{-2} , compared to -7.7W m^{-2}).

Obviously the semi-direct forcing is limited by the cloud radiative forcing in the control simulation. For example, the semi-direct forcing in BOMEX could not be greater than 7.7 W m^{-2} even if all cloud disappeared instantly in the aerosol simulation. This partly explains why there is a smaller semi-direct forcing in BOMEX, but furthermore, the cloud in BOMEX is relatively less responsive. For example, the cloud fraction reduces by 17 % of the mean amount, whereas the cloud fraction reduces by 35% of the mean amount in ATEX.

LWP changes are also necessary to fully explain the changes in cloud radiative forcing (the semi-direct forcing). LWP was significantly reduced by the aerosols, and in both cases the relative decline in LWP was higher than the relative decline in cloud fraction. This shows that the LWP per unit area of cloud was lower in the aerosol simulations; i.e clouds, on average, had a lower albedo. This must contribute to the semi-direct forcing because the relative cloud fraction changes are not enough to explain the relative reductions of cloud radiative forcing. For example, in ATEX cloud fraction was 35% lower than the mean amount in the aerosol simulation but cloud radiative forcing was 46% lower. The remaining cloud therefore must have had a 12% lower average albedo, which is consistent with the 17% reduction in LWP per unit area of cloud. In BOMEX the mean LWP per unit area of cloud reduced by 33% and the mean albedo fell by 10%.

3.6 Conclusions and discussion

In this chapter the LEM has been used to explore the semi-direct effect for two trade cumulus scenarios using idealized absorbing aerosol distributions. The scenarios are based on the observation of undisturbed trade-wind cumulus from ATEX and BOMEX. In each case the cumulus convection is constrained by a low level inversion but this inversion is stronger, and slightly lower in ATEX, providing a more restrictive lid to the convection. The cloud fraction in ATEX is much higher (20-40%) and is dominated by the spreading of passive anvil cloud beneath the inversion, where relative humidity is almost 100%. In BOMEX the sea surface temperature was 3K higher and the convection is more vigourous. However, the cloud fraction was actually quite low in BOMEX (around 10%) because the relative humidity around the inversion was much lower (around 80%) and there was is no anvil cloud.

The semi-direct effect was simulated by placing absorbing aerosols in the BL that gave a diurnal mean solar heating rate of about 1 K day^{-1}. The aerosol single scattering albedo was 0.88, and the aerosol optical depth was 0.4 (values given for $\lambda = 0.55\mu m$).

The ATEX-based experiment gave a much higher semi-direct forcing than the BOMEX-based experiment (8.0 W m^{-2} compared to 1.9 W m^{-2}) because, in ATEX, there was a big reduction in the amount of anvil cloud. There was also a reduction in the fractional coverage of active (buoyant) clouds, associated with a suppression of convective activity. However, the response from the detraining anvil cloud was far greater because the coverage of this cloud was high and was particularly sensitive changes in ambient relative humidity, which impacted the detrainment rate.

The main conclusion of this chapter is that the magnitude of the semi-direct effect depends greatly on meteorological conditions, particularly, the amount and type of cloud. Even small differences in the vertical structure of the BL were important in determining the cloud distribution and semi-direct forcing. For instance, in BOMEX the cloud fraction was only 10% and the semi-direct forcing was small (1.9 W m^{-2}), whereas in ATEX daytime cloud fraction was moderate (20 %) and the semi-direct forcing was moderate (8.0 W m^{-2}). In the stratocumulus experiment A-088 (see section 2.2.4), where cloud cover was 100 %, the semi-direct forcing was large (16.3 W m^{-2}). This shows a correlation between the semi-direct forcing and the cloud fraction. This correlation is not surprising since the amount of cloud limits the potential response.

However, the control-case cloud fraction is not the only variable determining the strength of the semi-direct effect. The type of cloud is also important, as different types of cloud respond in different ways.

In ATEX the main cloud response came from variability in the amount of passive anvil cloud, as this was particularly sensitive to changes in relative humidity. In BOMEX the main response came from variability in the intensity of convection, as this largely determined the cloud fraction and LWP. In the stratocumulus experiment the cloud response was entirely driven by changes in LWP as a result of a temperature increase in the cloud layer, and an enhancement of the decoupling of the BL.

These results show that, to predict the semi-direct effect, it is important to correctly characterise the cloud regime, and accurately represent the cloud amount. Also, it is important to correctly predict the way that the clouds responds to subtle changes in relative humidity or thermodynamic structure. This is certainly a challenge for general circulation models. To have confidence in GCM estimates of the semi-direct forcing it is first necessary to show that the cloud parameterizations respond consistently with the LES results. This problem is addressed in chapter 4 where the LES results from the FIRE stratocumulus experiment are compared with results from the single column climate model.

The semi-direct forcings in ATEX and BOMEX are outweighed by the negative direct forcings (shown in Table 3.2) so that the total aerosol forcings are negative. For the cumulus regime, the semi-direct effect is probably not as important as the direct effect, even for quite highly absorbing aerosols ($\omega = 0.88$). This contrasts starkly with results from chapter 2 that showed the semi-direct effect to be several times more important than the direct effect in determining the total radiative forcing. There are several reasons for this. Firstly, the semi-direct forcing was much higher, secondly, a much lower aerosol optical depth was used because the BL was much shallower. Thirdly, the direct effect was greater in magnitude (more negative) in the cumulus experiments because the aerosol lay mostly over dark sea. Thus, the relative importance of the direct effect also depends on the meteorological regime.

The ATEX experiment in this chapter is very similar to the LES study of Ackerman *et al.* (2000). The experimental setup and initial conditions were very similar, and the aerosol properties and distribution used are very similar to those used in this chapter. The aerosol optical depth and single scattering albedo used in their INDOEX-99 experiment are 0.4 and 0.88, respectively, the same as for the ATEX and BOMEX experiments. The aerosols also had a similar vertical distribution, being located mainly in the BL. Their experiment had very similar changes in cloud clover and LWP. For example the INDOEX-99 aerosol reduced the daytime cloud cover from about 20 to 10% , and the daytime LWP from around 15 to 5-10 g m^{-2} (see Table 3.1 to compare with our ATEX experiment).

Ackerman *et al.* (2000) do not actually calculate the semi-direct forcing in the way defined by this thesis but infer that it must be present because there is a positive radiative forcing despite a negative clear-sky

direct aerosol forcing. For example, there was a 4.5 W m^{-2} increase in TOA net radiation between the INDOEX-99 experiment ($\tau = 0.4, \omega = 0.88$) and the control, which had non-absorbing aerosols ($\omega = 1.00$), and a lower τ of 0.17. The clear-sky aerosol radiative forcing associated with this change in aerosol τ and ω was -3.0 W m^{-2}. The difference in cloudy and clear sky radiative forcings (7.5 W m^{-2}) is explained by the semi-direct effect, plus an unquantified change in direct aerosol radiative forcing between clear and cloudy skies. It is likely that the clouds would have increased the direct forcing of the aerosols by 2-3 W m^{-2} (based on offline calculations). Therefore, the semi-direct effect in Ackerman *et al.* (2000) INDOEX-99 experiment was probably a little less than 7.5 W m^{-2}. and definitely lower than in our ATEX experiment (8.0 W m^{-2}).

The difference is probably due to subtle differences in cloud dynamics resulting from differences in aspects of the model setup such as vertical resolution, or subgrid turbulence schemes, because Ackerman *et al.* (2000) used the same meteorological data, and very similar aerosols. Ackerman *et al.* (2000) noted that the semi-direct forcing was larger for high cloud droplet concentrations, where the clouds had a higher albedo for a given LWP. In addition they found a higher semi-direct effect for simulations that had a higher specific humidity in the free troposphere and higher cloud cover. This finding supports the main conclusion of this chapter: that meteorological conditions and cloud amounts are key in determining the semi-direct forcing.

CHAPTER 4

SCCM experiments

4.1 Introduction

Whilst high resolution models are crucial to develop our understanding of the semi-direct effect, estimating the global impact of the semi-direct effect essentially requires General Circulation Models (GCMs). These have played a major role in discerning the semi-direct aerosol effect and estimating its importance to global climate (Hansen *et al.* (1997), Lohmann and Feichter (2001), Jacobson (2002), Cook and Highwood (2003)). However, there is yet no consensus on the global impact of the semi-direct effect as these studies disagree on the strength of the effect (see section 1.5). Therefore, it is important to assess the performance of GCMs in producing a semi-direct effect, as compared with Large-Eddy Simulations (LES).

As shown in section 2.2.3, the semi-direct effect arises from subtle interactions between radiative heating, turbulent transports and entrainment processes. These were resolved explicitly in the LEM, but large-scale models can only deal with such interactions via the responses of their various physical parameterization schemes. It is well known that large-scale models have difficulties in representing stratocumulus layers (e.g. Bechtold *et al.* (1996), Duynkerke *et al.* (2000)). Small scale features such as the inversion are poorly resolved and small scale process such as cloud microphysical processes, cloud-top longwave cooling, turbulent mixing and cloud-top entrainment present a significant parameterization challenge (e.g. Grenier and Bretherton (2001)). Amongst GCMs there is a tendency to underestimate the fractional coverage and liquid water path (LWP) of marine stratocumulus (e.g. Chen and Roeckner (1997), Jakob (1999), Duynkerke and Teixeira (2001)). There is also a tendency to underestimate the diurnal cycle of LWP. This shows that the modelled clouds in GCMs do not respond sufficiently to solar heating, and indicates that GCMs may underestimate the semi-direct effect of absorbing aerosols in the Boundary Layer (BL).

The main questions addressed in this chapter are:

- Can GCMs produce a realistic cloud response to absorbing aerosols, as compared with the re-

sponse in a high resolution model?

- Do estimates of the semi-direct forcing from GCMs agree with those from the LEM?

- What possible reasons are there for disagreement between different GCMs?

- What could be done to improve the cloud response in GCMs?

This chapter presents simulations of marine stratocumulus, with the Single column Community Climate Model (SCCM) of the National Center for Atmospheric Research (NCAR) and compares them with the LEM simulations from chapter 2. The advantages of single column models over GCMs is that they are quick to run and easy to interpret. A single column in isolated and the influence of the large-scale dynamics are represented through mean forcing terms. This allows a straightforward examination of interactions between various physical parameterizations the influence of the large-scale environment. The disadvantage of using a single column model is that there are no large-scale dynamical feedbacks, and no variability in the large-scale flow.

The SCCM was chosen because it uses relatively simple, but well established parameterizations and reflects many of the common aspects of contemporary GCMs (see Appendix B for an outline of the SCCM and its parameterizations). The SCCM and supporting software are available on the internet (www.cgd.ucar.edu/cms/sccm/sccm.html) and provided an ideal research tool for the experiments in this chapter.

In this chapter the SCCM has been used to simulate marine stratocumulus and the evaluate the semi-direct forcing of absorbing aerosols in the BL. The results are then analysed and compared with LEM results from chapter 2.

4.2 Experimental setup

The marine stratocumulus simulations in this chapter are based on the observations of FIRE (see section 2.1.3). The initial conditions, geostrophic winds, boundary conditions, and large-scale forcings are the same as those used in the LEM experiments of chapter 2. Details are found in section 2.2.1. The SCCM has been run with the standard vertical grid that has 30 atmospheric layer, eight of which are in the lowest 2000 m, and four of which are in the lowest 650 m. Climate simulations typically use fewer layers, around 18. Increasingly though, regional climate simulations are using the same resolution as would be used in global forecast models (around 30 levels). Only changes in the BL are of interest, the

free troposphere is essentially a constant external. Therefore, the temperature, humidity and winds in the upper 23 layers are relaxed to the initial condition with a time-scale of 3 hours.

Aerosols are placed in the lowest 4 model levels, from the surface to 650 m. As was the case in the LEM experiments, the aerosols are a dry external mixture of soot and ammonium sulphate. The mass mixing ratio is set to 3×10^{-8} kg kg^{-1}, and the soot to ammonium sulphate ratio is set to give a single scattering albedo (ω) of 0.88 at 550 nm, as in the LEM experiments (see table 2.2, in section 2.2.1, page 38). The aerosol optical depth in the SCCM experiments was a little lower than in the LEM experiments (0.13 compared to 0.15) because the aerosol mass mixing ratio went straight to zero at the top of the BL (650 m) in the SCCM experiments, whereas in the LEM experiments the aerosol mass mixing ratio decreased linearly with height between 600 and 900 m. Reproducing the exact same aerosol vertical distribution was not possible with the limited vertical resolution.

The simulations are started 1 July 0000 h (local time) at latitude 32.1^{o}N, and run for 20 days with a model time step of 1200 s. After the first 3-4 days of simulation the model fields follow a periodic diurnal cycle with no discernible long term trends or inter-day variability. However, to minimise any bias from such variability the results from the final 10 days of the simulation (10-20 July) are composited to obtain average diurnally varying fields. The SCCM experiments are compared with the average diurnally varying fields from the final 5 days of the ten-day long LEM experiments control-10 and A-088-10 (see section 2.2.6).

4.3 Representation of the BL structure and cloud properties

The SCCM reproduces the basic features of the SCBL: a well-mixed layer cloud-topped BL beneath a strong low-level potential temperature inversion (Fig. 4.1 (a)). However, the inversion, cloud top, and cloud base are poorly resolved as the vertical grid spacing is too coarse ($\sim$ 200 m, see Table 4.1). The lack of sufficient vertical resolution means that potential temperature and moisture gradients across the inversion are far too low compared with observations LEM simulations (Fig. 4.1 (a) & (b)). Also, the specific humidity in the BL, and the cloud liquid water content (Fig. 4.1 (c)) are much lower than in the LEM. The cloud layer is also slightly cooler than in the LEM, so that despite a lower specific humidity, the RH is sufficiently high for the formation of a cloud layer (Fig. 4.1 (c) & (d)).

The SCCM simulations produce three different types of cloud, large-scale low cloud, stratus and shallow moist convective cloud. Each cloud type is controlled by a different scheme (see section B.2). The
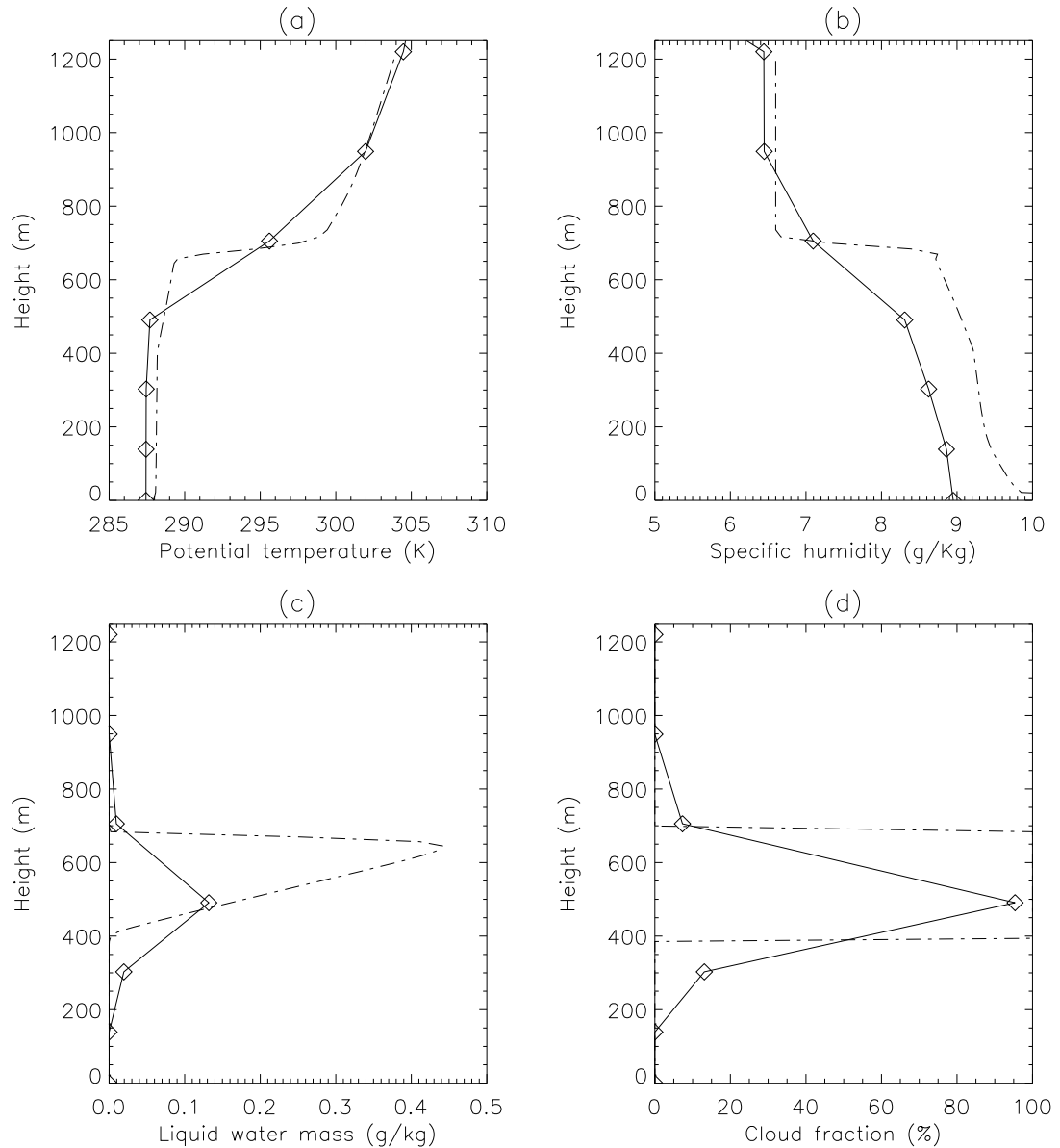
Figure 4.1: *Diurnal mean (a) potential temperature, (b) specific humidity, (c) liquid water content, and (d) cloud fraction, as a function of height for the SCCM control simulation (solid line with diamonds, which indicate vertical resolution) and the LEM simulation (dot-dash line). SCCM results are averaged over the final 10 days of the 20-day experiment. LEM results are averaged over the final 5 days of the 10-day experiment*

dominant cloud type produced in the simulation is stratus. This forms in level 4, below the inversion (Fig. 4.1 (d), and Table 4.1) and has the maximum possible cloud fraction allowed by the scheme (95%). The criterion for maximum stratus coverage are that the magnitude of potential temperature gradient in the layer above exceeds 0.25 K mb^{-1}, that the pressure of the stratus level is above 900 mb, and that the RH in the layer below the stratus (level 3) remains above 90% (the dependence of stratus

Level	Height range (m)	Mean cloud fraction	Dominant cloud scheme
1	0-130	0	
2	130-280	0	
3	280-460	0.13	Large-scale low cloud
4	460-650	0.95	Low-level stratus
5	650-890	0.07	Shallow moist convection
6	890-1140	0	
7	1140-1460	0	
8	1460-2030	0	

Table 4.1: *SCCM vertical grid spacing, mean cloud fraction, and dominant cloud schemes in the lowest 8 model levels, in the SCCM control simulation.*

fraction on relative humidity is shown in Fig. 4.2). Since these criterion are met almost continually, the cloud fraction at this level is essentially specified at the maximum value of 0.95. Large-scale low cloud forms if the relative humidity (RH) exceeds 90% , and the cloud fraction is a quadratic function of RH (see Fig 4.2). Some large-scale cloud forms in level 3 (280 - 460 m) (Fig. 4.1), as the RH at that level remains above 90% for most of the time (Fig. 4.5).
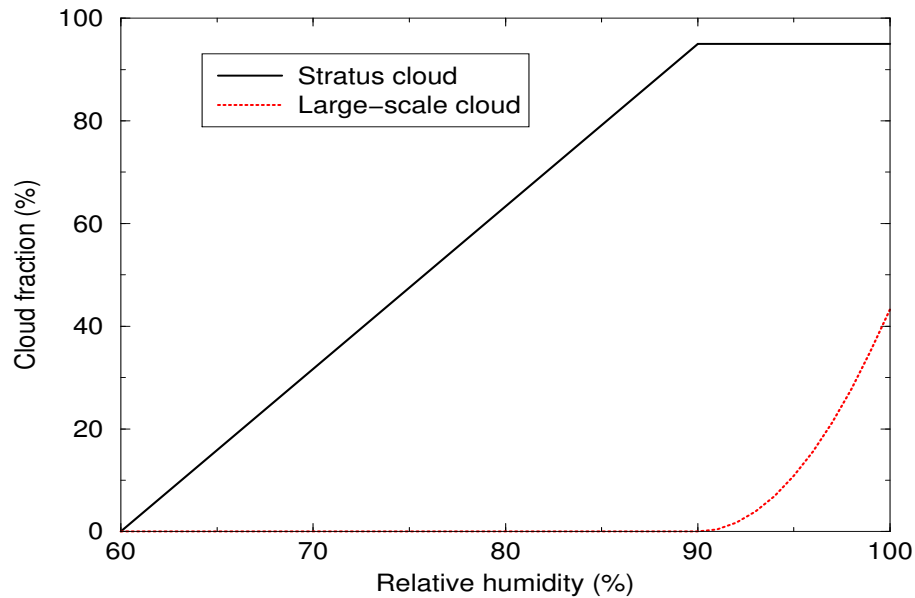
Figure 4.2: *Dependence of stratus, and large-scale cloud fraction on relative humidity (in level 3) in the SCCM simulation. Note that the large-scale cloud fraction at 100% relative humidity is only 43%(not 100%), because of the additional dependence on the subsidence rate. For zero or negative subsidence large-scale cloud fraction would reach 100% at 100% relative humidity (see section B.2).*

There is also some cloud in the inversion layer (level 5) (Fig. 4.1, and Table 4.1), associated with shallow moist convection. The presence of cloud at this level is somewhat unphysical, as the grid-box average RH is only as 55 %. This shallow moist convection scheme is triggered by instability in the BL resulting from longwave cooling in the cloud layer (Fig. 4.3) and gentle surface sensible and latent heat fluxes (Fig. 4.4). The shallow moist convection scheme is based on a simple model for non-entraining cumulus convection (see section B.4). In this simulation it operates across levels 3-5 transporting latent heat vertically at a rate of 20 W m^{-2}, and mixing the potential temperature across the region. This resembles the action of buoyant cumulus plumes rising through the BL, penetrating the inversion and detraining. In reality any convective elements in the SCBL would be strongly capped by the inversion. However, the lack of sufficient vertical resolution means that there is an overlap between the convective cloud and the inversion. Again, this illustrates how problems can arise from poor vertical resolution.
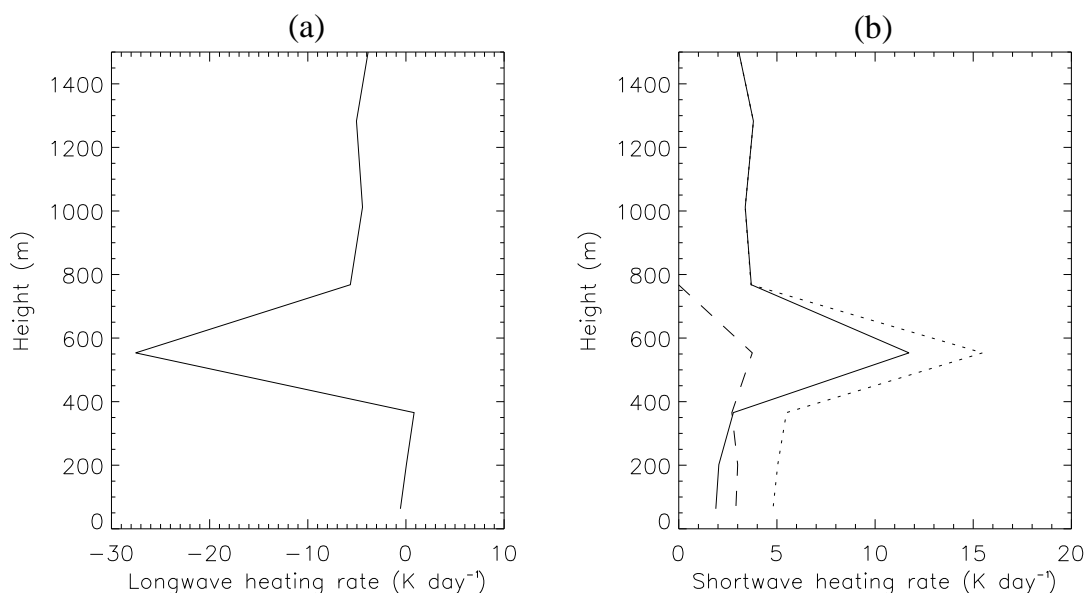
Figure 4.3: *(a) Diurnal average longwave heating rate in the SCCM control simulation. (b) Shortwave heating rate at 1200 h in the SCCM control simulation (solid line), aerosol simulation (dotted line), and the difference, which is the aerosol heating rate (dashed line).*

The SCCM predicts a relatively low LWP ($\sim$ 40 g m^{-2}) compared to observations (e.g. Duynkerke and Hignett (1993), Blaskovic *et al.* (1991)), and compared to the LEM (Fig 4.4 (a)). This problem is mainly due to the way that liquid water content is diagnosed in the SCCM. The liquid water in any given layer is proportional to the cloud fraction, multiplied by an empirical function that varies mainly with height (see section B.2). The liquid water content is independent of cloud depth, and only reaches 0.15 g kg^{-1} in layer 4 in these simulations (see Fig. 4.1 (c)). In contrast, observations and
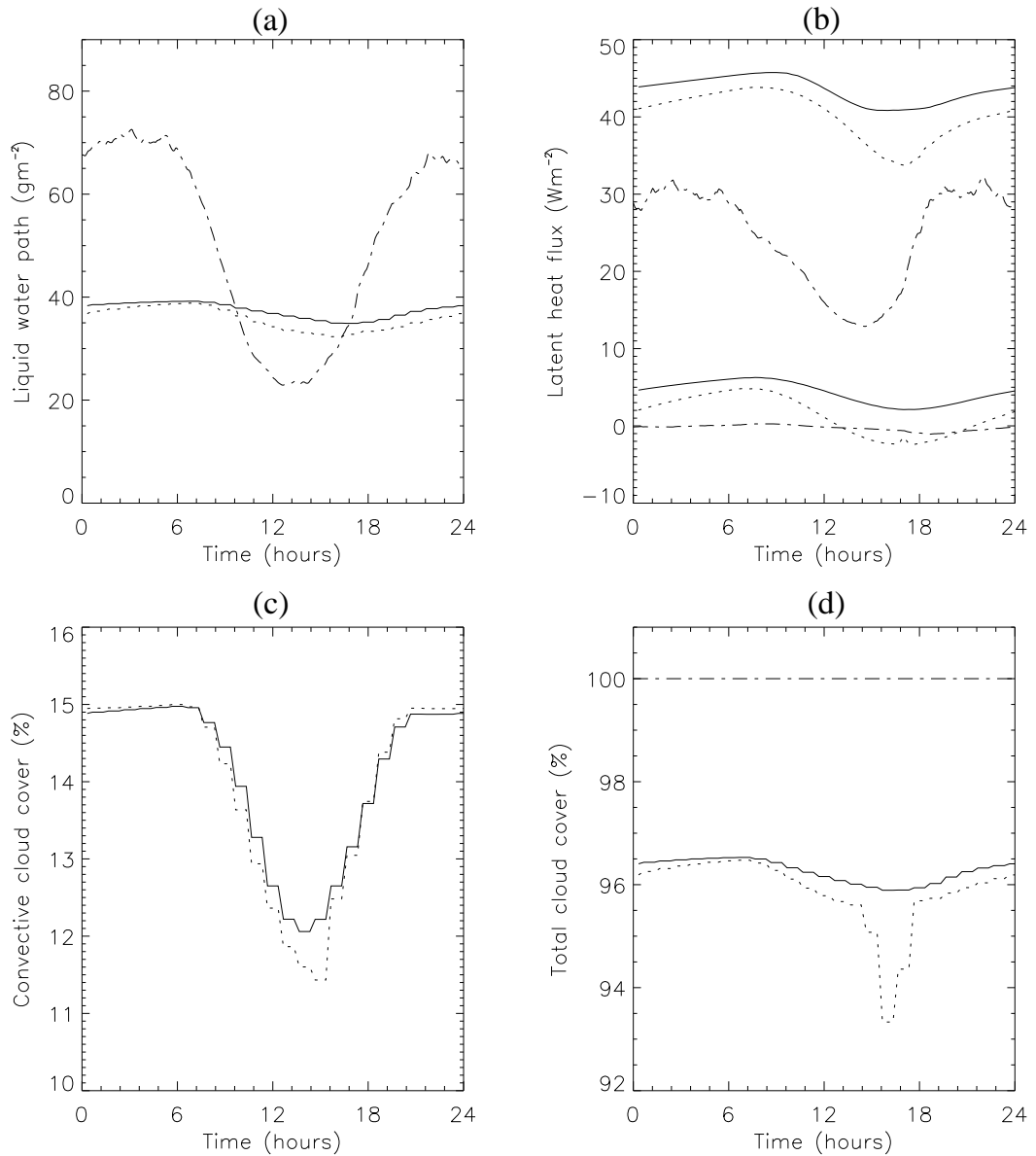
Figure 4.4: *(a) Liquid water path (g m^{-2}), (b) surface latent heat flux (upper lines) and surface sensible heat flux (lower lines) (W m^{-2}), (c) Convective cloud cover (%), and (d) total cloud cover (%) in the SCCM control simulation (solid line), aerosol simulation (dotted line), and LEM control simulation (dot-dashed line).*

LES of stratocumulus (Fig. 4.1) show that liquid water content increases almost linearly with height, at approximately the adiabatic rate (assuming that total water and liquid water potential temperature are constant in the cloud layer). If the liquid water content increases linearly with height from cloud base to cloud top then the LWP will vary as the square of the cloud thickness. However, in the SCCM the LWP is linearly proportional to the cloud thickness. This will lead to an underestimate of the LWP for thick stratocumulus cloud layers and an underestimate of of the LWP variability.

Heat and moisture fluxes between the surface and the cloud layer are well accounted for in the SCCM. Mean surface latent and sensible heat fluxes agree reasonably with the LEM (Fig. 4.4 (b)), and the non-local mixing scheme maintains the well-mixed state of BL. Turbulent transfers in the cloud layer are dominated by the shallow moist convection scheme. The convection scheme also leads to mixing across the between the BL and the free troposphere, which implicitly accounts for the fluxes associated with entrainment. However, this is not really an adequate representation of the turbulent process that occur at the BL top, and it leads to problems such as the smoothing of potential temperature and moisture gradients between the BL and free troposphere, and the existence of cloud in the inversion layer. In reality, entrainment occurs over a layer a few tens of metres thick around the cloud top, and maintains the potential temperature and humidity gradients across the inversion.

4.4   Diurnal variation of BL properties and clouds

The temperature in the BL varies by about 1K between dawn and late afternoon (Fig. 4.5), in reasonable agreement with the LEM (Fig. 2.17 (a), section 2.2.2, page 43). However, the SCCM does not reproduce the internal stratification, or decoupling in the BL shown by the LEM. Rather, the BL potential temperature profile becomes less stratified during the day. It is not clear why this is so. Certainly, the SCCM does not resolve the vertical distribution of longwave and shortwave heating rates in the cloud. For example the cloud base longwave warming is not resolved (Fig. 4.3 (a)), and it is not possible for the SCCM to simulate the influence that this has on decoupling. Since there is no decoupling, the expected daytime drying of the cloud layer is not observed in the model (Fig. 4.5 (a)).

Cloud amount and LWP vary very little on the diurnal timescale (Fig. 4.4 (a) & (d)), despite the increases in temperature, and a decreases in RH (Fig. 4.5 (a) & (c)). In the control simulation LWP varies by only 5 g m^{-2}, compared to 50-60 g m^{-2} in the LEM simulation. The main reason for the low variability in LWP is that the fractional coverage of stratus cloud in the layer beneath the inversion (level 4) is essentially fixed at the specified maximum of 95 % because there is no dependence on RH until it falls below the threshold, 90 % (Fig 4.2). RH drops below this threshold only in the aerosol simulation, between 1400 and 1800h, leading a sudden dip in the total cloud fraction from 96 % to 93 % (Fig. 4.4 (d)). Otherwise the fractional coverage and liquid water content in level 4 do not vary.

Most of the diurnal variation of LWP in the simulation is driven by variation in the fractional coverage of large-scale cloud, which only forms in level 3 (table 4.1). The large-scale cloud fraction varies between 5 and 18 % in the control simulation and between 0 and 17% in the absorbing aerosol simulation.
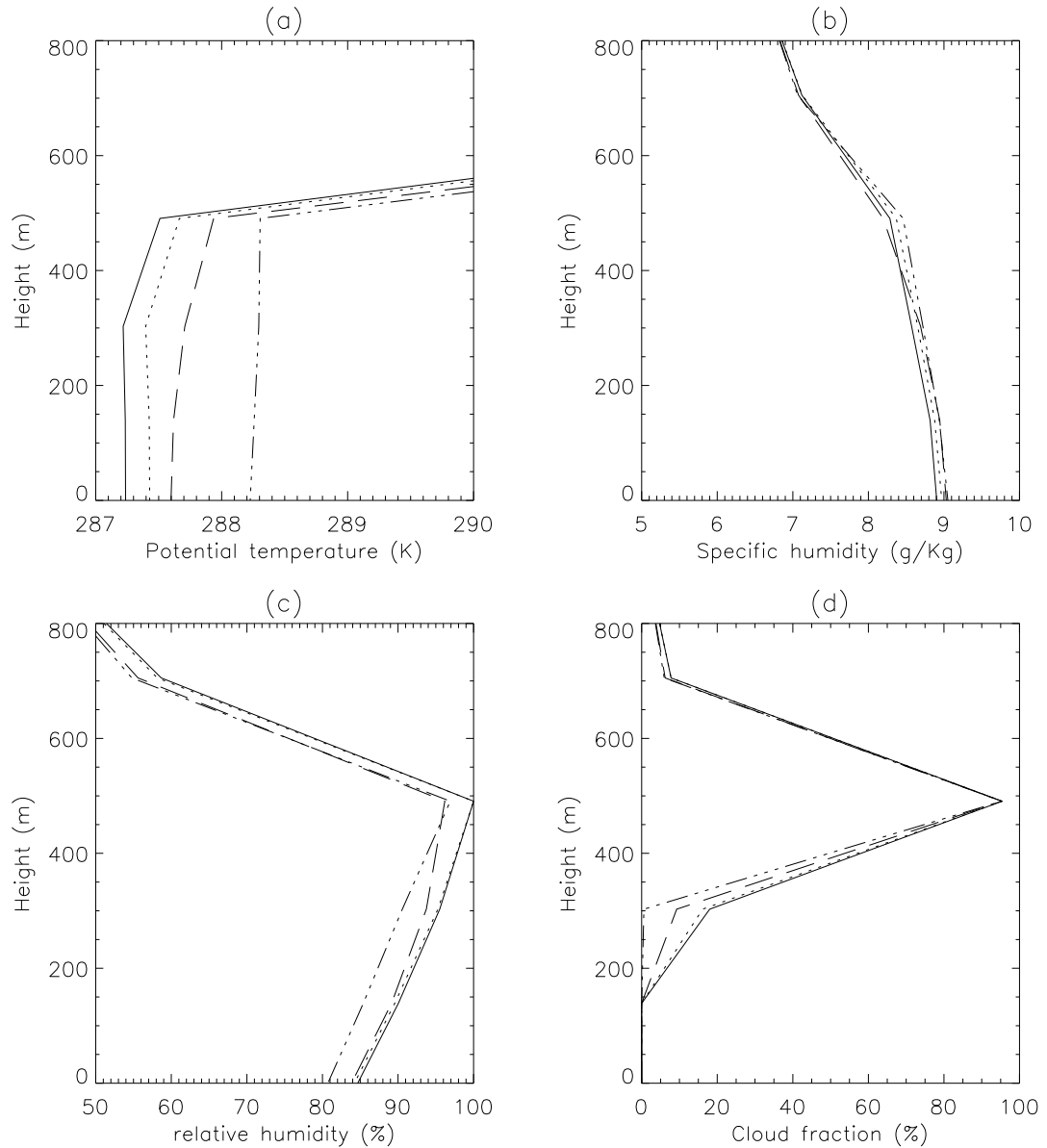
Figure 4.5: *(a) Potential temperature, (b) specific humidity, (c) relative humidity, and (d) cloud fraction as a function of height in the SCCM control simulation at 0500 h (solid line) and 1400 h (dashed line), and in the SCCM aerosol simulation at 0500 h (dotted line) and 1400 h (dot-dot-dashed line).*

The additional solar heating leads to the complete disappearance of this cloud for a few hours in the afternoon (Fig. 4.5 (d)).

The model also gives rise to convective cloud in levels 4 and 5. The convective cloud fraction reduces during the daytime (Fig. 4.4 (b)) as solar heating in the cloud reduces the generation of convective instability in the BL. The suppression of convection contributes only a little to the overall variability in total cloud cover and LWP because most of the convective cloud is in layer 4 and overlaps with

the stratus cloud (see Table 4.1). When different cloud types overlap in the same layer the LWP does not change because the LWP depends on the total cloud fraction in that layer. Thus, very little of the daytime reduction of total cloud cover and LWP is explained by changes in convective cloud fraction. In fact, the reduction in convective activity allows moisture to accumulate in the BL, so actually enhances the RH and large-scale cloud fraction. This subtracts from the diurnal variability of LWP.

4.5   Semi-direct radiative forcing
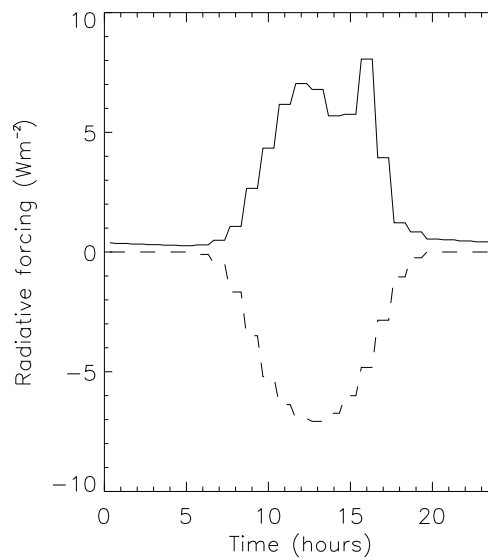
Figure 4.6: *Semi-direct (solid line) and direct (dashed line) aerosol radiative forcing (W m^{-2}) as a function of time (hours), averaged over the last 10 days of the experiment.*

The semi-direct forcing is calculated by the same method as that used for the LEM experiments: the semi-direct forcing is the total forcing minus the direct forcing. The total radiative forcing is the difference is net radiative flux at the top of the atmosphere between the aerosol and control simulations. The direct forcing is calculated within the aerosol simulation by running the radiation scheme an additional time with identical cloud properties but without aerosols.

The mean semi-direct forcing (integrated over the ten-day experimental period) is 2.5 W m^{-2}; this is several times smaller than the forcing from the LEM, which was around 15 W m^{-2} for the equivalent experiment (Table 2.3, section 2.2.4, page 50). This is because the cloud response to the absorbing aerosols is much smaller in the SCCM. For example, the difference in LWP between the aerosol and

control simulation at 1200 h is only 3 g m^{-2}, whereas it was reduced by about 10 g m^{-2} at that time in the LEM experiment (Fig. 4.4 (a)).

The pattern of semi-direct forcing over the day has two features: a broad peak centered around 1200 h and a second, narrower peak around 1600 h (Fig. 4.6). The biggest contribution to the mean semi-direct forcing comes from the broad peak, which is related to the decrease in the fractional coverage of large-scale cloud in level 3 (Fig. 4.4 (d)). This is the main contributor to the daytime decrease in LWP (Fig. 4.4 (a)), although there is not much change in total cloud fraction (Fig. 4.4 (d)) because most of the large-scale cloud overlaps with the stratus cloud. The secondary peak at 1600 h is related to the sharp fall in stratus cloud cover in the aerosol simulation, between 1400 and 1800 h. This leads to a dip in total cloud fraction in the afternoon (Fig. 4.4 (d)), allowing more solar radiation through to the surface. A small contribution to the semi-direct forcing also comes from the reduction in convective cloud fraction in the afternoon (Fig. 4.4 (c)). Thus, the fractional coverage of large-scale cloud in level 3, and stratus in level 4 are the key contributors to the semi-direct forcing. Both of these are controlled by the RH in level 3. The functional relationships are shown in Fig. 4.2.

4.6 Sensitivity of semi-direct forcing to experimental set up

Further experiments show that the mean semi-direct forcing is sensitive to aspects of the experimental set-up, especially those that influence the mean RH. Tables 4.2 and 4.3 show the variation of mean semi-direct forcing with the specific humidity above the inversion (levels 6 and 7, 900 - 1500m), and with the large-scale moisture tendency. Also, shown is the mean RH in level 3 (280 - 460 m), because this was found to be the key variable controlling the magnitude of the semi-direct forcing in the SCCM experiments (see paragraph above). It is interesting to note that either increasing, or decreasing moisture from original levels can lead to a higher semi-direct forcing in the simulations.

For example, increasing the specific humidity in the lower troposphere by 1 g kg^{-1} (from 6.6 to 7.7 g kg^{-1}), leads to an increase in the mean semi-direct forcing from 2.5 to 3.7 W m^{-2}(Table. 4.2). In the moister simulation (with a specific humidity of 7.7 g kg^{-1} in levels 6 and 7) the mean RH was about 1% higher in level 3, but the daytime reduction of RH due to aerosols was about the same as in the experiment with the standard experiment (with 6.6 g kg^{-1} specific humidity in levels 6 and 7). However, there was a bigger change in the large-scale cloud fraction in the moister experiment, essentially because the relationship between RH and large-scale cloud fraction is quadratic (Fig. 4.2), and gives a non-linear response.

Humidity in levels 6 and 7 (g kg^{-1})	Mean RH (%) in level 3 Control simulation	Mean RH (%) in level 3 Aerosol simulation	Semi-direct forcing (W m^{-2})
3.6	92.4	91.2	3.6
4.6	93.2	91.9	2.6
5.6	93.9	92.6	2.0
6.6 (standard)	95.3	93.1	2.5
7.6	95.8	93.9	3.7

Table 4.2: *Variation of the 10-day mean relative humidity (%) in level 3, and semi-direct forcing (W m^{-2}) with specific humidity in the lower troposphere (levels 6 and 7) (g kg^{-1})*

Moisture tendency (g kg^{-1}day^{-1})	Mean RH (%) in level 3 Control simulation	Mean RH (%) in level 3 Aerosol simulation	Semi-direct forcing (W m^{-2})
1	96.3	95.4	4.6
0.5	96.6	94.6	3.9
0	95.3	93.1	2.5
-0.5	93.2	91.8	2.7
-1.0	91.7	90.3	5.5
-1.5	90.2	88.0	9.2
-2.0	88.0	97.5	4.6

Table 4.3: *Variation of the 10-day mean relative humidity (%) in level 3, and the semi-direct forcing (W m^{-2}) with large-scale moisture tendency (g kg^{-1} day^{-1})*

Decreasing the specific humidity in the lower troposphere to 3.6 g kg^{-1} gives a mean semi-direct forcing of 3.6 W m^{-2} (Table. 4.2). This is because RH dropped significantly below 90% in the aerosol simulation during the afternoon, leading to a much greater reduction of stratus cloud fraction than in the standard experiment. The semi-direct forcing was lowest for a lower tropospheric humidity of 5.6 g kg^{-1}, where the mean RH in level 3 is around 92% (Table. 4.2) and both types of cloud response are small.

The semi-direct forcing was even more sensitive to changes in the large-scale moisture tendency. For example, applying a drying rate of 1.5 g kg^{-1} day^{-1} led to a mean semi-direct forcing of 9.2 W m^{-2} (Table. 4.3). Interestingly, increasing the drying rate further, to 2 g kg^{-1}, brings the mean semi-direct forcing back down to 4.6 W m^{-2}. In that simulation the moisture fluxes were unable to support the BL to that depth and the inversion switched down to level 4. The stratus cloud was then in level 3, and the large-scale cloud in level 2. This meant that the cloud fraction varied mainly with RH in level 2, and this happened to be quite high and the semi-direct forcing was the same as for a large-scale moistening of 1 g kg^{-1} day^{-1} (Table 4.3).

Increasing the subsidence rate by 40% also caused the inversion to drop down one level, and had a similar effect. Decreasing the subsidence rate by 20% lead to the inversion and cloud layers shifting up one level but RH in the level below the inversion was quite low and the semi-direct forcing was high. Thus, the vertical movement of the inversion between levels leads to abrupt changes in the semi-direct forcing. None of these sensitivities are actually physical. They are an artifact of the discontinuous and non-linear nature of the relative humidity to cloud fraction relationships in the model (see Fig. 4.2), and the low vertical resolution. This indicates that improvements are necessary to obtain a more reliable prediction of the semi-direct forcing. Improvements may include changes to the model physics, and the cloud scheme, or an increase in vertical resolution.

A further experiment was carried out with a deeper BL and higher sea surface temperature, typical of trade cumulus conditions (same set up as in the ATEX experiment in chapter 3). This gave a larger forcing of 8 W m^{-2} because there were a greater number of levels with large-scale cloud that responded to daytime reductions of relative humidity. Although the semi-direct forcing actually matches the result from the ATEX experiment with the LEM (see section 3.5.5) the cloud responses that produced the semi-direct forcing in the SCCM experiment are very different from the cloud responses that produced the semi-direct forcing in the LEM experiment. In the LEM the semi-direct forcing was produced mainly by changes in the amount of cloud immediately below the inversion, and through changes in the intensity of convection. These response were not reproduced in the SCCM, cloud fraction immediately

below the inversion was almost fixed (as in the standard stratocumulus experiment described above), and there were modest changes in cloud fraction (a few %) in the 2 - 3 levels below. Thus, in the cumulus experiment, the semi-direct effect was misrepresented in the SCCM even though the semi-direct forcing agreed with LEM results. Furthermore, the sensitivity of the semi-direct forcing to meteorological conditions has the opposite sense to the sensitivity shown by the LEM. In the LEM experiments the semi-direct forcing was lower in the cumulus cases than in the stratocumulus cases, but in the SCCM the opposite was true.

4.7 Sensitivity of the semi-direct forcing to an increase in vertical resolution

The main aim of this section is to establish whether increasing the vertical resolution is beneficial in simulating BL processes and in predicting the semi-direct forcing. The previous section showed that serious improvements in the representation of the BL system were necessary for the SCCM to produce a realistic response to aerosol heating. Some of the problems with the SCCM simulation in the previous sections were related to insufficient resolution, whereas some were related to limitations of the parameterizations. With only 6 levels in the lowest 1200 m the vertical structure of the BL was poorly resolved. The inversion was too broad and the internal stratification (decoupling) was not captured. This lead to too much mixing across the inversion and an underestimate in the diurnal cycle in the BL. However, problems such as the underestimation of LWP variability were related to the inflexibility of the stratus parameterization.

Another particular problem associated with low resolution was that vertical structure of radiative heating in the cloud layer could not be represented. The intense longwave cooling at cloud top has an important role in producing BL turbulence. The shortwave heating falls off more slow with decreasing height from cloud top, and there is gentle longwave warming at the cloud base. The sum of the longwave and shortwave heating rates is an overall warming of mid and lower parts of the cloud but intense cooling at the top. It is this heating structure that tends to constrain mixing to the cloud layer and decouple the BL. Several levels would be required to represent this structure but in the SCCM simulations above there was only one level for the main body of the cloud.

The standard resolution SCCM simulation has been repeated with approximately 3 times the vertical resolution. The enhanced grid has 20 levels below 1200 m and a vertical spacing of $\sim$ 50 m in the BL.

The grid spacing above the BL increases rapidly with height, converging to the original grid spacing in the mid troposphere. In total there are 50 levels. The SCCM was run once with the absorbing aerosols, and once without, and the semi-direct forcing is evaluated.

Results
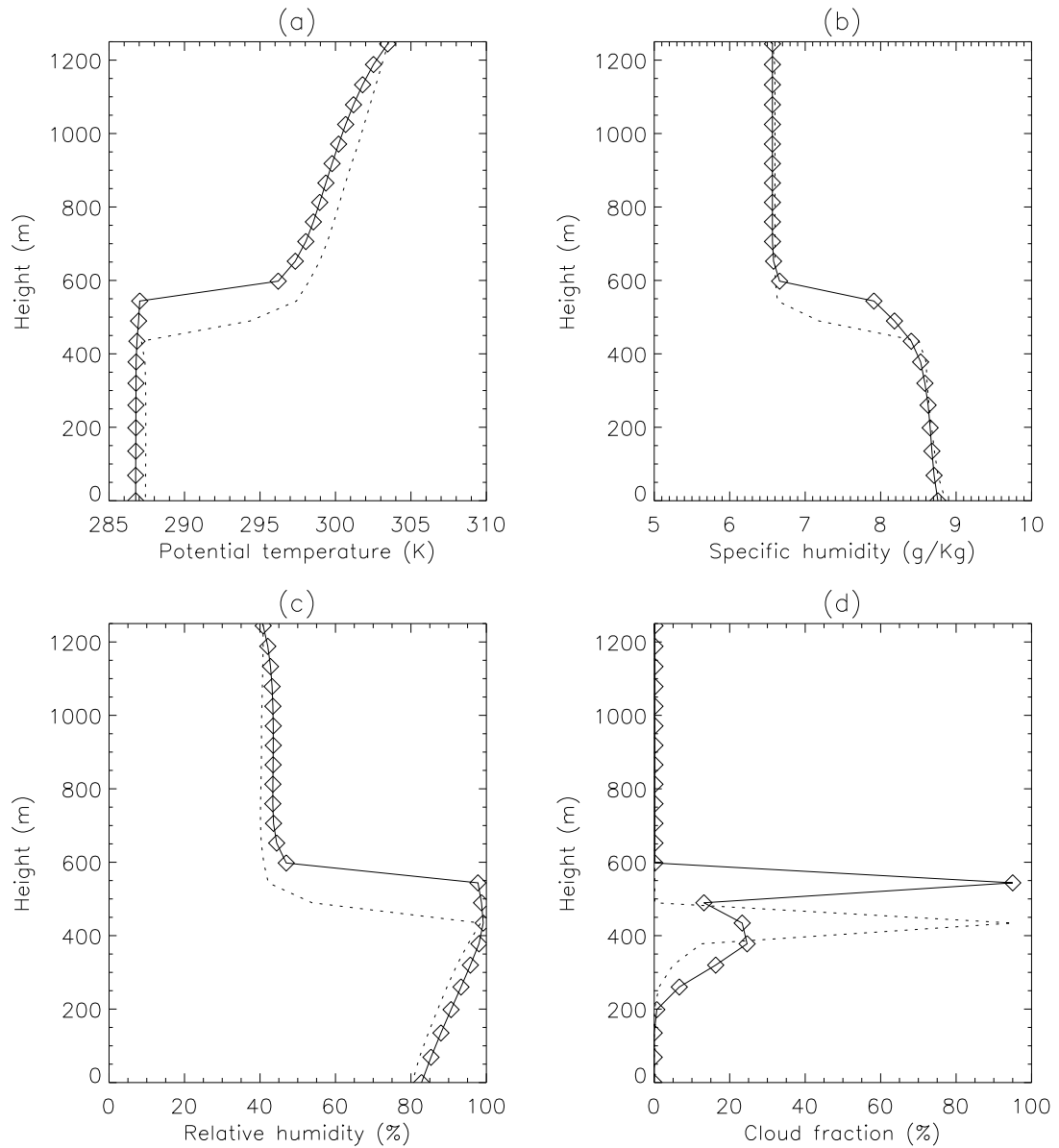
Figure 4.7: *Ten day means of (a) potential temperature (K), (b) specific humidity (g kg^{-1}), (c) relative humidity (%), and (d) cloud fraction (%), as a function of height in the high resolution SCCM control simulation (solid line), and aerosol simulation (dotted line).*

Increasing the resolution does tighten up the inversion (Fig. 4.7 (a)) and constrain the vertical extent of the mixing so that there is a strong hydrolapse across the inversion (compare Fig. 4.7 (a) & (c)
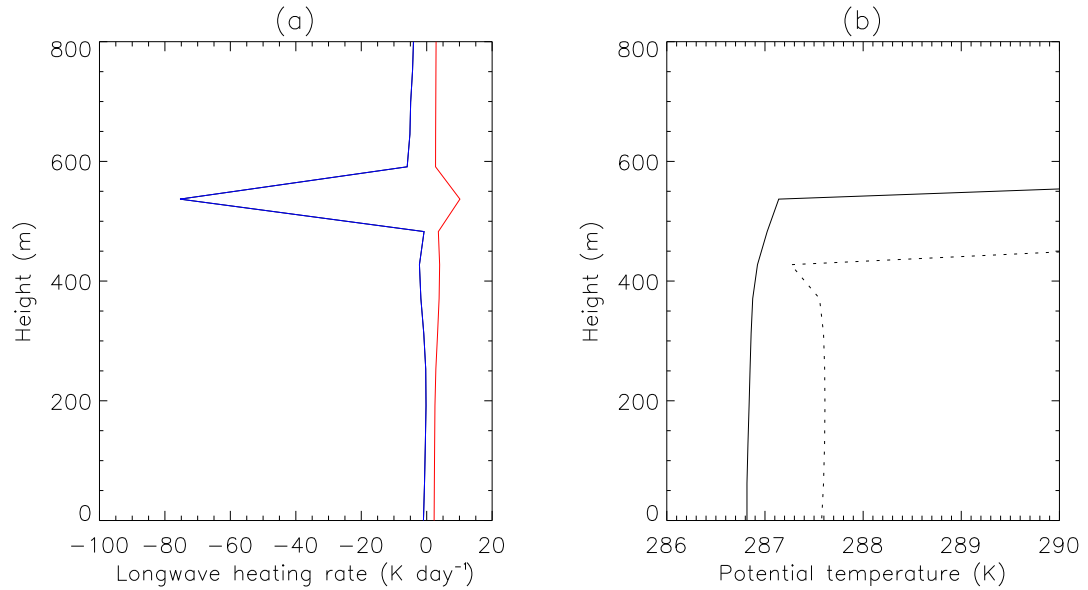
Figure 4.8: *(a) Longwave (blue) and shortwave (red) radiative heating rates (K day^{-1}) in the high resolution SCCM control simulation at 1200 h local time. (b) Potential temperature (K) at 1200 h local time in the high resolution control simulation (solid line), and aerosol simulation (dotted line).*

with Fig. 4.5 (a) & (b)). The longwave cooling at cloud top is also much more sharply resolved than before (compare Fig. 4.8 with Fig. 4.3). However, there is still no longwave warming at the cloud base (Fig. 4.8 (a)). This could be because the cloud fraction increases gradually with height in the BL (Fig. 4.7 (a)) so that upwelling longwave from the surface is gradually absorbed. In contrast, there is a well defined transition from clear sky to cloud in the LEM and a notable longwave warming in the lowest 100 m of the cloud (see Figs. 2.12 & 2.19 (a)). The moist thermodynamic structure of the BL is still no closer to that given by the LEM. The low bias in water vapour mixing ratio remains (Fig. 4.7 (c)), and the BL structure in the daytime does not reflect any tendency for decoupling (Fig. 4.7 (a)). Furthermore, the thermodynamic structure is quite different in the aerosol simulation; it is internally less stratified, with a dip in temperature in the highest cloud level (Fig. 4.7 (b)). This is not consistent with the LEM results (compare dotted line in Fig. 4.7 (b) with the dot-dash line in Fig. 4.1 (a)).

The stratus layer is still only in one level (Fig. 4.7 (d)), as determined by the parameterization. However, the thickness of the stratus layer has been reduced to a third, following the increase in vertical resolution. There is some cloud below the stratus (200 - 500 m) produced by the large-scale cloud parameterization but the fractional coverage is only 25% , or less (Fig. 4.7 (d)). The large-scale cloud fraction is limited by the dependence on subsidence rate (see section B.2). The subsidence rate increases linearly with height (as specified in the experimental set up), which has the effect of almost
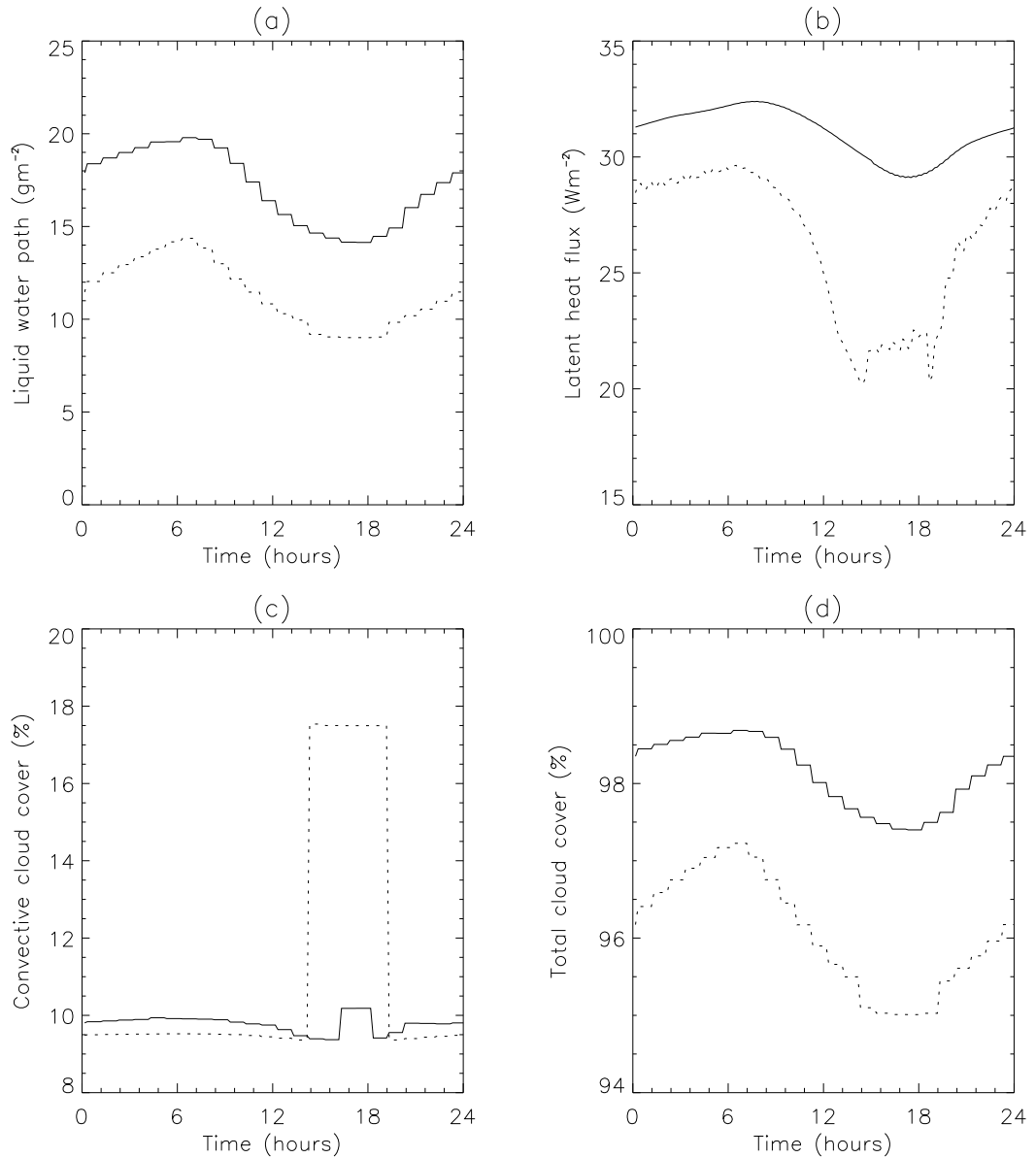
Figure 4.9: *Ten day average (a) Liquid water path (g m^{-2}), (b) surface latent heat flux (W m^{-2}), (c) convective cloud fraction, and (d) total cloud fraction (%), as a function of local time (hours), in the control simulation (solid line), and aerosol simulation (dotted line).*

preventing the possibility of large-scale cloud formation in the upper part of the BL. Also, the potential cloud fraction falls quite rapidly with relative humidity from 100% to 90%, as shown in Fig. 4.2, which explains why the cloud fraction decreases with decreasing height below 400 m (Fig. 4.7 (d)).

Thus, increasing the vertical resolution led to a thinner cloud layer and a lower LWP (15 - 20 g m^{-2}) (Fig. 4.9 (a)) than in the standard resolution simulation (35 - 40 g m^{-2}), and a much lower than in the LEM simulation (20 - 70 g m^{-2}) (compare Fig. 4.9 (a) with Fig. 4.4 (a)). The very low diurnal

variation in LWP remains a problem, as before. In the high resolution aerosol simulation the LWP is even lower (on average 5.5 g m^{-2} lower than in the high resolution control) because of the lack of large-scale cloud beneath the stratus layer (Fig. 4.7 (d)). There are two reasons for this: Firstly the relative humidity below the stratus layer (> 400 m) is slightly lower in the aerosol simulation (Fig. 4.7 (c)) because of the aerosol heating (Fig. 4.7 (b)). Secondly, the inversion has shifted down by two levels (~ 110 m), limiting the potential number of levels with cloud (Fig. 4.7 (a)).

The collapse in the BL depth is linked to the suppression of surface moisture fluxes (Fig. 4.9 (b)), caused by the stabilising influence of aerosols in the BL. Essentially, in the long term, the surface moisture flux must balance the drying related to subsidence to close the moisture budget. The subsidence rate increases linearly with height (as specified by the experimental set up) so if moisture fluxes decrease then the inversion height must decrease to maintain the balance. Although this is physically realistic, the reduction (~ 110 m) is a bit excessive. The ten-day long LEM experiment shows a 70 m reduction of cloud-top height between the control and aerosol simulation (see Fig. 2.26 in section 2.2.6.1).

No such shift occurred in the low resolution simulation (see Fig. 4.5 (a)); the resolution was probably too coarse (~ 150 m) to allow it. Instead, to maintain the moisture budget the reduction of surface moisture fluxes was balanced by a decline in convective mass flux (Fig. 4.4 (c)), as the shallow convection scheme tended to remove moisture from the BL. Thus, increasing the vertical resolution has led to a very different response, a response that involves a greater reduction of total cloud fraction and LWP (compare Figs. 4.9 (a) & (d) with Figs. 4.4 (a) & (b)). The result is that the higher resolution simulation gives a greater semi-direct forcing. The ten-day mean semi-direct forcing was 8.7 W m^{-2}, considerably higher than in the standard resolution simulation (2.5 W m^{-2}, see section 4.5), but still only about 60% of the semi-direct forcing in the equivalent LEM experiment (~ 15 W m^{-2}, see Table 2.3, section 2.2.4, page 50)).

On that basis, it could be stated that the higher resolution simulation gave a more accurate estimate of the semi-direct effect. However, the higher resolution simulations do not seem any more realistic than the low resolution simulations. As shown above, the underestimation of LWP has actually got worse, and the model still does not represent the decoupling of the BL, despite improvements in the vertical structure of radiative heating. Furthermore, there is a step increase in convective cloud fraction from 9.5 to 17.5% between 1330 and 1900 h (Fig. 4.4 (d)). Whilst discontinuities such as this are generally unphysical, the result is also contrary to the result in the low resolution experiment. In the low resolution simulation aerosol heating suppressed the shallow convection scheme during the

daytime. The convective cloud is not actually very important to the semi-direct forcing because it mostly overlaps the stratus cloud, thereby having very little effect on the calculated total cloud fraction or LWP. Nevertheless, the sudden increase of convective cloud in the high resolution aerosol simulation does not seem to make any physical sense and is a warning that the behaviour of the model is sometimes simply an artifact of the discretization or parameterization of continuous features or processes.

Finally, in the high resolution experiment the semi-direct forcing is still driven through changes in the fractional coverage produced by the large-scale cloud parameterization. In the LEM the cloud was one solid layer (cloud fraction was virtually 100% from top to bottom, see Fig. 4.5 (d)) with an approximately adiabatic liquid water content. Changes in LWP, and the semi-direct forcing occurred through a reduction in the thickness of the stratocumulus layer, not by internal variations of cloud fraction.

4.8   Conclusions from SCCM experiments

The SCCM has been used to simulate marine stratocumulus and cumulus using the same meteorological set-up that was used to drive the LEM experiments in chapters 2 (see section 2.2.1). The SCCM captures the basic thermodynamic structure of the BL, but there are some notable deficiencies: low specific humidity in the BL, low liquid water content in the stratus cloud layer, and the presence of convective cloud within the inversion layer. The inversion itself is poorly resolved, and processes such as entrainment and convective mixing are poorly represented. The vertical resolution is insufficient to capture the vertical structure of radiative heating / cooling and turbulent fluxes in the BL, or the daytime decoupling.

The mean cloud fraction and LWP are in reasonable agreement with the LEM, but the diurnal cycle of LWP is severely underestimated. This problem arises mainly because the parameterized stratus cloud fraction is insensitive to changes in RH whilst RH remains above 90%. Also, the liquid water is a specified function of height and is not linked to the actual condensation process or to the thickness of the cloud layer. This led to an underestimate of LWP variability. As a result the mean semi-direct forcing was only 2.5 W m^{-2}, a factor of 5 smaller than in the LEM.

The magnitude of the semi-direct forcing was found to be sensitive to aspects of the meteorological set up such as, the large-scale moisture forcing, the humidity in the free troposphere, and the large-scale subsidence rate. Moister or drier conditions gave a larger semi-direct forcing. This sensitivity arises

from the non-linearity, and discontinuity in the dependence of cloud fraction on RH (Fig 4.2). When RH was less than 90% the stratus cloud fraction varied strongly with RH but there was no large-scale cloud. When RH was greater than 90% the stratus cloud fraction was fixed at the maximum value but large-scale cloud formed and varied weakly, or strongly, with RH, depending on whether RH was just over 90% , or approaching 100% .

Increasing the vertical resolution by a factor of three led to a higher semi-direct forcing (8.7 W m^{-2}) that was closer to the magnitude of the semi-direct forcing in the LEM experiment (15 W m^{-2}). The response to the absorbing aerosols was quite different in the high resolution simulation. The inversion and cloud layers dropped two levels ($\sim$ 110 m) in response to lower surface fluxes. This reduced the potential number of cloud layers in the BL and was the main contributor to the semi-direct forcing. However, there was no great improvement in the representation of the BL structure or cloud properties. Decoupling was still not captured, the diurnal variation of LWP was still underestimated, and the mean LWP was underestimated by a factor of 2.

In experiments with a deeper BL and higher sea surface temperature, typical of trade cumulus conditions the semi-direct forcing was higher (8.0 W m^{-2}). Although this result matches the result in the equivalent LEM experiment (ATEX) the cloud response were not realistic and the agreement could be viewed as a coincidence. For example, the semi-direct forcing in the SCCM came mainly from changes in cloud amount in the middle of the BL, whereas in the LEM the semi-direct forcing came mainly from changes in cloud amount near the top of the BL.

The major problems identified in these experiments show that a more appropriate, physically based representation of the BL and of BL clouds is needed for GCMs to simulate the semi-direct effect in marine stratocumulus. GCMs must be able to deal with the complexity of BL processes, even at low vertical resolution, yet meet the requirement for simplicity and numerical efficiency. Over the last 10 years or so major efforts have been made to improve the treatment of clouds (e.g. EUROCS (Duynkerke *et al.*, 2000), and the Global Energy and Water Cycle Experiment (GEWEX) Cloud Systems studies (GCSS) (Bretherton, 2002)). Most state of the art GCMs now have prognostic treatment of cloud water (e.g Smith (1990) [UKMO]; Tiedtke (1993) [ECMWF]; DelGenio *et al.* (1996) [GISS]; Rotstayn (1997a) [CSIRO]; Zhao and Carr (1997) [NCEP ETA]), rather than a diagnostic treatment (as in the SCCM), and this has led to significant progress in the representation of clouds globally (e.g Rotstayn (1997b), Zhao *et al.* (1997), DelGenio *et al.* (1996), Jakob (1999)). Prognostic treatment of liquid water tends to give a better prediction of cloud LWP, and the way that it changes with diabatic heating, turbulence and so on. Therefore, it is possible these models would give a better estimates of the semi-

direct forcing. However, all the cloud schemes referred to above, except Tiedtke (1993), still diagnose cloud fraction based on relative humidity (as in the SCCM). Because of this the semi-direct forcing would be sensitive to the functional dependence of cloud fraction on relative humidity, just as found in the SCCM experiments.

One way of improving cloud schemes might be to use a probability density function (PDF) for the total water in the gridbox, as in Smith (1990) but to parameterize the higher order moments of the distribution (variance, skew, etc) in some way (Pincus and Klein, 2000). The variability of total water within a gridbox depends on many factors such as turbulence, precipitation, the type of cloud forming, and the variability of total water at the resolved scale. Any of these could be used as a basis for parameterizing the total water PDF. This approach may offer a solution to the problems that were experienced in the SCCM experiment where the RH to cloud fraction relationship was not well suited to marine stratocumulus. The Tiedtke (1993) scheme actually treats cloud fraction as a prognostic variable. This parameterizes sources of cloudy air from convection, BL turbulence, and stratiform condensation, and parameterizes the sink of cloudy air from evaporation. This adds computational expense but it is a move towards a more physical treatment of clouds that may respond more realistically to semi-direct effect.

Recently, there has been a move towards BL parameterizations that include entrainment, and the interaction between cloud-top longwave cooling and turbulent mixing (e.g. Lock *et al.* (2000), Lock (2001), Grenier and Bretherton (2001)). This seems vital if large-scale models are to faithfully produce the interaction between aerosol heating and cloudiness in cloud-topped BLs. Bechtold *et al.* (1996) evaluated the performance of 6 one-dimensional models in simulating the nocturnal marine BL. The turbulence scheme in these models ranged from simple bulk models, to 1.5 order models that relate the eddy-diffusivity to a prognostic turbulent kinetic energy equation, to more detailed turbulence models that have prognostic equation for the second or third order moments. At high vertical resolution (25 m) models with higher order schemes gave a more accuracy of simulations was shown to of BL turbulence, as compared with the LES. However, most global or regional climate models can only afford resolution of 100-300 m in the BL at present. Bechtold *et al.* (1996) also showed that at low resolution (200 m) the simpler bulk model performed better as it was more specifically designed to allow for poor resolution.

This experiment shows that simple GCMs may not give realistic, or reliable estimates of the semi-direct effect. Specifically, the semi-direct forcing for absorbing aerosols in a marine stratocumulus-capped BL could be underestimated. This poses a serious problem for advancing our understanding of the way

that absorbing aerosols influence the climate system. Global studies such as Hansen *et al.* (1997) and Cook and Highwood (2003) necessarily rely on simple, numerical efficient models where the vertical resolution is restricted. Lohmann and Feichter (2001) and Jacobson (2002) were able to use GCMs with more sophisticated cloud and aerosol physics, but they differ quite markedly on their predictions of the relative strength of the semi-direct effect. Neither of these studies provided comprehensive analysis of how the absorbing aerosols affected the modelled cloud fields and it is difficult to say why they differed. It is well known (IPCC, 2001) that the cloud-climate feedbacks vary considerably between GCMs (Cess *et al.*, 1989) and are shown to be sensitive to cloud modelling assumptions (Yao and DelGenio (1999), Rotstayn (1999b)). The semi-direct effect may, for similar reasons, be model dependent. Thus, current GCM estimates of the semi-direct effect need to be treated with caution.

This chapter presents results from a relatively simple climate model. Most of the problems in capturing the semi-direct effect were associated with the somewhat crude nature of the cloud scheme. It is possible that other current climate models, with more sophisticated cloud schemes, would give more realistic responses. Further studies with other current models would help to determine what is necessary to capture the semi-direct effect accurately within a GCM. As part of this, cloud responses should be compared (validated) with those from higher resolution models such as LES or Cloud Resolving Models (CRM).

CHAPTER 5

Sensitivity to aerosol vertical distribution

5.1 Introduction

In chapters 2-4 it was was assumed that aerosols were located mainly in the Boundary Layer (BL). In every experiment the aerosol mass mixing ratio was constant within the BL and reduced linearly to zero a small distance above the inversion. This simple assumption for the aerosol vertical distribution was chosen to elucidate some of the basic mechanisms of the semi-direct effect. However, it is important to consider whether the aerosol vertical distribution is important in the semi-direct effect.

It is generally observed that aerosol concentrations are greatest in the lowest 1 - 2 km of the troposphere, roughly coinciding with the depth of the BL. This is because aerosols have a short residence time in the atmosphere, and vertical mixing is often inhibited by an inversion at the top of the BL. However, observations (e.g. Clarke *et al.* (1996), Johnson *et al.* (2000)) show that aerosol layers advected over the ocean are often located both in and above the marine BL. During the Atlantic Stratocumulus Transition Experiment (ASTEX) 1992, and the Aerosol Characterisation Experiment (ACE) 1997, polluted continental airmasses with deep well-mixed BLs (2-3 km) were advected over the North Atlantic Ocean. A much shallower marine BL ($\sim$ 1 km) formed over the relatively cool ocean, leaving a significant proportion of the aerosol mass above the local inversion. Deep aerosol layers were found also over the Indian Ocean during the Indian Ocean Experiment (INDOEX) 1998-99 (Ackerman *et al.*, 2000) where the marine BL was overlain by a polluted residual continental BL between 1.5 - 3.5 km.

Where continental airmasses have originated from elevated land surfaces, the polluted air that is advected over the ocean may be lifted well above the marine BL. For example, during the Southern African Regional Science Initiative (SAFARI-2000) biomass-burning aerosols, originating from Central-Southern Africa, were found over the Southern Atlantic between altitudes of 2 and 5 km (Haywood *et al.*, 2003). Thus, it is possible for absorbing aerosols to be located both in and above the BL, and in some cases only above the BL. This raises the question: Do absorbing aerosols above the marine BL have any influence on clouds in the BL, i.e. do they lead to a semi-direct effect? Furthermore, it is important to know whether vertical variation in the aerosol concentration within the BL influences the

semi-direct effect.

Vertical variation within the BL may arise for several reasons. For example, entrainment of cleaner air at the top, or moist deposition processes would reduce the aerosol concentration in the cloud. Entrainment of more polluted air would have the opposite effect. In shallow cloud-capped BLs mixing would tend to disperse aerosols quite quickly in the vertical. However, gradients in aerosol concentration could arise in deep and decoupled BLs.

In addition, internal mixing between absorbing aerosols and cloud droplets may lead to vertical variation of aerosol optical properties. The specific absorption coefficient of black carbon aerosol increases when they are located within a cloud droplet, perhaps by a factor of 2, although the exact level of increases is still a matter of debate (see section 1.3.1).

If all black carbon aerosols were mixed within cloud droplets the aerosol shortwave heating rate in the cloud would be increased by the same factor. However, the proportion of black carbon mixed with water droplets is thought to be low, but is very uncertain. Measurements of aerosol concentration and optical properties in clouds are inherently problematic. Nevertheless, the influence of vertical variation within the BL on the semi-direct effect remains an important and interesting question.

In this chapter the LEM is used to perform simulations for marine stratocumulus and trade-wind cumulus, similar to those in chapters 2 and 3. A range of aerosol vertical distributions have been used to test the sensitivity to aerosols in the following regions:

(FT) In the free troposphere (above the inversion).

(BL) Within the BL, and uniform with height.

(CL) Within the cloud layer only.

(BCL) Below the cloud layer only.

(BLFT) Both in and above the BL.

Vertical distribution (BLFT) will test if there is linearity of response to aerosols at different heights; i.e if the sum of responses to aerosols above and below the inversion is the same as the response to aerosols in both regions. The aerosol vertical distributions are idealised and held fixed with time relative to the instantaneous height of the inversion so that the mechanisms responsible for cloud responses can more easily be distinguished. In every case the aerosol mass mixing ratio within the specified region is fixed

at 3×10^{-8} kg kg^{-1} (the same as in all previous experiments in chapters 2-4). The mid-visible single scattering albedo is 0.88 for all experiments except for experiment SC-FTS, which investigates the sensitivity to scattering aerosols above the inversion. Details on how aerosol optical properties were derived are found in section 2.2.1.

5.2 Marine stratocumulus

The meteorological scenario is based on the FIRE stratocumulus experiment (see section 2.1.3 for background details), and the experimental set up follows that used in chapter 2 (section 2.2.1), except for a few changes:

1. The domain size was reduced from 2.5 km x 2.5 km to 1.6 km x 1.6 km to allow time to complete the experiments. It is possible that this reduction increases bias from sampling errors, but as in section 2.2.6.2, the semi-direct forcing for this case was robust with domain size and sampling errors were only 2-3 W m^{-2}, even for a smaller domain size of 1 km x 1km.

2. The model top was extended from 1200 m to 1600 m with the addition of 8 extra levels to accommodate the deeper aerosol layers. Also, the height at which relaxation to initial conditions occurred was moved up from 1000 m to 1400 m. This was important to enable the air above the inversion to warm in response to heating from the aerosols.

3. The simulations were started at midnight, and run for 48 hours. The 5-6 hours before dawn are sufficient as a spin-up period for the LEM to generate a realistic nocturnal BL structure.

These changes had little effect on the mean structure, liquid water path (LWP), or turbulent characteristics of the BL. Seven simulations were performed: five with absorbing aerosols, one with scattering aerosols, plus an aerosol-free control. Vertical distributions and aerosol optical depths for the six aerosol experiments are shown in Table. 5.1. The aerosol vertical distribution are set with reference to the instantaneous horizontal mean inversion height (Z_{inv}). The aerosol distributions are therefore not absolutely fixed, but vary interactively with Z_{inv} so that the regions of aerosol heating conform exactly to the experimental design, irrespective of the drift of Z_{inv}.

Experiment name	Aerosol layer height range	Optical depth at 0.55μm	Semi-direct day 1	Semi-direct day 2	Direct mean	Total mean
SC-BL	0 to Z_{inv}	0.12	22.2	23.4	-2.3	20.5
SC-CL	Z_{inv}/2 to Z_{inv}	0.06	20.4	17.1	-1.1	17.7
SC-BCL	0 to Z_{inv}/2	0.06	0.5	3.6	-1.0	1.1
SC-FT1	Z_{inv} to 1.6 km	0.2	-6.9	-11.9	10.2	0.7
SC-FT2	2 to 3 km	0.2	-4.0	-1.3	8.8	6.2
SC-FTS	Z_{inv} to 1.6 km	0.2	-1.1	0.9	-7.3	-7.4
SC-BLFT	0 to 1.6 km	0.32	15.5	4.9	5.2	15.4

Table 5.1: *Summary of marine stratocumulus experiments: Aerosol layer height ranges, mid-visible optical depths, semi-direct forcings on days 1 and 2, direct forcing averaged over days 1 and 2 (the direct forcing does not vary significantly between the days), and total aerosol radiative forcing, averaged over days 1 and 2. Radiative forcings are in $W\,m^{-2}$.*

5.2.1   Aerosols in the BL

In chapter 2 it was shown that absorbing aerosols lead to a large positive semi-direct forcing when located almost exactly in the BL. The aerosols led to an enhanced daytime thinning of the cloud mainly by raising the temperature, leading to evaporation. The aerosols also enhanced the daytime decoupling because the aerosol heating rate was higher in the cloud layer and offset cloud-top longwave cooling. This led to a reduction of moisture fluxes into the cloud from the surface. In the light of these results it is expected that absorbing aerosols would have a much greater semi-direct effect if located in the cloud, than if located below the cloud. To test this hypothesis, the response is examined for absorbing aerosol in the upper half of the BL (roughly corresponding to the cloud layer; experiment SC-CL), and in the lower half of the BL (roughly corresponding to the sub-cloud layer; experiment SC-BCL), and these are compared with the response from aerosols uniformly distributed throughout the BL (experiment SC-BL).

(i) Experiment SC-BL - Aerosols uniformly distributed in the BL

The aerosol distribution in experiment SC-BL is very similar to that in experiment A-088 from chapter 2 (see section 2.2.1). The only difference is that in experiment A-088 there was also some aerosol above the inversion; the aerosol mass mixing ratio reduced linearly to zero between the inversion and 300 m above. In experiment SC-BL the aerosol mass mixing ratio went to zero immediately at the

inversion. Experiments A-088 and SC-BL lead to very similar outcome. In both experiments aerosols lead to a rise in cloud base, a decrease in LWP, and a decrease in surface fluxes because of increased stability near the surface, and reduced turbulence. There is also a reduction of the entrainment rate leading to a lower cloud top height and, over time, higher moisture levels in the BL. Since the results for experiment SC-BL were qualitatively similar to experiment A-088 the reader is referred back to section 2.2.3 for further details.

The diurnal mean semi-direct forcing is somewhat higher in experiment SC-BL (23.4 W m^{-2}, for day 2, see table 5.1) than in experiment A-088 (14.0 W m^{-2}, for day 2, see table 2.3 in section 2.2.4). Although turbulent variability may explain some of the difference, it is likely that the higher diurnal mean semi-direct forcing in experiment SC-BL is related to the lack of any aerosols above the inversion. As will be shown in section 5.2.2, heating the air above the inversion leads to a lower entrainment rate and tends to increase the LWP.
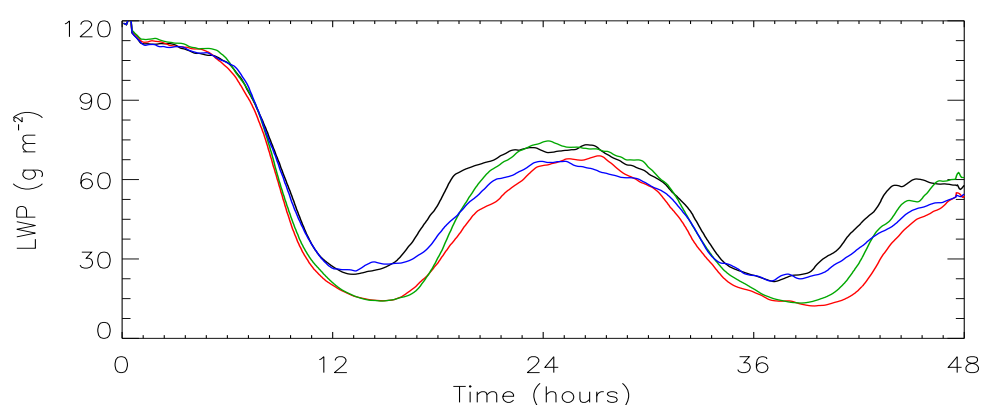
Figure 5.1: *Horizontal average liquid water path (g m^{-2}) in experiments SC-BL (red), SC-CL (green), SC-BCL (blue), and the control (black).*

Indeed there is a bigger daytime reduction of LWP in experiment SC-BL than in experiment A-088 (compare Fig. 5.1 with Fig. 2.18 (a) in section 2.2.2). Also, in experiment SC-BL the LWP remains well below the control throughout the night, whereas in experiment A-088 the LWP rose above the control for a few hours around dawn of day 2. As a result there is a brief period of negative semi-direct forcing on day 2 in experiment A-088 (Fig. 2.18 (a)), but a positive forcing throughout day 2 in experiment SC-BL because the LWP remained above the LWP of the control (Fig. 5.1). In this way, the difference in the dawn value of LWP contributes significantly to the diurnal mean semi-direct forcing. Both turbulent variability in LWP, and differences in the aerosol vertical distribution contribute to the difference in dawn values of LWP.

(ii) Experiment SC-CL - Aerosols in the cloud layer

In experiment SC-CL the semi-direct forcing was positive, and almost as large for experiment SC-BL, even though aerosols were only located in the upper half of the BL (the cloud layer), and the optical depth is only half. The diurnal mean semi-direct forcing for day 1 was 20.4 W m^{-2} in experiment SC-CL, and 22.2W m^{-2} in experiment SC-BL (Table 5.1). Also, the LWP curves (Fig 5.1 (a)) for these two experiments are almost identical until about 1800 h. After this time the LWP increases at a faster in experiment SC-CL and is higher through the night and into the second day. Because of this the diurnal mean semi-direct forcing is therefore a little lower on day 2 in experiment SC-BL; it is 17.1 W m^{-2} , compared with 23.4 W m^{-2} for experiment SC-BL.

Figure 5.2: *Horizontally averaged profiles: (a) Liquid water potential temperature (K), (b) total water mixing ratio (g kg^{-1}), (c) turbulent kinetic energy (J kg^{-1}), and (d) turbulent latent heat flux (W m^{-2}), in experiments SC-BL (red), SC-CL (green), SC-BCL (blue), and the control (black). Profiles are time averaged between 1200 and 1500 h.*

Figure 5.2 shows the influence of each aerosol distribution on early afternoon BL structure and turbulent fluxes. The main influence of the aerosols in experiment SC-CL is to heat the cloud layer and

generate a stable layer just below cloud base (Fig. 5.2 (a)). Even though the cloud layer does not heat up as much as in experiment SC-BL, the stabilisation is more pronounced because of the absence of aerosols in the subcloud layer. The greater stabilisation leads to a lower daytime cloud base latent heat fluxes (Fig. 5.2 (d)), and a lower total water content in the cloud (Figs. 5.2 (b) & 5.3 (b)), helping to keep the LWP nearly as low as in experiment SC-BL. However, more moisture accumulates in the surface layer during the daytime, because of the greater decoupling. In the evening, when re-coupling takes place this moisture is redistributed through the BL, explaining the rapid increases of cloud layer total water (Fig. 5.3 (b)) and LWP (Fig. 5.1). At dawn on day 2 the cloud layer in experiment SC-BL is slightly cooler (Fig. 5.3 (a)), mainly because there was less aerosol heating on the previous day, and LWP is about 10 g m^{-2} higher (Fig. 5.1). Thus, the response of the cloud layer to absorbing aerosols in the cloud layer is almost as strong as for aerosols throughout the BL, but the absence of absorbing aerosol in the subcloud layer limits the strength of the semi-direct forcing, particularly on the second day.

In experiment SC-CL the LWP even exceeds the LWP in the control simulation in the second half of the night (Fig. 5.1). At the same time the cloud layer is actually cooler than the control (Fig. 5.3 (a)) despite the aerosol heating in the preceding day. The reason, is that there was also a lower entrainment rate during the preceding day (evident from a 30 m relative drop in cloud top height (not shown)). The lower rate of entrainment heating more than compensates for the aerosol heating giving a cooler cloud layer at night, once the decoupling breaks down and the BL becomes well-mixed.

(iii) Experiment SC-BCL - Aerosols in the sub-cloud layer

Aerosols below the cloud layer led to a small positive semi-direct forcing. The diurnal mean was 0.5 W m^{-2} on day 1, and 3.6 W m^{-2} on day 2, giving a mean semi-direct forcing of 2.1 W m^{-2} (Table 5.1). These forcings are comparable to the uncertainty associated with turbulent variability of LWP, which was estimated to be $\pm$ 2 W m^{-2} for the diurnal mean semi-direct forcing on any one day (see section 2.2.6.2). Therefore, the magnitude of the mean semi-direct forcing in experiment SC-BCL is rather small and uncertain. In the daytime the LWP is not very different from the control, but the LWP is significantly lower at night and up till midday on day 2 (Fig. 5.1). This explains why the semi-direct forcing is larger on day 2 (Table 5.1).

It is interesting that the diurnal range of LWP is lower than in the control (Fig. 5.1). This is because the BL is much less decoupled in experiment SC-BCL. For example, there is no step-like change in liquid water potential temperature or total water mixing ratio below cloud base, and the BL is generally
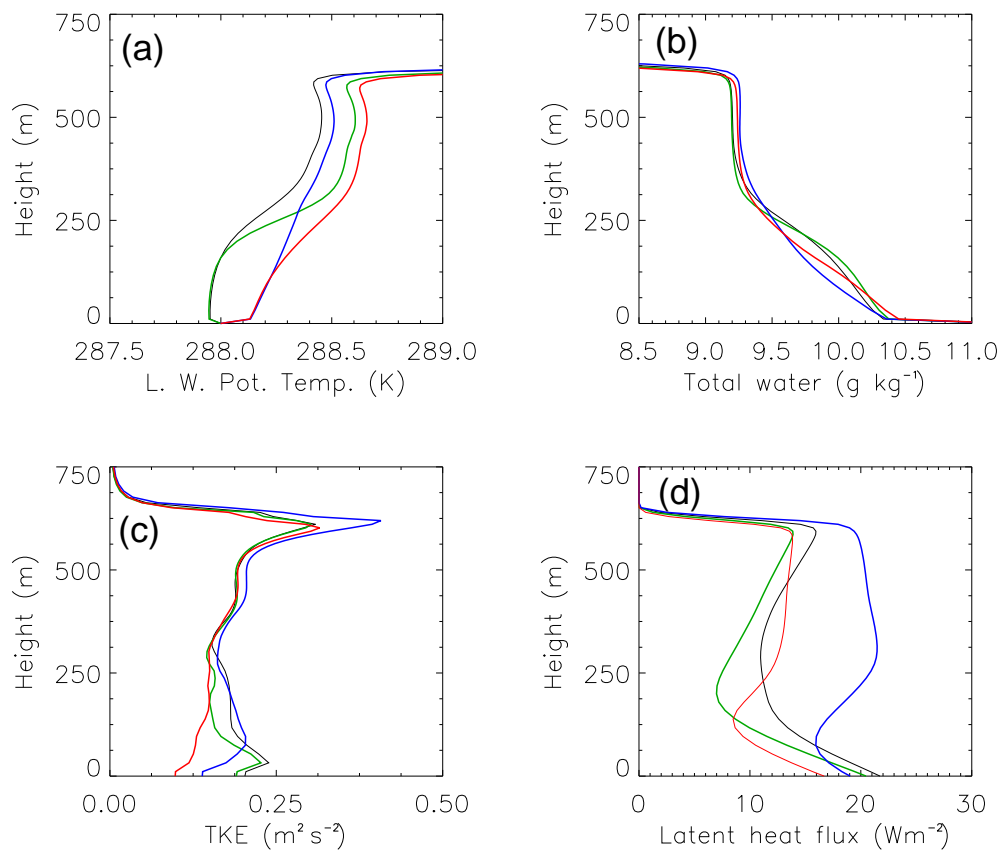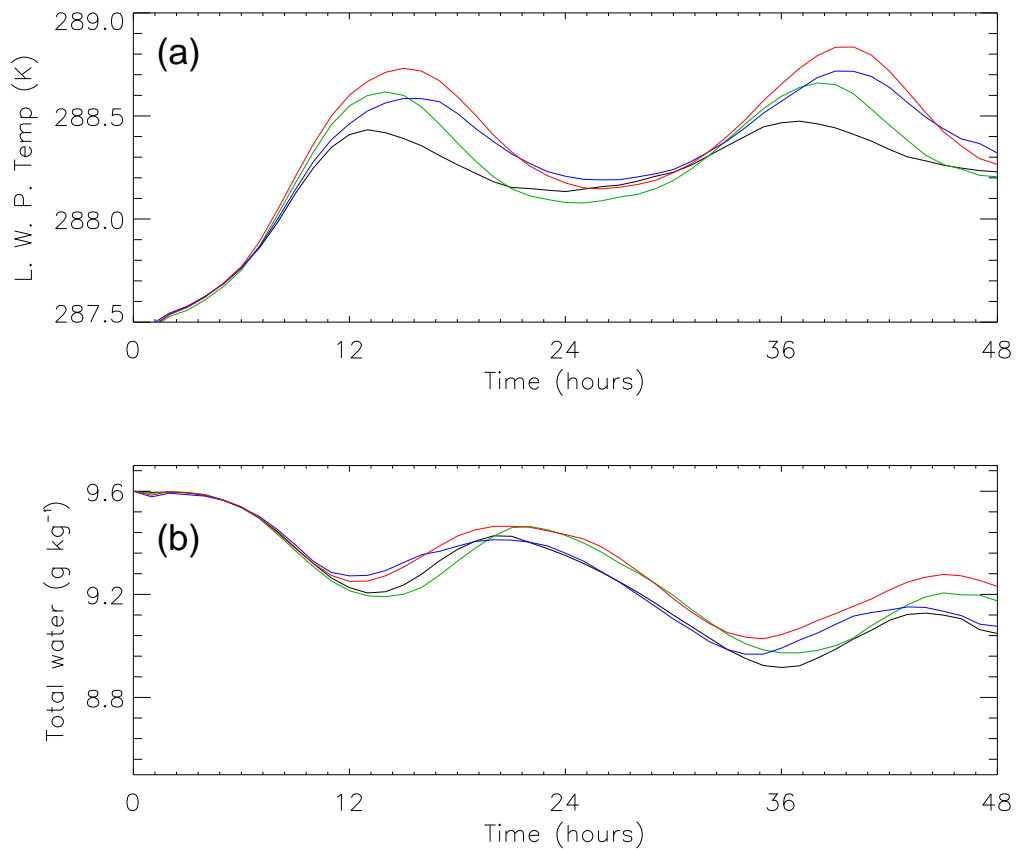
Figure 5.3: *Horizontally averaged (a) liquid water potential temperature (K) and (b) total water mixing ratio (g kg^{-1}) in the cloud layer (upper half of the BL), in experiments SC-BL (red), SC-CL (green), SC-BCL (blue), and the control (black). Here, the BL is defined as the levels up to, and including the cloud top peak in liquid water.*

less stratified (Fig. 5.2 (a) & (b)). This allows greater moisture fluxes between the sub-cloud layer and the cloud layer (fig 5.2 (d)), leading to higher total water in the cloud layer (Fig. 5.3 (b)), but lower total water below (Fig. 5.2 (b)). Some of the heat absorbed by the aerosols in the lower half of the BL is transported vertically leading to higher temperatures in the cloud layer (Fig 5.2 (a) & 5.3 (a)). The effects of heat and moistening in the cloud layer roughly compensate so there is little impact on LWP in the daytime (Fig. 5.1). However, at night the LWP is lower than in the control because the cloud layer is still warmer (Fig. 5.3 (a)), but moisture levels in the cloud layer are no higher than in the control (Fig. 5.3 (b)) owing to a greater entrainment rate.

5.2.2   Aerosols above the BL

Absorbing aerosols above the inversion could impact on BL clouds in two principal ways:

(1) Aerosols may sufficiently reduce the down-welling shortwave radiation reaching the cloud to decrease the shortwave heating rate within the cloud.

(2) Heating the air immediately above the inversion may increase the potential temperature contrast between the BL and the free troposphere leading to a lower entrainment rate.

Both these effects would tend to favour the persistence of a stratocumulus layer, and promote the formation of stratiform cloud in the trade-wind BL. It is important to assess the potential of both mechanisms to alter stratocumulus LWP. Experiment SC-FT2 has absorbing aerosols well above the model top, between 2 and 3.2 km. This specifically tests hypothesis (1). Experiment SC-FT1 has absorbing aerosols in a layer 1 km thick immediately above the inversion and tests hypothesis (2). Experiment SC-FTS has scattering aerosol immediately above the inversion and assesses whether scattering aerosols have an influence on the stratocumulus, mainly via mechanism (1).

(i) Experiment SC-FT1 - Aerosols immediately above the inversion

It was found that placing aerosols immediately above the inversion leads to a moderately strong negative semi-direct forcing (-6.9 W m^{-2} for day 1, and -11.9 W m^{-2} for day 2, see Table 5.1). The aerosols heat the air above the inversion at a rate of about 1 k day^{-1}, leading to a 1.5-2 K increase in potential temperature above the inversion by the end of day 2. The strengthening of the inversion results in a lower entrainment rate, as shown by the relative decline of cloud top height (Fig. 5.4 (b)). It is estimated that the mean entrainment rate (W_e) has reduced by 30 m day^{-1}, from a mean rate of 300 m day^{-1} (calculated using W_e = -W_{subs} + dZ_{ct}/dt, where W_{subs} = Z x D, where W_{subs} is the subsidence rate (m s^{-1}), Z is the height (m), D is the divergence rate = 5.5 x 10^{-6} s^{-1}, Z_{ct} is the cloud top height (m), and t is time (s)).

The lower entrainment rate results in a slightly cooler, moister BL (Figs. 5.5 & 5.6), and a higher LWP during both the day and the night (Fig. 5.4 (a)). The semi-direct forcing is stronger (more negative) on day 2 because the temperature above the inversion is higher on day 2 than on day 1. Thus, the inversion strength, and the impact on the entrainment rate are greater on day 2.

The aerosol layer also leads to a small reduction of the heating rate in the cloud layer due to their attenuation of the down-welling flux (Fig. 5.7). The extent to which this cooling contributes to the
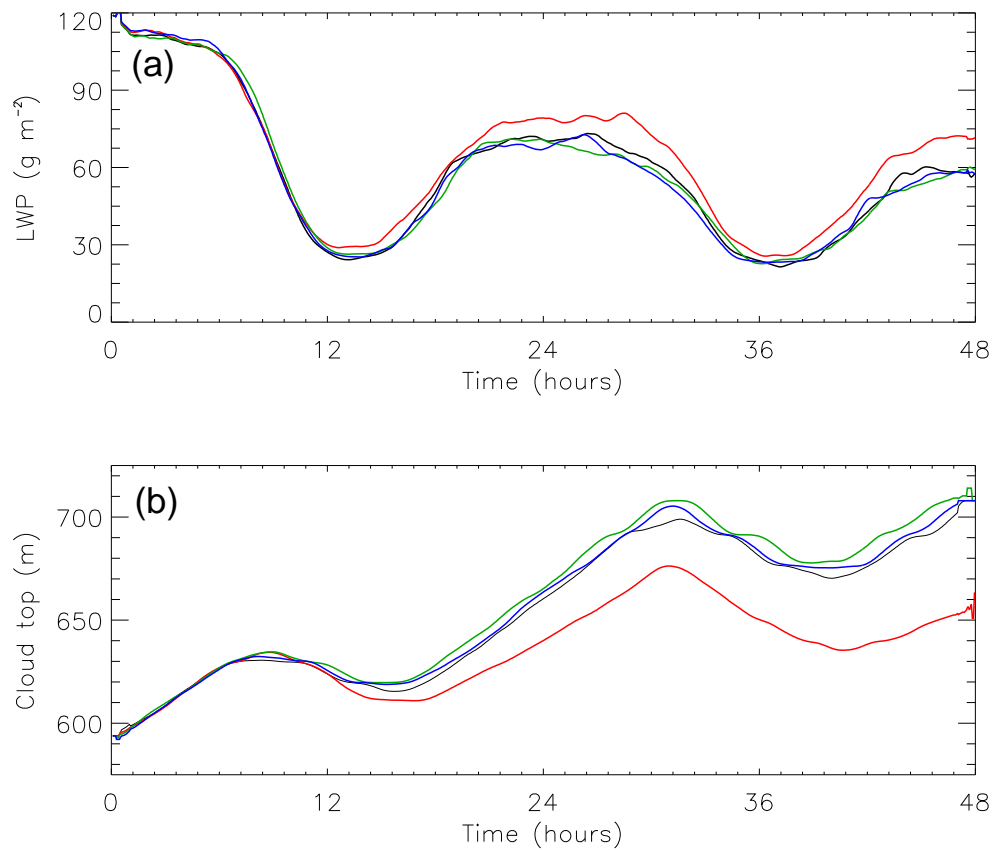
Figure 5.4: *(a) Domain average liquid water path (g m^{-2}) and (b) maximum cloud top height (m) in experiments SC-FTS (blue), SC-FT2 (green), SC-FT1 (red), and the control (black).*

increased LWP, and the negative semi-direct forcing is addressed in the next experiment.

(ii) Experiment SC-FT2 - Aerosols far above the inversion

In experiment SC-FT2 the absorbing aerosol layer aloft leads to a cooling of the cloud layer, just as in experiment SC-FT1 but there is no heating immediately above the inversion (Fig. 5.7). Figure 5.4 shows only small changes in LWP and cloud top heights, and Fig. 5.5 shows only small changes in vertical profiles of liquid water potential temperature and total water mixing ratio. The diurnal mean semi-direct forcing in experiment SC-FT2 was -4.0 W m^{-2} on day 1 and -1.3 W m^{-2} on day 2, giving a mean of -2.7 W m^{-2} (Table 5.1). This is much smaller in magnitude than the mean semi-direct forcing in experiment SC-FT1 (which was -10.2 W m^{-2}), and is not very large compared to the uncertainty ($\pm$ 2 W m^{-2}) due to turbulent variability (estimated in section 2.2.6.2).

These results shows that the influence of aerosols on down-welling shortwave fluxes is probably not very important to the semi-direct effect. Absorbing aerosols above the inversion have a large influence
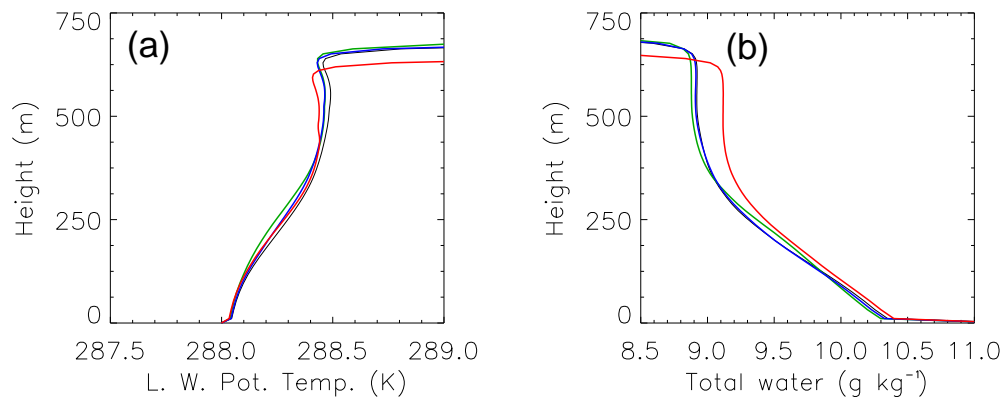
Figure 5.5: *Horizontal averaged profiles: (a) Liquid water potential temperature, (b) total water mixing ratio, in experiments SC-FTS (blue), SC-FT2 (green), SC-FT1 (red), and the control (black). Profiles are time averaged between 3600 and 3900 h.*

on the cloud layer only if they heat the air immediately above the inversion and increase the inversion strength.

(iii) Experiment SC-FTS - Scattering aerosols immediately above the inversion

Experiment SC-FTS tests whether scattering aerosols above the inversion have a negative semi-direct effect by decreasing the downwelling shortwave flux. The scattering aerosol layer, which has an optical depth of 0.2, reduces (attenuates) the downwelling solar flux by about 3%. Consequently, there is a small reduction of heating rate in the cloud interior (Fig. 5.7 (b)). However, there is also a slight warming near the cloud top. The warming occurs because scattering increases mean path lengths, and therefore increases absorption by cloud droplets, for low solar zenith angles. The path length effect becomes less important in the cloud interior where multiple scattering by cloud droplets quickly increases path lengths. The overall heating rate change is quite small because the effects of attenuating the downwelling solar flux and increasing path-lengths are quite minor and partially cancel each other anyway.

Not surprisingly, the semi-direct forcing is close to zero; it is -1.1 W m^{-2} for day 1, and 0.9 W m^{-2} for day 2, giving a mean of practically zero (see Table 5.1). The semi-direct forcings are not significant compared to the uncertainty ($\pm$ 2 W m^{-2}) due to turbulent variability of LWP (estimated in section 2.2.6.2). There were no significant changes in LWP, or cloud top height (Fig. 5.4), nor any significant changes in thermodynamic profiles (Fig 5.5).
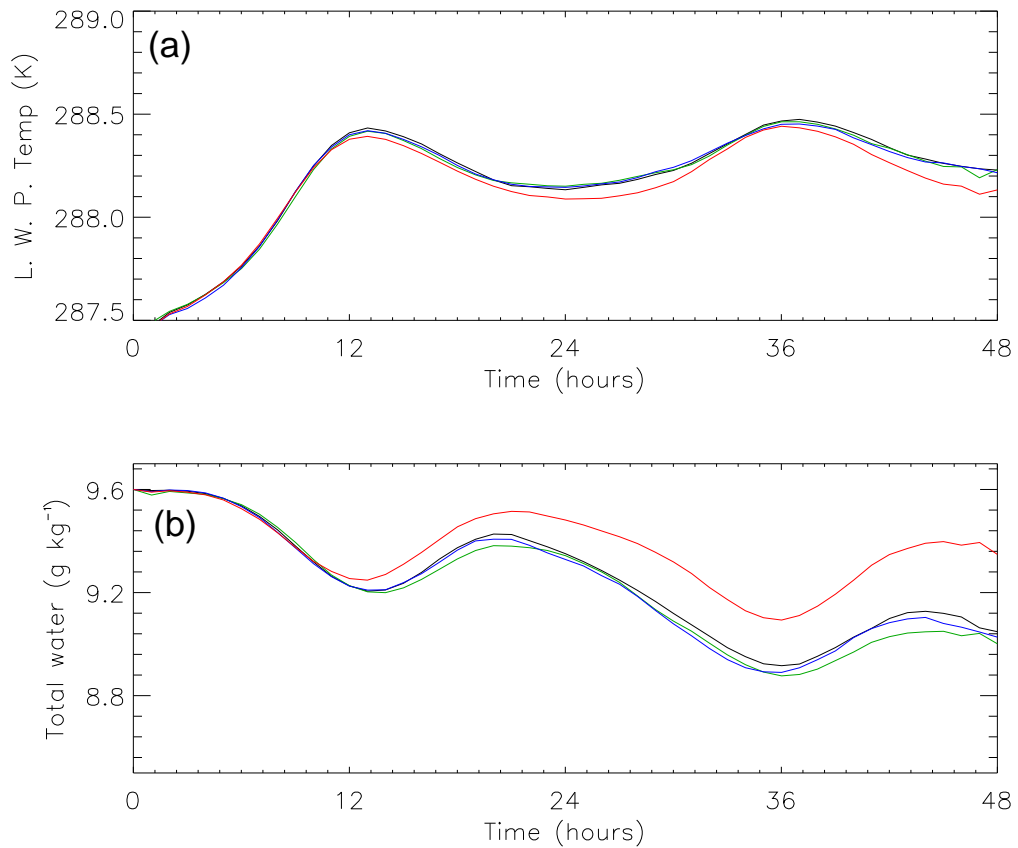
Figure 5.6: *(a) Horizontal mean value of liquid water potential temperature in the upper half of the BL (cloud layer), (b) mean value of total water mixing ratio in the upper half of the BL, in experiments SC-FT1 (red), SC-FT2 (green), SC-FTS (blue), and the control (black). Here the BL is defined as the levels up to, and including the cloud top peak in liquid water.*

This further confirms that the attenuation effect of aerosols above the inversion is not very important, as in experiment SC-FT2, and shows that aerosols above the inversion only have a significant influence on the cloud layer if the heat the air immediately above the inversion and increase the inversion strength. It is possible that for higher optical depths the impact on heating rates would be enough to give a significant semi-direct effect. Offline calculations show that a scattering optical depth of 1.0 would reduce midday heating rates by about 2 K day^{-1} near the cloud top. This would probably lead to a moderate negative semi-direct effect because it is quite a large reduction in heating rate in comparison to the heating rate in SC-BL (Fig. 5.7). However, aerosol optical depths are more typically in the range 0.05-0.2, so typically the semi-direct effect of scattering aerosol would be negligible.
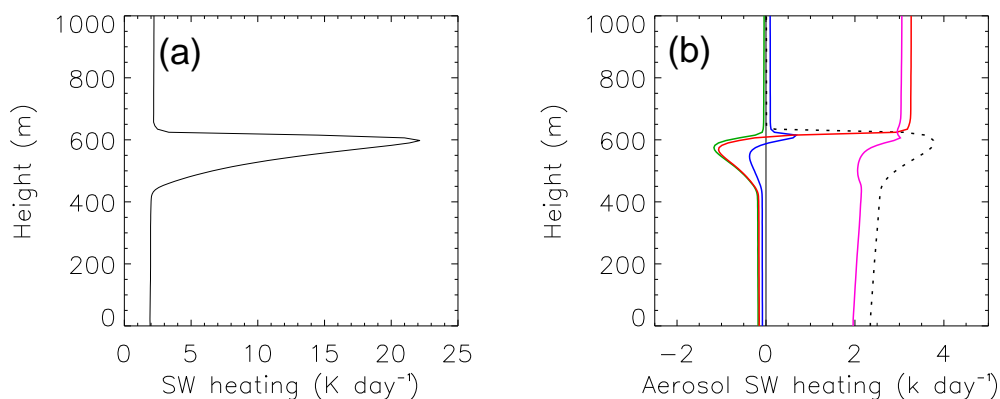
Figure 5.7: *(a) Shortwave heating rate (K day $^{-1}$) in the control simulation at 1200 h on day 2. (b) Impact of aerosols of shortwave heating rate at 1200 h on day 1 in the experiments SC-BL (dotted line), SC-FTS (blue line) SC-FT2 (green), SC-FT1 (red), and SC-BLFT (pink).*

5.2.3   Linearity of response to aerosols above and below the inversion

Experiment SC-BLFT has absorbing aerosol both in and above the inversion; the aerosol profile is the sum of the aerosol profiles in experiments SC-BL and SC-FT1 (see Table 5.1). If the semi-direct effect were linear with aerosol layers then the semi-direct forcing in experiment SC-BL would be the sum of the semi-direct forcings is experiments SC-BL and SC-FT1. This linearity holds on day 1; the diurnal mean semi-direct forcing for experiment SC-BLFT is 15.5 W m^{-2}, and the sum for experiments SC-BL and SC-FT1 is 15.3 W m^{-2} (Table 5.1). However, on day 2 the linearity breaks down. The diurnal mean semi-direct forcing in experiment SC-BLFT is only 4.9 W m^{-2} and the sum from experiments SC-BL and SC-FT1 is 11.5 W m^{-2} (Table 5.1). Thus, there is a difference of -6.6 W m^{-2}, which is significant compared to the $\pm$ 2 W m^{-2} estimated error from turbulent variability of LWP (see section 2.2.6.2). The LWP in experiment SC-BLFT is higher than the expected (see Fig. 5.8 (a)), particularly in the night and through to day 2. This suggests some underlying process, whereby the impacts of aerosols above and below the inversion interact to give a higher LWP than expected.

One explanation is that the aerosol heating rate in the BL is not as high in experiment SC-BLFT as in experiment SC-BL (as shown in Fig. 5.7 (b)) because the downwelling shortwave radiation has been attenuated by the aerosols above the inversion. However, experiments SC-FT2 and SC-FTS showed that the attenuation effect was not very important, as it did not cause a large enough change in heating rate (Fig. 5.7 (b)). In this experiment (SC-BLFT) the aerosol heating rate in the BL is reduced by approximately 5% (estimated from offline radiation calculations), in addition to the reduction of cloud
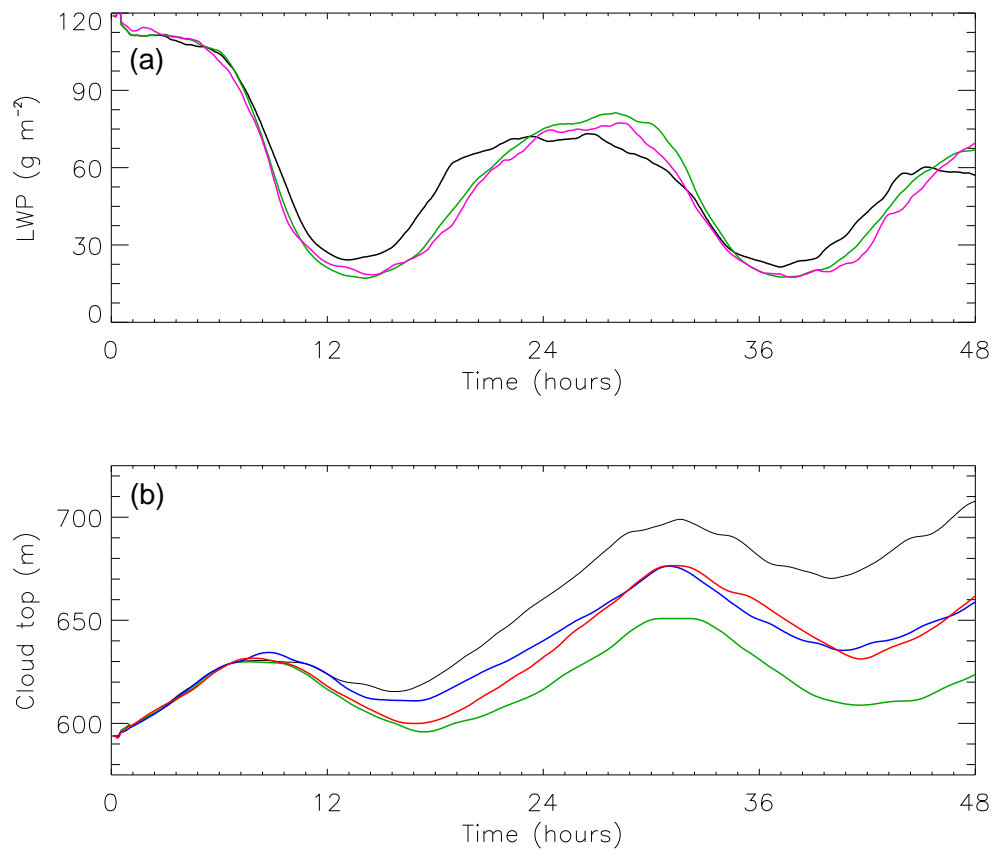
Figure 5.8: *(a) Liquid water path (g m^{-2}) in the control (black), experiment SC-BLFT (green) and in the expected LWP for experiment SC-BLFT (red): LWP$_{SC-BL}$ + LWP$_{SC-FT}$ - LWP$_{control}$. (b) Cloud top height (m) in the control simulation (black), experiment SC-FT1 (blue), experiment SC-BL (red) and experiment SC-BLFT (green).*

heating rate, due to the aerosols above. Assuming that the semi-direct forcing from aerosols in the BL is linear with the aerosol heating rate (as suggested by results in chapter 2, see section 2.2.4), then the semi-direct forcing would be reduced by an amount equal to 5% of the semi-direct forcing in experiment SC-BL; this is about 1 - 1.5 W m^{-2}. This cannot fully explain the 6.6 W m^{-2} differences between the semi-direct forcing in experiment SC-BLFT and the expected semi-direct forcing (SC-BL + SC-FT1, see table 5.1).

Experiments SC-BLFT, SC-BL, SC-FT, and the control were run for a third day to make sure that the low value of day 2 semi-direct forcing in experiment SC-BLFT was not an outlier. On day 3 the semi-direct forcing in SC-BLFT was even lower (1.1 W m^{-2}) than on day 2 (4.9 W m^{-2}), and was 10.9 W m^{-2} lower than the expected semi-direct forcing (i.e. the sum of the semi-direct forcings from experiments SC-BL and SC-FT). This shows that the response to aerosols layers at different heights

definitely is non-linear, and the non-linearity has quite a large impact on the semi-direct forcing beyond the first day.

Perhaps linearity should not be expected as the impact of aerosol above the inversion does not compensate in every way for the impact of the aerosols in the BL. For example, placing aerosols in either region leads to a reduction of the entrainment rate. In experiment SC-BLFT having aerosols in both regions combines to give a much lower cloud top height than in either experiment SC-BL or SC-FT1 (Fig. 5.8 (b)). Since the subsidence rate at the cloud top is proportional to the cloud top height, there is a lower mean cloud top subsidence rate in experiment SC-BLFT than either experiments SC-BL or SC-FT. This may explain why the cloud layer has a higher LWP than expected. This hypothesis could be tested with further experiments by using different subsidence rate profiles. However, there may be other factor contributing to the non-linearity, for example the BL depth may influence the susceptibility of the BL to decoupling and thereby modulate the response to the aerosols in the BL. It would be very difficult to clarify the importance of any one process on the non-linearity of the semi-direct forcing.

5.3   Cumulus experiments

In chapter 3 it was shown that absorbing aerosols led to a decrease in the intensity of convection, and a reduction in cloud amount. The intensity of convection was influenced by the stability of the cloud layer relative to the surface layer, but the cloud amount was more sensitive to relative humidity, particularly near the top of the BL.

It seems likely that cumulus cloud cover would be sensitive to the aerosol vertical distribution of absorbing aerosols. For example, locating aerosols near the top of the BL would perhaps have a greater effect on cloud cover and LWP by decreasing the relative humidity and the lifetime of detraining clouds. Absorbing aerosols in the surface layer may reduce the intensity of convection by reducing surface moisture fluxes and reducing the Convective Available Potential Energy (CAPE). Also, strengthening the inversion through absorbing aerosols in the free troposphere may have a particularly strong effect because cloud amounts in the intermediate trade cumulus regime are very sensitive to the relative humidity near the cloud top (as shown in chapter 3). A stronger inversion would lead to lower entrainment, a higher relative humidity and an increase in the fractional cover of detraining stratiform cloud. If the effect were large enough it could even lead to a transition back towards a stratocumulus-capped BL. As explained in section 2.1, the strength of the inversion is a key parameter in determining the stability of a stratocumulus cloud layer (Cloud Top Entrainment Instability (CTEI)).

Experiment	Location of aerosol layer	optical depth
CU-BCL	Aerosols in the subcloud layer (0 to 500 m)	0.1
CU-FT	Aerosols above the inversion (1750 - 3500 m)	0.4

Table 5.2: *Summary of cumulus experiments: location of aerosol layer, and optical depth.*

Unfortunately it is not possible to explore all these possibilities as the computation expense for cumulus simulations is particularly high. Cumulus simulations require a much larger domain size (about ten times the area of stratocumulus experiments) to gain representative results because of their stochastic nature. In this section two experiments are performed to address the following questions:

(1) Do absorbing aerosols in the subcloud layer impact on the intensity of convection by reducing surface fluxes and decreasing CAPE?

(2) Do absorbing aerosols above the inversion impact on cloud cover by strengthening the inversion and reducing the entrainment rate?

The first question is addressed by experiment CU-BCL, which has experiment absorbing aerosols in the subcloud layer only (from 0 to 500 m), and the second question is addressed by experiment CU-FT, where absorbing aerosols are located from 1.75 - 3.5 km (Table 5.2). The aerosol optical depths (see Table 5.2) are roughly proportional to the layer thicknesses because the aerosol mass mixing ratio is a constant value (3×10^{-8}).

The meteorological scenario and experimental set up follows that used in chapter 3 (section 3.2), based on the Atlantic Trade-wind Experiment (ATEX) (also see section 3.1 for background details). In experiment CU-FT the model top is extended from 2.5 to 3.5 km by adding another 10 layers, increasing the total to 102 layers. The base of the relaxed layer (see section 3.2 for more details) was moved up from 2 to 3km to allow the aerosol heating to modify temperatures in the free troposphere. Both experiments are started at midnight and run for 48 hours. The control run for experiment CU-BCL is the same as that used for the ATEX simulations in chapter 3 but a new control run was performed for experiment CU-FT because of the changes made to the height of the model top and the base of the relaxed layer.

5.3.1 Aerosols in the subcloud layer

In experiment CU-BCL the absorbing aerosols in the sub-cloud layer led to a small reduction of cloud cover and LWP (Table 5.3), and a small positive semi-direct forcing (Table 5.4); which is 0.8 W m^{-2}

Experiment	Cloud cover	LWP
CU-BCL	-2.9/31.0	-1.7/14.6
CU-FT	6.6/28.2	1.1/13.9

Table 5.3: *Change in two-day mean cloud cover (%) and liquid water path (g m^{-2}) relative to the two-day mean control values for experiments CU-BCL and CU-FT.*

Experiment	Semi-direct			Direct
	Day 1	Day 2	two-day mean	two-day mean
CU-BCL	0.8	2.2	1.5	-3.3
CU-FT	-0.4	-3.3	-1.8	-10.5

Table 5.4: *Semi-direct forcing (W m^{-2}): diurnal mean for days 1 and 2, and two-day mean, and two-day mean direct forcing (W m^{-2}) in the cumulus experiments.*

on day 1, and 2.2 W m^{-2} on day 2, giving a mean of 1.5 W m^{-2}. The ATEX experiment in chapter 3 had a semi-direct forcing of 8.0 W m^{-2} where aerosols were located throughout the BL with the same mass mixing ratio and single scattering albedo as in these experiments. Thus, the semi-direct forcing for absorbing aerosols in the subcloud layer is relatively small. The total cloud fraction is lower in the aerosol run for most of the time, except during the mornings (Fig. 5.9), and the mean cloud fraction is lower by 2.9% . The reduction in cloud fraction is largest in the afternoon and evening.

The aerosols led to a 0.5 K rise in potential temperature and a 2-3 % reduction of mean relative humidity in the subcloud layer (Fig. 5.10 (a) & (b)), and raised the cloud base height by about 100 m (Fig. 5.10 (c) & (d)). There was also a reduction in the peak value of cloud fraction near the cloud base (at 600 m in CU-BCL, and 500 m in the control, see Fig. 5.10 (c)). Air lifted from near the surface had further to travel before reaching the lifting condensation level. This may have reduced the likelyhood of forced clouds forming as the eddies ascending through the subcloud layer would have had longer to mix with environmental air and to be retarded by frictional forces before reaching the lifting condensation level. There was a significant reduction of cloud fraction in the middle of the cloud layer (800-1200 m) where the relative humidity was reduced (Fig. 5.10 (b) & (c)).

Contrary to expectations the surface latent heat flux was almost unaffected by the aerosol heating in the subcloud layer. In the cumulus experiments in chapter 3 the absorbing aerosols reduced the average surface latent heat flux by 15 W m^{-2} (see section 3.5.3) but in CU-BCL the average surface latent heat flux is only 1 W m^{-2} lower than in the control. It is not clear why there was such a small response, but

it shows that the changes in the cloud fields must have been related to other processes.

Figure 5.12 shows the CAPE in CU-BCL and the control, calculated from temperature difference between a moist adiabatic, lifted from the second level above the surface, and the environmental air, integrated from the level of free convection to the level of neutral buoyancy (see section section 3.3 for more details). The CAPE is generally lower in CU-BCL than in the control with the greatest difference (~ 10 J kg^{-1}) during the afternoon on day 2 (see Fig. 5.12). This reduction is related mainly to the difference in the vertical thickness of the cloud layer. In CU-BCL the cloud base rises (Fig. 5.13 (c)) but the inversion height has not changed (Fig. 5.13 (a)). In these simulations CAPE varied approximately with the square of the vertical distance between the level of free convection (just above cloud base) and the level of neutral buoyancy (roughly corresponds to cloud top). This is because the temperature difference between the moist adiabat and the environment increases approximately linearly with height between the level of free convection and the level of neutral buoyancy. Therefore, even a small change in cloud layer thickness can lead to moderate change in CAPE. The slight warming of the cloud layer in experiment CU-BCL (Fig. 5.10 (a)) also contributes to the CAPE reduction as this reduces the relative buoyancy of cloud parcels rising through the cloud layer.

Figure 5.9: *Smoothed hourly average cloud cover (%) as a function of time in the control (solid line) and experiment CU-BCL (dashed line).*

However, despite the rise in cloud base (Fig. 5.10 (c)) and the decrease in CAPE (Fig. 5.12), the mean cloud mass flux (Fig. 5.11) is not significantly reduced in the aerosol simulation (the slight reduction of cloud mass flux is smaller than the standard error, indicated by the shading). There were no significant changes in the total water flux, and turbulent kinetic energy profiles (not shown), or the inversion height (see Fig. 5.10 (a)). This suggests that convective transports and turbulent mixing were not significantly affected by the aerosol heating in the sub-cloud layer.
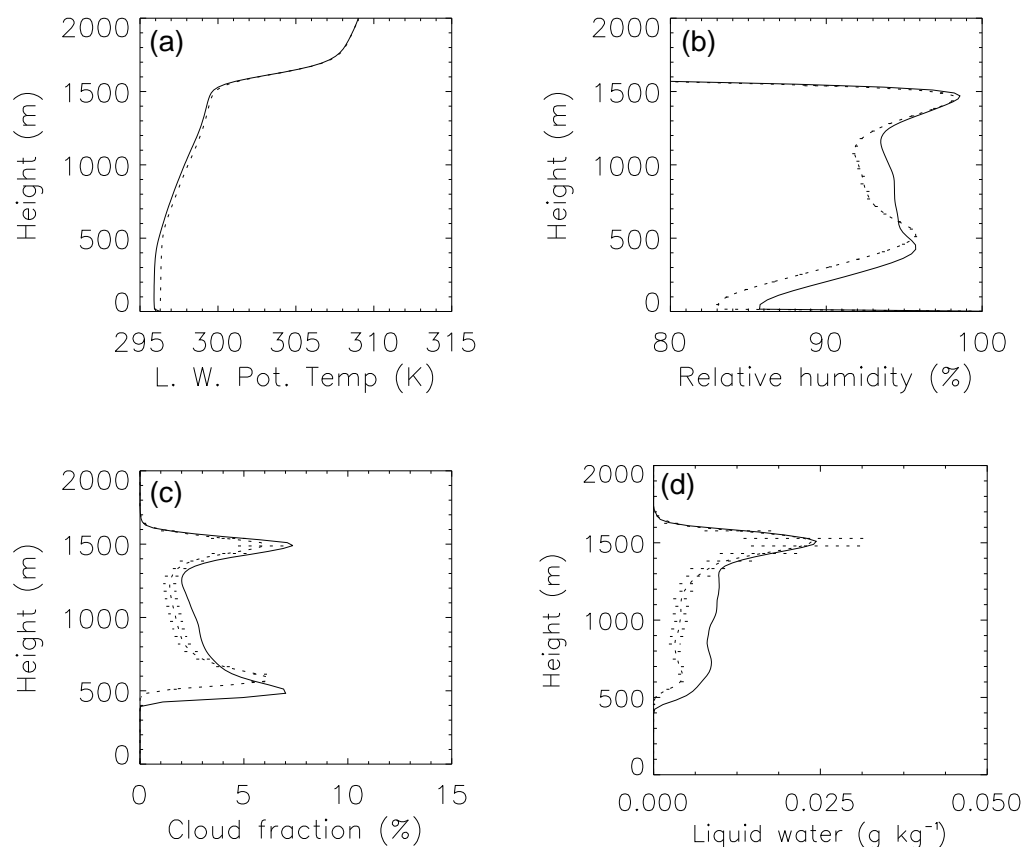
Figure 5.10: *Horizontally averaged (a) liquid water potential temperature (K), (b) relative humidity (%), (c) cloud cover (%), and (d) liquid water mixing ratio (g kg^{-1}) as a function of height (m), averaged between 3600 and 4100 h in the control (solid line), and experiment CU-BCL (dotted line). Shading indicates the standard error from temporal variability in experiment CU-BCL.*

Thus, absorbing aerosols in the sub-cloud layer had no significant impact on the intensity of cumulus convection. The reduction of total cloud cover and LWP, and the semi-direct forcing are relatively small, and rather uncertain. For example, there is no physical explanation for the relatively high cloud cover on the morning of day 1 in the aerosol simulation; it is probably just part of the natural variability in the simulations, yet it is the main reason for the lower semi-direct forcing on day 1 (see Table 5.4). Further experiments, either initial condition ensembles, or simulations with much bigger domains would be required to quantify the impact of such variability on the semi-direct forcing, and to reduce uncertainty in the results.
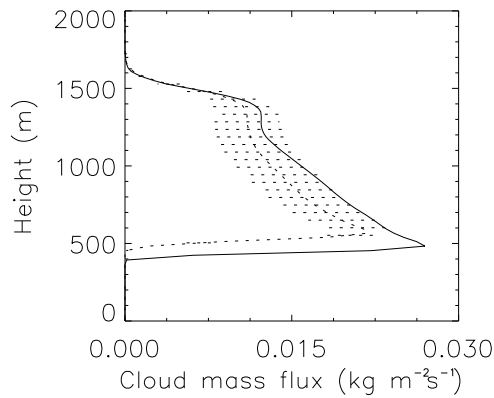
Figure 5.11: *Horizontally averaged cloud mass flux (kg m^{-2} s^{-1}) as a function of height (m), averaged between 3600 and 4100 h in the control simulation (solid line) and experiment CU-BCL (dotted line). Shading shows the standard error in experiment CU-BCL, derived from the temporal variability.*
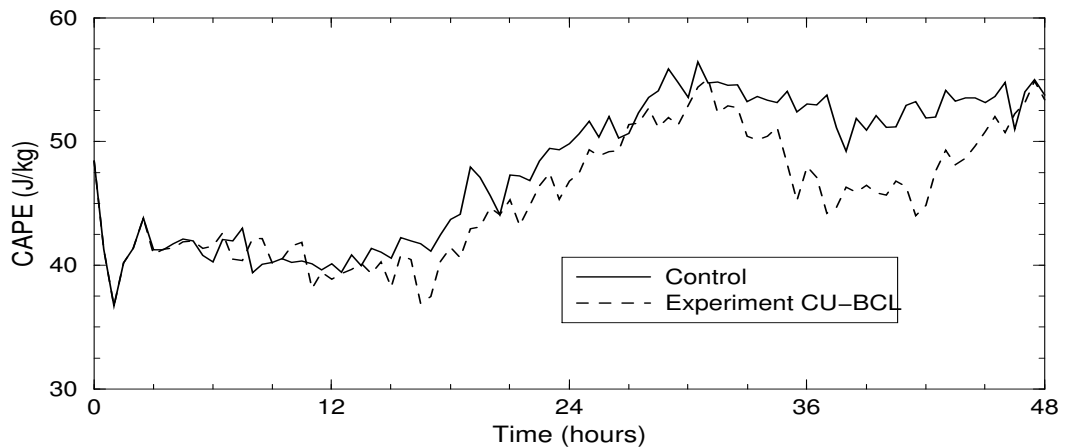
Figure 5.12: *Convective available potential energy (J kg^{-1}) in the control simulation (solid line) and experiment CU-BCL (dotted line).*

5.3.2 Aerosols above the inversion

In experiment CU-FT the absorbing aerosols above the inversion increased cloud cover by about 7% (Table 5.3), and led to a small negative semi-direct forcing (Table 5.4). The two-day mean semi-direct forcing (-1.8 W m^{-2}) was much lower than the mean semi-direct forcing in the equivalent stratocumulus experiment (-10.2 W m^{-2} , see experiment SC-FT1 in Table 5.1)).

The aerosols increase the potential temperature above the inversion by about 2 K by the afternoon of the second day (Fig. 5.13 (a)). This suppresses entrainment of free tropospheric air into the BL, leading
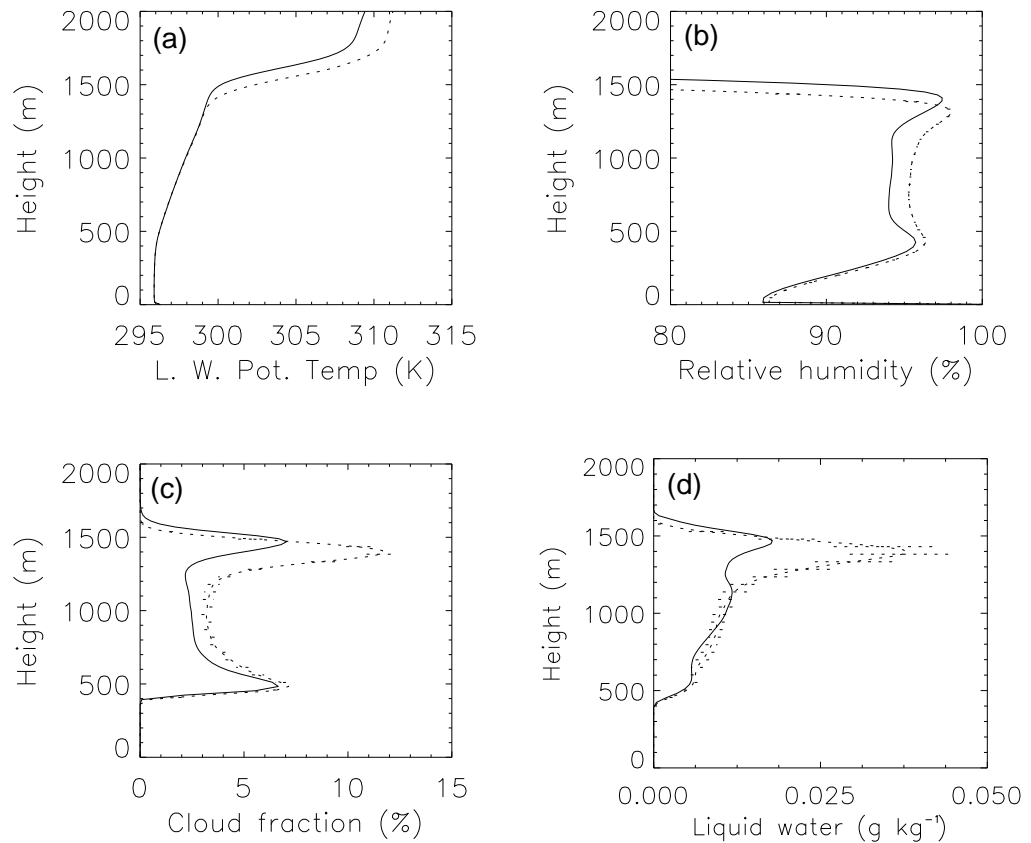
Figure 5.13: *Horizontally averaged (a) liquid water potential temperature (K), (b) relative humidity ($\%$), (c) cloud cover ($\%$) and (d) liquid water mixing ratio (g kg^{-1}) as a function of height (m), averaged between 3600 and 4100 h in the control (solid line), and experiment CU-FT (dotted line). Shading shows the standard error in experiment CU-FT, derived from the temporal variability.*

to an increase in relative humidity, cloud fraction, and cloud liquid water in the BL (Fig. 5.13 (b) - (d)). The reduction of entrainment rate is evident from the 100 m relative drop of the inversion and cloud top height (Figs. 5.13 (a) & 5.14 (b)).

The increase in cloud cover is not immediate on day 1 (Fig. 5.9); actually it is not until mid-afternoon that the upward trend becomes apparent. It takes time for the semi-direct effect to develop, just as the heating of the air above the inversion takes time. The difference in cloud cover is also more pronounced at night. This is because the mean relative humidity is higher at night due to the longwave cooling, and is very close unity at the cloud top. As the average relative humidity just beneath the inversion approaches unity, the cloud fraction increases rapidly and becomes more sensitive to any change in mean relative humidity, in this case caused by the change in entrainment rate.
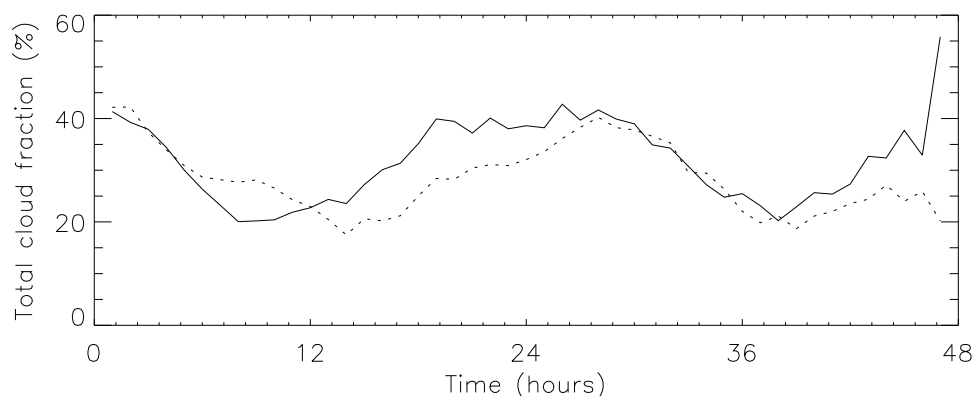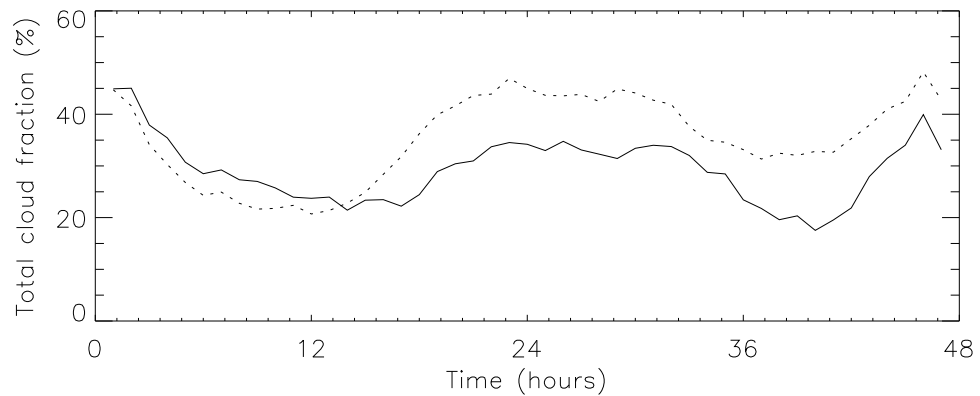
Figure 5.14: *Smoothed hourly average cloud cover (%), as a function of time in the control (solid line) and experiment CU-FT (dotted line).*

5.4 Conclusions and comparison with direct forcing

Large-eddy simulations of the stratocumulus and intermediate trade cumulus BLs have been performed with a idealised range of aerosol vertical distributions. These show that the magnitude and sign of the semi-direct effect depend on the location of absorbing aerosols relative to the cloud. The semi-direct effect is positive and relatively strong when the aerosols are located in the BL, but moderate-small and negative when the aerosols are located above the cloud-top inversion. This conclusion holds for both stratocumulus and cumulus regimes although the magnitude of response was smaller for cumulus, which is consistent with the findings from chapter 3.

The positive semi-direct effect is maximised when the aerosols are located within the cloud layer so that the cloud is strongly heated and the BL is stabilised. The negative semi-direct effect was strongest when the aerosols are located directly above the inversion so that they increase the potential temperature contrast across the inversion and reduce the entrainment rate. Absorbing aerosol layers have a small negative semi-direct effect even if they are far above the inversion because they attenuate the down-welling solar flux, which reduces shortwave absorption in the clouds below. Scattering aerosols above the inversion also attenuate the down-welling solar flux and decrease the total solar absorption by the cloud. However, they also increase radiation path lengths, increasing the solar heating rate near the top of the cloud. As a result, the semi-direct effect of scattering aerosol is negligible for moderate aerosol optical depths (0.2 or less).

It is important to gauge these semi-direct forcings estimates against their direct radiative forcings to de-

termine their relative importance and the overall radiative forcing. In chapter 2 the semi-direct forcing was found to be seven times more important than the direct forcing in determining the total radiative effect of increasing aerosol absorption. However, for absorbing aerosols above the inversion the semi-direct and direct forcings are about equal in magnitude and roughly cancel each other out because the semi-direct forcing is negative and the direct forcing is positive. An absorbing aerosol layer above a reflective cloud absorbs much more solar radiation than an absorbing aerosol layer below the cloud and gives a positive, and much larger direct forcing (compare experiment SC-BL with experiments SC-FT2 and SC-FT1, Table 5.1). Thus, for aerosols above the inversion the direct forcing becomes relatively more important and the semi-direct forcing is relatively less important. For aerosols far above the inversion the semi-direct forcing is only a small negative offset to the positive direct forcing (see Table 5.1, experiment SC-FT2).

In conclusion, the assumption that aerosols are confined mainly to the BL (chapters 2 and 3) may lead to an overestimate of the semi-direct forcing, and an overestimate of its importance relative to the direct aerosol forcing. Deeper aerosols layers that extend well above the local inversion will lead to a much smaller semi-direct effect, or even a negative one if most of the aerosol mass is above the inversion. The global semi-direct forcing is likely to be positive because the positive semi-direct forcing for aerosols in the boundary was more than twice the magnitude than the negative semi-direct forcing from aerosols above the inversion. Also, aerosols concentrations are generally observed to be higher in the BL than above the BL. However, this chapter shows that predicting the semi-direct effect in any model requires accurate knowledge of the aerosol vertical distribution, in addition to accurate prediction of the BL depth, and cloud properties.

CHAPTER 6

An observed marine stratocumulus example

6.1 Introduction

In chapters 2 and 5 it was shown that the semi-direct forcing could be large and positive for situations where absorbing aerosols are located in a marine stratocumulus Boundary Layer (BL). Observations from the First International Satellite Cloud Climatology Project Regional Experiment (FIRE) were used to simulate the stratocumulus-capped BL and idealised aerosol vertical distributions with specified optical properties were used to evaluate the semi-direct forcing. The simplicity of this approach enabled an exploration of the mechanisms involved in the semi-direct effect and its dependence on the aerosols. Chapter 2 showed that the semi-direct forcing was linearly proportional to the single scattering co-albedo (which sets the aerosol heating rate) and chapter 5 showed that the magnitude, and even the sign of the semi-direct forcing depends on the aerosol vertical distribution. Also, chapter 3 showed that the semi-direct forcing for a given aerosol heating rate depended on the cloud conditions, particularly the amount and type of cloud.

Therefore, to estimate the importance of the semi-direct effect in further experiments, the aerosol optical properties, their vertical distribution, and the meteorological conditions used should be based on coincident observations. Unfortunately aerosol observations are not available from FIRE, ATEX or BOMEX, but two recent field campaigns: the Atlantic Stratocumulus Transition Experiment (ASTEX), July 1992, and the second Aerosol Characterization Experiment (ACE-2), June-July, 1997 provide a wealth of aerosol observations over the northeast Atlantic Ocean, along with meteorological observations of the marine BL, including observations of cloud properties. During these field campaigns there were frequent outbreaks of continental pollution that brought moderately absorbing aerosols into regions where stratocumulus and cumulus clouds commonly formed. ASTEX and ACE-2 therefore provide very useful data on which to base an LEM experiment.

The aim of this chapter is to evaluate the semi-direct forcing for an observed, representative case study involving moderately absorbing anthropogenic aerosols within a stratocumulus dominated region. This will assess how important the semi-direct forcing is in a more realistic situation. Another aim of this

chapter is to establish whether results from the previous idealised experiments can be scaled appropriately to estimate the magnitude of the semi-direct effect for the ASTEX case. If this were possible then perhaps the semi-direct forcing could be parameterized, given information about the aerosols and the cloud conditions. A method for estimating the semi-direct effect is shown in section 6.3.1 and compared with the results from the LEM experiment in section 6.5.

6.2 Observations of aerosols and clouds over the northeast Atlantic

The LEM experiment in this chapter is based on unpublished aircraft data from the Met Office C-130, and data from the National Center for Atmospheric Research (NCAR) Electra, reported in Clarke *et al.* (1996), hereafter CLK96. Both aircraft were a key part of ASTEX and collected measurements through a polluted continental airmass on 15-16 June 1992, approximately 1500 km west from the coast of Portugal. The C-130 took standard meteorological measurements, including cloud water, and also measured the aerosol number concentration using the Passive Cavity Aerosol Spectrometer Probe (PCASP) (Strapp *et al.*, 1992). However, aerosol optical properties were not measured on the C-130 so measurements taken from the Electra aircraft are used to determine the aerosol composition and single scattering albedo.

The essential parameters required for the LEM experiment are the aerosol single scattering albedo and optical depth, some information on how the aerosols were distributed in the vertical, and meteorological measurements (temperature, humidity and cloud water). The meteorological conditions and aerosol vertical distribution for the LEM experiment were taken from one particular profile, taken by the C-130. The optical depth was also calculated from the C-130 aerosol data, using information from the Electra to determine the aerosol composition and single scattering albedo. The following sections give an overview of ASTEX and ACE-2 and the typical conditions during pollution outbreaks over the stratocumulus regions in the northeast Atlantic Ocean. Measurements of aerosol vertical distributions, single scattering albedo, and optical depth are presented in sections 6.2.4, 6.2.5 and 6.2.6 including the measurements from the C-130 and Electra that have been used to set up the LEM experiment.

6.2.1 ASTEX and ACE-2

ASTEX and ACE-2 were major field campaigns that took place in the northeastern Atlantic Ocean. Each involved measurements from a variety of ships, aircraft, satellites and ground-based stations.

The primary focus of ASTEX was the transition of stratocumulus to trade cumulus in the marine BL (Albrecht *et al.*, 1995a), whereas the primary focus of ACE-2 was to characterise the physical, chemical, radiative, and cloud nucleating properties of major aerosol types in that region (Raes *et al.*, 2000). However, ACE-2 also provided good measurements of cloud properties (e.g. Johnson *et al.* (2000)), and aerosols measurements were also taken during ASTEX as part of the Marine Aerosol and Gas Experiment (MAGE) (Huebert *et al.*, 1996). ASTEX took place in June 1992 in an area between the Canary Islands (28°N, 15°W) and the Azores (40°N 25°W) (Albrecht *et al.*, 1995a). ACE-2 took place in June and July 1997 in a similar area between the Canary Islands, the Azores and the coast of Portugal (40°N, 10°W) (Raes *et al.*, 2000).

6.2.2   Pollution outbreaks

The prevailing wind direction during the summer in this region is northeasterly, and polluted air from continental Europe is frequently advected over the region (e.g. Johnson *et al.* (2000), Verver *et al.* (2000), Muller and Ansmann (2002)). Airmass back-trajectories were used to identify the origins of air and make distinctions between marine and continental flows. An overview of the synoptic flow and pollution outbreaks during ACE-2 is given in Verver *et al.* (2000). In situ measurements were also used to distinguish between 'polluted' and 'unpolluted' air. For example, an airmass was defined as polluted if the aerosol absorption coefficient was greater than 1.2 x 10^{-6} m^{-1} indicating a significant anthropogenic black carbon content. Polluted airmasses also had a high sulphate content; Putaud *et al.* (2000) estimate 75% of the aerosol mass to be sulphates (principally ammonium sulphate) in European continental airflows measured at Tenerife (28°N, 16°W). Other aerosol constituents include organic carbon, nitrates, sea salt, and dust (Putaud *et al.*, 2000).

A schematic of a European pollution outbreak is shown in Fig. 6.1 based on the Lagrangian experiments (Johnson *et al.*, 2000) and other experiments carried out during ACE-2. Over the continent strong surface heating in the summer months produces a deep (2 - 5 km) convectively-driven BL. The convection mixes pollution vertically through the continental BL. As the continental airmass is advected over the relatively cool Atlantic Ocean a shallow marine BL forms, trapping some of the pollution. Polluted air is also advected over the top of the marine BL in what becomes the residual continental BL. The wind strength and direction often vary with height (differential advection) and the residual continental BL may gradually be replaced with cleaner air from the Atlantic, depending on the synoptic scale flow. Also, the depth of the residual continental BL will reduce with time due to large-scale subsidence, which is usually present in the sub-tropics. The marine BL grows with time
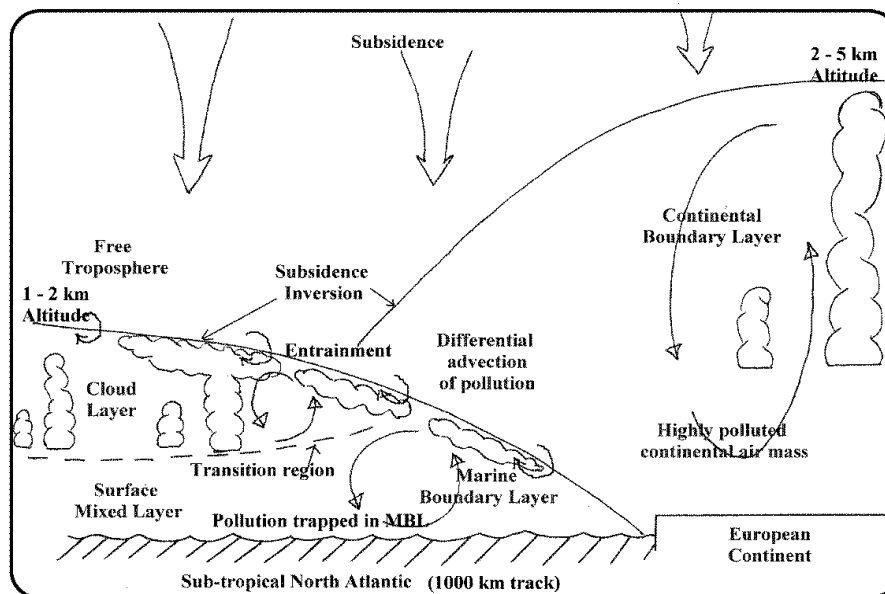
Figure 6.1: *Main features of a continental outbreak of pollution over the sub-tropical northeast Atlantic Ocean. The diagram is taken from Johnson* et al. *(2000) and is based on observations from ACE-2.*

entraining air from the residual continent BL until it encompasses all the polluted air. After this, clean free tropospheric air will be entrained at the top of the marine BL diluting pollution levels. By this stage the marine BL may be decoupled (not well mixed) so that the upper part of the BL (or cloud layer) becomes more dilute than the surface layer. The development of the marine BL and the evolution of the polluted airmass depicted in Fig. 6.1 occurs over a spatial scale of 1000 - 2000 km and over 2-5 days.

6.2.3   Clouds in the marine BL

In parallel with the growth of the marine BL is a transition of cloud types (see Fig. 6.1). The stratocumulus layers that form a few hundred kilometres off the Continent are eventually replaced with broken cumulus clouds as the BL depth increases further downstream (e.g. Bretherton (1992), Klein and Hartmann (1993), Wyant *et al.* (1997)). The transition in cloudiness is reflected in the regional distribution of cloud fraction shown in satellite data (see Fig. 2.1 in section 2.1 and Fig. 3.1 in section 3.1 for satellite maps of stratocumulus and cumulus cloud amounts). During intermediate stages the BL becomes decoupled and cumulus often develop helping to sustain the stratocumulus layer. See section 2.1.2 for an explanation of the stratocumulus to cumulus transition. A full introduction to stratocumulus and the marine BL is presented in chapter 2, section 2.1.
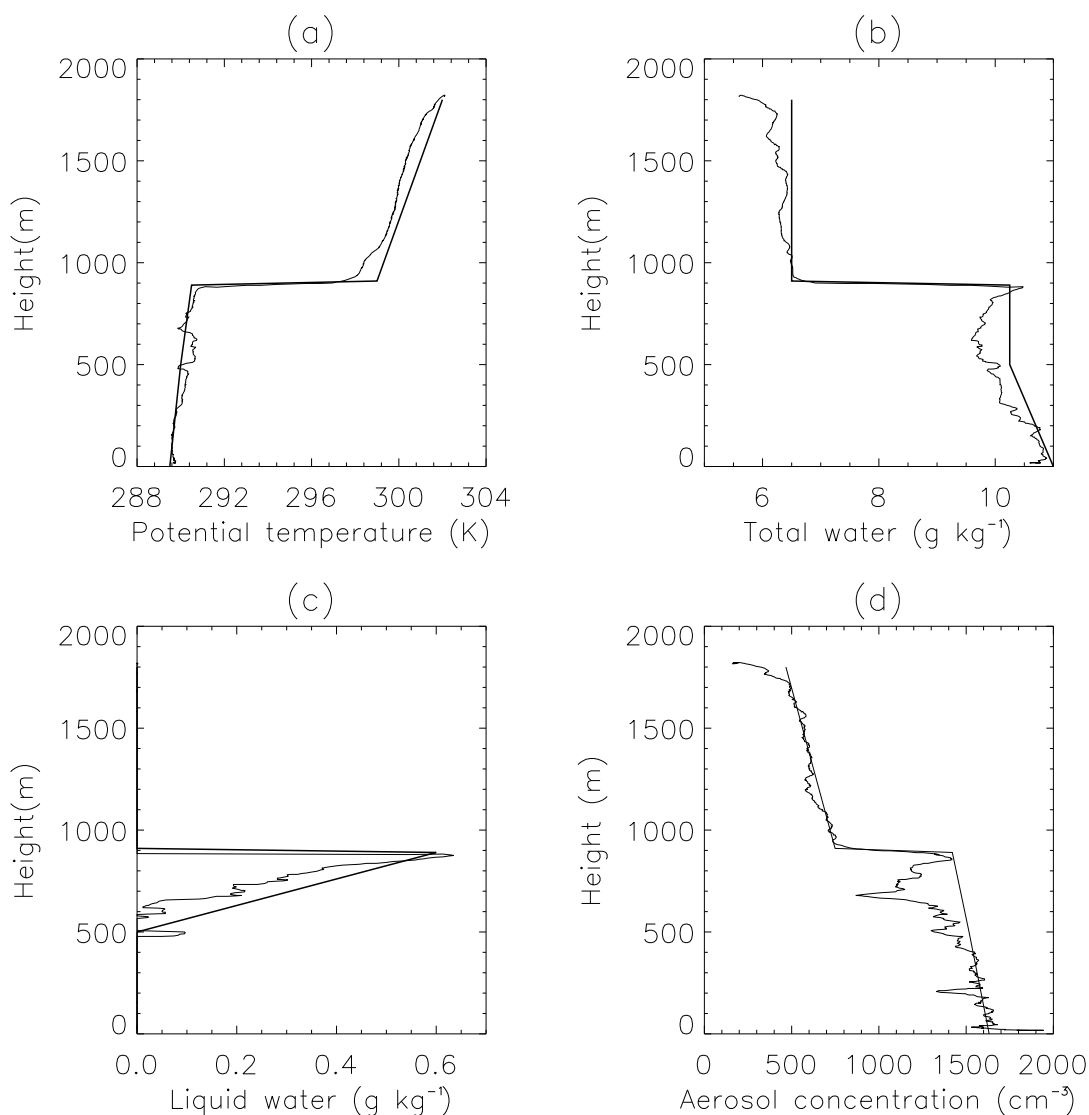
Figure 6.2: *Aircraft observations from the Met Office C-130 flight A212, profile p2.8 taken at 1300 GMT on June 16, 1992 during ASTEX: (a) Liquid water potential temperature (K), (b) total water mixing ratio (g kg^{-1}), (c) liquid water mixing ratio (g kg^{-1}), and (d) aerosol number concentration (cm^{-3}). Thin lines are the profile data and thick straight lines are fits to the data showing the values that were used to set up the LEM experiments.*

Figure 6.2 (a) - (c) shows profiles of liquid water potential temperature (θ_l), total water mixing ratio (Q_t), and cloud liquid water mixing ratio (Q_l) taken by the Met Office C-130 aircraft from the top of a polluted layer (1800 m) to 30 m above the surface. This particular profile (p2.8 from flight A212) was taken at 1300 GMT on June 16, 1992 at 37°N, 19°W, about 1400 km west from the southern tip of Portugal. This profile was selected as the basis for the LEM experiment; the fitted lines in Fig. 6.2 show the actual inputs used to initialise the LEM. The profile was chosen from a large number of

profiles because it was taken through a continuous section of stratocumulus and therefore provides a good sample of the structure of the BL and the cloud. The BL is relatively deep (900 m) and slightly decoupled (Fig. 6.2 (a) & (b)), with a peak in liquid water at 500 m (Fig. 6.2 (c)), which suggests that small cumulus were forming beneath the main stratocumulus cloud base (650 m). Thus, the selected profile is an example of a deepening-decoupling stratocumulus-capped BL, as illustrated in the transition region of the schematic above (Fig. 6.1). The inversion at 900 m was relatively strong ($\Delta\theta = 8.5$ K) with a moderate jump in total water ($\Delta q_t = 4$ g kg^{-1}), which would have favoured the persistence of the stratocumulus (based on cloud-top entrainment instability and observations e.g. Albrecht (1991)).

6.2.4 Measurements of the vertical distribution

The vertical distribution of aerosols over the northeast Atlantic during pollution outbreaks varies with distance from the continent (and also with time), following the evolution of the polluted air, and the marine BL illustrated in Fig. 6.1. This is influenced by the depth and structure of the BL in the continental source regions. The air at different heights may also have different origins due to differential advection. Once the airmass has moved over the Atlantic, large-scale subsidence and the growth of the marine BL are the dominant processes affecting the aerosol vertical distribution. Not surprisingly, the vertical distribution of aerosols varied considerably with space and time during ASTEX and ACE-2.
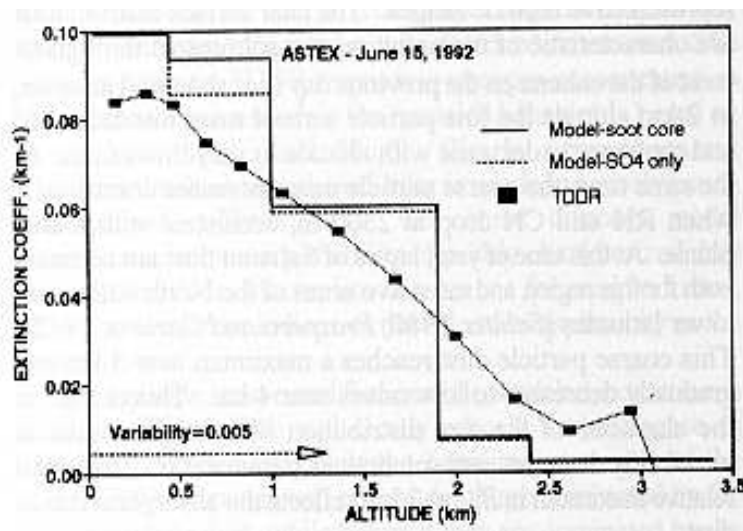
Figure 6.3: *Vertical distribution of aerosol extinction coefficient from the total-direct-diffuse radiometer (TDDR), and from a model (see section 6.2.5) taken from the Electra on June 15, 1992, during ASTEX. The figure is taken from CLK96.*

Muller and Ansmann (2002) and Ansmann *et al.* (2002) present vertical profiles of aerosol extinction and backscatter, taken from a lidar at Sagres on the southwest tip of Portugal. Within continental airmasses the aerosol mass concentration generally decreased with height gradually in the lowest 1 - 2 km and then more rapidly, tending towards very low values somewhere between 2 and 3 km. During the ACE-2 second and third Lagrangian experiments, the Met Office C-130 research aircraft made many profiles through the polluted layer a few hundred kilometers southwest of Portugal; examples of these are shown in Osborne *et al.* (2000) and Wood *et al.* (2000). The continental pollution layer extended to an altitude of around 1.5km and the marine BL inversion was at 1 km. Further downstream in the Canary Islands the pollution-related aerosols were mainly found within the lowest 1 km (Ostrom and Noone, 2000) with clean free tropospheric air entraining at the top of the BL ($\sim$ 2 km). Elevated dust layers between 2.5 and 5km, were also observed off the African coast at times (Schmid *et al.*, 2000)).

Figure 6.2 (d) shows the Passive Cavity Aerosol Spectrometre Probe (PCASP) number concentration from the C-130 profile with fitted lines showing the values used to set up the aerosol mass mixing ratio profile in the LEM. The aerosol concentration was higher in the BL than the free troposphere and the data suggest a sharp decline across the inversion. However, the aerosol concentration measurements in the cloud may be subject to errors from contamination by shattered water droplets entering the instrument (personal communication Simon Osborne). Cloud contamination was an unavoidable problem as the purpose of the chapter was to use coincident aerosol and meteorological data from stratocumulus conditions. The fitted line assumes that the aerosol concentration in the BL decreased at a uniform rate with height based on the concept of a reasonably well mixed BL. There is a sharp decline in aerosol concentration at the inversion (900m) between the high values in BL and in the medium values in the free troposphere (residual continental BL). Above the inversion the aerosol concentration decreases gradually with height. The profile only sampled up to 1800m but other deeper profiles from the flight show that there was very little aerosol above 2 km in that region. This vertical distribution is consistent with profile data from the Electra (see Fig. 6.3) although that data does not show a discontinuity related to an inversion because it comprises of many profiles averaged together.

6.2.5 Aerosol single scattering albedo measurements

In ACE-2 the aerosol single scattering albedo was determined by in-situ measurements, multiwavelength lidar, and as a best-fit parameter when comparing measured and calculated radiative flux changes at the surface. Flux best-fits of measured and calculated radiative fluxes yielded a column average midvisible ω of 0.90 ± 0.04 (Russell *et al.*, 2002) over 6 pollution outbreaks during ACE-2, and an average

mid-visible ω of 0.98 ± 0.03 for 8 clean periods. A multi-wavelength aerosol lidar operated at Sagres on the southwest tip of Portugal and used an inversion technique to reconstruct the aerosol size distribution and refractive indices from measured backscatter and extiction coefficients at 6 wavelengths (Muller and Ansmann, 2002). An average ω of 0.95 ± 0.06 was estimated for European continental airmasses.

In-situ measurements of aerosol scattering and absorption were made using nephelometers and absorption photometers from the ACE-2 ship (Quinn *et al.*, 2000), and from the Pelican aircraft (Ostrom and Noone, 2000). Also, Carrico *et al.* (2000) made in-situ measurements from the Sagres site in Portugal using nephelometer and absorption aethelometer. The average mid-visible single scattering albedos from these techniques were as follows: 0.95 ± 0.04 (Quinn *et al.*, 2000) and 0.95 ± 0.02 (Carrico *et al.*, 2000) for 23 polluted days during June-July 1997, and 0.83 ± 0.08 (Ostrom and Noone, 2000) for 4 flights through polluted airmasses. The probability distribution function of observed single scattering albedos from Carrico *et al.* (2000) is shown in Fig. 6.4 with the flux best-fit estimate (labelled as VHH99).

One difficulty in comparing in-situ and remotely sensed column integrated measurements is that ω increases with relative humidity (see section 1.3.1). Remotely sensed column measurements (flux best-fit and lidar methods) measure the column average ω at ambient humidity, which may vary widely through the column. In situ instruments tend to modify the relative humidity of the air sample as it enters the instrument. The measurements of Quinn *et al.* (2000) and Carrico *et al.* (2000) were made at controlled relative humidities of 55% and 82% , respectively. The measurements of Ostrom and Noone (2000) were taken at lower than ambient relative humidities ($> 40\%$). This may explain why Ostrom and Noone's ω estimate is comparatively low. Furthermore, the inlet on the Pelican aircraft rejected most particles larger than 2.5 μ m and undersampled sea salt, which may also have led to a low bias.

The single scattering albedo was also measured from the Electra aircraft during ASTEX through a combination of in-situ measurements and Mie calculations (CLK96). The size distribution required for the calculations was measured by two instruments. A laser optical particle counter sized particles in the range 0.15-7.5μm, and a differential mobility analizer sized particles of sizes 0.02-0.6μm. The laser optical particle counter also operated at three different temperature (40º, 150º, 300ºC) to characterize the aerosol volatility and thereby gain information about the composition of the aerosols. For example, about 30% of the aerosol mass was lost at 150ºC and 92% was lost at 300ºC, leaving a residual composed mainly of black carbon. The high volatility of the fine aerosol indicated that a large fraction (0.7-0.9) of the fine-mode mass was probably sulphate. Chemical analysis of filter extract also con-
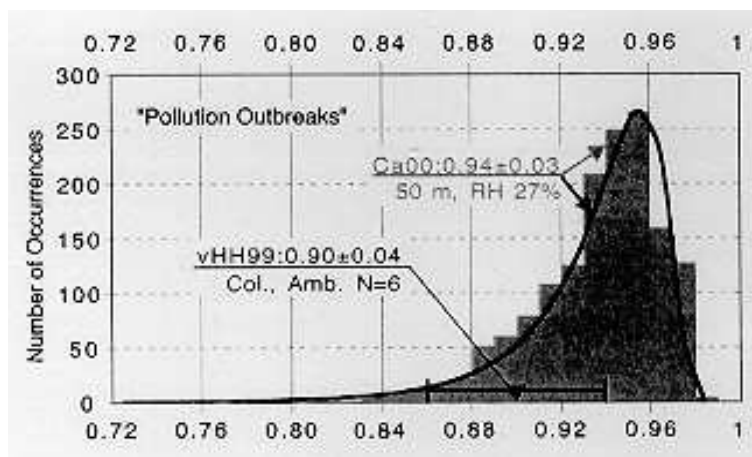
Figure 6.4: *Probability distribution function of mid-visible single scattering albedo during pollution outbreaks over the ACE-2 region, taken from Russell* et al. *(2002). The data originates from absorption photometer and nephelometer measurement Carrico* et al. *(2000) (Ca00), and best fits of modelled and measured radiative fluxes (unpublished data from von Hoyningen-Huene, 1999) (VVH99).*

firmed this finding. An absorption aethelometer was used to measured the light attenuation of aerosols collected on a filter. This gave the aerosol absorption coefficient and the black carbon concentration by assuming black carbon was the principal absorber and by using the black carbon calibration of Gundel *et al.* (1984).

This information about the aerosol chemical composition was used to estimate the refractive indicies required for the Mie calculations. Using these refractive indicies, and the size distribution data (corrected to account for wet growth using Tang and Munkelwitz (1977)) optical properties were calculated. The mean single scattering albedo and specific extinction coefficient were estimated as 0.91-0.96, and 4 ± 0.7 m^2 g^{-1} for the 2 flights. This is consistent with the range of estimates ACE-II during periods affected by continental pollution (see 2 paragraphs above). In the LEM experiment a single scattering albedo of 0.94 was used as it was in between the upper and lower range of estimates from the Electra.

6.2.6   Aerosol optical depth measurements

Aerosol optical depths were estimated for ACE-2 using satellite measurements from the National Oceanographic and Atmospheric Administration (NOAA) Advanced Very High Resolution Radiometer (AVHRR). During 'unpolluted' conditions the aerosol optical depth was generally 0.05-0.1 (at mid-visible wavelengths) but rose sharply during pollution outbreaks, often to over 0.2, and sometimes to over 0.4 when there were incursions of Saharan dust (Durkee *et al.*, 2000). The regional mean aerosol

optical depth for ACE-2 was estimated as 0.16 (Durkee *et al.*, 2000). Sunphotometer measurements taken from the ACE-2 ship give aerosol optical depths of 0.16-0.18 at 500 nm on July 10 and 22, days when the ship was in continental air from Western Europe.

Aerosol optical depths were also measured from the NCAR Electra aircraft during ASTEX using two methods. Firstly from a multi-wavelength total-direct-diffuse radiometer (TDDR), and secondly from a combination of in-situ aerosol measurements and Mie-scattering calculations (see above). The TDDR gave a mean aerosol optical depth of 0.16 ± 0.07 and the second technique gave an optical depth of 0.157 ± 0.04 for the two flights, as reported by CLK96.

To obtain an optical depth for the LEM experiment the refractive indicies from CLK96 were used along with the size distribution from the C-130 PCASP data to calculate aerosol optical properties via mie scattering. This method gave an optical depth of 0.20 for the selected aerosol concentration profile shown in Fig. 6.2 (d) (fitted lines were used rather than the raw data). This estimate is close to the estimate from CLK96 (0.16), the observations from Livingstone *et al.* (2000) (0.16-0.18), and the region mean estimate from Durkee *et al.* (2000) (0.16). Therefore, the estimate from the C-130 data (0.20 at 550 nm) seems representative / realistic and was used in the LEM experiment.

6.3   Parameterization of the semi-direct forcing?

One aim of this chapter is to see whether the semi-direct forcing for a unique cloud and aerosol situation can be predicted using previous results from idealised experiments, i.e. is there potential for the semi-direct forcing to be parameterized? A parameterization could use some diagnosis of the cloud conditions and information about the distribution of absorbing aerosol material to estimate the semi-direct forcing. This would enable regional or even global estimates of the semi-direct forcing.

The success or failure of such a method depends on just how sensitive the semi-direct forcing is to the exact distribution of absorbing aerosol, and meteorological factors such as cloud amount and BL depth. In this section a simple empirical model is devised and used to estimate the semi-direct forcing for the ASTEX experiment. Later in the chapter this estimate will be compared with the actual result to see whether the the empirical model was successful, or not.

The absorbing aerosol will lead to evaporation and enhanced decoupling (as shown in chapter 2) tending to reduce the LWP giving a positive semi-direct forcing. The absorbing aerosol above the inversion will help to reduce the entrainment rate by strengthening the inversion (as shown in chapter 3) and this

will tend to increase LWP and decrease the semi-direct forcing. This may only be a relatively small offset to the positive forcing since the aerosol mass mixing ratio above the BL in ASTEX-aerosol is about half the value in the BL.

However, to estimate the semi-direct forcing in the ASTEX experiment several other factors need to be considered. Firstly, in the ASTEX experiment the single scattering albedo is higher than in the idealised experiments of chapter 5 (0.94, compared to 0.88) so the aerosols are only half as absorbing. Also, the aerosol mass mixing ratio in the BL is also a little lower in the ASTEX experiments than in the experiments of chapter 5. In addition, in ASTEX-aerosol there are vertical gradients in the aerosol mass mixing ratio both in and above the BL; the mixing ratio decreases gradually with height. Furthermore, the BL structure in the ASTEX stratocumulus case is different from that in the FIRE stratocumulus. Mainly, the BL is 50% deeper in ASTEX (900 m, compared to 600 m) and is initially not well-mixed. A rough estimate of the semi-direct forcing in the ASTEX experiment has been made using a few simple assumptions.

6.3.1   Empirical model

In chapter 5 it was shown that absorbing aerosols in the BL give a strong positive semi-direct forcing but absorbing aerosols in the free troposphere (FT) give a moderate negative forcing. When aerosols were located both in and above the BL, with equal mass concentrations, the semi-direct forcing was moderate and positive. The ASTEX experiment in this chapter has absorbing aerosols located both in and above the BL but with a lower mass concentration above the BL (Fig. 6.2 (d)). Therefore, a positive semi-direct forcing is expected in the ASTEX experiment although the magnitude will depend on other factors such as the aerosol single scattering albedo (ω).

For simplification it is assumed that the semi-direct forcing can be separated into two independent contributions: a positive one from absorbing aerosol in the BL (SDF_{BL}), and a negative one from absorbing aerosol in the FT (SDF_{FT}). These add together linearly to give the semi-direct forcing (SDF):

$$SDF = SDF_{BL} + SDF_{FT} \tag{6.1}$$

An experiment in chapter 5 showed that the linearity assumption is good for the first day of an experiment but on subsequent days the semi-direct forcing was significantly lower than expected from the linear sum of the two contributions. Therefore, this assumption could lead to an overestimation of the semi-direct forcing for multi-day experiments.

The strength of each contribution (SDF_{BL}, SDF_{FT}) is assumed to be linearly proportional to the mean aerosol heating rate in that region. The assumption of linearity between aerosol heating rate and semi-direct forcing is justified by the set of experiments in chapter 2 (see Fig. 2.22, in section 2.2.4) as long as the aerosol heating rate is not so great as to completely evaporate the cloud. For a given solar insolation the dominant factor determining the aerosol heating rate is the rate of change of absorption optical depth with pressure; $(1 - \omega)d\tau/dp$. Scattering by the aerosol is not considered as there was no significant impact from purely scattering aerosols in previous experiments (experiment A-100 in section 2.2.4, and experiment SC-FTS in section 5.2.2). Therefore, the mean heating rate in the BL or FT region is proportional to the change in absorption optical depth, $\Delta\tau(1 - \omega)$, divided by the change in pressure over the region Δ P. The semi-direct forcing contributions are simply:

$$SDF_{BL} = C_{BL}(\Delta\tau(1 - \omega)/\Delta P)_{BL} \tag{6.2}$$

$$SDF_{FT} = C_{FT}(\Delta\tau(1 - \omega)/\Delta P)_{FT} \tag{6.3}$$

In this example BL is taken as the region below the inversion, and FT is taken to be the region between the inversion and the top of the aerosol layer at 1800 m. The term $\Delta\tau_a/\Delta P$ is the *potential aerosol heating rate*. The constants C_{BL}, C_{FT} simply relate the semi-direct forcing to the *potential aerosol heating rate*, which depends on the reduction in LWP for a given aerosol heating, and the strength of the incident solar radiation. In the ASTEX experiment the incident solar insolation was about the same as in the FIRE case because the latitude and date were similar, and in both cases the underlying surfaces were ocean and there was a full stratocumulus layer with a similar diurnal cycle of LWP (see Fig. 6.5 in section 6.5.2). Therefore, a dependence on incident solar radiation does not need to be included in this example. Also, since the cloud conditions were very similar in the FIRE and ASTEX simulations it is assumed that the LWP response for a given aerosol heating rate will be the same. Therefore, with all other factors equal the constants C_{BL}, C_{FT} can be determined from the FIRE stratocumulus in chapter

5 (experiment SC-BL and SC-FT1):

$$C_{BL} = SDF_{SC-BL}/(\Delta\tau(1-\omega)/\Delta P)_{SC-BL} \tag{6.4}$$

$$C_{FT} = SDF_{SC-FT1}/(\Delta\tau(1-\omega)/\Delta P)_{SC-FT1} \tag{6.5}$$

where SDF_{SC-BL} and SDF_{SC-FT1} are the semi-direct forcing results for experiments SC-BL and SC-FT1 which were 23 W m^{-2} and -10 W m^{-2}, respectively. The optical depths for SC-BL and SC-FT1 were 0.12 and 0.2, respectively, and the single scattering albedo was 0.88 in both SC-BL and SC-FT1. This method gives a very rough estimate for the semi-direct forcing, which is 7.5 W m^{-2} for the ASTEX experiment. The individual contributions to this are: $SDF_{BL} = 9.1$ W m^{-2}, and SDF_{FT} = -1.6 W m^{-2}.

The key assumption in these estimates is that the semi-direct forcing in ASTEX will be the same in the FIRE cases for a given aerosol heating rate in a given region (BL or FT). This assumes that the LWP of the cloud will respond in the same way, or at least will have the same level of response in ASTEX and FIRE for a given aerosol heating rate. This seems plausible; the aerosol heating rate will determine the evaporation rate of the cloud and the rate at which the BL or FT stabilises. However, chapter 2 showed that the semi-direct forcing was intimately related to the turbulent processes in the BL, the decoupling, the inversion characteristics and the entrainment rate. Therefore, the difference in the BL height, turbulence structure, mean entrainment rates and latent heat fluxes between FIRE and ASTEX simulations may lead to a different level of response in each case. Comparing the semi-direct forcing estimate above with the result from the ASTEX experiment (section below) will show whether differences such as these are important in determining the strength of the semi-direct forcing.

For simplicity, the method above is based only on the mean heating rates in the BL or FT regions. This neglects the possible impact of vertical variation within the BL or FT region. In the ASTEX experiment there are moderate vertical gradients of aerosol mass mixing ratio both in the BL and above it (see Fig. 6.2 (d)). Experiments in chapter 5 showed that the semi-direct forcing was roughly five times greater for aerosols in the upper part of the BL, than in the lower part of the BL because heating the cloud layer enhanced the decoupling and lead more readily to evaporation of the cloud. Also, experiments SC-FT1 and SC-FT2 showed that absorbing aerosol immediately above the inversion (first few hundred

metres) had a greater influence than absorbing aerosol far above the inversion (1 km or more) because changes in temperature immediately above the inversion were more important than the attenuation of solar radiation caused by the aerosols above the inversion. Accounting for these effect in the empirical model above would would lead to a lower semi-direct forcing for the ASTEX case. The contribution from the BL aerosol would be lower, and a lower (more negative) semi-direct forcing contribution from the FT aerosol because of the vertical gradients in aerosol mass mixing ratio within the BL and FT (see Fig. 6.2 (d)). In addition the assumption that the contributions from absorbing aerosols above and below the inversion added linearly also would have led to the method giving an overestimate (as mentioned earlier).

6.4   Experimental setup

The initial meteorological conditions are derived from the temperature, relative humidity and liquid water content data obtained from the selected C-130 profile (P2.8, flight A212). Fig. 6.2 shows the θ_l and q_t values calculated from the raw data and the best-fit lines that were used for the initial model state (point values are also shown in Table 6.1).

The sea surface temperature was set to 292 K by extrapolating the potential temperature data to the surface. The surface pressure was 1025 mb, as calculated from the profile data. The initial and geostrophic wind speed was set to 6 m s^{-1}, based on an analysis for June 16, 1992 from the National Centers for Environmental Prediction (NCEP) and synoptic analyses for June 1992 from the European Centre for Medium range Weather Forecasts (see Albrecht *et al.* (1995a)). The subsidence rate, W$_{subs}$, was set using:

$$W_{subs} = D * Z \quad \text{for } (0 < Z < 1000 \text{ m)}, \tag{6.6}$$

$$W_{subs} = D * 1000 \quad \text{for } (Z > 1000 \text{ m)} \tag{6.7}$$

where Z is height and D is the large-scale divergence rate, which was set to 4.5 x 10^{-6}, such that W$_{subs}$ approximately balanced the model entrainment rate. This balance was imposed to prevent appreciable drift of the inversion height during simulations, which was a necessary condition for the experiment. A cooling rate of 2 K day^{-1} was applied below the inversion (900 m) to account for the advective cooling

Height(m)	θ_l (K)	Q_t (g kg^{-1})	Q_l (g kg^{-1})	Aerosol (g kg^{-1}) / 10^{-8}
0	289.5	11.0	0.0	2.55
500	290.0	10.25	0.0	2.37
890	290.5	10.25	0.6	2.22
910	299.0	6.5	0.0	1.17
1800	302.0	6.5	0.0	0.73

Table 6.1: *The initial conditions: liquid water potential temperature (θ_l), total water mixing ratio (Q_t), liquid water mixing ratio (Q_l), and aerosol mass mixing ratio. These are the point values of the fitted lines shown in Fig. 6.2.*

that would have occurred in the observed situation as the winds were from the north to northeast coming from areas with cooler sea surface temperatures (see Albrecht *et al.* (1995a)). This cooling rate was higher than in the FIRE simulations of chapters 2 and 5 mainly because the wind direction was roughly parallel with the sea surface temperature gradient in ASTEX, but almost perpendicular to the sea surface gradient in FIRE.

The domain size was 2.5 km x 2.5 km in the horizontal (the same as the main stratocumulus experiments in chapter 2) and there were 92 levels in the vertical between 0 and 1800 m. The same approach was taken for the resolution as in previous stratocumulus experiments. The horizontal resolution was 50 m and the vertical resolution was variable, ranging from 30 m in the sub-cloud layer, to 7 m around cloud top, and then increasing gradually to 50 m in the free troposphere.

There were two simulations, one with the aerosols, plus the aerosol-free control. These simulation were started at midnight run for 48 hours. The radiation scheme was set for July 15 and at latitude 33ºN (the same as for all previous LEM experiments in this thesis). Using the exact date and latitude (June 16, 35ºN) corresponding to the flight data would have made very little difference (1-2%) to the diurnal mean solar irradiance at the top of the atmosphere or the temporal variation of zenith angle. Consistency with the previous experiments was preferred to allow straightforward comparison of semi-direct forcing results.

As before, a dry external mixture of ammonium sulphate and soot was used to represent the aerosols. The ratio of soot to ammonium sulphate was set to 0.0409 to give a single scattering albedo of 0.94 at 550 nm that matched the single scattering albedo estimates from CLK96 and other data from ACE-2 (see section 6.2.5). The aerosol mass mixing ratio profile was constructed to give a total aerosol optical depth of 0.20 (as calculated from the PCASP data in section 6.2.6), and to have the same vertical

distribution as the PCASP number aerosol concentration profile (Fig. 6.2 (d)). Essentially, the aerosol mass mixing ratio was calculated by scaling the aerosol concentration by an amount that would give the necessary aerosol optical depth in the column.

6.5 Results and comparison with previous results from FIRE experiments

An investigation of the way that absorbing aerosols produce a semi-direct forcing in stratocumulus-capped BLs has already been presented in chapters 2 and 5. Therefore, a full exploration of such processes will not be given in this chapter. The focus of the following sections will be to highlight key differences between the results from the ASTEX experiment and results from the previous FIRE stratocumulus cases and to describe processes that were unique to the ASTEX case.

In the following sections result from the ASTEX simulations are presented and compared with results from the FIRE control simulations of chapters 2 and 5 (see sections 2.2.1 & 5.2), and the absorbing aerosol simulation of chapter 5 (see section 5.2). The FIRE simulations of chapter 2 were started at 0600 h local time, whereas the ASTEX simulations and the simulations in chapter 5 both start at 0000 h and are generally more compatible for comparison purposes. However, the simulations in chapter 5 had a reduced horizontal domain size (from $(2.5 \text{ km})^2$ to $(1.6 \text{ km})^2$) so chapter 2 simulations were more compatible in some instances.

6.5.1 Semi-direct forcing

The diurnal mean semi-direct forcing was 9.9 W m^{-2} on day 1, and 12.1 W m^{-2} on day 2, giving a mean semi-direct forcing of 11.0 W m^{-2} (as shown in table 6.2). This is significantly higher than expected based on previous experiments that used the FIRE stratocumulus case. The semi-direct forcing estimate from the method above was 7.5 W m^{-2}, and it was argued that a lower estimate would have been obtained if the assumptions about the aerosol vertical distribution and linearity of response to layers above and below the inversion had been relaxed. The discrepancy between the result and the estimate suggests that the stratocumulus LWP was for some reason more readily reduced by the aerosol heating in the ASTEX experiment than in the previous FIRE experiments, leading to higher semi-direct forcing than expected. The discrepancy could not be explained by cloud fraction changes as these were nil.

Radiative forcing (W m^{-2})	DAY 1	DAY 2	MEAN
Direct	1.5	1.5	1.5
Semi-direct	9.9	12.1	11.0
Total	10.4	13.6	12.5

Table 6.2: *The direct, semi-direct and total radiative forcing (W m^{-2}) for the ASTEX experiment, including diurnal mean for day 1 and 2, and the 2-day mean.*

It is likely that the higher susceptibility in ASTEX is related to differences in the meteorological set up between ASTEX and FIRE. As already mentioned, the BL was deeper and more decoupled in the ASTEX simulation with small cumulus developing below the stratocumulus. Chapter 2 showed that the semi-direct effect is intimately related to turbulent processes in the BL such as turbulent moisture fluxes, entrainment, and the decoupling of the BL. Also, chapter 3 showed that the semi-direct forcing was linked to the amount and type of cloud. The following sections explore the response to the aerosol heating in the ASTEX simulation and possible reasons for the unexpectedly high semi-direct forcing.

6.5.2 LWP variability and semi-direct forcing
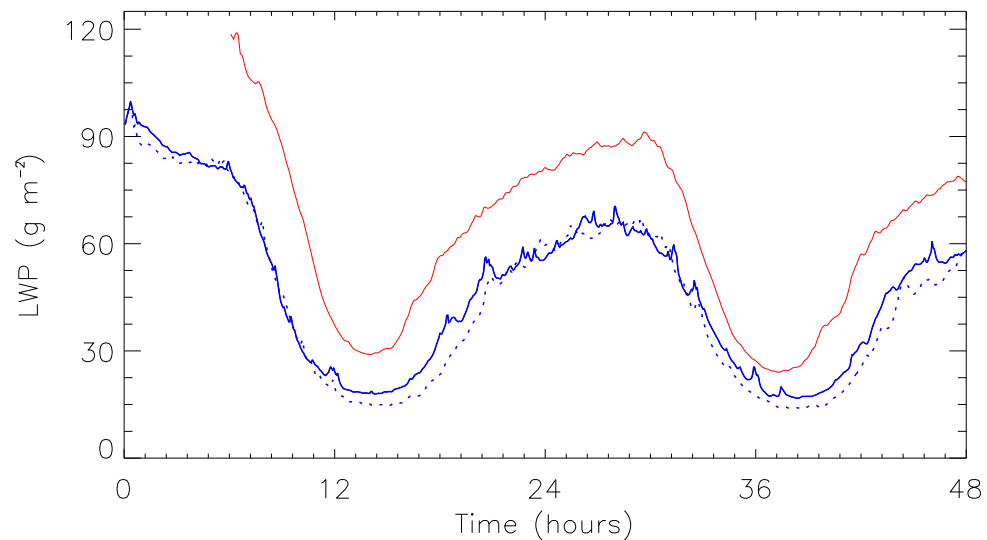
Figure 6.5: *Liquid water path (g m^{-2}) with local time (hours) in the ASTEX control simulation (blue solid line), ASTEX aerosol simulation (blue dotted line), and FIRE control simulation (red solid line).*

Figure 6.5 shows the variation of LWP with time in the aerosol and control simulations and also compares them with the LWP in the FIRE control simulation of chapter 2. The LWP follows a similar

diurnal cycle as in the FIRE simulation but with slightly lower values. In the afternoon the LWP falls to about 20 g m^{-2} in the control simulation and about 15 g m^{-2} in the aerosol simulation. The difference in LWP leads to the semi-direct forcing shown in Fig. 6.6.
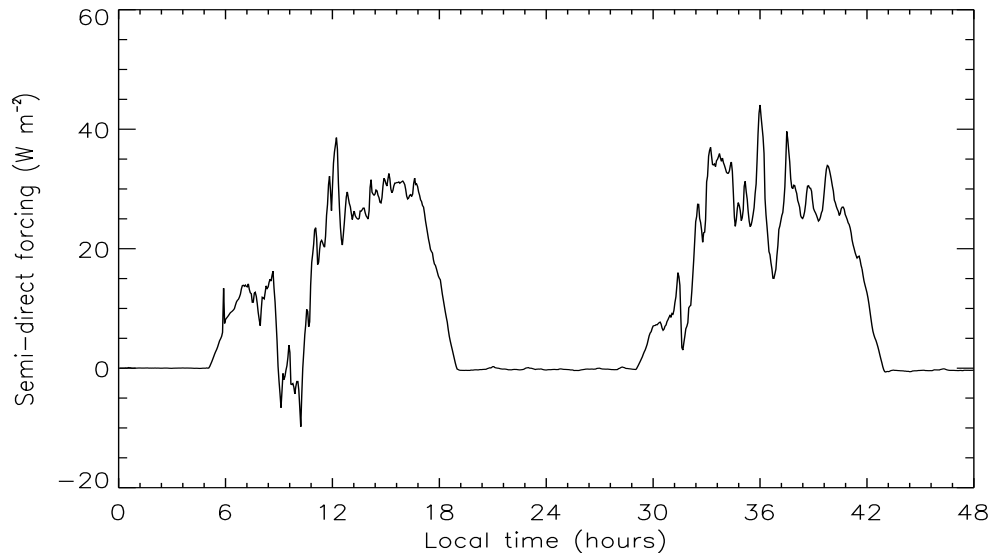
Figure 6.6: *Semi-direct forcing (W m^{-2}) with local time (hours) in the ASTEX experiment.*

The LWP and semi-direct forcing time series are more noisy in ASTEX than FIRE (see Fig. 6.5 and compare Fig. 6.6 with Fig. 2.21, in section 2.2.4). For example, there are more pronounced fluctuations in the semi-direct forcing such as the a dip between 1000 and 1100 h and the peak at 1200 h (Fig. 6.6). Such dips and peaks are related to spikes (small peaks) in the LWP time series (Fig. 6.5) caused by intermittent penetrations of the stratocumulus layer by cumulus (see Fig. 6.7 (b) - (d), and section below for more details). There also seems to be a higher degree of horizontal inhomogeneity in the stratocumulus liquid water content into the ASTEX simulations than in the FIRE stratocumulus simulations (compare Fig. 6.7 (a) with Fig. 2.15 from section 2.2.2). It is possible that turbulent variability had a greater influence on the diurnal mean semi-direct forcing in ASTEX than in the FIRE experiments. This could perhaps account for some of the discrepancy between the estimated semi-direct forcing and the result.

The uncertainty in the diurnal mean semi-direct forcing due to turbulent variability was estimated as $\pm$ 2 W m^{-2} for the FIRE experiments (see section 2.2.6.2). Even if this uncertainty were doubled in ASTEX, the two-day mean semi-direct forcing uncertainty would be only $\pm$ 2 $\sqrt{(2)}$ W m^{-2} , or roughly $\pm$ 3 W m^{-2} (averaging together two independent days reduces the uncertainty by a factor of $\sqrt{(2)}$). Thus, the semi-direct forcing result would be 11.0 $\pm$ 3 W m^{-2} . This uncertainty range still
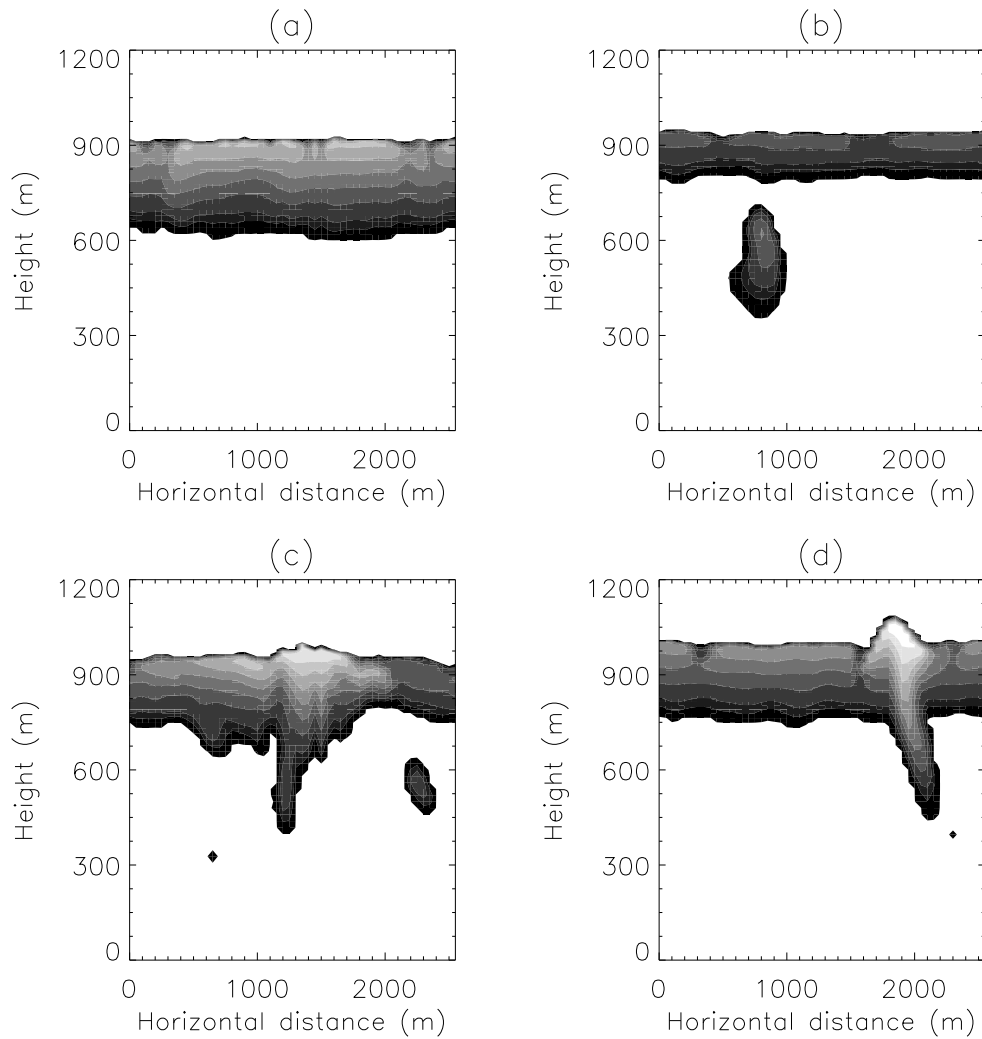
Figure 6.7: *Vertical-horizontal cross-sections of liquid water content (g kg^{-1}) from the control simulation at the following times: (a) 0200 h, (b) 1400 h, (c) 2100 h, and (d) 3100 h. Contour intervals are 0.1 g kg^{-1} and white areas have values greater than 0.8 g kg^{-1} .*

does not encompass the estimated semi-direct forcing from the empirical model, which was 7.5 W m^{-2} . Furthermore, it was argued that the empirical model overestimated the semi-direct forcing. Therefore, it is unlikely that uncertainty alone explains the difference between the empirical model estimate and the experimental result; there is probably a physical explanation for the discrepancy.

6.5.3   Suppression of turbulent moisture fluxes

The semi-direct forcing in the ASTEX experiments was caused mainly by two processes: firstly the heating of the cloud layer by the aerosol, and secondly the reduction of moisture fluxes into the cloud.

The same processes were responsible for the semi-direct forcing in the FIRE experiments that had absorbing aerosol in the BL. However, Figs. 6.8 and 6.9 suggest that the decoupling and reduction of moisture fluxes was relatively more important in the ASTEX simulations, with heating of the cloud layer being less important. For instance the cloud layer heated up by an additional 0.3 K in the FIRE SC-BL simulation compared to the control, but the cloud layer was less than 0.1 K higher in the ASTEX aerosol simulation than in the ASTEX control (Fig. 6.8 (a)). This is not surprising as the aerosol heating rate in the cloud was 2-3 times higher in SC-BL than in the ASTEX aerosol simulation. However, the aerosol-induced suppression of the moisture fluxes at the stratocumulus base was 2-3 W m^{-2} during the daytime (0600 - 1800 h) in both the ASTEX experiment and the FIRE experiment (Fig. 6.9), despite the lower aerosol heating rate in ASTEX. The relatively strong suppression of moisture fluxes seems to be the main reason for the unexpectedly high semi-direct forcing in the ASTEX experiment, compared to the expected semi-direct forcing.

6.5.4   The role of decoupling

Whilst decoupling was found to be of some importance in the FIRE stratocumulus simulations, it has a more prominent role in ASTEX and could explain the heightened suppression of moisture fluxes. In ASTEX simulations the BL is deeper and more decoupled. The inversion height is 900 - 1000 m in ASTEX simulations, and 600 m in FIRE simulations, and there is a greater increase of θ_l between the surface and the cloud layer in ASTEX simulations (Fig. 6.8 (a)). There is also a much greater decrease in total water mixing ratio between the surface mixed layer (0 - 300 m) and the cloud layer (600 - 900 m in ASTEX simulations, 300 - 600 m in FIRE simulations) (Fig. 6.8 (b)), which indicates less mixing through the BL in ASTEX.

The ASTEX case is an example of a deepening-decoupling stratocumulus BL, whereas the FIRE case is an example of a stratocumulus BL which has not yet, or has only just, begun such a transition. The deepening and decoupling of the marine BL is part of the transition observed in the subtropics and is related to a number of factors. One important factor is the increase of sea surface temperature as air is advected downstream towards the ocean interior and the ITCZ. Another important factor is the decrease in the strength of the inversion and the increase in cloud-top entrainment rates (for further explanation of the stratocumulus transition see section 2.1.2). The sea surface temperature is 292 K in ASTEX, 3 K higher than in the FIRE simulations and the inversion is less strong with an 8.5 K jump in θ_l, compared to a 12 K θ_l jump in FIRE. Consequently, surface moisture fluxes are higher in ASTEX and the entrainment rate was higher in ASTEX. The mean surface latent heat flux was 37.3
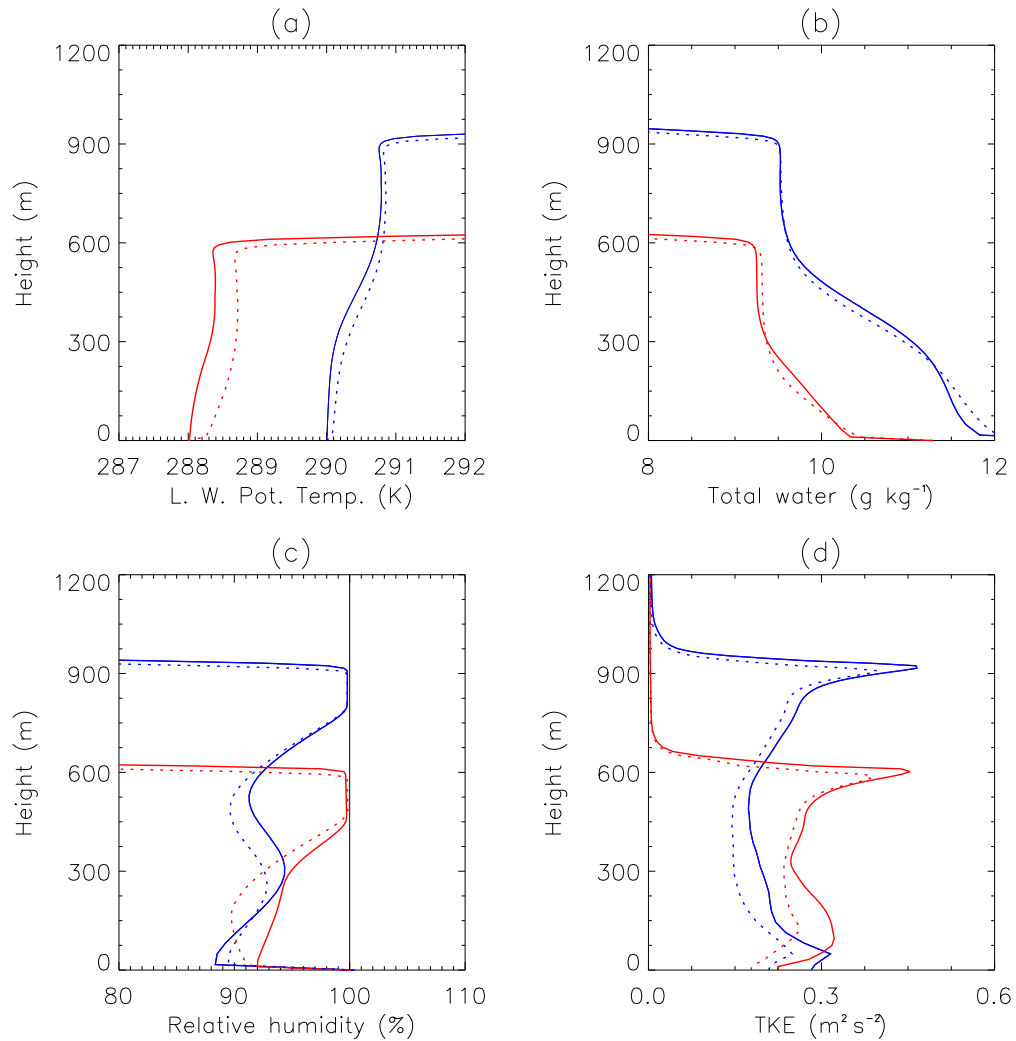
Figure 6.8: *(a) Liquid water potential temperature (K), (b) total water mixing ratio (g kg^{-1}), (c) relative humidity (%), and (d) turbulent kinetic energy (J kg^{-1}), averaged over 1200 - 1800 h local time in the control simulations (solid lines) and aerosol simulations (dotted lines), in the FIRE SC-BL experiment (red lines) and ASTEX experiment (blue lines).*

W m^{-2} in the ASTEX control and 25.4 W m^{-2} in the FIRE control simulation of chapter 5. The mean entrainment rate was 5.5 mm s^{-1} in the control simulation ASTEX and 3.5 mm s^{-1} in the FIRE control simulation of chapter 5 (calculated from the rate of change of cloud top height with time, plus the subsidence rate at the cloud top, see sections 6.4 & 2.2.1 for details on subsidence rates).

Figure 6.9 shows a much greater decrease in the turbulent moisture flux between the surface and the stratocumulus cloud layer in ASTEX simulations than in FIRE simulations. The turbulent kinetic energy in the middle of the BL is also considerably lower in ASTEX simulations than in FIRE simulations (Fig. 6.8 (d)). These results indicate that turbulent exchange between the cloud layer and the surface
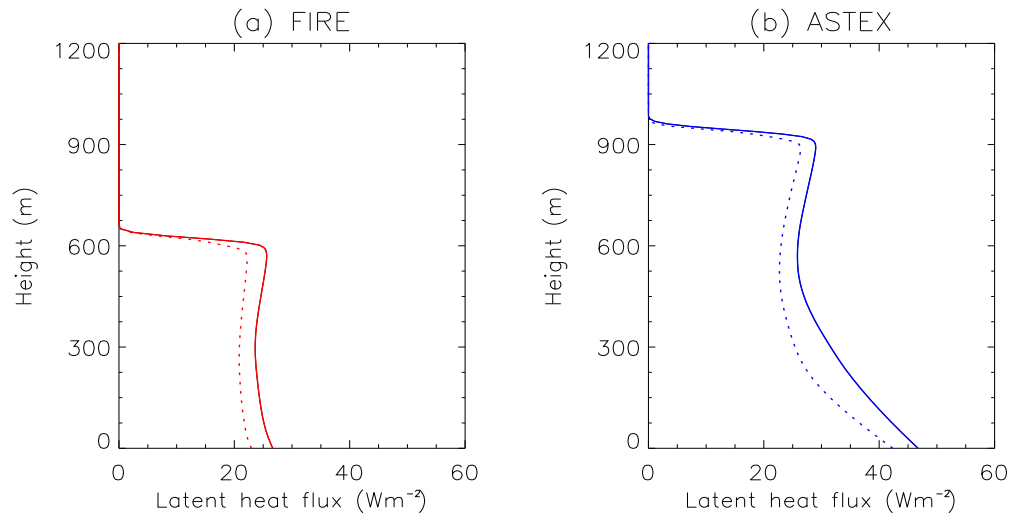
Figure 6.9: *Total turbulent vertical moisture flux (W m^{-2}), averaged over 0600 - 1800 h local time in the ASTEX experiment (a) and the FIRE SC-BL experiment (b), for control simulations (solid lines) and aerosol simulations (dotted lines).*

mixed layer was more limited in ASTEX simulations. This suggests that decoupling may have had a relatively greater role in determining stratocumulus LWP, and the semi-direct forcing in the ASTEX experiment. The greater BL depth and the more decoupled nature of the BL in ASTEX simulations (Fig. 6.8 (a)) may have lead to a greater semi-direct forcing as it enhanced the susceptibility to further decoupling, allowing a greater suppression of moisture fluxes from the aerosol heating.

6.5.5 The role of cumulus rising into the stratocumulus layer

The development of small cumulus below the stratocumulus layer was unique to the ASTEX simulations largely due to the greater depth and decoupling of the BL. Moisture built-up in the surface layer (0 - 300 m) (Fig. 6.8 (b)) leading to the development of a conditional unstable transition layer between the top of the surface mixed layer and the stratocumulus base (600 - 800 m). The presence of cumulus within the domain can be inferred at times when the minimum cloud base drops to the top of the surface mixed layer (300 - 400 m) (see Fig. 6.10). When cumulus are absent in the domain the minimum cloud base height switches to the height of the stratocumulus base (600 - 800 m).

Figure 6.7 shows examples of: (b) cumulus clouds forming at the top of the surface mixed layer, (c) penetrating the stratocumulus layer, and (d) overshooting into the inversion. The penetration of cumulus into the stratocumulus layer appears to enhance the liquid water content of the stratocumulus
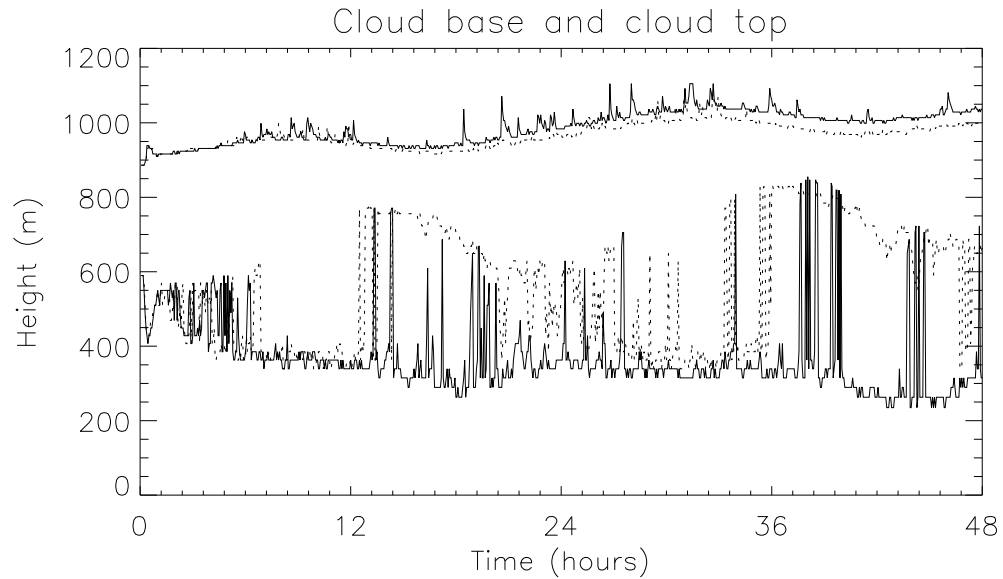
Figure 6.10: *Maximum cloud top height and minimum cloud base height (m) with local time (hours) in the ASTEX control simulation (solid line) and ASTEX aerosol simulation (dotted line).*

(Figs. 6.7 (c) & (d)). Strong cumulus penetrations, indicated by 50 - 100 m high spikes in cloud top height, coincide with small peaks in LWP at 1200, 1815 and 2030 h in the control simulation (see Figs. 6.10 & 6.5). This suggests that the cumulus may play a significant role in enhancing the LWP of the cloud layer.

Penetrating cumulus provide a link between the surface mixed layer and the stratocumulus layer, once they have been partially separated by decoupling. In this way the cumulus convection aids vertical transport of moisture through the BL and may act to sustain the overlying stratocumulus (Nicholls, 1984). The penetration of cumulus into stratocumulus layers is also likely to increase the turbulence in the stratocumulus layer and enhance the entrainment rate. This is especially true if cumulus overshoot and locally distort the inversion surface, as did occur in these simulations (see Fig. 6.7 (d)). Bretherton (1992) suggests that vigourous cumulus convection eventually leads to the dissipation of the stratocumulus layer leading to the transition to broken cumulus (see section 2.1.2 for further explanation). However, it is argued that gentle cumulus penetration has a sustaining effect on the stratocumulus (Martin *et al.*, 1995). During ASTEX Martin *et al.* (1995) found the stratocumulus layer to be thicker with a higher liquid water path in regions where cumulus clouds penetrated and Rogers *et al.* (1995) suggested that penetrating cumulus enhanced the nighttime development of stratocumulus. The correlation between cumulus penetrations (shown as spikes in cloud top height, Fig. 6.10) and LWP (Fig. 6.5) in the ASTEX simulations seems to agree with those studies, and suggests that the role of cumu-

lus was to sustain, rather than dissipate the stratocumulus, and supports the hypothesis that cumulus suppression by the absorbing aerosol enhanced the semi-direct forcing.
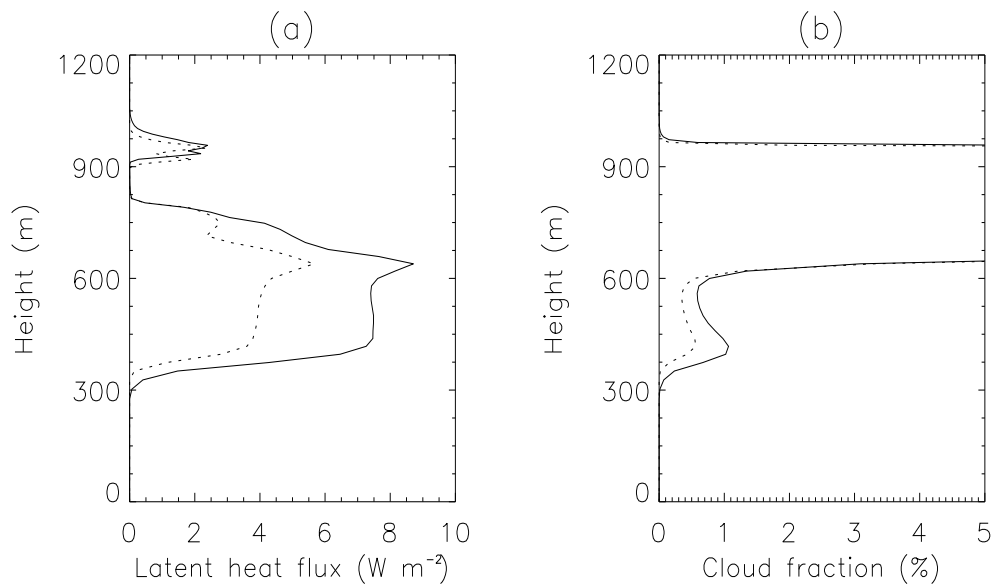
Figure 6.11: *(a) The vertical flux of total water (W m^{-2}) associated with cumulus clouds, and (b) the cloud fraction (%), averaged over 0600 - 1800 h in the ASTEX control simulation (solid line) and ASTEX aerosol simulation (dotted line).*

Figure 6.11 (a) shows the vertical flux of total water (latent heat flux) associated with cumulus clouds averaged over 0600 - 1800 and 3200 - 4200 h. This was calculated as the product of the cloud mass flux and the average total water perturbation within the cumulus clouds (within the stratocumulus layer itself the cumulus flux goes to zero where as the fractional cloud cover reaches 100 % , see Fig. 6.11 (a) & (b)). The cumulus total water flux at the stratocumulus cloud base (600 -700 m) was about 8 W m^{-2} in the control simulation (Fig. 6.11 (a)), which accounts for about 25 % of the total turbulent moisture flux at the stratocumulus cloud base (see Fig. 6.9). Thus, the cumulus are probably quite important in maintaining the stratocumulus LWP throughout the day (Fig. 6.5), even though the cumulus cloud fraction is only around 1 % (Fig. 6.11 (b)). However, the cumulus total water flux is also only about 4 W m^{-2} lower in the aerosol simulation, which more than accounts for the reduction of total turbulent moisture fluxes at the stratocumulus base (Fig. 6.9). This shows that the suppression of cumulus activity was a dominant factor in the suppression of moisture fluxes into the stratocumulus layer, and probably contributed to the lower LWP in the absorbing aerosol simulation (Fig. 6.5) thereby enhancing the semi-direct forcing (Fig. 6.6).

The greater suppression of cumulus in the aerosol simulation is probably due the decrease in relative

humidity in the transition layer (300 - 600 m) (Fig. 6.8 (c)). This is a result of the aerosol heating (Fig. 6.8 (a)) and a slight drying of the transition layer (Fig. 6.8 (b)) due to a reduction of moisture fluxes through the surface layer (0 -300m) related to the increased stability between the near-surface air and the transition layer (Fig. 6.8 (a)). The decline in relative humidity (Fig. 6.8 (c)) both raises the cloud base and reduces the likelyhood of cloud formation (i.e. reduces the cloud fraction) in the transition layer (300 - 600m) (Fig. 6.11 (b)). The enhanced daytime suppression of cumulus in the aerosol simulation is quite clear in time series of minimum cloud base (Fig. 6.10); there are no cumulus present between 1300 - 2000 h and 3600 - 4600 h, whereas cumulus are present in the control simulation for the most of the time during these periods. The reduced frequency and intensity of spikes in cloud top and LWP (Figs. 6.10 & 6.5) also suggest reduced cumulus activity in the aerosol simulation.

6.6 Summary and conclusions

In this chapter the semi-direct forcing has been evaluated with the LEM for an observed scenario of marine stratocumulus forming in polluted continental air. In previous experiments the aerosols were not based on any specific observations but idealised to allow a straightforward exploration of the semi-direct effect. However, in this chapter the meteorological fields, aerosol optical properties and vertical distribution were set up using aircraft data from the Atlantic Stratocumulus Transition Experiment (ASTEX). The aircraft observations were taken within a stratocumulus-capped BL and are representative of the conditions over the northeast Atlantic during moderate ourtbreaks of pollution from Europe.

Previous chapters have already showed that marine stratocumulus is particularly sensitive to the semi-direct effect. The presence of absorbing aerosols in the BL leads to a large positive semi-direct forcing. The proximity of the northeast Atlantic stratocumulus region to sources of anthropogenic pollution in Europe therefore leads to the potential for a significant regional semi-direct forcing. However, as shown in chapter 5, the magnitude, and even the sign of the forcing depends on the vertical distribution of the aerosols relative to the cloud, as well as the concentration of absorbing material. Therefore, to obtain an estimate of the semi-direct forcing in a particular scenario, coincident, and vertically resolved information on the aerosols and the meteorological conditions are required. Such observations are available from ASTEX, and from the second Aerosol Characterization Experiment (ACE-2), which took place in the same northeast Atlantic region in the summer 1997. These provide an ideal opportunity to construct an observationally-based LEM experiment of the semi-direct effect in marine stratocumulus.

In this experiment the aerosol optical depth was 0.2, the single scattering albedo was 0.94 and the aerosol was located both in and above the marine BL. The stratocumulus layer had a similar LWP as in previous LEM stratocumulus experiments (chapters 2 and 5) but the BL was much deeper, more decoupled and small cumulus were forming at the top of the surface layer and penetrating the stratocumulus layer. On the basis of previous experiments (chapters 2 and 5) a moderate positive semi-direct forcing was expected. A simple empirical model was presented that gave a semi-direct forcing estimate of 7.5 W m^{-2}. It was argued that this way likely to be an overestimate because the model did not fully account for the influence of vertical variation in aerosol mass concentration. The actual LEM experiment gave a semi-direct forcing of 11 W m^{-2}, somewhat higher than expected.

The semi-direct forcing was mainly caused by a strong reduction of moisture fluxes through the BL. The aerosol heating stabilised the BL with respect to the surface, reducing surface moisture fluxes. The aerosol heating also suppressed turbulent mixing by enhancing the decoupling and by suppressing the formation of small cumulus below the stratocumulus layer. Decoupling had a relatively greater role in determining the semi-direct forcing in the ASTEX-based experiment than in the previous experiments that were based on stratocumulus observations from the First International Satellite Cloud Climatology Project Regional Experiment (FIRE). Also, cumulus suppression was an additional mechanism, unique to the ASTEX-based experiment, that contributed to the reduction of moisture fluxes and the semi-direct forcing.

These results show that the semi-direct forcing in marine stratocumulus is sensitive to details such as the BL depth and the internal thermodynamic structure. This conclusion somewhat parallels findings from chapter 3. There it was shown that subtle differences in the BL thermodynamic structure, had a major influence on the cloud conditions and the magnitude of the semi-direct forcing. Because of this sensitivity it seems unlikely that any simple parameterization of the semi-direct effect would be successful.

As shown in this chapter, many assumptions were required to formulate the empirical model of the semi-direct forcing even though there were many similarities between the ASTEX-based experiment and previous FIRE-based idealised experiments. The empirical model estimate and the experimental result were not in agreement, even when allowing for generously for uncertainty related to turbulent variability of the semi-direct forcing.

The best way forward for quantifying the global or regional impact of semi-direct forcing is not through empirical methods, nor through multiple LEM experiments of every possible scenario, as this would

be computationally exhaustive. Once again, this chapter points once again to the need for large-scale models that can accurately represent clouds and the processes governing their formation or dissipation (see conclusions in chapter 4). Accurate representation of aerosol properties and their vertical distribution is also crucial. ASTEX and ACE-2 observations showed considerable space-time variability in the distribution and properties of aerosols. Also, comparison between different measurement techniques showed difficulties in constraining parameters such as the single scattering albedo, which is fundamental in determining the semi-direct effect. Therefore, improvement in the understanding of aerosols, and their treatment in large-scale models is also critical in gaining an estimate for the global importance of the semi-direct effect.

The large semi-direct forcing obtained in this chapter (11 W m^{-2}) further highlights the potentially large warming influence that the semi-direct effect may have on climate. The scenario used in this experiment is not hypothetical, but representative of moderately polluted conditions observed over the northeast Atlantic during summer. The regional season mean black carbon concentration in some areas of the world, for example southern Asia, is much higher than used in this experiment. The semi-direct forcing estimate obtained in this chapter is by no means an upper limit, or 'worse-case' scenario.

CHAPTER 7

Conclusions and discussion

7.1 Summary

This thesis investigated the semi-direct aerosol effect, whereby heating from absorbing aerosol evaporates clouds, particularly at low levels in the atmosphere where aerosols are most abundant, leading to a positive radiative forcing. First proposed by Hansen *et al.* (1997), the semi-direct effect is a relatively new concept that has entered the debate of how aerosols influence clouds and climate. As yet, there is a rather rudimentary understanding of how the semi-direct effect works, only a few studies have addressed the problem (Ackerman *et al.* (2000), Lohmann and Feichter (2001), Cook and Highwood (2003)), and there is yet no consensus on how important it is to climate. Important questions are raised, such as: How does the semi-direct forcing depend on the meteorological conditions, the aerosol properties and vertical distribution? Are simple General Circulation Models (GCMs) able to give reliable estimates of the semi-direct forcing?

The aim of this thesis is to explore the semi-direct effect, and assess its importance compared to the direct and indirect aerosol effects. The UK Met Office Large-Eddy-Model (LEM) is used to evaluate the semi-direct forcing under different cloud conditions and to investigate the sensitivity of the semi-direct forcing to aerosol single scattering albedo, and aspects of the aerosol vertical distribution. Although computationally expensive, Large-Eddy-Simulations offer the most faithful and realistic representation of clouds and small scale dynamic processes. Individual clouds and large turbulent eddies are explicitly resolved in three dimensions over a limited horizontal domain. This allows accurate simulations of cloud systems and their response to absorbing aerosols. The LEM captures small changes in the cloud structure and liquid water path as a result of small changes in the thermodynamic structure and turbulent processes within the Boundary Layer (BL).

The thesis focused on marine BL clouds (stratocumulus and cumulus), as these have an extensively global coverage and significantly enhance the planetary albedo. Also, these clouds are particularly sensitive to the absorption of solar radiation as there is close connection between radiative heating and processes that contribute to cloud formation in the BL, such as turbulence, convection, moisture

fluxes, and cloud-top entrainment. This study is the first to use the LES technique to evaluate the semi-direct effect for a range of meteorological scenarios, and a variety of idealised and observed aerosol distributions. Some experiments were also conducted with the NCAR Single Column Community Climate Model (SCCM) to assess difficulties that simple GCMs have in capturing the semi-direct effect.

7.2 Conclusions

1. Absorbing aerosols can have a considerable semi-direct forcing through local changes in cloud cover and liquid water path.

The presence of absorbing aerosols in the BL leads to a marked reduction of liquid water path and a large positive semi-direct forcing. For example, a moderate amount of highly absorbing aerosols (mid-visible aerosol optical depth of 0.15, and mid-visible single scattering albedo (ω) of 0.88) led to a local semi-direct forcing of around 15 W m^{-2}. This is several times greater than the global annual mean radiative forcing from a doubling of carbon dioxide (4 W m^{-2}). Even moderately absorbing aerosols ($\omega = 0.96$) gave a reasonably large semi-direct forcing (5 - 6 W m^{-2}) that exceeded the negative direct forcing. It should be noted however, that the semi-direct forcing was a local radiative forcing taken at 33$^{\text{o}}$N during summer; the global annual mean radiative forcing from the same change in cloud albedo would be somewhat smaller.

The semi-direct effect in marine stratocumulus works through two principal mechanisms. Firstly, solar heating by absorbing aerosols leads in a straightforward way to evaporation of the cloud. Secondly, heating in the cloud layer offsets the generation of turbulence by cloud top longwave cooling and helps to decouple the BL leading to a reduction of moisture fluxes into the cloud. In deep decoupled BLs the heating can also suppress the formation of small cumulus that transport moisture into the cloud and help to sustain an overlying stratocumulus layer.

Marine stratocumulus cover about 25% of the globe and the high semi-direct forcing found in the marine stratocumulus experiments suggests there may be a significant global impact. However, it is difficult to indicate the magnitude of the global annual mean semi-direct forcing because absorbing aerosols are so variable. Some marine stratocumulus regions, such as those in the northeast and southeast Pacific are remote from major sources of anthropogenic pollution and are typically pristine. Other marine stratocumulus regions, are frequently affected by polluted airmasses. For example, the

northeast Atlantic is subjected to absorbing aerosols from Europe and there is scope for a significant semi-direct forcing with the marine stratocumulus that form in that region.

2. The strength of the semi-direct effect depends strongly on meteorological conditions.

Further experiments showed that the semi-direct forcing was highly dependent upon cloud regime, and details of the BL structure that influenced the amount and type of cloud. A deeper more decoupled BL was found to give a higher semi-direct forcing than expected because daytime decoupling and suppression of small cumulus were more prominent. Because of this sensitivity it is not possible to generalise results to predict what the semi-direct forcing would be under different conditions.

Cumulus were much less sensitive to the semi-direct effect than marine stratocumulus. The semi-direct forcing was between a half a sixth the magnitude compared to marine stratocumulus, for the same aerosol single scattering albedo and mass mixing ratio, but a higher aerosol optical depth (because the BL was deeper but aerosol mass mixing ratio in the BL was assumed to be the same). The strength of the semi-direct forcing in the cumulus experiments depended mainly on the fractional coverage of the clouds. In one case where there was a strong capping inversion the cumulus tended to spread out generating a patchy layer of passive cloud beneath the inversion that detrained slowly. The fractional coverage of this passive cloud was very sensitive to the relative humidity. Heating from absorbing aerosol led to a significant reduction of total cloud fraction and a moderate semi-direct forcing. In another case there was a weaker inversion, a lower relative humidity in the upper part of the BL, and no layer of passive cloud. In that experiment the semi-direct forcing was a third smaller even though there were only small changes in the BL thermodynamic structure.

3. The semi-direct effect is highly sensitive to the vertical distribution of aerosol.

The semi-direct forcing was previously thought to be positive. However, when absorbing aerosols are located above the cloud layer the semi-direct forcing can be negative. In this case absorbing aerosols heat the air above the BL, tending to increase the strength of the inversion and reduce the cloud top entrainment rate. In marine stratocumulus experiments this led to an increase in liquid water path (LWP) leading to a moderate negative semi-direct forcing. In the cumulus experiments it led to an increase in cloud cover and a small negative semi-direct forcing. The aerosols also attenuated downwelling shortwave radiation, reducing shortwave absorption in the cloud. In this way the absorbing aerosols gave a small negative semi-direct forcing even if they were located far (> 1 km) above the inversion. Thick elevated layers of absorbing aerosols, related to biomass burning, were recently observed above marine stratocumulus off the coast of Namibia (Haywood *et al.*, 2003). Therefore, it is not implausible to sug-

gest the semi-direct forcing could be negative in some regions and seasons. However, since aerosols generally reside in the BL, and considering that positive response to aerosols in the BL was stronger than the negative forcing from aerosols above the inversion, it seems likely that the semi-direct effect would be positive globally.

Vertical variation of the aerosol vertical distribution within the BL was also shown to be important. Absorbing aerosols have the greatest positive semi-direct forcing when located within the cloud layer, rather than below it. Observations (e.g. Ostrom and Noone (2000)) show that there can be strong gradients of aerosol mass concentration within deep decoupled BLs. The high sensitivity to aerosol vertical distribution is a major source of uncertainty in estimating the semi-direct effect. Accurate knowledge of the aerosol distribution relative to the cloud is required to accurately predict the semi-direct forcing.

4. GCMs with simple parameterizations do not adequately capture the semi-direct effect.

Comparison of results with the SCCM shows that better treatment of clouds and BL processes is necessary to give a realistic simulation of the semi-direct effect. The SCCM grossly underestimated the semi-direct forcing for absorbing aerosols in a stratocumulus-capped marine BL, and showed a large sensitivity of results to details of the experimental set up. The model did not give a realistic simulation either of the BL, or the stratocumulus cloud. In short, the parameterizations were too simple. They did not include relevant processes such as entrainment and BL turbulence driven by longwave cloud top cooling, and the stratocumulus cloud fraction and liquid water content were effectively specified in the parameterization. Consequently, the thermal structure of the BL was poorly resolved, there was no daytime decoupling, and the stratocumulus cloud LWP varied very little during the day. Increasing the vertical resolution gave a higher semi-direct forcing but did little to improve the representation of the BL, or the clouds.

Summary: This thesis has provided local estimates of the semi-direct forcing for a limited range of cloud regimes and aerosol scenarios. This approach has led to a better understanding of the semi-direct effect and shown that it could compete with the direct and indirect aerosol effects. However, because of the sensitivity of the semi-direct effect to meteorological conditions, aerosol optical properties, and their vertical distribution the global impact of the semi-direct effect in marine stratocumulus is highly uncertain. Further work is required to answer the question of how important the semi-direct effect is on the global scale.

7.3   Suggestions for future work

7.3.1   Extension of LEM experiments

Because of the sensitivity to meteorological conditions, shown in this thesis, it is not clear how important the semi-direct forcing would be under conditions other than marine stratocumulus and cumulus. To gain a better understanding of the global impact of the semi-direct effect the set of LES experiments could be extended to include other cloud systems. For example, the impact of absorbing aerosols on deep convection would be an interesting problem to explore. Deep convection in the tropics is required so that radiative cooling in the atmosphere is balanced by latent heat release. By heating the troposphere, absorbing aerosols offset radiative cooling and could slow down convection. Absorbing aerosols also tend to reduce surface moisture fluxes by stabilising the air near the surface. This partly explained the suppression of shallow cumulus by absorbing aerosols shown in this thesis. The same mechanism could also act to reduce the intensity of deep convection, thereby reducing cloud amounts. The sign of the semi-direct forcing would depend on the vertical distribution of cloud changes. Reducing cloud amount at low levels would give a positive semi-direct forcing, reducing outflow cirrus could lead to a negative semi-direct forcing through an increase in outgoing longwave radiation.

Another way of extending this thesis would be to consider the semi-direct effect of clouds over land. Black carbon is associated with anthropogenic emissions and mass concentrations are generally higher over continental regions than over the ocean. Therefore, understanding the way that clouds respond to absorbing aerosols, in continental regions, is key to estimating the global importance of the semi-direct effect. In the marine BL turbulence and moisture fluxes are driven mainly by cloud top longwave cooling and latent heat release in the cloud. Here, the semi-direct effect worked by offsetting cloud top cooling and enhancing the decoupling of the BL. However, over land surface heating during the daytime is usually what drives convection and moisture fluxes in the BL. Possibly, the reduction of net radiation at the surface due to aerosols would lead to a less convective BL and inhibit the formation of fair weather cumulus. At present the LEM has not been developed to include land surface processes but similar LES models have been coupled with land surface schemes, and simulations of cumulus developing over land surfaces have been successful (e.g. Golaz *et al.* (2001)).

To further develop understanding of the semi-direct effect, future LES studies could include aerosols and cloud microphysical processes in a more interactive way. For example, Adrian Hill and Steven Dobbie from Leeds University have recently coupled the LEM to a microphysics scheme that provides

a detailed binned representation of both cloud condensation nuclei and cloud droplet number and mass concentration (Hill and Dobbie, 2003). This kind of model will allow a more sophisticated study of the interaction between aerosols, radiation, dynamics, and cloud microphysics. This could be important uncovering any feedbacks of the semi-direct effect on cloud microphysics, for example by altering the cloud dynamics and liquid water contents. It could also provide a more realistic comparison between the magnitudes of the semi-direct and indirect radiative forcing, a key stage in assessing the relative importance of the semi-direct effect.

Although, the LES technique provides a powerful tool for investigating the semi-direct effect, it is can only give estimates of the semi-direct forcing for selected scenarios. It would be computationally impossible to run a LES experiment for every likely cloud and aerosol scenario. Also, LES is fundamentally limited in that it can not take into account feedbacks on the large scale dynamics. The influence of large-scale advection and subsidence are specified, yet it is plausible that radiative heating in the atmosphere by aerosols will decrease the subsidence rate locally, or regionally. Furthermore, it is not possible, to simulate large-scale systems, such as cyclones and fronts with three dimensional LES. Therefore, LES alone cannot lead to global estimates of the semi-direct forcing.

7.3.2   General circulation model experiments

Ultimately, GCMs are required to estimate the global annual mean semi-direct forcing and determine whether the semi-direct effect is important to climate. To give reliable estimates, GCMs must accurately simulate the distribution of aerosols and clouds, and give realistic cloud responses. To capture the semi-direct effect for BL clouds the effects of longwave cloud top cooling, entrainment, and decoupling need to be properly represented within the BL scheme. For this greater vertical resolution (100 - 200 m) in the BL may be necessary. Also, more sophisticated cloud schemes (e.g. Tiedtke (1993)) with prognostic treatment of both liquid water and cloud fraction may give more realistic cloud responses to absorbing aerosols. An in-depth analysis of cloud responses, including validation of local cloud responses with LES, would be crucial to ascertain whether more sophisticated GCMs give more realistic semi-direct forcing estimates.

To estimate the semi-direct forcing in GCMs, aerosols can either be prescribed from observations or predicted from emissions data. Observations have several limitations. The coverage of the ground-based observation sites is poor is remote regions, satellite measurement of aerosol properties over land are hindered by the variability of land surface albedo, and it is difficult to retrieve the vertical distri-

bution from radiometer instruments. Predicting aerosol properties within the model from emissions data requires treatment of the transport of several gas and aerosol species, chemical transformations, and depositional processes. Aerosol-chemistry schemes vary in complexity but even at their simplest will add a considerable computational burden to GCM experiments. So far GCM experiments with prognostic treatment of aerosols have been run for limited periods, for example, 5 years (Lohmann and Feichter (2001) and Jacobson (2002)). To ensure that any semi-direct effects are distinguished above natural variability in the model it may be necessary to run for longer periods (e.g. 20 - 30 years), but at great computational expense.

To increase confidence in semi-direct forcing estimates the black carbon burden, or aerosol single scattering albedo predicted in GCMs would need validation with in-situ, or ground based measurements, for example, from AERONET (see Holben *et al.* (1998)). Also, the sensitivity of the semi-direct forcing to assumptions about the mixing state of black carbon needs consideration. Treating black carbon as an external mixture could potentially introduce a factor of 2 - 3 uncertainty in the amount of absorption, and therefore the magnitude of the semi-direct forcing.

7.3.3   Observing the semi-direct effect

So far the semi-direct effect has only been shown through modelling experiments. To observe it in the real world would help to establish whether it is an important effect to consider. However, observing the semi-direct effect would be a very difficult task in practise. The semi-direct effect is produced by small changes in cloud cover and LWP that may be difficult to distinguish above natural variability. To infer the semi-direct effect from observations a control experiment is needed where meteorological/cloud conditions are almost constant in space or time but there is a strong variation in aerosols in space or time. Even modest changes in the large-scale, or mesoscale circulation can produce changes in cloud cover or LWP and it is important that the influence of these are taken into account when looking for any aerosol-induced change. In general low-level clouds forming under steady anticyclonic conditions would be best suited to such an experiment. Subtropical marine stratocumulus would probably be ideal because of the strong sensitivity to the semi-direct effect, and because it can be found in extensive, fairly homogeneous layers. Large contrasts in aerosols are generally found at the boundaries between continental and marine airmasses. However, there may also be large contrasts in meteorological conditions between different airmasses. In that case it would not be possible to implicate the semi-direct effect as the cause of changes in cloud conditions between airmasses.

The semi-direct effect may be distinguishable in plumes of aerosols from large point sources such as forest fires or industrial centres. Observing the semi-direct effect would require intensive observations inside and outside the plume, preferably from a variety of observing platforms, satellite, aircraft and ground stations, to measure cloud and aerosol properties. A major challenge would be measuring the aerosol optical depth and absorption in the presence of clouds. Also, it is important to be aware of sources of sampling bias. If the LWP is only measured in pixels that are cloudy then results could be misleading. Coakley and Walsh (2002) reported a reduction of LWP in plumes of ship exhaust ('ship tracks') through pristine marine stratocumulus clouds. Initially the result appeared to be evidence of the semi-direct effect. However, a later paper by Ackerman *et al.* (2003) explained that the LWP signal was an artifact of sampling only overcast clouds. They suggest that cloud cover increases in the ship tracks, due to the second indirect effect, but that LWP increases only a little so that the average LWP of cloudy pixels is reduced. Therefore, clear sky pixels should not be filtered out in the analysis of cloud properties.

Interference from the indirect effect is a major obstacle in inferring the semi-direct effect from observations. Black carbon is usually found in conjunction with sulphate and organic carbon aerosols which act as effective cloud condensation nuclei and would tend to reduce cloud droplet sizes. The second indirect effect proposes that a decrease in cloud droplet sizes reduces precipitation efficiency, increasing cloud lifetimes. This would mean an increases in LWP and cloud cover to offset the semi-direct effect. In contrast, LEM experiments of marine stratocumulus showed that reducing the droplet effective radius from 10 to 8μm lead to a 5 g m^{-2} reduction of LWP in the afternoon. This occured because reducing the effective droplet radius increases the shortwave absorption optical depth of the cloud increasing the daytime heating of the cloud. This reduction was comparable to the reduction caused by moderately absorbing aerosols through the semi-direct effect. The cloud lifetime effect was not included in our LEM experiments and it is currently an open question as to whether the indirect effects would increase or decrease cloud LWP. In the light of this uncertainty it would be difficult to account for indirect aerosol effects and infer the semi-direct effect in any observed changes of cloud cover and LWP.

7.3.4   Fundamental uncertainties in aerosol properties

Uncertainty in the global distribution of aerosols and their properties are fundamental sources of uncertainty in semi-direct effect. Single scattering albedo (ω) is a critical parameter determining whether aerosols will give a significant semi-direct forcing, and is also important in determining the direct

aerosol forcing. Unfortunately, this has been one of the most difficult properties to measure because absorption by aerosols, although important, is usually very slight compared to scattering. Also, ω depends on ambient relative humidity. This complicates the comparison of in-situ measurements of ω with column average measurements of ω from remote sensing methods. Thus, better knowledge of aerosol physical, chemical, and optical properties are required from observations. New instrumental techniques promise advances in satellite remote sensing. As mentioned in chapter 1, it is now becoming possible to observe aerosols over both land and ocean using the Moderate Resolution Imaging Spectroradiometer (MODIS) (Chu *et al.*, 2003), mounted on a low earth-orbiting satellite.

Improvements in modelling of aerosols are also necessary, including modelling of emissions. Current estimate of global black carbon emissions are a factor of two uncertain (Cooke *et al.*, 1999). This uncertainty will translate into uncertainty in semi-direct forcing estimates from GCMs that use emissions data to predict aerosol properties. Recent advances in assimilation techniques have now been employed to assimilate satellite aerosol observations from the Advanced Very High Resolution Radiometer (AVHRR) into the National Center for Atmospheric Research (NCAR) Climate System Model (Collins *et al.* (2001)), as mentioned in chapter 1. Thus, there is potential to reduce uncertainties in aerosol properties and their global distribution. Such improvements will give a clearer understanding of the direct aerosol forcing, and more complex issues associated with aerosol-cloud interactions (indirect and semi-direct effects) will come to the fore.

7.4 Final summary

This thesis has shown that the semi-direct effect from anthropogenic aerosols could have a significant warming influence on climate, counteracting the negative radiative forcing from direct and indirect aerosol effects. The expected cooling from aerosols is often seen as the 'missing' forcing, required to explain discrepancies between model simulations and observations of recent climate change (past 150 years or so). However, given the uncertainty in climate sensitivity and other radiative forcings (e.g. ozone, solar variability) there is no basis to reject the hypothesis that anthropogenic aerosols have contributed a strong positive radiative forcing through the semi-direct effect. If this were true then a heightened focus on controlling black carbon emissions would be appropriate, as a possible means of mitigating global warming. However, there are many uncertainties in understanding aerosols and their role in anthropogenic climate change. Further modelling studies, and possibly observational evidence, are required to assess the true importance of the semi-direct effect, compared to other climate forcings.

APPENDIX A

Large-Eddy-Model (LEM)

The Met Office LEM is a 3-dimensional atmospheric model with periodic lateral boundary conditions designed for use at high resolution over a limited spatial domain. The resolution and domain size are flexible depending on the application. As the name suggests the purpose of the model is to explicitly resolve large eddies associated with boundary layer turbulence and convection. LES simulate the 3-dimensional flow on a limited domain (typically 2.5 - 6 km in the horizontal, 1.5 - 3 km in the vertical), with periodic lateral boundary conditions, at a resolution of between tens and a hundred metres. The same models are also used at coarser resolution (hundreds to thousands of metres) and much larger domains (100-1000 km in the horizontal, 20 - 30 km in the vertical) to explicitly represent deep convection. In this application the term 'cloud resolving model' is used. This appendix summarises the main features of the LEM and discusses some relevant details. A full description of the model equations can be found in Derbyshire *et al.* (1994) and Gray *et al.* (2001).

A.1 Dynamics

The evolution of the model state is solved using the incompressible Boussinesq equations, in which a mean reference state is defined (ρ_s, p_s, θ_s), and deviations (ρ', p', θ') around the reference state are assumed to be small (ρ is density, θ is potential temperature and p is pressure, s denotes the reference state and ' denotes a perturbation from the reference state). For boundary layer applications the reference state is assumed constant with height. The 3-dimensional flow is solved using a filter operation to the Navier Stokes equations (Brown, 1999). The effect of large-scale dynamics are represented through forcing terms. For example, a subsidence rate can be specified and large-scale divergence of heat or moisture can be represented through large-scale heating and moistening tendencies. A large-scale pressure gradient can be represented by specifying the horizontal geostrophic winds.

Subgrid-scale turbulence is represented using first-order turbulence closure, based on the approach of Smagorinsky *et al.* (1965). This uses a basic mixing length, λ, to determine the subgrid fluxes ($\lambda = \Delta C_s$, where C_s is a specified, but flexible constant, and Δ is set to the horizontal grid spacing).

Subgrid diffusion is necessary to keep model fields smooth and prevent discretization errors. However, excessive diffusion smears out features, reducing the effective resolution of the model. In the stratocumulus experiments a value of $C_s = 0.23$ was used, as recommended by Gray *et al.* (2001). In the cumulus experiments C_s was reduced to 0.115 because subgrid diffusion was tending to dissipate clouds too quickly. Further details on the subgrid model are found in Derbyshire *et al.* (1994) and Brown *et al.* (1994).

A.2 Moisture

The LEM uses the conserved scalars total water mixing ratio (q_t) and the liquid water potential temperature (θ_l), which are defined as:

$$\theta_l = \theta - q_l \frac{L}{c_p}; \quad q_t = q + q_l \tag{A.1}$$

where L is the latent heat of condensation (2.5 x 10^6 J kg^{-1}), and c_p is the specifc heat capacity at constant pressure (1004 J kg^{-1} K^{-1}), q is the water vapour mixing ratio, and q_l is the liquid water mixing ratio. All simulations in this thesis were of warm clouds; no ice was involved. The liquid water mixing ratio, q_l is diagnosed at each grid point as $q_l = q_t - q_{sat}$, for $q_t > q_{sat}$, where q_{sat} is the local saturation mixing ratio. The LEM uses θ_l and q_t as model prognostic variables, which means that latent heat is intrinsically accounted for and conserved in the model. Because cloud structure is explicitly resolved no diagnosis of cloud fraction within a grid cell is necessary; a grid cell is either clear or cloudy depending on whether liquid water is present or not. The LEM has a detailed treatment of cloud microphysics. However, in the simulations in this thesis the liquid water content was too low for there to be any significant precipitation. For computational efficiency the microphysics scheme was switched off.

A.3 Boundary conditions

Surface fluxes are calculated using Monin-Obukhov similarity theory, full details are given in Bull and Derbyshire (1990). The surface momentum, sensible heat, and moisture fluxes are essentially a

function of the vertical gradients of those quantities between the surface and the lowest model, with additional dependency on the stability and shear just above the surface. In every simulation (within this thesis) the bottom boundary was taken to be ocean with a specified sea surface temperature. The surface humidity is taken to be the saturated value at sea surface temperature, and velocity is zero at the surface (no slip). The top boundary is a stress-free rigid lid. Near the model top the temperature was relaxed to the initial conditions with a 3-hour time-scale to prevent drift of the temperature with time. The relaxation also prevented reflection of gravity waves. The lateral boundary conditions are periodic.

A.4   Radiation

The LEM uses the Edwards and Slingo (1996) radiation code to calculate shortwave and longwave radiative fluxes for every column, every 200 seconds. Edwards and Slingo (1996) is a two-stream radiation code with flexible spectral resolution. In the LEM a spectral resolution of 8 longwave bands, and 6 shortwave bands is used. Gaseous absorption by water vapor, ozone, and carbon dioxide is treated in both the shortwave and the longwave. In addition, absorption by oxygen, and Rayleigh scattering is treated in the shortwave. Absorption by methane, nitrous oxide and CFCs 11 and 12 are treated in the longwave. Liquid cloud droplets are treated in both the shortwave and longwave (simulations only involved warm clouds; no ice was involved). Cloud optical depth, τ is given through:

$$\delta\tau(\lambda) = \frac{3}{4}\frac{LWC}{r_e\rho_l}Q_{ext}(\lambda)\,\delta z \tag{A.2}$$

where LWC is the liquid water mixing ratio, r_e is the effective droplet radius, ρ_l is the density of liquid water (1000 kg m^{-3}), Q_{ext} is the extinction efficiency as a function of wavelength, λ. The effective droplet radius was specified as 10 μm, based on observations from unpolluted marine stratocumulus clouds (e.g. Francis *et al.* (1997)). The indirect aerosol effect (Twomey effect) can be included in a crude way, by reducing the specified value of r_e (section 2.2.5). The shortwave surface albedo for ocean is 0.07 for diffuse radiation, and a function of zenith angle for direct radiation, following Briegleb and Ramanathan (1982).

Previously, aerosols were not included in the LEM but in this thesis the LEM-radiation interface was

adapted so that a dry externally-mixed mixture of soot (black carbon) and ammonium sulphate could be included in the shortwave radiation code. Optical properties were derived from Mie calculations using size distributions, densities and refractive indicies from WCP (1986) (see Haywood (1995) or Haywood and Shine. (1997) for details). Interaction of these aerosols with longwave is negligible (because of their small size) and was neglected. The ratio of soot and ammonium sulphate is varied to give a chosen mid-visible (0.55μ m) aerosol single scattering albedo for the mixture. The vertical distribution of mass mixing ratio is specified but can vary during simulations, adjusting to changes in the boundary layer depth.

APPENDIX B

Single Column Community Climate Model (SCCM)

The SCCM is the single column version of the National Center for Atmospheric Research (NCAR) Community Climate Model (CCM). In this thesis version 3.6, released 1999, was used. The SCCM, and supporting software are freely available on the internet (wwwcgd.ucar.edu:80/cms/sccm/sccm.html). This webpage gives details on the SCCM and links to the full scientific documentation. This appendix give an outline of the SCCM, focussing on parameterizations that were important to the simulations in this thesis.

B.1 Evolution of the model state

In the SCCM the evolution of the model state (θ, q, u, v) depends only on tendencies from physical parameterizations, and specified large-scale forcing terms (the subsidence rate, and large-scale heat, moisture and momentum divergence). Physical parameterizations that were relevant to the simulations in this thesis include: vertical diffusion and boundary layer turbulent mixing, shallow moist convection (distinct from deep convection, which was not present in our simulations), surface fluxes of heat, moisture and momentum, longwave and shortwave radiation, treatment of cloud radiative properties, and precipitation from convection and large-scale condensation.

B.2 Cloud parameterization

The cloud scheme is that of Slingo (1987). Three different types of cloud feature in our simulations: stratus cloud (stratocumulus associated with a low-level inversion), large-scale cloud (from condensation associated with large-scale vertical motion), and convective cloud (from shallow moist convection). The fractional coverage of each of these cloud types (A_{str}, A_{ls}, A_{conv}) is calculated separately at each level. Convective cloud fraction (A_{conv}) is determined by the convective mass flux (M) in that layer:

$$A_{conv} = min[0.8, 0.035ln(1 + M)] \tag{B.1}$$

Stratus cloud may form in a layer if a low-level inversion is diagnosed in the layer above (p > 750 mb, $\frac{d\theta}{dp} < -0.125$ K mb^{-1}). Stratus cloud fraction depends on relative humidity, the static stability of the inversion layer, and pressure. The dependence on pressure reflects the observation that cloud fraction tend to decrease as the boundary layer grows and stratocumulus gives way to shallow cumulus with a lower fractional coverage (see section 2.1.2):

$$A_{str} = 0.0 \quad \text{for RH'} \leq 0.6 \tag{B.2}$$

$$A_{str} = min[0.95, (-6.67\frac{d\theta}{dp} - 0.667)](1 - \frac{0.9 - RH'}{0.3})(\frac{p - 750}{150}) \quad \text{for } 0.6 \leq RH' \leq 0.9 \tag{B.3}$$

$$A_{str} = min[0.95, (-6.67\frac{d\theta}{dp} - 0.667)](\frac{p - 750}{150}) \quad \text{for RH'} \geq 0.9 \tag{B.4}$$

where RH' is the adjusted relative humidity: $RH' = \frac{RH - A_{conv}}{1 - A_{conv}}$.

Large-scale cloud fraction (A_{ls}) depends on the vertical velocity (ω) and relative humidity:

$$A_{ls} = 0 \quad \text{for } \omega > \omega_c \tag{B.5}$$

$$A_{ls} = (\frac{\omega - \omega_c}{\omega_c})(\frac{RH' - 0.9}{0.1})^2 \quad \text{for } 0 \leq \omega \leq \omega_c \tag{B.6}$$

$$A_{ls} = (\frac{RH' - 0.9}{0.1})^2 \quad \text{for } 0 \leq \omega \leq \omega_c \tag{B.7}$$

where ω_c is the critical vertical velocity, which is 50 mb day^{-1}. Large-scale cloud only forms if stratus

cloud is not present. Therefore, the total non-convective cloud (A_c) is equal to either A_{str} or A_{ls}. The total cloud in a layer (A) is calculated as:

$$A = A_{conv} + A_c(1 - A_{conv}) \tag{B.8}$$

The liquid water mixing ratio in a layer (q_l) is calculated by multiplying the cloud fraction by an empirical function, which depends mainly on height:

$$q_l = q_l^o exp^{(-z/h_l)} \tag{B.9}$$

where h_l depends on precipitable liquid water (PLW):

$$h_l = 700 \log(1 + PLW/g) \tag{B.10}$$

The cloud optical depth is calculated from the liquid water path and cloud drop effective radius (r_e), which is set to 10 μ m (same method as in the LEM, see equation in Appendix 1). The random overlap assumption is used to calculate the total cloud fraction and radiative fluxes.

B.3   Radiation

The SCCM uses the two-stream δ-Eddington radiation scheme of Briegleb (1992) for shortwave radiation. This treats absorption and scattering by gases, clouds and aerosols. Gaseous absorption is represented using 18 exponential sum-fit terms, 7 for water vapor, 7 for ozone, 3 for carbon dioxide, and 1 for the visible, see Briegleb (1992) for full details. The method employed to represent longwave radiative transfer is based on the absorptivity/emissivity formulation of Ramanathan and Downey (1986), see Kiehl and Briegleb (1992) for a description of how fluxes are solved. The scheme treats clouds, and the following gases: carbon dioxide, water vapour, ozone, methane, nitrous oxide, and CFCs.

B.4   Convection and vertical mixing

The vertical diffusion scheme, and the shallow moist convection scheme both contribute to vertical mixing of heat, moisture and momentum. The vertical diffusion scheme also includes an extension to account for mixing in the boundary layer.

The vertical diffusion scheme takes a first-order approach, i.e. turbulent fluxes such as $\overline{\theta'w'}$ and $\overline{q'w'}$ are paramterized in terms of first order moments (θ, q, u, v), employing the general method of Smagorinsky *et al.* (1965); see Holtslag and Boville (1993) for details. The method assumes that vertical fluxes of quantities depends on the local vertical gradient of those quantities multiplied by an 'eddy-diffusivity'. The eddy diffusivity is a function of local stability and shear, the height above the surface, and a mixing length scale. The mixing length scale in some sense related the vertical displacement of eddies in the free atmosphere under stratified conditions. In the CCM the mixing length scale is set to 30 m. In the atmospheric boundary layer, which is often neutral or convective unstable, a different approach is taken.

In the BL scheme eddy-diffusivity depends on the hieght above the surface, the diagnosed boundary layer height, and a turbulent velocity scale, which depend also on local stability and surface shear. Furthermore, 'non-local' transport by convective turbulence in the BL is accounted for through a counter gradient term. This accounts for vertical fluxes associated with large eddies that are driven by surface heating. Such eddies are often larger than the local grid spacing and bring heat and moisture from the surface even when local gradients are small, or zero. This 'non-local' transport depends on the surface fluxes, the boundary layer height and the turbulent velocity scale. Full details are given in Holtslag and Boville (1993).

The shallow moist convection scheme is based on the concept of a non-entraining, detraining cumulus plume. This determines vertical transports from the convective mass flux. The mass flux is generated where there is conditionally instability and is removed by detrainment in the upper-most layer of the cumulus plume. This has the effect of drying lower layers, moistening upper layers, and adjusting the temperature profile towards a moist adiabat. Details of the scheme can be found at www.cgd.ucar.edu:80/cms/ccm3/TN-420/ or in Hack (1994).

References

Ackerman, A. S. and Toon, O. B. (1994). Unrealistic desiccation of marine stratocumulus clouds by enhanced solar absorption. *Nature*, **372**, 250.

Ackerman, A. S., Toon, O. B., Stevens, D. E., and Jr., J. A. C. (2003). Enhancement of cloud cover and suppression of nocturnal drizzle in stratocumulus polluted by haze. *Geophys. Res. Lett.*, **30 (7)**. 1370, doi:10.1029/2002GRL016634.

Ackerman, S., Toon, O. B., Stevens, D. E., Heymsfield, A. J., Ramanathan, V., and Welton, E. J. (2000). Reduction of tropical cloudiness. *Science*, **288**, 1042–1047.

Adams, K. M. (1988). Real time in situ measurements of the optical absorption properties in the visible via photoaccoustic spectroscopy: Evaluation of photo-accoustic cells. *Appl. Opt.*, **27**, 4052–4056.

Adams, K. M. (1994). Chemical characterization of atmospheric particles. *Conference Proceedings European Research Course on Atmospheres*. Grenoble, France, January 10 - February 9, 1994.

Albrecht, B. A. (1989). Aerosols clouds and microphysics. *Science*, **245**, 1227–1230.

Albrecht, B. A. (1991). Fractional cloudiness and cloud-top entrainment instability. *J. Atmos. Sci*, **48**, 1519–1528.

Albrecht, B. A., Penc, R. S., and Schubert, W. H. (1985). An observational study of cloud-topped mixed layers. *J. Atmos. Sci*, **42**, 800–822.

Albrecht, B. A., Randall, D. A., and Nicholls, S. (1988). Observations of marine stratocumulus clouds during FIRE. *Bull. Amer. Meteor. Soc*, **69**, 618–626.

Albrecht, B. A., Bretherton, C. S., Johnson, D., Scubert, W. H., and Frisch, A. S. (1995a). The Atlantic Stratocumulus Transition Experiment - ASTEX. *Bull. Amer. Meteor. Soc*, **76**, 889–904.

Albrecht, B. A., Jensen, M. P., and Syrett, W. J. (1995b). Marine boundary layer structure and fractional cloudiness. *J. Geophys. Res*, **100**, 14209–14222.

Ansmann, A., Wagner, F., Muller, D., Althausen, D., Herber, A., von Hoyningen-Huene, W., and Wandinger, U. (2002). European pollution outbreaks during ACE-2: Optical particle properties inferred from multiwavelength lidar and star-sun photometry. *J. Geophys. Res*, **107 (D15)**. 4259, doi: 10.1029/2001JD001109.

Augstein, E., Riehl, H., Ostapoff, F., and Wagner, V. (1973). Mass and energy transports in an undisturbed Atlantic trade-wind flow. *Mon. Wea. Rev*, **101**, 101–111.

Augstein, E., Schmidt, H., and Ostapoff, F. (1974). The vertical structure of the atmospheric planetary boundary layer in undisturbed trade winds over the Atlantic Ocean. *Bound. Lay. Meteorol.*, **6**, 129–150.

Bates, T. S., Huebert, B. J., Gras, J. L., Griffiths, F. B., and PA, P. A. D. (1998). International

Global Atmospheric Chemistry (IGAC) project's first Aerosol Characterization Experiment (ACE 1): Overview. *J. Geophys. Res*, **103 (D13)**, 16297–16318.

Bechtold, P., Kruegar, S. K., Lewellen, W. S., van Meijgaard, E., Randall, C. H. M. D. A., van Ulden, A., and Wang, S. (1996). Modelling a stratocumulus-Topped PBL: Intercomaparison amoung different one-dimensional codes and with Large-eddy simulation. *Bull. Amer. Meteor. Soc*, **77**, 2033–2042.

Bennetts, D. A., McCallum, E., Nicholls, S., and Grant, J. R. (1986). Stratocumulus: An introductory account. *The Meteorological Magazine*, **115**, 65–76.

Betts, A. K. (1990a). A cloudiness transition in a marine boundary layer. *J. Atmos. Sci*, **47**, 1480–1487.

Betts, A. K. (1990b). Diurnal variation of California coastal stratocumulus from two days of boundary layer soundings. *Tellus*, **42A**, 302–304.

Blaskovic, M., Davies, R., and Snider, J. B. (1991). Diurnal variation of marine stratocumulus over San Nicholas Island during July 1987. *Mon. Wea. Rev*, **119**, 1469–1478.

Bohren, C. F. and Huffman, D. R. (1983). *Absorption and scattering of light by small particles*. wiley, New York.

Boucher, O. and Lohmann, U. (1995). The sulphate-CCN-cloud albedo effect: A sensitivity study with two general circulation models. *Tellus*, **47B**, 281–300.

Bougeault, P. (1985). The diurnal cycle of the marine stratocumulus layer: A higher order model study. *J. Atmos. Sci*, **42**, 2826–2843.

Brand, P., Ruoss, K., and Gebhart, J. (1992). Performance of a mobile aerosol spectrometer for an in situ characterization of environmental aerosols in Frankfurt City. *Atmos. Env.*, **26 (13)**, 2451–2457.

Bretherton, C. S. (1992). A conceptual model of the stratocumulus-trade-cumulus transition in the subtropical oceans. *Prot. 11th Int. Conf. on Clouds and Precipitation*, **1**, Montreal, PQ, Canada, Int. Comm. on Clouds and Precipitation and Int. Assoc. of Meteor. and Atmos. Phys., 374–377.

Bretherton, C. S. (2002). World Climate Research Program (WCRP) Global Energy and Water Cycle Experiment (GEWEX) Cloud Systems Study (GCSS) Working group I - Boundary layer clouds. http://www.gewex.org/gcss.html.

Bretherton, C. S., Macvean, M. K., Bechtold, P., Chlond, A., Cotton, W. R., Cuxart, J., Cuijpers, H., Khairoutdinov, M., Kosovic, B., Lewellen, D., Moeng, C. H., Siebesma, P., Stevens, B., Stevens, D. E., Sykes, I., and Wyant, M. C. (1999). An intercomparison of radiatively driven entrainment and turbulence in a smoke cloud, as simulated by different numerical models. *Q. J. R. Meteorol. Soc*, **125**, 391–423.

Briegleb, B. P. (1992). Delta-Eddington approximation for solar radiation in the NCAR Community

Climate Model. *J. Geophys. Res*, **97**, 7603–7612.

Briegleb, B. P. and Ramanathan, V. (1982). Spectral and diurnal variation in clear sky planetary albedo. *J. Appl. Meteor.*, **25**, 214–226.

Brill, K. and Albrecht, B. A. (1982). Diurnal variation of the trade-wind boundary layer. *Mon. Wea. Rev*, **110**, 601–613.

Brost, A. K., Lenschow, D. H., and Wyngaard, J. C. (1982). Marine stratocumulus layers. Part I: Mean conditions. *J. Atmos. Sci*, **39**, 800–817.

Brown, A. R. (1999). The sensitivity of large-eddy simulations of shallow cumulus convection to resolution and subgrid model. *Q. J. R. Meteorol. Soc*, **125**, 469–482.

Brown, A. R., Derbyshire, S. H., and Mason, P. J. (1994). Large-eddy simulation of stable atmospheric boundary layers with a revised stochastic subgrid model. *Q. J. R. Meteorol. Soc*, **120**, 1485–1512.

Browning, K. A. and the GEWEX Cloud System Science Team (1993). The GEWEX Cloud System Study (GCSS). *Bull. Amer. Meteor. Soc*, **74**, 387–400.

Brummer, B. and Augstein, E. (1974). On the low-level wind structure in the Atlantic trades. *Q. J. R. Meteorol. Soc*, **100**, 109–121.

Bull, J. M. and Derbyshire, S. H. (1990). Numerical solution of the surface layer equations. *Met Office Turbulence and Diffusion Note*, **197**.

Carrico, C. M., Wood, M. J., Ogren, J. A., Neusub, C., Wiedensohler, A., and Heintzenberg, J. (2000). Aerosol light scattering properties measured at Sagres, Portugal, during ACE-2. *Tellus*, **52B**, 694–715.

Caughey, S. J., Crease, B. A., and Roach, W. T. (1982). A field study of nocturnal stratocumulus: II. Turbulence structure and entrainment. *Q. J. R. Meteorol. Soc*, **108**, 125–144.

Cess, R. D., Potter, G. L., Blanchet, P. J., Boer, G. J., Ghan, S. J., Kiehl, J. T., Letreut, H., Li, Z. X., Liang, X. Z., Mitchell, J. F. B., Morcrette, J. J., Randall, D. A., Riches, M. R., Roeckner, E., Schlese, U., Slingo, A., Taylor, K. E., Washington, W. M., Wetherald, R. T., and Yagai, I. (1989). Interpretation of cloud-climate feedback as produced by 14 atmospheric general circulation models. *Science*, **245**, 513–516.

Charlson, R. J., Pueschel, R. F., and Horvath, H. (1967). The direct measurement of atmospheric light scattering coefficient for studies of visibility and air pollution. *Atmos. Env.*, **1**, 469–478.

Chen, C. T. and Roeckner, E. (1997). Cloud simulations with the Max Planck Institute for Meteorology General Circulation Model ECHAM4 and comparison with observations. *J. Geophys. Res*, **102**, 9335–9350.

Chlond, A. and Wolkau, A. (2000). Large-eddy simulation of a nocturnal stratocumulus-topped marine

atmospheric boundary layer: An uncertainty analysis. *Bound. Lay. Meteorol.*, **95**, 31–35.

Chu, D. A., Kaufman, Y. J., Ichoku, C., Remer, L. A., Tanre, D., and Holben, B. N. (2003). Validation of MODIS aerosol optical depth retrieval over land. *J. Geophys. Res*, **29 (12)**, 1617.

Chung, C. E., Ramanathan, V., and Kiehl, J. (2002). Effects of the south Asian absorbing aerosol haze on the northeast monsoon and surface-air heat exchange. *J. Clim*, **15**, 2462–2476.

Chylek, P., Lesins, G. B., Videen, G., Wong, J. G. D., Pinnick, R. G., Ngo, D., and Klett, J. D. (1996). Black carbon and absorption of solar radiation by clouds. *J. Geophys. Res*, **101**, 23365–23371.

Chylek, P. V. (1995). Effect of black carbon on the optical properties and radiative forcing of sulphate aerosols. *J. Geophys. Res*, **100**, 16325–16332.

Clarke, A. D., Porter, J. N., Valero, F. P. J., and Pilewskie, P. (1996). Vertical profiles, aerosol microphysics, and optical closure during the Atlantic Stratocumulus Transition Experiment: Measured and modeled column optical properties. *J. Geophys. Res*, **101**, 4443–4453.

Coakley, J. A. and Walsh, C. D. (2002). Limits of the aerosol indirect radiative effects derived from observations of ship tracks. *J. Atmos. Sci*, **59**, 668–680.

Coakley, J. A., Bernstein, R. L., and Durkee, P. (1987). Effect of ship-stack effluents on cloud reflectivity. *Science*, **237**, 1020–1022.

Collins, W. D., Rasch, P. J., Eaton, B. E., Khattatov, B., Lamarque, J. F., and Zender, C. S. (2001). Simulating aerosols using a chemical transport model with assimilation of satellite aerosol retrievals: Methodology for INDOEX. *J. Geophys. Res*, **106**, 7313–7336.

Cook, J. and Highwood, E. J. (2003). Climate response to tropospheric absorbing aerosol in an Intermediate General-Circulation Model. *Q. J. R. Meteorol. Soc*. in press.

Cooke, W. F., Liousse, C., Cachier, H., and Feichter, F. (1999). Construction of a 1 x 1 degree fossil fuel emission data set for carbonaceous aerosol and implementation and radiative impact in the ECHAM4 model. *J. Geophys. Res*, **104**, 22137–22162.

Cuijpers, J. W. M. and Duynkerke, P. G. (1993). Large eddy simulation of trade wind cumulus clouds. *J. Atmos. Sci*, **50**, 3894–3907.

d'Almeida, G. A., Koepke, P., and Shettle, E. P. (1991). *Atmospheric Aerosols. Global Climatology and Radiation Characteristics*. A. Deepak Publishing, Hampton, Virginia, USA.

de Roode, S. R. and Duynkerke, P. G. (1997). Observed lagrangian transition of stratocumulus into cumulus during ASTEX: Mean state and turbulence structure. *J. Atmos. Sci*, **54**, 2157–2173.

Deardorff, J. W. (1980). Cloud top entrainment instability. *J. Atmos. Sci*, **37**, 131–147.

DelGenio, A. D., Yao, M. S., Kovari, W., and Lo, K. K. W. (1996). A prognostic cloud water parameterization for global climate models. *J. Clim.*, **9**, 270–304.

Derbyshire, S. H., Brown, A. R., and Lock, A. P. (1994). The Met Office Large-Eddy Simulation Model. *Met Office (APR) Turbulence and Diffusion Note*, **213**.

Dore, A. J., ans S. R. Osborne, D. W. J., Choularton, T., Bower, K. N., Andrea, M. O., and Bandy, B. J. (2000). Evolution of the boundary-layer aerosol particles due to in-cloud chemical reactions during the 2nd langrangian experiment of ACE-2. *Tellus*, **52B**, 452–462.

Durkee, P. A., Nielsen, K. E., Smith, P. J., Russell, P. B., Schmid, B., Livingston, J. M., Holben, B. N., Tomasi, C., Vitale, V., Collins, D., Flagan, R. C., Seinfeld, J. H., Noone, K. J., Ostrom, E., Gasso, S., Hegg, D., and Russell, L. M. (2000). Regional aerosol optical depth characteristics from satellite observations: ACE-1, TARFOX and ACE-2 results. *Tellus*, **52B**, 484–497.

Duynkerke, P. G. (1989). The diurnal variation of a marine stratocumulus layer: A model sensitivity study. *Mon. Wea. Rev*, **117**, 1710–1725.

Duynkerke, P. G. and Hignett, P. (1993). Simulation of diurnal variation in a stratocumulus-capped marine boundary layer. *Mon. Wea. Rev*, **121**, 3291–3300.

Duynkerke, P. G. and Teixeira, J. (2001). Comparison of the ECMWF reanalysis with FIRE I observations. *J. Clim*, **14**, 1466–1478.

Duynkerke, P. G., Jonker, P. J., Chlond, A., Zanten, M. C. V., Cuxart, J., Clark, P., Sanchez, E., Martin, G., Lenderink, G., and Teixeira, J. (1999). Intercomparison of three- and one-dimensional model simulations and aircraft observations of stratocumulus. *Bound. Lay. Meteorol.*, **92**, 453–487.

Duynkerke, P. G., Jonker, P. J., and van Dijk, A. (2000). FIRE I observations for the model inter-comparison of EUROCS: Stratocumulus over the ocean. http://www.cnrm.meteo.fr/gcss/EUROCS/Project.html.

Edwards, J. M. and Slingo, A. (1996). Studies with a flexible radiation code. I: Choosing a configuration for a large-scale model. *Q. J. R. Meteorol. Soc*, **122**, 689–719.

Esbensen, S. (1975). An analysis of subcloud-layer heat and moisture budgets in the western Atlantic trades. *J. Atmos. Sci*, **32**, 1921–1933.

Fischer, H. D., Wagenbach, and Kipfstuhl, J. (1998). Sulphate and nitrate firn concentrations on greenland ice sheet 2. tempoary anthropogenic deposition changes. *J. Geophys. Res*, **103**, 21935–21942.

Foot, J. S. (1979). Spectrophone measurements of the absorption of solar radiation by aerosols. *Q. J. R. Meteorol. Soc*, **105**, 275–283.

Francis, P. N., Taylor, J. P., Hignett, P., and Slingo, A. (1997). On the question of enhanced absorption of solar radiation by clouds. *Q. J. R. Meteorol. Soc*, **123**, 419–434.

Fuller, K. A. (1994). Scattering and absorption cross-sections of compounded spheres. 1. Theory for external aggregation. *J. Opt. Soc. Am. A*, **11**, 3251–3260.

Golaz, J. C., Jiang, H., and Cotton, W. R. (2001). A large-eddy simulation study of cumulus clouds over land and sensitivity to soil moisture. *Atmos. Res.*, **59-60**, 373–392.

Gray, M. E. B., Petch, J., Derbyshire, S. H., Brown, A. R., Lock, A. P., Swann, H. A., and Brown, P. R. A. (2001). Version 2.3 of the Met Office Large Eddy Model: Part II. Scientific documentation. *Met Office, (APR) Turbulence and Diffusion*, **276**.

Grenier, H. and Bretherton, C. S. (2001). A moist PBL parameterization for large-scale models and its application to subtropical cloud-topped marine boundary layers. *Mon. Wea. Rev*, **129**, 357–378.

Gundel, L. A., Dod, R. L., Rosen, H., and Novakov, T. (1984). The relationship between optical attenuation and black carbon for ambient and source particles. *Sci. Total Environ.*, **36**, 197–202.

Hack, J. J. (1994). Parameterization of moist convection in the National Center for Atmospheric Research Community Climate Model (CCM2). *J. Geophys. Res*, **99**, 5551–5568.

Han, Q. W., Rossow, W. B., Chou, J., and Welch, R. M. (1998). Global survey of the relationships of cloud albedo and liquid water path with droplet size using ISCCP. *J. Clim.*, **11**, 1516–1528.

Hansen, J. E., Sato, M., and Ruedy, R. (1997). Radiative forcing and climate response. *J. Geophys. Res*, **102**, 6831–6864.

Hanson, H. P. (1991). Marine stratocumulus climatologies. *Int. J. Clim.*, **11**, 147–164.

Hartmann, D. L., Ockert-Bell, M. E., and Michelsen, M. L. (1992). The effect of cloud type on Earth's energy balance: Global analysis. *J. Clim.*, **5**, 1281–1304.

Haywood, J. M. (1995). *Model investigations into the Radiative forcing of climate by Anthropogenic Emissions of sulphte and soot aerosol*. Ph.D. thesis, Dept. Meteorology, University of Reading, Reading RG6 6BB UK.

Haywood, J. M. and Boucher, O. (2000). Estimates of the direct and indirect radiative forcing due to tropospheric aerosols: A review. *Rev.Geophys*, **38**, 513–543.

Haywood, J. M. and Shine, K. P. (1995). The effect of anthropogenic sulfate and soot aerosol on the clear-sky planetary radiation budget. *Geophys. Res. Lett.*, **22**, 603–606.

Haywood, J. M. and Shine., K. P. (1997). Multi-spectral calculations of the direct radiative forcing of tropospheric sulfate and soot aerosol using a column model. *Q. J. R. Meteorol. Soc*, **123**, 1907–1930.

Haywood, J. M., Osborne, S. R., Francis, P., Keil, A., Formenti, P., Andreae, M., and Kaye, P. (2003). The mean physical and optical properties of regional haze dominated by biomass burning aerosol measured from the C-130 aircraft during SAFARI 2000. *J. Geophys. Res*, **108**, 8473, doi:10.1029/2002JD002226.

Hegg, D. A., Fereck, R. J., and Hobbs, P. V. (1993). Light scattering and cloud condensation nucleus activity of sulfate aerosol measured over the northeastern Atlantic Ocean. *J. Geophys. Res*, **102**,

25293–25303.

Heintzenberg, J., Charlson, R. J., Clarke, A. D., Liousse, C., Ramanathan, V., Shine, K. P., Wendisch, M., and Helas, G. (1997). Measurements and modelling of aerosol single-scattering albedo: Progress, problems and prospects. *Beitr. Phy. Atmosph*, **70**(4), 249–263.

Highwood, E. J., Haywood, J., Silverstone, M., Newman, S., and Taylor, J. (2003). Radiative properties and direct effect of Saharan dust measured by the C-130 aircraft during SHADE. 2. Terrestrial spectrum. *J. Geophys. Res*. in press.

Hignett, P. (1991). Observations of diurnal variation in a cloud-capped marine boundary layer. *J. Atmos. Sci*, **48**, 1474–1482.

Hill, A. and Dobbie, S. (2003). A bin-microphysical LES model for an evaluation of the semi-direct effect. *Book of abstracts: Climate processes and climate change*. Royal Meteorological Society Conference, UEA, Norwich, Sept 1-5, 2003.

Hogg, D. C., Guuiruad, F. O., Snider, J. B., Decker, M. T., and Westwater, E. R. (1983). A steerable dual-channel microwave radiometer for measurements of water vapor and liquid in the troposphere. *J. Climate Appl. Meteor.*, **22**, 789–806.

Holben, B. N., Eck, T. F., Slutsker, I., Tanre, D., Buis, J. P., Setzer, A., Reagan, E. V. J. A., Kaufman, Y. J., Nakajima, T., Lavenu, F., Jankowiak, I., and Smirnov, A. (1998). AERONET - A federated instrument network and data archive for aerosol characterization. *Remote Sensing of Environment*, **66 (1)**. 1-16 Oct.

Holland, J. Z. and Rasmusson, E. M. (1973). Measurements of the atmospheric mass, energy and momentum budgets over a 500km square of tropical ocean. *Mon. Wea. Rev*, **101**, 44–55.

Holtslag, A. A. M. and Boville, B. A. (1993). Local versus non-local boundary layer diffusion in a global climate model. *J. Clim.*, **6**, 1825–1842.

Hongbin, Y., Liu, S. C., and Dickinson, R. E. (2002). Radiative effects of aerosols on the evolution of the atmospheric boundary layer. *J. Geophys. Res*, **107 (D12)**, 4142, doi: 10.1029/2001JD000754.

Horvath, H. (1993). Atmospheric light absorption - A review. *Atmos. Env.*, **27A**, 293–317.

Houghton, D. D. (1974). The central programme for the GARP Atlantic Tropical Experiment. GATE. *Report No. 3. World Meteorological Organisation*. pp.35.

Huebert, B. J., Pszenny, A., and Blomquist, B. (1996). The ASTEX/MAGE experiment. *J. Geophys. Res*, **101**, 4319–4329.

Huebert, B. J., Bates, T., Russell, P., Shi, G., Kim, Y., Kawamura, K., Carmichael, G., and Nakajima, T. (2003). An overview of ACE-Asia: Strategies for quantifying the relationships between Asian aerosols and their climatic impacts. *J. Geophys. Res*, **108**. in press.

Ichoku, C., Remer, L. A., Kaufman, Y. J., Levy, R., Chu, D. A., Tanre, D., and Holben, B. N. (2003). MODIS observation of aerosols and estimation of aerosol radiative forcing over southern Africa during SAFARI 2000. *J. Geophys. Res*, **108 (D13)**, 8499, doi:10.1029/2002JD002366.

IPCC (2001). Climate change 2001: Scientific basis. Third assessment of the Inter-govermental Panel on Climate Change (IPCC). Cambridge.

Jacobson, M. J. (2001). Strong radiative heating due to the mixing state of black carbon in atmospheric aerosols. *Nature*, **409**, 695–697.

Jacobson, M. Z. (2002). Control of fossil-fuel particulate black carbon and organic matter, possibly the most effective method of slowing global warming. *J. Geophys. Res*, **107 (D19)**. 4410, doi: 10.1029/2001JD001376.

Jakob, C. (1999). Cloud cover in the ECMWF reanalysis. *J. Clim.*, **12**, 947–959.

Jiang, H. and Cotton, W. R. (2000). Large eddy simulation of shallow cumulus convection during BOMEX: Sensitivity to microphysics and radiation. *J. Atmos. Sci*, **57**, 582–594.

Johnson, D. W., Osborne, S., Wood, R., Suhre, K., Johnson, R., Businger, S., Quinn, P. K., Wieden-sohler, A., Durkee, P. A., Russell, L. M., Andreae, M. O., Noone, K. J., Bandy, B., Rudolph, J., O'Dowd, C., and Rapsomanikis, S. (2000). An overview of the lagrangian experiments undertaken during the North Atlantic regional Aerosol Characterisation Experiment (ACE-2). *Tellus*, **52B**, 290–320.

Jones, A. and Slingo, A. (1996). Predicting cloud-droplet effective radius and indirect sulphate aerosol forcing using a general circulation model. *Q. J. R. Meteorol. Soc*, **122**, 1573–1595.

Joshi, M. M., Shine, K. P., Ponater, M., Stuber, N., Sausen, R., and Li, L. (2003). A comparison of climate response to different radiative forcings in three general circulation models: Towards an improved metric of climate change. *Clim. Dyn.*, **20**, 843–845.

Kaufman, Y. J., Tanre, D., and Boucher, O. (2002). A satellite view of aerosols in the climate system. *Nature*, **419**, 215–223.

Keil, A. and Haywood, J. M. (2003). Solar radiative forcing by biomass burning aerosol particles over marine clouds during SAFARI-2000. *J. Geophys. Res*, **108 (D13)**, 8467, doi:10.1029/2002JD002315.

Kiehl, J. T. and Briegleb, B. P. (1992). A new parameterization of the absorptance due to the 15 micron band system of carbon dioxide. *J. Geophys. Res*, **96**, 9013–9019.

Klein, S. A. and Hartmann, D. L. (1993). The seasonal cycle of low stratiform clouds. *J. Clim*, **6**, 1587–1606.

Klein, S. A., Hartmann, D. L., and Norris, J. R. (1995). On the relationships among low-cloud struc-

ture, sea-surface temperature, and atmospheric circulation in the summertime northeast pacific. *J. Clim.*, **8**, 1140–1155.

Krueger, S. K., McLean, G. T., and Fu, Q. (1995). Numerical simulation of the stratus-cumulus transition in the subtropical marine boundary layer. Part I: Boundary layer structure. *J. Atmos. Sci*, **52**, 2839–2850.

Langner, J. and Rodhe, H. (1991). A global three-dimensional model of the tropospheric sulphur cycle. *J. Atmos. Chem.*, **13**, 225–263.

Larson, K., Hartmann, D. L., and Klein, S. A. (1999). The role of clouds, water vapor, circulation, and boundary layer structure in the sensitivity of the tropical climate. *J. Clim.*, **12**, 2359–2374.

Lavanchy, M. G., Schotterer, U., Schwikowski, M., Gaggeler, H. W., and Baltensperger, U. (1999). Historical record of carbonaceous particle concentrations from a european high-alpine glacier. *J. Geophys. Res*, **104**, 21227–21236.

Lesins, G., Chylek, P. V., and Lohmann, U. (2002). A study of internal and external mixing scenarios and its effect on aerosol optical properties and direct radiative forcing. *J. Geophys. Res*, **107 (D10)**. 4094, doi: 10.1029/2001JD000973.

Lilly, D. K. (1968). Models of cloud-topped mixed layers under a strong inversion. *Q. J. R. Meteorol. Soc*, **94**, 292–309.

Lin, C. I., Baker, M., and Charlson, R. J. (1973). Absorption coefficient of atmospheric aerosols: A method for measurement. *Appl. Opt.*, **12**, 1356–1363.

Liou, K. N. (1980). *Introduction to atmospheric radiation*. Academic press,, San Diego, California.

Liu, L., Mishchenko, M. I., Menon, S., Macke, A., and Lacis, A. A. (2002). Estimation of black carbon effect on light scattering and absorption by cloud water droplets. *Proceedings of the 11th Conference on Atmospheric Radiation. Amer. Meteorol. Soc.*, pages 36–38. Ogden, Utah, June 2002.

Livingstone, J. M., Kapustin, V. N., Schmid, B., Russell, P. B., Quinn, P. K., Bates, T. S., Durkee, P. A., Freudenthaler, P. J. S. V., Wiegner, M., Covert, D. S., Gasso, S., Hegg, D., Collins, D. R., Flagan, R. C., Seinfeld, J. H., Vitale, V., and Tomasi, C. (2000). Shipboard sunphotometer measurements of aerosol optical depth spectra and columnar water vapor during ACE-2, and comparison with selected land, ship, aircraft, and satellite measurements. *Tellus*, **52B**, 594–619.

Lock, A. P. (1996). *Entrainment in clear and cloudy boundary layers (PhD)*. Ph.D. thesis, University of Manchester Institute of Science and Technology, Department of Physics, Manchester, UK.

Lock, A. P. (2001). The numerical representation of entrainment in parameterization of boundary layer turbulent mixing. *Mon. Wea. Rev*, **129**, 1148–1163.

Lock, A. P. and Macvean, M. K. (1999). The parametrization of entrainment driven by surface heating

and cloud-top cooling. *Q. J. R. Meteorol. Soc*, **125**, 271–299.

Lock, A. P., Brown, A. R., Bush, M. R., Martin, G. M., and Smith, R. N. B. (2000). A new boundary layer mixing scheme. Part I: Scheme description and single-colomun tests. *Mon. Wea. Rev*, **128**, 3187–3199.

Lohmann, U. and Feichter, J. (2001). Can the direct and semi-direct aerosol effect compete with the indirect effect on a global scale? *Geophys. Res. Lett.*, **28**, 159–161.

Ma, C. C., Mechoso, C. R., Robertson, A. W., and Arakawa, A. (1996). Peruvian stratus clouds and the tropical circulation: A coupled ocean-atmosphere GCM study. *J. Clim*, **9**, 1635–1646.

Macke, A. (2000). Monte carlo calculations of light scattering by large particles with multiple internal inclusions in light scattering by non-spherical particles: Theory measurements and applications. Academic Press. San Diego. Editied by M. I. Mishchenok, J. W. Hovenier and L. D. Travis. pp.309-329.

Macvean, M. K. (1993). A numerical investigation of the criterion for cloud-top entrainment instability. *J. Atmos. Sci*, **50**, 2481–2495.

Markel, V. A. and Shalaev, A. M. (1999). Absorption of light by soot particles in micro-droplets of water. *J. Quant. Spec. and Radiat. Trans.*, **63**, 321–329.

Martin, G. M., Johnson, D. W., and Spice, A. (1994). The measurement and parameterisation of effective radius of droplets in warm stratocumulus clouds. *J. Atmos. Sci*, **51**, 1823–1842.

Martin, G. M., Johnson, D. W., Rogers, D. P., Jonas, P. R., Minnis, P., and Hegg, D. A. (1995). Observations of the interaction between cumulus clouds and warm stratoucmulus in the marine boundary layer during ASTEX. *J. Atmos. Sci*, **52**, 2902–2922.

Menon, S., Hansen, J., Nazarenko, L., and Luo, Y. (2002). Climate effects of black carbon aerosols in China and India. *Science*, **297**, 2250–2253.

Mie, G. (1908). Beigrade zur optik medien, speziell kolloidaler mettallosungen. *Ann. Physik.(4)*, **25**, 377–445.

Miller, R. L. (1997). Tropical thermostats and low cloud cover. *J. Clim*, **10**, 409–440.

Mitchell, J. F. B. and Johns, T. C. (1997). On modification of global warming by sulfate aerosols. *J. Clim*, **10**, 245–267.

Moeng, C. H. (2000). Entrainment rate, cloud fraction, and liquid water path of PBL stratocumulus clouds. *J. Atmos. Sci*, **57**, 3627–3643.

Moeng, C. H., Cotton, W. R., Bretherton, C. S., Chlond, A., Khairoutdinov, M., Kruegar, S., Lewellen, W. S., MacVean, M. K., Pasquier, J. R. M., Rand, H. A., Siebsma, A. P., Stevens, B., and Sykes, E. I. (1996). Simulation of a stratocumulus-topped planetary boundary layer: Intercomparison amoung

different numerical codes. *Bull. Amer. Meteor. Soc*, **77**, 261–278.

Muller, D. and Ansmann, A. (2002). European pollution outbreaks during ACE-2: Microphysical particle properties and single scattering albedo inferred from multiwavelength lidar observations. *J. Geophys. Res*, **107 (D15)**. 4248, doi: 10.1029/2001JD001110.

Neggers, R. A. J., Jonker, H. J. J., and Siebesma, A. P. (2003). Size statistics of cumulus cloud populations in large-eddy simulations. *J. Atmos. Sci*, **60**, 1060–1074.

Nicholls, S. (1984). The dynamics of stratocumulus: Aircraft observations and comparison with a mixed layer model. *Q. J. R. Meteorol. Soc*, **110**, 783–870.

Nicholls, S. and Leighton, J. (1986). An observational study of the structure of stratiform cloud sheets. Part I: Structure. *Q. J. R. Meteorol. Soc*, **112**, 431–460.

Nieuwstadt, F. T. M. and Duynkerke, P. G. (1996). Turbulence in the atmospheric boundary layer. *Atmos. Res.*, **40**, 111–142.

Nitta, T. (1975). Observational determination of cloud mass flux distributions. *J. Atmos. Sci*, **32**, 73–91.

Nitta, T. and Esbensen, S. (1974). Heat and moisture budget analyses using BOMEX data. *Mon. Wea. Rev*, **102**, 17–28.

Osborne, S. R., Johnson, D. W., Wood, R., Bandy, B. J., Andreae, M. O., O'Dowd, C. D., Glantz, P., Noone, K. J., Gerbig, C., Rudolph, J., Bates, T. S., and Quinn, P. (2000). Evolution of the aerosol, cloud and boundary-layer dynamic and thermodynamic characteristics during the 2nd Lagrangian experiment of ACE-2. *Tellus*, **52B**, 375–400.

Ostrom, E. and Noone, K. J. (2000). Vertical profiles of aerosol scattering and absorption measured in situ during the North Atlantic Aerosol Characterization Experiment ACE-2. *Tellus*, **52B**, 526–545.

Ovtchinnikov, M., Mechem, D. B., Kogan, Y. L., Ackerman, T. P., cahalan, R. F., Davis, A. B., Ellingson, R., and Takara, E. (2002). Longwave cooling rates in inhomogeneous stratocumulus clouds: 3D radiation transfer versus independent pixel approximation calculations. *Proceedings of the 11th Conference on Cloud Physics and Atmospheric Radiation. Amer. Meterol. Soc.*, page J177. Ogden, Utah, June, 2002.

Paluch, I. R. and Lenschow, D. H. (1991). Stratiform cloud formation in the marine boundary layer. *J. Atmos. Sci*, **48**, 2141–2158.

Pelly, J. L. and Belcher, S. E. (2001). A mixed layer model of the well-mixed stratocumulus-topped boundary layer. *Bound. Lay. Meteorol.*, **100**, 171–187.

Pennell, W. T. and Monde, M. A. L. (1974). An experimental study of turbulence structure in the fair-weather trade-wind boundary layer. *J. Atmos. Sci*, **31**, 1308–1323.

Penner, J. E. and Zhang, S. Y. (2003). Soot and smoke may not warm climate. *J. Geophys. Res*, **108 (D21)**. 4657, doi:10.1029/2003/JD003409.

Philander, S. G. H., Gu, D., Lambert, G., Li, T., Halpern, D., Lau, N. C., and Pacanowski, R. C. (1996). Why the ITCZ is mostly north of the equator. *J. Clim.*, **9**, 2958–2972.

Pincus, R. and Klein, S. A. (2000). Unresolved spatial variability and microphysical process rates in large-scale models. *J. Geophys. Res*, **102**, 27059–27065.

Plank, V. G. (1969). The size distributions of cumulus clouds in representative Florida population. *J. Appl. Meteorol.*, **8**, 46–67.

Podgorny, I. A., Conant, W., Ramanathan, V., and Satheesh, S. K. (2000). Aerosol modulation of atmospheric and surface solar heating over the tropical Indian Ocean. *Tellus*, **52B**, 947–958.

Putaud, J. P., Dingenen, R. V., Mangoni, M., Virkkula, A., Raes, F., Maring, H., Prospero, J. M., Swietlicki, E., Berg, O. H., Hillamo, R., and Makela, T. (2000). Chemical mass closure and assessment of the origin of the submicron aerosol in the marine boundary layer and the free troposphere at Tenerife during ACE-2. *Tellus*, **52B**, 141–168.

Quinn, P., Bates, T. S., Coffman, D. J., Miller, T. L., Johnson, J. E., Covert, D. S., Putaud, J. P., Neusub, C., and Novakov, T. (2000). A comparison of aerosol chemical and optical properties from the 1st and 2nd Aerosol Characterisation Experiments. *Tellus*, **52B**, 239–257.

Raes, F., Bates, T., McGovern, F., and Liedekerke, M. (2000). The 2nd Aerosol Characterization Experiment (ACE-2): General overview and main results. *Tellus*, **52B**, 111–125.

Ramanathan, V. and Downey, P. (1986). A non-isolthermal emissivity and absorptivity formulation for water vapor. *J. Geophys. Res*, **91**, 8649–8666.

Ramanathan, V., Barkstrom, B. R., and Harrison, E. F. (1989). Climate and the Earth's radiation budget. *Physics Today*, **42**, 22–32.

Ramanathan, V., Crutzen, P. J., and Rossenfeld, D. (2001a). Aerosols, climate and the hydrological cycle. *Science*, **294**, 2119–2124.

Ramanathan, V., Crutzen, P. J., Lelieveld, J., Mitra, A. P., Althausen, D., Anderson, J., Andreae, M. O., Cantrell, W., Cass, G. R., Chung, C. E., Clarke, A. D., Coakley, J. A., Collins, W. D., Conant, W. C., Dulac, F., Heintzenberg, J., Heymsfield, A. . J., Holben, B., Howell, S., Hudson, J., Jayaraman, A., Kiehl, J. T., Krishnamurti, T. N., Lubin, D., McFarquhar, G., Novakov, T., Ogren, J. A., Podgorny, I. A., Prather, K., Priestley, K., Prospero, J. M., Quinn, P. K., Rajeev, K., Rasch, P., Rupert, S., Sadourny, R., Satheesh, S. K., Shaw, G., Sheridan, P., and Valero, F. P. J. (2001b). Indian Ocean Experiment: An integrated analysis of the climate forcing and effects of the great Indo-Asian haze. *J. Geophys. Res*, **106**, 28371–28398.

Randall, D. A. (1980). Conditional instability of the first kind upside-down. *J. Atmos. Sci*, **37**, 125–130.

Randall, D. A., Coakley, J. A., Fairall, C. W., Kropfli, R. A., and Lenschow, D. H. (1984). Outlook for research on subtropical marine stratiform clouds. *Bull. Amer. Meteor. Soc*, **65**, 1290.

Riehl, H., Yeh, C., Malkus, J. S., and Seur, N. E. L. (1951). The northeast trade of the Pacific Ocean. *Q. J. R. Meteorol. Soc*, **77**, 598–626.

Roach, W. T., Brown, R., and Caughey, S. J. (1982). A field study of nocturnal stratocumulus: I. Mean sturcture and budgets. *Q. J. R. Meteorol. Soc*, **108**, 103–123.

Roeckner, E., Bengtsson, L., Feichter, J., Lelieveld, J., and Rodhe, H. (1999). Transient climate change simulations with a coupled atmosphere-ocean GCM including the tropospheric sulfur cycle. *J. Clim.*, **12**, 3004–3032.

Rogers, D. P., Yang, X., Norris, P. M., Johnson, D. W., Martin, G. M., Friehe, C. A., and Berger, B. W. (1995). Diurnal evolution of the cloud-topped marine boundary layer. Part 1. Nocturnal stratocumulus development. *J. Atmos. Sci*, **52**, 2953–2966.

Rossow, W. B. and Schiffer, R. A. (1999). Advances in understanding clouds from ISCCP. *Bull. Amer. Meteor. Soc*, **80**, 2261–2288.

Rotstayn, L. (1999a). Indirect forcing by anthropogenic aerosols: A general circulation model calculation of the effective-radius and cloud lifetime effects. *J. Geophys. Res*, **104**, 9369–9380.

Rotstayn, L. D. (1997a). A physically based scheme for the treatment of stratiform clouds and precipitation in large-scale models .1. Description and evaluation of the microphysical processes. *Q. J. R. Meteorol. Soc*, **123**, 1227–1282.

Rotstayn, L. D. (1997b). A physically based scheme for the treatment of stratiform clouds and precipitation in large-scale models. II: Comparison of modelled and observed climatological fields. *Q. J. R. Meteorol. Soc*, **124**, 389–415.

Rotstayn, L. D. (1999b). Climate sensitivity of the CSIRO GCM: Effect of cloud modeling assumptions. *J. Clim.*, **12**, 334–356.

Rotstayn, L. D. and Lohmann, U. (2002). Tropical rainfall trends and the indirect aerosol effect. *J. Clim.*, **15**, 2103–2116.

Russell, P. B., Hobbs, P. V., and Stowe, L. L. (1999). Aerosol properties and radiative effects in the United States East Coast haze plume: An overview of the Tropospheric Aerosol Radiative Forcing Observational Experiment (TARFOX). *J. Geophys. Res*, **104**, 2213–2222.

Russell, P. B., Redemann, J., Schmid, B., Bregstrom, R. W., Livingstone, J. M., McIntosh, D. M., Ramirez, S. A., Hartley, S., P.V.Hobbs, Quinn, P. K., Carrico, C. M., Rood, M. J., Ostrom, E.,

Noone, K. J., vov Hoyningen-Huene, W., and Remer, L. (2002). Comparison of aerosol single scattering albedos derived from diverse techniques in two North Atlantic experiments. *J. Atmos. Sci*, **59**, 609–619.

Satheesh, S. K. and Ramanathan, V. (2000). Large differences in tropical aerosol forcing at the top of the atmosphere and Earth's surface. *Nature*, **405**, 60–62.

Schmid, B., Livingstone, J. M., Russell, R. B., Durkee, P. A., Jonsson, H. H., Collins, D. R., Flagan, R. C., Seinfeld, J. H., Gasso, S., Hegg, D. A., Ostrom, E., Noone, K. J., Welton, E. J., Voss, K. J., Gordon, H. R., Formenti, P., and Andreae, M. O. (2000). Clear-sky closure studies of lower tropospheric aerosol and water vapor during ACE-2 using airborne sunphotometer, airborne in-situ, space-borne, and ground-based measurements. *Tellus*, **52B**, 568–593.

Schubert, W. H., Ciesielski, P. E., McKee, T. B., Kleist, J., Cox, S. K., Johnson-Pasqua, C. M., and jr, W. L. S. (1987a). Ananlysis of boundary layer sounding dataa from the FIRE marine stratocumulus project. *Colorado State University, Atmospheric Science, Ft. Collins, CO 80523. Paper No.*, **419**, 101.

Schubert, W. H., andP. E. Ceisielski, S. K. C., and Johnson-Pasqua, C. M. (1987b). Operation of a ceilometer during the FIRE marine stratocumulus experiment. *Colorado State University, Atmospheric Science, Ft. Collins, CO 80523. Paper No.*, **420**, 34.

Schwartz, S. E. and Slingo, A. (1995). Enhanced shortwave cloud radiative forcing due to anthropogenic aerosols, in clouds, chemistry and climate. *Global Environment*, **35**, 191–235.

Siebema, A. P. and Holtslag, A. A. M. (1996). Model impacts of entrainment and detrainment rates in shallow cumulus convection. *J. Atmos. Sci*, **53**, 2354–2364.

Siebesma, A. P. and Cuijpers, J. W. M. (1995). Evaluation of parametric assumptions for shallow cumulus convection. *J. Atmos. Sci*, **52**, 650–666.

Siebesma, A. P., Bretherton, C. S., Brown, A., Chlond, A., Cuxart, J., Duynkerke, P. G., Jiang, H., Khairoutdinov, M., Lewellen, D., Moeng, C., Sanchez, E., Stevens, B., and Stevenss, D. E. (2003). A large-eddy simulation intercomparison study of shallow cumulus convection. *J. Atmos. Sci*, **60**, 1201–1219.

Siems, S. T., Bretherton, C. S., Baker, M. B., Shy, S., and Breidenthal, R. E. (1990). Bouyancy reversal and cloud top entrainment instability. *Q. J. R. Meteorol. Soc*, **116**, 705–739.

Slingo, A., Borwn, R., and Wrench, C. L. (1982). A field study of nocturnal stratocumulus: III. High resolution radiative and microphysical observations. *Q. J. R. Meteorol. Soc*, **108**, 145–165.

Slingo, J. M. (1987). The development and verification of a cloud prediction scheme for the ECMWF model. *Q. J. R. Meteorol. Soc*, **113**, 899–927.

Smagorinsky, J., Manabe, S., and J. L. Holloway, J. (1965). Numerical results from a nine-level general circulation model of the atmosphere. *Mon. Wea. Rev*, **93**, 727–768.

Smith, R. N. B. (1990). A scheme for predicting layer clouds and their water content in a general circulation model. *Q. J. R. Meteorol. Soc*, **116**, 435–460.

Smith, W. S. and Kao, C. Y. J. (1996). Numerical simulations of the marine stratocumulus-capped boundary layer and its diurnal variation. *Mon. Wea. Rev*, **124**, 1803–1816.

Snider, J. B. (1988). Radiometric observations of liquid water during FIRE. *Proc. IGARSS Symp.* Edinburgh. September, 1988, pp.261-262.

Sommeria, G. (1976). Three-dimensional simulation of turbulent processes in an undistorted trade wind boundary layer. *J. Atmos. Sci*, **33**, 216–241.

Soong, S. T. and Ogura, Y. (1980). Response of trade wind cumulus to large scale processes. *J. Atmos. Sci*, **37**, 2035–2050.

Stevens, B., Ackerman, A. S., Albrecht, B. A., Brown, A. R., Chlond, A., Cuxart, J., Duynkerke, P. G., Lewellen, D. C., MacVean, M. K., Neggers, R. A. J., Sanchez, E., and Siebesma, A. P. (2001). Simulations of trade wind cumuli under a strong inversion. *J. Atmos. Sci*, **58**, 1870–1891.

Stevens, D. E. (2002). Effects of domain size and numerical resolution on the simulation of shallow cumulus convection. *J. Atmos. Sci*, **59**, 3285–3301.

Strapp, J. W., Leaitch, W. R., and Liu, P. S. K. (1992). Hydrated and dried aerosol size distribution measurements from the Particle Measuring Systems FSSP-300 probe and the deiced PCASP-100X probe. *J. Atmos. and Oceanic Tech.*, **9**, 548–555.

Stull, R. B. (1985). A fair weather cumulus cloud classification scheme for mixed-layer studies. *J. Climate Appl. Meteor.*, **24**, 49–56.

Syrett, W. J. (1988). Hourly wind, potential temperature and Richardson number profiles at San Nicholas Island during project FIRE. *FIRE Technical Report No. 2, Department of Meteorology, Penn State University, 503 Walker Building, University Park, PA 16803, USA*, page 49.

Tang, I. and Munkelwitz, H. R. (1977). Aerosol growth studies, III, ammonium bisulphate aerosols in a moist atmosphere. *J. Aerosol. Sci.*, **8**, 321–330.

Tang, I. N., Wong, W. T., and Munkelwitz, H. R. (1981). The relative importance of atmospheric sulphates and nitrates in visibility reduction. *Atmos. Env.*, **15**, 2463–2471.

Taylor, J. P., Glew, M. D., Coakley, J. A., Tahnk, W. R., Platnick, S., Hobbs, P. V., and Ferek, R. J. (2000). Effects of aerosols on the radiative properties of clouds. *J. Atmos. Sci*, **57**, 2656–2670.

Tett, S. F. B., andM. A. Allen andW. J. Ingram, P. A. S., and Mitchell, J. F. B. (1999). Causes of twentieth century warming. *Nature*, **399**, 569–572.

Tiedtke, M. (1993). Representation of clouds in large-scale models. *Mon. Wea. Rev*, **121**, 3040–3061.

Twomey, S. A. (1977). The influence of pollution on the shortwave albedo of clouds. *J. Atmos. Sci*, **34**, 1148–1152.

Vean, M. K. M. and Mason, P. J. (1990). Cloud top entrainment instability through small-scale mixing and its parametrization. *J. Atmos. Sci*, **47**, 1012–1030.

Verver, G., Raes, F., Vogelezang, D., and Johnson, D. (2000). The 2nd Aerosol Characterization Experiment (ACE-2): Meteorological and chemical context. *Tellus*, **52B**, 126–140.

Wang, Q. and Albrecht, B. A. (1994). Observations of cloud-top entrainment in marine stratocumulus clouds. *J. Atmos. Sci*, **51**, 1530–1547.

Wang, S. P. and Wang, Q. (1994). Roles of drizzle in a one-dimensional 3rd-order turbulence closure-model of the nocturnsl stratus-topped marine boundary-layer. *J. Atmos. Sci*, **51**, 1559–1576.

Wang, S. P., Wang, Q., and G, G. F. (2003). Turbulence, condensation, and liquid water transport in numerically simulated nonprecipitating stratocumulus clouds. *J. Atmos. Sci*, **60**, 262–278.

WCP (1986). A preliminary cloudless atmosphere for radiation computation. *Technical Report of the World Climate Programme WCP-112, WMO/TD-BO.24*. World Meteorological Organization, Geneva.

Whitby, K. T. (1984). Physical and optical behavoiur of sulphate-nitrate aerosols in equilibrium with atmospheric water vapour, ammonia and nitric acid. *Hygroscopic Aerosols*. L. H. Runke and A. Deepak (Eds.), pp45-63.

White, A. B. (1989). Temperature and humidity structure parameters deduced from sodar and radar reflectivities: An analysis of data from the marine stratocumulus phase of FIRE. *M.S. Thesis, Pennsylvania Sate University, Separtment of Meteorology, University Park, PA 16802*, page 137.

Wood, R., Johnson, D., Osborne, S., Andreae, M. O., Brandy, B., Bates, T. S., O'Dowd, C., Glantz, P., Noone, K., Quinn, P. K., Rudolph, J., and Suhre, K. (2000). Boundary layer and aerosol evolution during the 3rd langrangian experiment of ACE-2. *Tellus*, **52B**, 401–422.

Wyant, M. C., Bretherton, C. S., Rand, H. A., and Stevens, D. E. (1997). Numerical simulations and a conceptual model of the stratocumulus to trade cumulus transition. *J. Atmos. Sci*, **54**, 168–192.

Yao, M. S. and DelGenio, A. D. (1999). Effects of cloud parameterization on the simulation of climate changes in the GISS GCM. *J. Clim.*, **12**, 761–779.

Zhao, Q. Y. and Carr, F. H. (1997). A prognostic cloud scheme for operational NWP models. *Mon. Wea. Rev*, **125**, 1931–1953.

Zhao, Q. Y., Black, T. L., and Baldwin, M. E. (1997). Implementation of the cloud prediction scheme in the Eta model at NCEP. *Weather and forecasting*, **12**, 697–712.